

FAILURE ANALYSIS & MATERIAL EVALUATION
OF TMP REFINER PLATES

Yuding Jia

B.S., Xi'an Jiaotong University, Xi'an, China, 1982

M.S., Xi'an Jiaotong University, Xi'an, China, 1985

A dissertation submitted to the faculty of the
Oregon Graduate Institute of Science & Technology
in partial fulfillment of the requirements for the degree of
Doctor of Philosophy
in
Materials Science & Engineering

July 1996

The dissertation "Failure Analysis and Material Evaluation of TMP Refiner Plates" by Yuding Jia has been examined and approved by the following Examination Committee:

Paul Clayton, Thesis Advisor
Professor

Milt Scholl
Assistant Professor

David G. Atteridge
Professor

✓
Jack H. Devletian
Professor

ACKNOWLEDGEMENTS

First of all, I would like to thank the Forest Products Laboratory in Madison, Wisconsin for providing financial support during the course of this research. Special thanks are due to my thesis advisor, Dr. Paul Clayton, for the time, patience, and attention that he devoted to me and my research work and thesis writing. I am grateful to Dr. Milt Scholl for his generous help and valuable instruction during my thesis work. Deep thanks are also extended to the other members of my dissertation committee, Dr. Dave Atteridge and Dr. Jack Devletian, for their time and effort in reviewing the manuscript. Finally, I would like to thank everyone who has helped me throughout the years that I spent at OGI.

TABLE OF CONTENTS

TITLE PAGE	i
ACKNOWLEDGEMENTS	iii
TABLE OF CONTENTS	iv
LIST OF TABLES	vii
LIST OF FIGURES	viii
ABSTRACT	xiii
CHAPTER 1. PREFACE	1
CHAPTER 2. BACKGROUND	4
2.1. PULPING	4
2.1.1. Pulpwood	4
2.1.2. Pulping	6
2.1.3. Pulp	8
2.1.4. TMP Refining	9
2.2. TMP REFINER PLATE	10
2.2.1. Plate Design	10
2.2.2. Plate Alloy	14
2.2.3. Plate Damage	15
2.2.4. Plate Performance	17
2.3. PLATE FAILURE MECHANISMS	21
2.3.1. Material Failure Mechanisms	21
2.3.2. Plate Failure Analysis	30
2.4. PLATE MATERIALS	33

2.4.1. Plate Alloy Evaluation	33
2.4.2. Plate Material Development	36
2.5. PLASMA SPRAYING	38
2.5.1. Process Fundamentals	39
2.5.2. Physical Properties	41
2.5.3. Wear Performance	44
CHAPTER 3 EXPERIMENTAL	81
3.1. PLATE FAILURE ANALYSIS	81
3.1.1. Interrupted Mill Trials	81
3.1.2. Plate Damage Examination	81
3.1.3. Plate Damage Measurements	82
3.2. PLATE MATERIAL EVALUATION	84
3.2.1. Plate Alloys	84
3.2.2. Plasma Coatings	85
3.2.3. Wear Testing	86
CHAPTER 4 RESULTS	108
4.1. PLATE DAMAGE MEASUREMENT	108
4.1.1. Serration Damage	108
4.1.2. Pitting Damage	109
4.1.3. Bar Rounding Damage	110
4.2. PLATE DAMAGE OBSERVATION	110
4.2.1. Serration Damage	110
4.2.2. Pitting Damage	113
4.2.3. Bar Rounding Damage	115
4.3. WEAR TESTING OF PLATE ALLOYS	116
4.3.1. Alloy Characterization	116

4.3.2. Laboratory Wear Testing	118
4.3.3. Worn Surface Examination	119
4.4. WEAR TESTING OF PLASMA COATINGS	120
4.4.1. Coating Characterization	120
4.4.2. Wear Testing of Coatings	122
4.4.3. Worn Surface Examination	124
CHAPTER 5. DISCUSSION	190
5.1. PLATE FAILURE ANALYSIS	190
5.1.1. Serration Damage	190
5.1.2. Pitting Damage	196
5.1.3. Bar Rounding	204
5.2. PERFORMANCE EVALUATION	209
5.2.1. Wear Performance of Plate Alloys	209
5.2.2. Wear Performance of Plasma Coatings	214
5.2.3. Optimization of Coating Performance	216
5.2.4. Potential of Plasma Spraying in TMP Refining	221
CHAPTER 6 CONCLUSIONS	243
REFERENCES	245

LIST OF TABLES

Table 2.1. Properties of North American Pulpwoods [1]	48
Table 2.2. Typical Compositional Ranges For Plate Alloys [17]	49
Table 2.3. Qualitative Service Performance of Refiner Plate Alloys [17]	50
Table 3.1. Interrupted Mill Trials	89
Table 3.2. Plate Alloy Compositions	90
Table 3.3. Powder Compositions and Sizes	91
Table 3.4. Powder Physical Properties [120,161]	92
Table 3.5. Deposition Parameters	93
Table 4.1. Characteristics for Plates Removed from Trials 4 and 5	126
Table 4.2. Serrated Bar Top Surface Area Fraction	127
Table 4.3. Serrated Zone Width	128
Table 4.4. Pitted Bar Top Surface Area Fraction	129
Table 4.5. Pitted Bar Leading Edge Length Fraction	130
Table 4.6. Maximum Bar Rounded Width	131
Table 4.7. Characteristics of Plate Alloys	132
Table 4.8. Wear Rate of Plate Alloys	133
Table 4.9. Coating Characteristics	134
Table 4.10. Characteristics of Two Groups of Coatings	135
Table 4.11. Comparison of Coating's Wear Behavior by Samples	136
Table 4.12. Comparison of Coating's Wear Behavior by Groups	137
Table 4.13. Wear Rate of Fe-Mo-C and WC-Co Coatings	138
Table 4.14. Volume Loss Rate of All Materials Tested	139
Table 5.1. Hardness of Abrasives and Second Phases [46]	223

LIST OF FIGURES

Figure 1.1. Thesis scope.	3
Figure 2.1. Cross-sectional sketch of a mature stem [1].	51
Figure 2.2. Cell wall organization [6].	52
Figure 2.3. Microscopic and submicroscopic structure of cellulose [7].	53
Figure 2.4. Pulp properties.	54
Figure 2.5. TMP refiner system [9].	55
Figure 2.6. Fiber-to-fiber and fiber-to-metal contact during refining [1].	56
Figure 2.7. A typical TMP refiner plate.	57
Figure 2.8. Bar strength ratio [14].	58
Figure 2.9. Bars, grooves, and dams.	59
Figure 2.10. Plate taper [8].	60
Figure 2.11. Refiner plate specific volume curve [8].	61
Figure 2.12. Serration damage.	62
Figure 2.13. Pitting damage.	63
Figure 2.14. Bar rounding damage.	64
Figure 2.15. Plate deterioration modes and mechanisms.	65
Figure 2.16. Physical interactions between abrasives and surface of material in abrasion [47].	66
Figure 2.17. Ratio of microcutting to microplowing as a function of the ratio δ the attack angle α to the critical attack angle α_c [47].	67
Figure 2.18. Two-body abrasion and three-body abrasion.	68
Figure 2.19. Asperity bonding, asperity rupture, metal transfer, and debris formation in adhesion.	69
Figure 2.20. Mechanisms of wear during sliding contact [47].	70
Figure 2.21. Formation of wear sheets due to delamination [47].	71

Figure 2.22. Low angle erosion and high angle erosion.	72
Figure 2.23. Schematic representation of successive stages of nonsymmetrical cavity collapse with microjet impingement against a metallic surface [78].	73
Figure 2.24. Liquid impingement erosion by liquid jet or drop [61].	74
Figure 2.25. Schematic of pitting corrosion processes at an actively growing pit in iron [109].	75
Figure 2.26. Surface engineering.	76
Figure 2.27. Plasma spraying process [61].	77
Figure 2.28. Wire feed and powder feed.	78
Figure 2.29. Plasma spraying process variables.	79
Figure 2.30. Cross-section of plasma coating.	80
Figure 3.1. Sectioning of specimens from damaged plate.	94
Figure 3.2. Surface examination and subsurface examination.	95
Figure 3.3. Serrated area fraction and pitted area fraction.	96
Figure 3.4. Maximum bar rounded width.	97
Figure 3.5. Serrated zone width.	98
Figure 3.6. Pitted bar leading edge fraction.	99
Figure 3.7. Maximum surface displacement and deformed surface layer thickness.	100
Figure 3.8. Secondary dendritic arm spacing.	101
Figure 3.9. Schematic of the spray gun.	102
Figure 3.10. Metallographic coating specimen.	103
Figure 3.11. Roughness average - R_a	104
Figure 3.12. Schematic of abrasion test.	105
Figure 3.13. Schematic of erosion test.	106
Figure 3.14. Schematic of cavitation erosion test.	107
Figure 4.1. Serrated surfaces in the "smooth regions" for C20 plates.	140

Figure 4.2. Serrated subsurfaces in the "smooth regions" for C20 plates.	141
Figure 4.3. Serrated surfaces and subsurfaces in the "smooth regions" for C20 plates.	142
Figure 4.4. Serrated surfaces in the "rough regions" for C20 plates.	143
Figure 4.5. Serrated subsurfaces in the "rough regions" for C20 plates.	144
Figure 4.6. Serrated surfaces in the "smooth regions" for S17 plates.	145
Figure 4.7. Serrated subsurfaces in the "smooth regions" for S17 plates.	146
Figure 4.8. Serrated surfaces in the "rough regions" for S17 plates.	147
Figure 4.9. White surface layers near the bar trailing edges in the "smooth regions".	148
Figure 4.10. Deep pits in the pitted bar leading edges of the C20 plates.	149
Figure 4.11. Pitting damage process in the bar leading edges of the C20 plates.	150
Figure 4.12. Pitting damage process in the bar leading edges of the S17 plates.	151
Figure 4.13. Carbides at the pitted bar leading edges of C20 and S17 plates. . .	152
Figure 4.14. Pitting process on the pitted C20 plate bar leading edges.	153
Figure 4.15. Pitted bar leading edges of C20 and S17 plates.	154
Figure 4.16. Fatiguelike cracks on the pitted C20 plate bar leading edges. . . .	155
Figure 4.17. Rounded bar leading edges of C20 plates with whitewood and Douglas fir.	156
Figure 4.18. Rounded bar leading edges of C20 plates and S17 plates.	157
Figure 4.19. Microstructures of Ni-hard alloys and 20-2-1 alloys.	158
Figure 4.20. Microstructures of 440C steels, 25Cr iron, and 17-4 PH steel. . .	159
Figure 4.21. Plate alloy bulk hardness versus carbide hardness and matrix hardness.	160
Figure 4.22. DSRW abraded surfaces of 20-2-1 iron and Ni-hard iron.	161
Figure 4.23. DSRW abraded surfaces of 440C steel and 17-4 PH steel.	162

Figure 4.24. Eroded plate alloy surfaces.	163
Figure 4.25. Eroded plate alloy surfaces.	164
Figure 4.26. Various pits on the cavitation eroded alloy surfaces.	165
Figure 4.27. Various pits on the cavitation eroded alloy surfaces.	166
Figure 4.28. Cavitation eroded surfaces of various plate alloys.	167
Figure 4.29. Microstructures of alloy coatings.	168
Figure 4.30. Microstructures of ceramic coatings and cermet coatings.	169
Figure 4.31. Microstructures of cermet coatings.	170
Figure 4.32. Coating hardness versus spray distance.	171
Figure 4.33. Coating surface roughness versus spray distance.	172
Figure 4.34. Coating surface roughness versus powder size.	173
Figure 4.35. Hardness versus porosity for Fe-Mo-C and WC-Co coatings.	174
Figure 4.36. Surface roughness versus splat thickness for Fe-Mo-C coatings.	175
Figure 4.37. Abrasion rate versus spray distance.	176
Figure 4.38. Cavitation erosion rate versus powder size.	177
Figure 4.39. Correlations of abrasion rate with erosion and cavitation erosion rates.	178
Figure 4.40. Erosion and cavitation erosion rates versus coating hardness.	179
Figure 4.41. Erosion and cavitation erosion rates versus coating porosity.	180
Figure 4.42. Abrasion rate versus coating porosity.	181
Figure 4.43. Cavitation erosion rate versus surface roughness.	182
Figure 4.44. Cavitation erosion rate versus splat thickness for Fe-Mo-C coatings.	183
Figure 4.45. Comparison of cavitation erosion rate.	184
Figure 4.46. Comparison of erosion rate.	185
Figure 4.47. Comparison of abrasion rate.	186
Figure 4.48. Abraded coating surfaces.	187
Figure 4.49. Eroded coating surfaces.	188

Figure 4.50. Cavitation eroded coating surfaces.	189
Figure 5.1. Schematic of a disk refiner set-up.	224
Figure 5.2. Formation of circumferential grooving.	225
Figure 5.3. "Smooth region" and "rough region".	226
Figure 5.4. Formation of "smooth region" and "rough region".	227
Figure 5.5. Wood density and serration damage.	228
Figure 5.6. Local pressure pulse near a bar leading edge.	229
Figure 5.7. Performance ranking in pitting damage rate and cavitation erosion rate for 440C and 20-2-1 alloys.	230
Figure 5.8. Cavitation erosion in the breaker bar zone.	231
Figure 5.9. Cavitation erosion in the refining zone.	232
Figure 5.10. Liquid impingement erosion in the refining zone.	233
Figure 5.11. Pitting performance ranking for 440C and 20-2-1 plates worked with whitewood.	234
Figure 5.12. Comparison of bar rounding damage resistance and abrasion resistance.	235
Figure 5.13. Abrasion rate versus bulk hardness for plate alloys.	236
Figure 5.14. Cavitation damage versus Cr/C ratio for some carbide-containing alloys.	237
Figure 5.15. Total interfaces and splat size, porosity, and crack density.	238
Figure 5.16. Coating structure versus powder melting point.	239
Figure 5.17. Temperature and axial velocity isocontours for an Ar/H ₂ plasma.	240
Figure 5.18. Spray energy and coating microstructure.	241
Figure 5.19. Traverse speed and Traverse distance.	242

ABSTRACT

FAILURE ANALYSIS & MATERIAL EVALUATION OF TMP REFINER PLATES

Yuding Jia

Supervising Professor: Paul Clayton

In TMP process, refiner plates can play a significant role in the operation of any refiner which is the heart of the TMP refining system. During service, the plate surfaces usually deteriorate rapidly which may not only cause a shorter plate working life but also a reduced refining efficiency and pulp quality. To substantially improve the plate performance, the plate damage process must be fully understood and the plate materials must be well optimized. To date, however, no systematic plate failure analyses and material evaluation have been conducted.

The plate deterioration process was studied in terms of plate life, plate alloy, and wood species by performing the surface damage measurements and observations on the plates removed from various interrupted mill trials. The wear behavior of eight conventional plate alloys were evaluated under laboratory abrasion, erosion, and cavitation erosion test conditions, with the worn surfaces being examined and compared with those of the deteriorated refiner plates. To explore the potential of plasma spraying techniques in TMP refiner applications, various plasma coatings were deposited and examined in the three laboratory wear tests, and their wear rates were compared with those of the existing plate alloys.

Three major plate surface damage modes were identified: serration, bar rounding, and pitting, which occurred primarily early, middle, and late in the plate life, respectively. It was found that the serration damage was due to sliding wear during plate-to-plate contact, and the bar rounding was attributable mainly to abrasion/erosion. Breaker bar zone pitting can be attributed to cavitation erosion, while refining zone pitting was caused by very similar mechanism(s).

The laboratory abrasion and cavitation erosion tests are relevant to plate damage environment and can be used together to evaluate the durability of plate materials in TMP refining. The 20-2-1 and the 440C alloys were superior in abrasion and cavitation erosion behavior, respectively, while the 25Cr iron had better trade-off wear performance. Compared to the cast alloys, the plasma coatings were much less erosion and cavitation erosion resistant, but could be much more abrasion resistant and therefore still promising in some TMP refiner applications.

CHAPTER 1. PREFACE

Pulping is the process by which wood is reduced to a fibrous mass, or the means of rupturing the bonds within the wood structure [1]. Compared to other pulping processes, TMP (thermomechanical pulping) which was first commercialized in 1972 [2] is now a fast growing method with advantages of better pollution abatement and resource-saving than chemical pulping and higher pulp strengths than traditional mechanical pulping. However, TMP requires much greater energy than traditional mechanical pulping processes [1]. Also, TMP cannot replace chemical pulping in many applications due to inferior pulp strength properties. Instead, chemical pulps are often used as a reinforcement for mechanical pulps by additions of up to 20%. The major concerns in TMP, therefore, are the pulp quality and the energy expenditure.

Both pulp quality and refining efficiency, which is defined as the total energy expended per unit weight of pulp for a given pulp quality, have been well correlated to many process variables except the refiner plate. The plates play a significant role in the operation of any refiner which is the heart of the TMP refining system. Thus, great attention must be paid on plate performance in TMP refining. Here the term "performance" refers mainly to the pulp quality and the refining efficiency.

A literature review indicates that both increased pulp residence time and reduced plate surface damage may lead to better TMP refining performance. Being proportional to the friction coefficient between the wood particles and the disks, the pulp residence time is the time that the wood particles spend in the refining zone, and can, therefore, be substantially increased by changing the plate topography.

On the other hand, as all existing plate alloys are simply adapted from other industries regardless of the TMP refining environments and requirements, the plate bar leading edges and bar top surfaces usually deteriorate quickly, causing poor energy transfer and pulp properties. It should be possible, then, to increase the residence time by modifying the plate surface texture and reduce the plate surface damage through improving the plate metallurgy or by modifying plate surface properties.

Surface engineering may be the most promising way to improve the TMP refiner plate performance as it can modify the surface texture and surface properties of workpieces simultaneously. Of the many surface engineering methods, plasma spraying may best fit the TMP refiner application due to its versatility, efficiency, and ability to change the plate surface roughness and surface material. However, in order to select candidate materials for plasma spraying the plate failure mechanisms must be understood and the wear performance of both existing plate alloys and potential plasma coatings must be evaluated. As shown in Figure 1.1, therefore, the current study focuses mainly on plate failure analysis and material performance evaluation using various interrupted mill trials and laboratory wear tests of both plate materials and plasma sprayed coatings.

This thesis contains five chapters. The current chapter gives a brief and overall introduction to this research project. In the background section, Chapter 2, a detailed literature review is presented, involving pulping, TMP refining, plate failure mechanisms, plate materials, and plasma spraying. Experimental procedures for plate failure analysis and plate material evaluation are described in Chapter 3. The experimental results and discussions are given in Chapter 4 and Chapter 5 respectively. Finally, the conclusions are listed in Chapter 6.

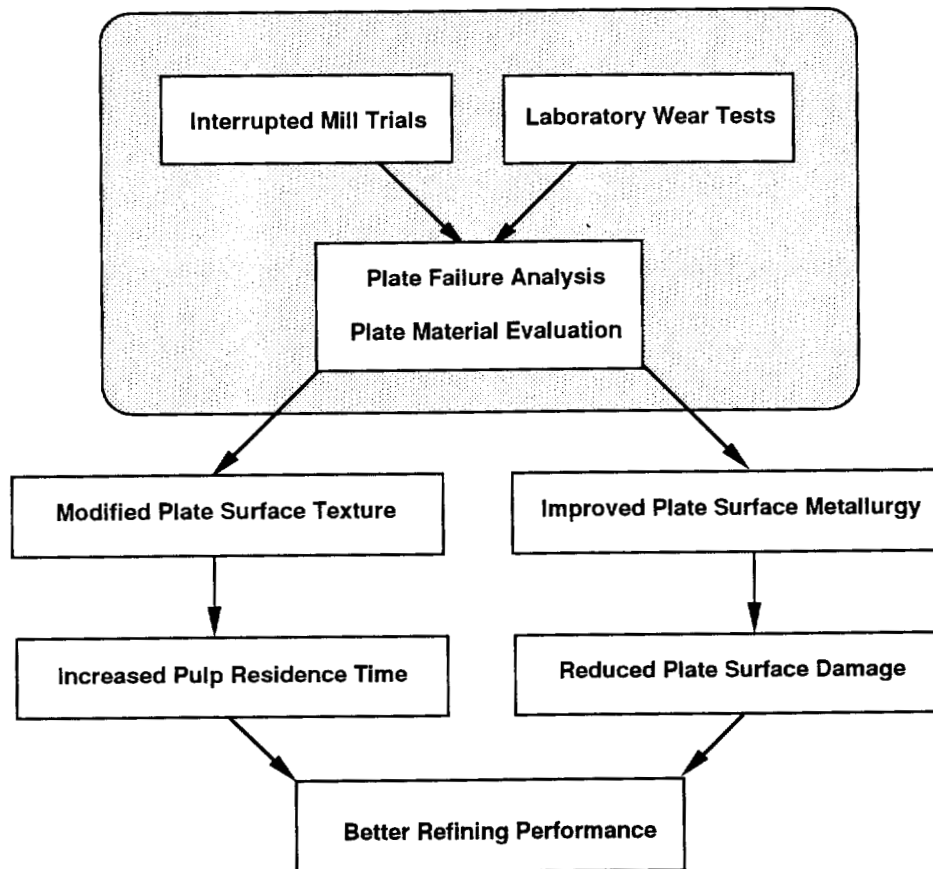


Figure 1.1. Thesis scope.

CHAPTER 2. BACKGROUND

2.1. PULPING

2.1.1. Pulpwood

Wood Species. Two groups of pulpwood are used in the paper making industry: softwoods and hardwoods. The softwoods (gymnosperms) are cone-bearing trees and are popularly called conifers or evergreens; the hardwoods (angiosperms) are usually broad-leaved and deciduous [3]. Fiber length is the major difference between the two groups with softwood fibers being two to three times longer than hardwood fibers [2]. The strength of the resulting paper depends strongly on fiber length with longer fibers yielding higher strengths. Fiber diameter (softwoods are usually twice the diameter of the hardwoods), fiber wall thickness and ultrastructure are other important structural features. Softwoods have lower densities than hardwoods which leads to a faster refining response and superior strength properties. Compared to hardwoods, softwoods contain less holocellulose (cellulose + hemicellulose) and extractives but more lignin. Softwoods are currently the most important in TMP refining while only a few low density hardwoods can yield thermomechanical pulps with acceptable strengths [4]. Table 2.1 shows the fiber properties of some North American pulpwoods [1].

Tree Structure. Figure 2.1 [1] depicts the cross-sectional structure of a mature stem. Laterally, the stem comprises bark and wood, with wood constituting the major part [5]. Bark has two zones: the outer dead bark and the inner living bark. Next to the

inner bark is a thin layer called the cambium where cell growth occurs. This layer subdivides to form both the woody tissue on its inner side and the bark tissue on its outer side. Sapwood is the newly formed wood on the inner side of the cambium, and heartwood is a core of dead woodcells in the stem center. Compared to sapwood, the heartwood is darker in color and more resistant to liquor penetration in chemical pulping due to the deposition of resinous organic compounds in the cell walls and cavities. The growth rate of wood varies with seasons, leading to the formation of thin wall fibers in the spring and thick wall fibers in the fall. Thus, the annual ring is apparent due to the difference in the growth rate of the early- and late-formed cells. The earlywood (springwood) cells have thinner walls and larger diameters than the latewood (summerwood) cells [3].

Cell Wall Structure. Over 90% of softwood volume is occupied by longitudinal fibers which are long, tubular cells with tapering ends. The cellulosic cell wall has four layers (Figure 2.2 [6]). The primary wall (P layer) is thin and relatively impermeable, including randomly oriented interwoven microfibrils. The secondary wall makes up the bulk of the cell wall, containing three layers (S1, S2, S3) which are distinguishable due to their different orientations of ordered microfibrils. The S1 and S3 are the outermost and innermost layers of the secondary wall, respectively. Both are about 0.1 μm thick. Total cell wall thickness is largely controlled by the S2 layer which is from 2 to 10 μm thick. During refining, the P wall must be removed to allow the fibers to hydrate and swell, increasing their flexibility and bonding power. The major portion of energy consumed in TMP is used to break up the P wall and peel the S1 layer. To get good mechanical pulp, it is vital to expose and partially fracture the S2 layer by removing the S1 wall [2]. The middle lamella (ML) is the intercellular region with a very high lignin content, cementing the fibers together. The lumen is the central canal of the fiber, occupying 1/4 to 1/2 the cell volume.

Fiber Chemistry. Major components of the cell wall include cellulose, hemicelluloses, lignin, and extractives. Cellulose, the chief component, determines the fiber character and permits its use in papermaking. Its microscopic and submicroscopic structure is depicted in Figure 2.3 [7]. The cellulose is made up of many sugar units, with a chemical formula of $(C_6H_{10}O_5)_n$, where n is the number of repeating sugar units with which the strength of cellulosic materials increases. Each straight chain molecule includes up to 10,000 repeating glucose monomers. Aggregates of molecules form threadlike microfibrils while bundles of microfibrils form lamellar macrofibrils, giving the wall a layered architecture. The matrix hemicelluloses encase the cellulose and support the microfibrils. Like the cellulose, they are strongly hydrophilic, allowing the fibers to hydrate and swell during refining. Lignin is highly polymerized and the major constituent of the middle lamella. Lignin's hydrophobic nature seriously resists water absorption during pulping, but its thermoplastic nature is utilized in TMP as at elevated temperatures most lignin can be easily removed from the fibers so that the fiber papermaking properties are optimized. Extractives include fatty acids, resin acids, turpenoid compounds, volatile oils, aromatic compounds, and alcohols. Most of these substances are soluble in water or neutral organic solvents. Many North American woods have less than 1% extractives, and the heartwood usually contains the largest portion of extractives in most woods [6].

2.1.2. Pulping

There are two types of pulping processes: chemical and mechanical, and they produce substantially different fibers. Compared to chemical pulping, mechanical pulping is growing more rapidly due to its lower cost, higher yield, and better environmental acceptability.

Chemical Pulping. The objective of chemical pulping is to dissolve lignin which bonds the fibers together and leave behind most of the holocellulose in the form of intact

fibers by using appropriate chemicals in an aqueous solution at elevated temperature and pressure. In practice, however, chemical pulping can successfully remove most of the lignin, but also degrade some hemicellulose and cellulose. Thus, the yield of pulp is lower (about 40 to 50% of the raw material) while the resultant fibers are longer, stronger, and more flexible than mechanical pulp fibers. It is used for many applications where the mechanical pulp is not suitable and is often utilized as a reinforcement for mechanical pulp. Chemical pulping is far more expensive and less environmentally acceptable than mechanical pulping. The two principle chemical pulping methods are the (alkaline) kraft process and the (acidic) sulfite process. In these two pulping methods, the wood chips are cooked in a solution of NaOH and Na_2S and a mixture of H_2SO_3 and HSO_3^- , respectively. The kraft process is more dominant due to advantages in chemical recovery and pulp strength.

Mechanical Pulping. Mechanical pulping occurs by the absorption of energy by repeated compression and relaxation of the fibers in the presence of water. It can convert up to 95% of wood into pulp but consumes a lot of energy. The pulp forms a highly opaque paper with good printing properties while the sheet is weak. Thus, long-fibered chemical pulp is often added to the mechanical pulp to get adequate sheet strength. Mechanical pulps are usually produced from softwoods by either a grinding or refining process. Stone groundwood (SGW) is a typical grinding process in which wood bolts are ground tangentially against an abrasive stone. As the oldest, but still a common method of mechanical pulping, it leads to high shive and fines content and short fibers, but its principle is simple and yield is high. Refiner mechanical pulping (RMP) is a more recent development in mechanical pulping and a typical refining process in which the chips are shredded and ground between the rotating disks of a device called a refiner, producing a longer-fibered and stronger pulp than SGW. TMP is similar to RMP, but at an elevated temperature and pressure. It can lead to improved energy expenditure and pulp quality due to presoftening of the chips, and is the fastest growing sector of the pulpmaking industry [2].

2.1.3. Pulp

Pulp Constituents. Pulp contains three major components: fibers, debris, and fines. Fibers constitute the main part of mechanical pulp and can be classified into fractions of different lengths. The "long fibers" are stiff and incompressible and are low in specific surface area and small in bonding power, requiring further refining to make them flexible and develop their strength potential. The "middle fractions" contain ribbonlike lamellae, fibrils, fiber wall fragments and broken fibers, having a large specific surface area and therefore a high bonding capacity [8]. Debris are undesirable materials in pulp, including shives, chop and dirt. As the largest particles in unscreened mechanical pulp (usually longer than 3 mm), shives are small fiber bundles that have not been well separated in pulping. Chop is the fiber bundles shorter than 3 mm. Dirt includes various nonfiber materials such as bark particles, sand, grit, and fly ash. Fines consist of parenchyma cells, very short fiber portions, fibrils, lamellae from the secondary wall, and fragments from the primary wall and middle lamellae, having an extremely high specific surface area and therefore a decisive influence on the freeness of the pulp and on the wet and dry strength of the sheet.

Pulp Properties. So far there is no general agreement on the scope of pulp properties, and many of them are defined or measured in different ways by different people. From the literature, the most commonly measured pulp properties include fiber fractions, strength properties, surface properties, optical properties, and pulp runnabilities (Figure 2.4). Different fiber fractions can be correlated to pulp freeness and wet or dry strength of the sheet. Strength properties are measured on handsheets, determining the papermaking potential of the pulp. Surface properties are important for printing since high print quality requires smooth papers. Optical properties indicate the ability for pulps to be incorporated into printing-grade papers. For example, sufficient opacity can prevent show-through when printing on both sides of the sheet. Pulp runnabilities represent the ability to run the wet-web through the process without breaks. The various

pulp properties can interact with each other, being determined by both the wood species and the operating conditions. For instance, a longer intrinsic fiber length may not necessarily lead to a stronger pulp because of poor refining operations. Of all pulp properties, freeness, which refers to the resistance of fibers to water flow, is sensitive to fiber length distribution and surface area development, and one of the most frequently measured, being extensively used as an indication of the pulp quality.

2.1.4. TMP Refining

Refining System. In TMP, the wood chips are usually refined between two rotating disks. Figure 2.5 [9] shows a double disk refiner with two opposing rotating disks. The disks are usually about 5 to 6 feet in diameter and made up of many segments or refiner plates, rotating with a narrow gap between them. Every refiner has a minimum gap below which it cannot run uniformly and severe fiber cutting and shortening will occur [10]. There are two sides in a TMP refiner. The side where raw material is introduced is called the feed side, and its counterpart is the control side. The chips are fed into the disk center along with water and move through the refining zone towards the periphery, being progressively refined into fibers. Either a single- or a two-stage refining system can be used, with the latter being more popular. The two-stage refining system has two refiners, i.e. primary and secondary refiners. The former can rapidly reduce wood chips into coarse pulp which will be further refined. The secondary refiner removes the P wall and the S1 layer of the wood fibers and releases the inner fibrils which are able to absorb moisture, expand and form strong bonds when pressed together, providing the final paper with its strength. Sheet formed from these fiber segments is strong due to more fiber-to-fiber contact [10].

Refining Mechanisms. TMP involves the presteaming and primary refining at an elevated temperature which softens the thermoplastic lignin, followed by second-stage atmospheric or pressurized refining. The presoftening of the chips improves the energy

usage and the pulp quality as the result of a higher percentage of long fibers and less shives. Two major actions are involved: shear stresses caused by rolling, twisting, and tensional actions, and normal stresses caused by bending, rolling, twisting, crushing, pulling, and pushing actions [1]. The papermaking properties of cellulosic fibers are greatly improved by refining, which removes the relatively impermeable P walls and allows the fibers to hydrate and swell, increasing their flexibility and bonding ability. As separated but full fibers are still stiff and cannot conform with other fibers to form a sheet due to limited fiber-to-fiber contact, peeling off the P wall and S1 layer, which consumes most of the energy used for fiber separation, will produce flexible ribbons with better bonding ability due to more fiber-to-fiber contact [8]. Some fiber cutting always occurs during refining due to the shearing action of the bar crossings, and is usually undesirable as it results in lower strength. Pearson [11] has suggested that the fibers are not bunched together in flocks but rather as a layer of fibers only two to three deep. Figure 2.6 [1] illustrates the fiber-to-fiber and fiber-to-metal contact in a refiner. The fibers are aligned perpendicularly, being stapled to the bars as they are sheared and compressed as the bars cross each other.

2.2. TMP REFINER PLATE

2.2.1. Plate Design

Plates are key to successful operation of TMP refiners and there are three main criteria for selection of plates: good pulp quality, low energy input, and low plate cost per ton of production [8]. These criteria depend heavily on many plate design characteristics including the patterns of bars, grooves, and dams, as well as plate taper. The primary purpose of plate design is to overcome the centrifugal forces and keep the pulp between the plates so that the required energy can be applied [10]. Although numerous plate patterns are used, the plate design is still a trial and error process and no one plate pattern is suitable to all wood species [11-12]. Figure 2.7 shows a typical

configuration of a refiner plate. There are many bars, grooves, and dams on the plate surface. According to the bar width and function, the plate surface can be divided into breaker bar zone, intermediate zone, and fine bar zone. The intermediate and fine bar zones make up the refining zone where the pulp is made.

Bar Pattern. The bars are used mainly to apply pressure to the fibers. The primary refiner plates have widely spaced, thick breaker bars close to the refiner axis. If size reduction of chips is not accomplished before entering the refining zone, refining will be affected and excessive wear will occur in the refining zone. The breaker bars function as a hammermill and rapidly shred the chips into coarse pulp. They can also permit the development of centrifugal forces which move and align the wood particles for optimum results in the refining zone. High speed photography [10,13] has shown that only fiberized material spreads through the refining zone of a first stage refiner as the reduction of chips into fibers and fiber bundles is largely accomplished in the breaker bar zone. The refining zone includes progressively narrower bars and grooves. In contrast, secondary refiner plates usually have a shorter breaker bar zone and a larger portion of refining area. Here the breaker bars are used mainly to align and impart centrifugal force to the partly refined pulp. The bar width should be no greater than the length of a fiber, and finer bars give more opportunity for fibers to enter the refining zone [8]. The fine bars are usually cast shallower and act as a dam so that the fibers can be expected to stay in the refining zone for a longer time. Wasikowski [14] stated that plate design is related to the bar strength ratio and a certain ratio of bar height to width must be maintained to resist bar breakage for a given application (Figure 2.8).

Groove Pattern. The grooves in the refiner plate, basically the regions between bars, are areas where the fibers are able to expand and for the excess water and steam to be conveyed to the plate periphery. Also, the grooves can provide the bar edges and surfaces needed for the refining action and transport the fibers through the refining zone [15]. The plate pattern can exert a desirable fractionating effect on the pulp, with the

finer fibers tend to migrate into the grooves with the long, undeveloped fibers being retained between the bars for further refining. Leask [8] indicated that the groove width needs to be less than the length of a fiber, otherwise the plates start to come together and are then forced violently apart again before they clash. In refiner plates the grooves and the bars are usually identical in width. As indicated by Kurdin [10], the groove width has an effect on pulp quality, with narrow grooves forcing more fiber bundles and undeveloped fibers to remain on the bar surfaces for further treatment. In addition, during refining a substantial amount of steam is always generated. A portion of the steam moves with the fibers and will be expelled from the disk refiner, while the rest flows back towards the inlet. As high-speed photography has proved, the steam movement occurs in the grooves between the bars. To avoid interfering with the back flow of steam, the grooves should be kept free of dams at least two-thirds of the distance from the disk center.

Dam Pattern. In most plates, partial dams between the bars at various intervals are used to either channel radially flowing pulp back into the gap between plate rings or prevent shive material from escaping the refining zone without reduction. Fibers in the refiner tend to move outward toward the plate periphery because of the centrifugal forces which depend on disk diameter and rotation speed. The damming of the refiner plates is more important for larger disk refiners due to the greater centrifugal force present. Frazier et al. [16] have shown a beneficial effect of primary dam depression on pulp quality but questioned the value of the dams in secondary refiners. Pearson [11] claimed that if dams are necessary they should be kept to millimeters below the beating surface, and if the dams are used the groove width and volume are too large. As indicated by Leask [8], plate damming can be accomplished by subsurface or surface dams in the grooves, or by a finer bar section at the outer plate periphery. The dams may also prevent plate clashing by restricting pulp through the plates and forcing them apart by the presence of material which cannot escape. Plates may also be made with a periphery rim, which actually acts as a type of dam, to increase the retention time of pulp between

the plates. Sub-surface dams may be utilized to provide the strength necessary to support the bars under high shear forces in the refiner, and strategically located dams can improve the bar breakage resistance by strengthening the bars [14]. Figure 2.9 schematically shows the bars, grooves, and dams.

Plate Taper. Refiner plates are often slightly ground to a specific taper which is normally less for a secondary-stage refiner than for a primary one. Figure 2.10 shows the taper for a refiner plate. Clearly, the tapered refining zone can be divided into two parts, with one being on the inlet side and another on the periphery side. Figure 2.11 depicts a very important criterion in refiner plate design - the specific volume curve which is a plot of the space between plates during operations as a function of the plate radius. The narrowest point is the zero steam velocity point - the point from which the generated steam can flow either backwards towards the inlet or forwards towards the outlet. As pointed out by Kurdin [10], the purpose of the taper is two-fold. On one hand, the size reduction of chips must be accomplished prior to entering the plate bars otherwise excessive wear will occur at the refining zone. Therefore, the taper on the inlet side provides a larger opening for chips to be reduced in size before they can enter the plate bars. On the other hand, every refiner disk deflects when operating at high speed and high load. Although the deflection can be minimized by heavier construction, there are practical limitations. Thus, this deflection can be compensated for by grinding a taper on the periphery side of the plate. The degree of the taper must ensure that during refining the plate bar sections beyond the turning point run parallel, i.e., flat against each other, as shown in Figure 2.11. If the taper is more than needed for deflection compensation, the plate outer portion will wear excessively and finally will prevent steam flow from the plate. Conversely, if the taper is insufficient the plate outer periphery will not be utilized and the pulp will not be retained between the plates. Although there is no rule for plate taper design, these problems can be easily identified by visual inspection of the used plates and the ideal taper for a given application can be determined through a trial-and-error process.

2.2.2. Plate Alloy

Conventional plate alloys can be classified into two families: cast white iron and cast stainless steel. The typical compositional ranges of the plate alloys are listed in Table 2.2 [17]. All these materials, except the 17-4 PH stainless steel, are carbide-containing alloys due to the presence of eutectic M_3C or M_7C_3 carbides caused by non-equilibrium cooling. These plate alloys, however, are directly adopted from other industries regardless of the TMP refining environments and requirements.

White Irons. In this family a carbon content of 2.5-3.5% produces a high carbide volume fraction, making these alloys very hard (54 to 60 HRC) and abrasion resistant without the need of expensive heat treatment. Their impact strength is primarily a function of carbon content, while their toughness and corrosion resistance are generally proportional to alloy additions of chromium, nickel, and molybdenum. This family contains four groups: Ni-hards, 25 Cr irons, and 20-2-1 (20% Cr, 2% Mo, 1% Cu) and 15-3-1 (15% Cr, 3% Mo, 1% Cu) alloys. Ni-hard is the least fracture-, corrosion- and wear-resistant in this family due to the net-like eutectic M_3C carbides which are brittle and relatively soft (about 900 HV), while the 25 Cr, 20-2-1, and 15-3-1 alloys are all high chromium white irons containing very hard M_7C_3 carbides (up to 1300 HV). The transformation from M_3C to M_7C_3 is due to the enhanced Cr/C ratio with which the carbide hardness increases. By increasing the chromium content the corrosion resistance is improved. The high chromium white irons, as a group, have much better wear and corrosion performance than the Ni-hards. While many white irons are used in the as-cast condition, the matrix can be heat treated to either austenite or martensite, based on desired properties.

Stainless Steels. The martensitic stainless steels most often used in TMP refiner plates are 440C and 17-4 PH alloys which are heat treated to attain proper hardness and microstructure. The 440C steels (about 1% C, 15-18% Cr, up to 0.75% Mo, and 2%

Ni) are designed to exhibit high corrosion resistance combined with strength and wear resistance. Owing to non-equilibrium cooling, many eutectic carbides form as in the white irons. After re-austenization, quenching and subsequent tempering, the final microstructure is one of eutectic and secondary carbides in a tempered martensitic matrix. Their fracture toughness is similar to or higher than that of high chromium white irons, but corrosion resistance is markedly improved [8]. The 17-4 PH steel is totally different from all other plate alloys due to the absence of eutectic carbides. After heat treatment the final microstructure is very fine copper precipitates distributed on a low carbon tempered martensitic matrix. These precipitates are unresolvable optically but responsible for providing much of the alloy strength.

2.2.3. Plate Damage

As TMP refining proceeds, the refiner plates will deteriorate in various patterns, resulting in degraded refining efficiency and pulp quality. A number of terms have been used to describe the plate damage by various investigators. To date, however, no general agreement has been made on the classification and definition of different plate damage modes. Wasikowski [18] broke down the TMP refiner plate failure modes into six distinct classifications: bar breakage, serration, abrasion, cavitation, corrosion, and edge deterioration. Thompson and Garner [19] defined bar rounding, clashing, and cavitation as the three major damage modes, and they [20] found no severe corrosion present on any of the used plates examined. Thompson [21] also ascribed the heavy pitting on the outer bars and breaker bars to cavitation erosion. Strictly speaking, however, the terms like "abrasion", "cavitation erosion", and "corrosion" shall not be used to represent plate failure modes because they usually refer to failure mechanisms. From these researchers, the terms serration and clashing, bar rounding and edge deterioration, and pitting and cavitation erosion stand for the same thing. Also, bar breakage can be attributed mainly to plate clashing and tramp materials in the refiner [14], or to the presence of casting defects [22], being a relatively rare form of plate damage. Thus, the major plate damage

modes can be reduced to three: serration, pitting, and bar rounding, while the terms like abrasion and corrosion are the possible mechanisms causing these damage modes.

Serration. Serration is characterized by deep circumferential grooving on bar top surface, usually towards the plate periphery. Serration damage initiates from somewhere in the refining zone but never extends to the breaker bar zone, being widely attributed to plate clashing during refining. If the plate-to-plate contact is severe, it may induce heat cracking and eventually break up entire segments, with possible major damage of the refiner [10]. Loss of bar height can attain a depth of several millimeters, as indicated by the lip of material left protruding above the serrated plate surface. After serration damage, the ridges formed on one set of plates exactly matches grooves in the mating plates and vice versa. Although many ridges and grooves can be seen visually (Figure 2.12), microscopically the serrated bar surface can be very smooth. The surface is usually heavily deformed in the direction of disk rotation. Grains are smeared in layers across the serrated bar tops. Localized melting and micro-cracking on the bar surface can also be observed. There are often material build-up and material flow which are particularly noticeable at the bar trailing edges. Serration should not be a common occurrence in TMP refining, but it is experienced in most mills and is most severe during start-up of an installation. It occurs more frequently in the secondary refiners than in the primary ones [2].

Pitting. Used refiner plates often show extensive pitting damage around the breaker bars or along the bar leading edges of the refining zone (Figure 2.13). The pitting is deep with the individual pits being inter-connected, exhibiting a honey-combed appearance [21]. It must be noted that here the term "pitting" shall not be confused with pitting corrosion. Pitting corrosion is a unique type of anodic reaction and an autocatalytic process, being a failure mechanism causing deep penetration at a number of individual spots, while pitting damage in TMP refiner plates refers to a failure mode at the bar leading edges or on the bar tops, being induced probably by a single or a

combination of failure mechanisms. The ASTM standards [23] defines pitting as a form of wear characterized by the presence of surface cavities induced by processes such as fatigue, local adhesion, or cavitation. The word "pitting" has been used in the literature to describe this type of plate damage [21,24]. Although it may not be the most appropriate, it is definitely better than "cavitation erosion" and "liquid impingement erosion" as these terms usually refer to failure mechanisms instead of failure modes. It is also better than the terms like "edge crumbling" or "edge deterioration" as it is very close to the definition given by ASTM standards and can more vividly depict the honey-combed appearance, without being confused with bar rounding damage.

Bar Rounding. Similar to the pitting damage discussed above, bar rounding damage also occurs mainly at the plate bar leading edges. It is characterized by the sharpness loss of the bar leading edges, as schematically shown in Figure 2.14. Although bar rounding and pitting may overlap each other along the bar leading edges, they usually occur early and late in the plate life respectively. In other words, bar rounding is dominant in early bar leading edge damage while the pitting governs the later stage edge deterioration. As the bar rounded width may vary remarkably along the deteriorated leading edges, bar rounding damage can be better measured by maximum bar rounded width. Visual inspection can only display a basically rounded bar edge surface. On a microscale, however, the hard phases like eutectic carbides in the bar rounded areas can protrude above the matrix, while the matrix is usually covered by a number of short scratches and grooves with various orientations. These carbides are often edge rounded but seldom fractured. In addition, severe surface deformation, cracking, and spalling are basically absent.

2.2.4. Plate Performance

The key point in TMP refining is how to improve the pulp quality and reduce refining energy expenditure. Many researchers have systematically studied both pulp

quality and refining efficiency, and correlated them to a number of pulpwood variables or operating variables. The refining effect, moreover, depends heavily on the refiner plates which are the key parts of any TMP refining system. However, the plate performance in TMP refining, which refers mainly to the resulting pulp quality and refining efficiency, has not been well investigated. Although some research work has been done in this field, few papers have been published and no general agreement has been reached. Therefore, the influences of most plate variables on TMP refining efficiency and pulp quality are still unknown.

Plate Design. Of all plate design variables, bar pattern plays a primary role in determining the plate performance. The number and severity of the stress impacts to which a fiber will be exposed were considered important [25], while the number of impacts increases with the number of bars [26]. Kerekes [27] indicated that a large number of gentle impacts leads to "fibrillation" while a small number of severe impacts causes "cutting". Fahey [28] also emphasized the effect of a large number of mild impacts on efficient refining. Miles and May [13] suggested that for a given energy expenditure the plate pattern will affect the pulp qualities by determining the frequency of bar passages rather than the residence time. In practice, many researchers did obtain better pulp strength properties by using finer pattern plates [29-31]. The dams are considered to cause inefficient refining although they can support the bars under the high shear forces within the refiner [10]. As claimed by Pearson et al. [12], the presence of dams consumed much more refining energy but led to substantially improved pulp quality. Frazier et al. [16] found a significant effect of primary dam depression on pulp quality but questioned the value of dams in secondary refining. Kurdin [10] emphasized the influence of groove width on pulp quality based on the fact that narrow grooves force more fiber bundles and undeveloped fibers to remain on the bar surfaces for further refining. In addition, it has been mentioned that plate taper shape could also affect pulp properties [32].

Plate Alloy. From the published literature, it is obvious that many researchers have been convinced that the effect of plate material on TMP refining actions is significant. Giffin [33] has pointed out that the correct choice of plate alloy will directly influence the pulp properties. Frazier [9] claimed that a hardness range of 50 to 55 HRC is appropriate for refiner plates since harder materials never "wear in " and produce poor quality pulp while softer materials erode too rapidly. From the mill trial results obtained by Bergstrom et al. [32], increased contents of chromium and nickel could allow the Ni-hard plates to make good pulp for a longer period than the standard Ni-hard alloy plates, but were still not suitable for high-speed refiner applications because of a considerable drop in pulp tear factor. In contrast, martensitic stainless steel plates were very good plate material for a high-speed refiner since they could result in satisfactory pulp quality after a very long time. Bergstrom et al. [32] also indicated that a good plate material can almost eliminate pulp quality vibrations and gives a much longer plate life than standard Ni-hard alloys. In general, however, few studies have been carried out in sufficient depth to provide a clear picture of the effects of plate alloy on TMP refining, and the correlations of plate material with refining efficiency and pulp quality are far from being fully understood.

Surface Texture. Some authors have tried to correlate refining performance with plate surface texture. Clayton et al. [2] mentioned a possible effect of bar surface topography on refining efficiency, and Leask [8] also considered it necessary to maintain a certain macro roughness on bar top surface to get efficient energy transfer and refining effect. According to Danforth [34], metallurgy can determine bar edge sharpness and bar surface roughness and these two variables may have a profound effect on refining. Franzen [35] recommended refiner plates made out of compound materials with the surface topography tailored to give optimum refining conditions. Ni-hard secondary plates have been said to produce superior pulp quality due to enhanced energy transfer from the bar top to the pulp during refining. Since the Ni-hard has poor corrosion behavior and its polarization test exhibits general corrosion of the matrix leaving a

network of carbides on the surface, the efficient energy transfer was attributed to the surface texture associated with the carbide network [36]. As during refining the bar top can be polished easily towards a rather smooth and even surface from which the pulp fibrillation suffers, Kettunen [37] considered slight continuous corrosion to be necessary to keep the bar top surface sufficiently rough. All the facts presented above may also imply that surface texture affects refining effect through modifying the pulp residence time. That is, a rougher bar top surface may lead to better pulp quality because the pulp residence time is increased due to greater friction between the wood particles and the disk surface.

Plate Damage. Many people have reported an adverse effect of plate wear on pulp quality [38-41], because aged or worn plates will result in more fiber cutting, lower long fiber fraction, and higher shive content [42-43]. Since the pulp quality depends more on the plate conditions in the secondary refiners than in the primary ones, it has been considered unwise to run the plates to maximum life as the pulp properties decrease much more quickly [15]. Plate damage has also been correlated with refining efficiency. For example, Strand and Mokvist [42,44] observed a significant effect of plate surface condition on the pulp quality - specific energy relationship, where the specific energy is defined as the energy consumed by a unit weight of pulp. More specifically, the refining performance has been related to bar leading edge deterioration. From Hietanen and Ebeling [45], if the bar edge is worn the pressure along it will cut fibers at the contact sites or at the contact points between the fibers. Leask [8] claimed that a plate must resist bar rounding to obtain the desired energy transfer and refining effect. As predicted by Pearson [11], bar rounding will reduce the bearing surface available for refining and increase the refining intensity which refers to the specific energy per impact, while Strand et al. [25] concluded that plate age will decrease the refining intensity which is reflected in a systematic drop in tensile index. According to Thompson [21], heavy pitting along the intermediate and fine bars can destroy the bar edges and profile, causing poor pulp quality, but Wasikowski [14,18] indicated that the cavitation damage around

breaker bars would not be detrimental to plate performance. In summary, it seems that plate damage, especially the bar leading edge damage in the refining zone, will be very detrimental to TMP refining effect.

2.3. PLATE FAILURE MECHANISMS

TMP refiner plate deterioration is a very complex process. It depends on many variables such as the wood species, chip cleanliness, specific energy, load stability, consistency, pH, dilution water, and the plate design [18]. Few research papers about plate failure analysis have been published and the plate damage process still remains poorly understood. Several researchers have tried to conduct some plate failure analyses and attributed the three major plate damage modes to various failure mechanisms including abrasion, adhesion, solid particle erosion, cavitation erosion, liquid impact erosion, and corrosion, either singly or in combination (Figure 2.15). To date, however, no systematic studies have been conducted and no general agreement has been formed. Even so, it is necessary, before introducing the plate failure analysis work performed by different authors, to briefly describe the material failure mechanisms that may contribute to the plate deterioration process.

2.3.1. Material Failure Mechanisms

Abrasion. Abrasion is the wear due to hard particles or protuberances forced against and moving along a solid surface, and is one of the most common forms of wear. So common is it, that often wear and abrasion are used synonymously. The problem of abrasion is widely encountered in mining, earth-moving, agriculture and many other industries. On the abraded surface are many directional scratches, gouges, and score marks. It has been estimated that abrasion alone can account for approximately 50% of all wear failures encounter in industrial situations [46].

As shown in Figure 2.16 [47], the key aspect of abrasion is its association with the microplowing, microcutting, and microcracking of a solid surface by harder particles or asperities. Microcracking usually occurs when highly concentrated stresses are imposed by abrasives in the surface of brittle materials. Microplowing and microcutting, however, are the dominant interactions in more ductile alloys. The proportion of wear groove volume displaced to the groove sides, which represents the ratio of microplowing to microcutting, depends on the attack angles of the abrasive particles, as shown in Figure 2.17. Microcutting will occur when this angle is greater than a critical value [48-50], and pure microcutting leads to a material loss equal to the volume of the wear groove produced. During microplowing, material is plowed aside repeatedly by passing particles and may break off by low cycle fatigue [51].

Abrasion can be divided into two-body or three-body abrasion (Figure 2.18). In two-body abrasion the cutting points are embedded in the counterface, while in three-body abrasion the cutting points are loose within the contact zone. Wear is about one to two orders of magnitude greater in two-body abrasion than in three-body abrasion, because in three-body abrasion only a small portion of the particles can cause wear due to the variations in attack angle [47]. Abrasion can also be classified into gouging abrasion, high-stress grinding abrasion, and low-stress scratching abrasion [52]. Gouging abrasion results in the removal of large particles from a metal surface, with the worn surfaces showing heavy gouges. High-stress grinding causes plastic flow and fatigue of ductile constituents and cracking of hard constituents of the metal surface, while low-stress scratching usually produces minute scratches on the metal surface. In this classification, the criteria for "low-stress" is that the stress imposed on the abrasive particle does not exceed the crushing strength of the abrasive.

Under classical abrasive wear theory, the abrasive must be at least as hard as the counterface. Khrushov [53] has correlated abrasion damage with the ratio of the abrasive hardness (H_a) to the hardness of the test metal (H_m). According to his theory,

if $H_a/H_m \geq K_1$, the wear damage has a definite maximum and constant magnitude regardless of the magnitude of H_a/H_m ; if $H_a/H_m \leq K_2$, no wear occurs and in this case the wear-resistance is infinite; if $K_1 \geq H_a/H_m \geq K_2$, the abrasive wear increases linearly with H_a/H_m . Here the Values of K_1 and K_2 are 1.3-1.7 and 0.7-1.1, respectively. However, it has been found that soft abrasives could also cause abrasion damage on hard metallic surfaces. For example, the abrasivity of paper has been reported by many investigators [54-56], although it was attributed mainly to the minerals and other particles contained in the filler or binder content of the papers instead of the paper fibers themselves [57-59]. Richardson [60] classified various abrasives into "hard abrasive" and "soft abrasive", based on whether the abrasive hardness is higher than that of the worn surface. It is evident, therefore, that very soft particles are also capable of damaging hard alloys abrasively, although the wear mechanism(s) may not necessarily be direct cutting or plowing.

Adhesion. Adhesion (or scoring, galling, seizing and scuffing) occurs between two metallic surfaces sliding against each other under a load. According to ASTM standards [23], adhesion is the wear due to localized bonding between contacting solid surfaces leading to material transfer between the two surfaces or loss from either surface. Similarly, Zum Gahr [47] defined adhesion as the formation and breaking of interfacial adhesive bonds. True adhesion is most often found under nonlubricated or dry-contact conditions between two metallic contacting surfaces. In lubricated contact, adhesion may also occur but on a much reduced scale. Figure 2.19 schematically shows the adhesion process. High local pressure between contacting asperities causes plastic deformation and the subsequent formation of junctions which increase in size as motion continues. Relative sliding can result in rupture of these bonded junctions from one or both of the interacting surfaces. Metal transfer will occur if the bond to one surface is stronger than the bond to the other, while wear debris is formed if the bonded junctions are fractured from both surfaces. Budinski [61] suggests that after the initial step pure adhesion in the sliding couple may no longer occur as the surfaces are usually covered by wear debris

which will cause abrasive wear. As pointed out by Eyre [46], adhesion is favored by clean surfaces, non-oxidizing conditions, and by chemical and structural similarities between the sliding couple, because bonding and welding are more likely. Transferred particles and wear debris may become considerably harder due to work hardening and, in some cases, phase hardening, leading to abrasive wear.

Sliding Wear. Sliding wear denotes wear due to the relative motion between two contacting solid bodies. Historically, the term adhesive wear has been used synonymously with sliding wear, but in fact much more than just adhesion may be involved. Other damage processes such as fatigue, abrasion, oxidation, and chemical reaction may also be active. Thus, adhesion alone usually cannot dominate this wear mechanism. Zum Gahr [47] states that various physical processes can be involved in sliding wear including adhesion, surface fatigue, tribochemical reaction and/or abrasion, as described by Figures 2.20a through d. Welded junctions are formed on clean mating surfaces due to adhesion, and due to relative motion material is detached and transferred which can cause grooving of softer material by the work-hardened transfer material (Figure 2.20a). Surface fatigue can produce sheet-like wear particles during repeated plastic deformation by a hard counterbody (Figure 2.20b), or result in cracking of brittle materials (Figure 2.20c). Moreover, the surface films formed by tribochemical reactions can be fractured, forming loose wear particles which may act abrasively (Figure 2.20d). Although sliding wear is one of the most researched wear modes, to date no satisfactory models have been developed due to its complexity [62].

One significant aspect associated with sliding wear is the formation of wear transformation layers which has been widely reported [63-67]. These layers are referred to as "hard", "white" or "non-etching" and usually called "white layers". As indicated by Eyre and Baxter [68], there has been a general agreement that the "white layers" are produced by a combination of surface temperature flashes and extensive cyclic deformation. In the ASM Handbook, the term "white layer" is defined as a white-

etching layer, typically associated with ferrous alloys, that is visible in metallographical sections of bearing surfaces, and interpreted as either an amorphous or a finely microcrystalline material [69]. In fact, the "white layers" can form in most ferrous alloys under a wide range of sliding conditions where ferrous surfaces wear against or cut each other. Therefore, the formation of "white layers" can be used to confirm the presence of sliding wear for most ferrous materials. The most remarkable feature of the "white layers" is their extremely high hardness. Based on a variety of studies, the white layer surface hardness levels were between 700 and 1200 HV for both steels and irons, which is considerably higher than the alloy bulk hardness that could be produced by any conventional hardening process [68].

Another frequently observed phenomenon in sliding wear is the presence of subsurface cracking and the resulting sheet-like debris under unlubricated and marginally lubricated conditions. Jahanmir and Suh [70] studied the stress field of the subsurface under an asperity or hard slider contact. According to their analysis, the subsurface region in front of a sliding asperity is plastically deformed by compressive stresses, while the region behind is elastically deformed by tensile stresses. The crack propagation rate is controlled by the field of tensile stresses. A delamination theory of sliding wear has therefore been developed [71-72], and Figure 2.21 [47] shows subsequent steps which result in flat, extended wear sheets (delaminates). During sliding, normal and tangential forces are transmitted through contact points by adhesive and plowing actions from one surface to another, thereby smoothing the softer surface by deforming and/or removing the asperities (Figure 2.21a). The contact points usually experience cyclic loading, and the asperities on the harder surface can induce plastic shear deformation on its softer counterpart, which accumulates with repeated loading (Figure 2.21b). Due to increased subsurface deformation, microcracks are initiated below the sliding surface and are extended parallel to the surface by further loading and deformation along with pre-existing cracks and voids (Figure 2.21c). The cracks are finally able to shear to the surface at certain weak positions, resulting in thin wear sheets (Figure 2.21d).

Erosion. Erosion, or solid particle erosion, is the loss of material from a solid surface due to relative motion in contact with a fluid containing solid particles. The term "low-angle erosion" sometimes refers to erosion in which the particles move nearly parallel to the solid surface, while "high-angle erosion" or "impact erosion" is used to describe erosion in which the solid particles move nearly normal to the solid surface, as schematically illustrated in Figure 2.22. In general, hard, sharp particles produce the highest material removal rates. The erosion of materials has been attributed to many mechanisms, including cutting, plowing, extrusion, fragmentation, elastic fracture, elastic-plastic fracture, and even melting [73]. In the erosion literature, materials are usually classified as ductile or brittle, based on the dependence of their erosion rate on impact angle [74]. Ductile materials, such as soft metals, have a maximum erosion rate at low angles (15 to 30°). For the brittle materials, such as ceramics and fully hardened tool steels, the maximum is at or near 90°, with the material removal being usually by microspalling/fracture [61].

Erosion rate can be influenced by impingement variables such as particle velocity, impact angle, and concentration, particle variables including particle shape, size, hardness, and frangibility, and the target material variables which refer to the material microstructure and mechanical properties. As indicated by Zum Gahr [47], the hardness, work hardening and capability of deformation are important physical properties for the target material to resist erosion. Dynamic hardness and work hardening of the target determine the amount of plastic deformation. During impact loading, the capability of deformation will affect the impact number required for the formation of wear debris. Thus, in some cases a softer metal may show better erosion performance than a harder one. For most wear resistant alloys, the microstructures usually contain very hard carbides, but these carbides have been considered detrimental to erosion behavior under a wide range of operating conditions [47]. Levy [75] has found that the minimum erosion rate occurred at a medium carbide spacing and attributed it to a competition between hardness and ductility. Besides, Zum Gahr [47] interpreted it as a preferential

erosion of the matrix at large carbide spacing and large carbide size, and an easy removal of very small carbides at small carbide spacing. Similarly, minimum erosion damage was obtained at a medium carbide volume fraction [76], and this phenomenon may be explained in the same way as the carbide spacing. McCabe et al. [77] reported that the erosion rate of steels increased with matrix hardness in the order of spheroidite, pearlite, tempered martensite, and martensite, and this may be due to the matrix capability of plastic deformation during erosion.

Cavitation Erosion. Cavitation is the formation and collapse of cavities, or bubbles, containing vapor, or gas, or both, in a liquid due to local pressure fluctuations. A vapor-filled cavity will implode, collapsing much more rapidly than a gas-filled one [78]. Cavitation erosion is the wear of a solid surface due to continuing exposure to cavitation. It shall be noted that the terms "cavitation" and "cavitation erosion" are different. Cavitation refers only to the formation and collapse of cavities in the liquid, without concerning any material damage induced by it, being often described as a mechanics or fluid dynamics problem. Cavitation erosion, however, refers mainly to the material wear caused by cavitation, being usually considered a materials science problem. As shown in Figure 2.23, bubble collapsing near a solid surface do not preserve spherical symmetry very far into the collapse. Instead they will form liquid microjets which may attain velocities up to 500 m/s [78]. Thus, cavitation erosion is due more to liquid microjet impact than imposition of shock waves from the center of an approximately symmetrical bubble collapse as proposed by Rayleigh [79], and the actual damaging process may be quite similar to that of liquid impingement [78].

Cavitation can be classified into flow cavitation and vibratory cavitation. Flow cavitation is due to a decrease in static pressure induced by changes in velocity of a flowing liquid. It usually occurs where there are sharp changes in geometry of the flow, that is, there are spatial variations in the fluid pressure. In contrast, vibratory cavitation is due to the liquid pressure fluctuations induced by the vibrations of a solid surface in

the liquid. It usually occurs where there are cyclic pressures, that is, there are temporal variation in the fluid pressure. The intensity of vibratory cavitation is generally much greater than that of flow cavitation so that the vibratory cavitation erosion rate is much higher than that caused by flow cavitation. As bubbles or cavities form where or when the local liquid pressure is lower than its vapor pressure and collapse where or when the local pressure is higher than the vapor pressure, the location of cavitation erosion is often quite separate from the location where cavities nucleate.

Cavitation erosion is generally considered a fatigue failure process caused by the cyclic stresses induced by the bubble collapse [80-82], because the worn surfaces are very similar to the fatigue fractured ones [83], and there are good correlations between cavitation erosion and fatigue tests [84-87]. On the other hand, cavitation damage usually initiates from the weakest phases such as graphite [88-89], ferrite [90], grain boundaries [91-92], carbide-matrix interface [21], or the second-phase particle-matrix interface [93]. Preece et al. [94] proposed that the ideal structure to resist cavitation attack would consist of a single-phase homogeneous solid solution of high intrinsic strength with an ultrafine grain size. In fact, any interfaces in the alloys may cause problems in resisting cavitation damage. Therefore, sufficient deformation capability and less interface area may lead to lower cavitation erosion rate. In addition, some workers have improved the cavitation erosion behavior of alloys using various surface engineering methods including laser surface melting [95-96], laser cladding [89], plating [97-98], shot peening [99], and plasma spraying [100-101].

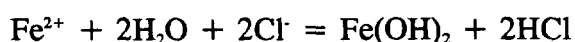
Liquid Impingement Erosion. As schematically shown in Figure 2.24, liquid impingement erosion is the wear of a solid surface due to continued exposure to impacts by liquid drops or jets which can exert forces of a magnitude sufficient to permanently deform and fracture the solid surface. The damaged surfaces are very similar to those caused by cavitation erosion, and it is difficult to differentiate them microscopically. Liquid impingement erosion is often studied in conjunction with cavitation erosion as

usually these two are inextricably combined [79]. They are considered sufficiently similar processes for researchers to use a cavitation test to predict liquid impingement erosion behavior or vice versa [102]. As reported by Hammitt et al. [78], in cavitation erosion approximately only one in 30,000 bubble collapses produces visible surface damage, while in liquid impingement each collision from a liquid drop may cause damage. Thus, the plate surface pitting damage is more likely to be a result of liquid impingement than cavitation.

The material removal in liquid impingement erosion depends on both drop velocity and drop size, and the threshold velocity V_c below which no damage occurs has been found to depend on drop size. Heymann [103] proposed a relation $V_c^2 d = \text{constant}$, where d is the drop diameter. Hancox et al. [104] produced erosion damage on copper with a jet diameter of 1.35 mm at velocities up to 80 m/s. Hoff et al. [105] concluded that the erosion damage decreased with drop size when drop diameter was less than about a millimeter, but was independent of drop size when larger drops were used. From Brunton et al. [106], it is the larger drops, rather than the drops of average size, that control the degree of damage. More importantly, Field et al. [107] indicated that if a drop is oscillating it is not the size of the largest drop that is important, but the largest radius of curvature that this drop can reach at the impact surface. This means that a drop can act effectively as a much larger drop. To date, no general correlation between drop velocity, drop size, and erosion damage valid for a wide range of materials has been found. Among various alloys, tool steels, Stellite alloys and maraging steel have been found to be the most damage resistant [108].

Pitting Corrosion. Corrosion is caused by the unintended chemical or electrochemical reaction of a material with its environment. All forms of corrosion, except uniform corrosion which occurs under normal service conditions, belong to localized corrosion, with pitting corrosion being a typical example which causes deep penetration at only a few spots. Although every engineering alloy is susceptible to

pitting corrosion, Jones [109] indicated that pitting corrosion of the stainless steels containing chromium and nickel are of the greatest practical interest, with most failures in stainless alloys occurring in neutral-to-acid solutions with chloride or ions containing chloride. As a unique type of anodic reaction and an autocatalytic process, pitting corrosion within a pit can produce conditions favorable and necessary for the continuing activity of the pit. Pitting corrosion results from a failure of the passive film. Figure 2.25 shows a simplified model for pitting of stainless steel in a slightly alkaline chloride solution. Copious anodic production of Fe^{2+} attracts Cl^- to the initiation site. Hydrolysis by



reduces local pH and leads to a self-propagating mechanism of pit growth. The acid chloride solution further accelerates anodic reaction, which in turn further concentrates chloride in the pit. When Fe^{2+} diffuses out of the acid pit it is oxidized to Fe^{3+} and precipitates in the neutral bulk solution, forming an insoluble cap of $\text{Fe}(\text{OH})_3$ corrosion products at the pit mouth. The cap impedes easy escape of Fe^{2+} but is porous enough to allow migration of Cl^- into the pit, thereby maintaining a high acid chloride concentration in the pit. For stainless steels, the additional anodic reactions for nickel and chromium are similar to that for iron in the pit.

2.3.2. Plate Failure Analysis

Serration Damage. Severe circumferential grooving can always be observed visually on serrated plate surface, and it has been proposed that the grooves are caused by the hard carbides wearing into a much softer matrix during plate clashing caused by improper plate design, insufficient pulp mat, interrupted chip or pulp feed, or a pulp unable to support the load [10]. On a microscale, however, the groove surface produced by serration is often rather smooth. Failing to find any signs of metal transfer and metal

deformation in these grooves, Rideout et al. [110] attributed this form of damage to localized corrosion similar to electro-chemical machining. Conversely, other researchers [18,22,24,111] felt it unlikely due to numerous distinct signs of metal-to-metal contact such as thermal cracking, plastic deformation, material flow, phase transformation, and localized surface melting. Watson et al. [112] produced wear scars similar to those on serrated plates through a high-stress abrasion test. Thompson et al. [24] related serration to some combination of adhesion and abrasion, and proposed a high-stress abrasion mechanism with the abrasives being sand and metallic wear particles from the plates. Stationwala et al. [43] also ascribed serration to abrasion. Clayton et al. [17], however, found no evidence for abrasion as a significant plate damage factor. Instead, based on the fact of surface melting, they ascribed the smoothness of the serrated grooves to thermal effects. From the research work summarized above, serration damage appears undoubtedly related to the plate-to-plate contact during clashing. However, further work must be done to understand what mechanism(s) was involved in the metal-to-metal contact and whether abrasion played a significant role.

Pitting Damage. Due to a substantial amount of dilution water present, the breaker bar zone pitting has been widely accepted as a cavitation damage process [9,37], although liquid impingement erosion [16] and localized corrosion [14] are also considered contributing factors. The breaker bar zone pitting usually is not very harmful to plate performance [18]. In contrast, there is no general agreement on the cause of the refining zone pitting [21]. Wasikowski [14] defined it as a more detrimental form of cavitation damage and ascribed the preferential corrosion in these areas to both the chromium depletion of the matrix near the eutectic carbides and the galvanic corrosion between the carbides and the matrix. Therefore, he doubted whether cavitation alone or a localized corrosion and erosion combination should be the major cause for the refining zone pitting [18]. Clayton et al. [22] attributed this pitting to a combination of preferential corrosion and mechanical action, with the localized chromium depletion being a significant factor. However, Thompson et al. [20,24] related all pitting damage on the plate surface to

cavitation erosion as they reproduced the damage features by a cavitation erosion rig, and they also predicted that the pitting damage can be greatly accelerated by corrosion since cavitation erosion depends strongly on pH. As the wet environment in the refiner is acidic (pH 4.5-5.5) [37], the cavitation damage can be markedly reduced by raising the pH [21]. Some investigators have proposed that the plate damage problems may also be related to pitting corrosion [111,113], particularly when the stainless steel plates are used in mills with high concentration of chloride [113]. Due to the great amount of mechanical wear during TMP refining, however, actually no severe corrosion could be observed [14,17-18,20]. Based on the limited papers published, no conclusion can be drawn about pitting mechanisms. However, the pitting damage in all plate zones seems to be caused by very similar mechanisms because the damage features in all three zones are basically the same.

Bar Rounding Damage. Bar rounding damage is usually considered as a normal wear pattern in a TMP refiner [10,14,18], and many researchers have correlated it with abrasion. As uncontaminated paper fibers will cause little wear when sliding or rubbing against steel [57], sand or grit entrained in the stock have been considered to play a major role in bar rounding [10,111]. Sometimes the matrix in the bar rounded areas is preferentially removed, leaving the primary carbides in relief, while in other cases deep scratches and severe plastic deformation occur. Thompson et al. attributed both phenomena to abrasion [20,24] and related the bar rounding closely to the passage of pulp stock over the plate bars, with its mechanism being similar to that of slurry abrasion or slurry erosion due to the nature of the pulp stock [19]. Clayton et al. [2] claimed that bar rounding is caused by abrasion which occurs most often in primary plates due to more extraneous abrasives like silica in primary refining. As indicated by Kurdin [10], steam generated inside the refiner is under high pressure and will move in any direction towards a pressure drop, producing great turbulence, while water is most severe on the leading bar edges, being often the reason for replacing the plates. The wood chips, if not well washed, may contain sand and other abrasive materials. Thus, he ascribed bar

rounding to abrasion caused by contact between pulp and bar surface, as well as to water and/or steam sand erosion which removes the matrix and exposes the carbides. Plate alloy structure has also been considered important to bar rounding. From Wasikowski [14,18], bar rounding damage may also be related to the presence of softer ferrite in plate alloys, and therefore an optimized combination of carbides and matrix is needed. In summary, it seems that bar rounding has been universally attributed to abrasion and/or erosion, but which mechanism is predominating still remains unclear.

2.4. PLATE MATERIALS

2.4.1. Plate Alloy Evaluation

As mentioned before, some laboratory testings such as abrasion, cavitation erosion, and corrosion have been conducted for the existing TMP refiner plate alloys. Their service performance has also been qualitatively rated. The evaluation work was aimed at ranking the resistance of these alloys to various failure modes, understanding the plate damage process, examining the relevance of the laboratory tests to the TMP refiner environments, or developing new plate materials with potentially better TMP refining performance.

Abrasion Testing. Few papers have involved the laboratory abrasion performance of TMP refiner plate alloys. Although different types of abrasion testers were utilized, the performance ranking orders for the plate materials were basically consistent. Thompson et al. [19] used a slurry abrasion rig to test the bar rounding resistance of plate alloys. The test rig consistently ranked the plate alloys in an order that correlated with field experience, and developed surface textures similar to those seen on the leading bar edges. From their laboratory test results, in white water the wear rate of these alloys depended on both corrosion and abrasion resistance, and the martensitic Ni-hard cast iron had the highest wear rate while the martensitic stainless steel and the

high chromium white irons had the lowest. In buffered distilled water, however, wear of these plate alloys was solely determined by the abrasion resistance, with the stainless steel being much less wear resistant than both Ni-hard cast iron and the high chromium cast irons. A similar trend has been found by Scholl and Clayton [114] in standard DSRW tests using rounded silica sand. As demonstrated by their test data, the 20-2-1 high chromium white iron had a much higher abrasion resistance than the 440C stainless steel. Based on these findings, therefore, it can be inferred that the bar rounding resistance of plate alloys may be well predicted by their abrasion behavior, and the high chromium white irons should be very bar rounding resistant owing to their superior abrasion performance.

Cavitation Erosion Testing. Some cavitation erosion tests have been conducted on existing plate alloys, while the test conditions were very different and the studies were not comprehensive. Clayton et al. [2] showed similarities between the surface appearance of damaged plate breaker bars and cavitation eroded specimens using scanning electron microscopy. Wasikowski [18] also indicated that the cavitation eroded surface features were similar to those of damaged refiner plates. Therefore the pitting damage, or at least breaker bar zone pitting, might be attributed to cavitation erosion. In tests by Christensen et al. [115], 20-2-1 white iron was damaged much faster than 440C steel, and the poor behavior could be ascribed to its higher carbide content which provides more interfacial areas for the cavitation erosion to initiate. Similarly, by examining the cavitation erosion rate of eight different plate alloys, Thompson [21] found a superior performance of stainless steels over white irons, but attributed it to lower primary carbide contents and higher matrix martensite concentrations in the steels. He also concluded that the quantity of carbide-matrix interfaces available and the pH of the solution were two key issues in cavitation damage. He observed a substantial cavitation erosion reduction by changing the solution from mildly acid (pH 4.5) to neutral (pH 7.0). Wasikowski [18] reported that stainless steels were more damage resistant than the white irons, while within the stainless steel family the most highly alloyed alloy had the best

behavior. From the results introduced above, at least two findings are in common: the surface similarity between damaged plates and cavitation eroded specimens and the superior cavitation erosion behavior of stainless steels. Also, the cavitation erosion tests seemed to be relevant to the plate damage environments, and can be effectively used for pitting performance ranking of various plate alloys.

Corrosion Testing. Due to the great amount of mechanical actions present during refining, corrosion alone is unlikely to play a predominant role in plate deterioration. However, some researchers still studied the corrosion behavior of plate alloys as corrosion might considerably affect the plate damage in different ways. In a potentiostatic corrosion testing using sulfuric acid solution, Clayton et al. [22] examined the corrosion behavior for eight typical plate alloys, with Ni-hard showing the most corrosion and 17-4 PH the least. The test setup was inadequate to produce useful electrochemical data with the synthetic white water which is the most common refining environment, but their SEM observations of the corroded plate alloys provided useful evidence of material response to this solution. Through a polarization test, Wasikowski [18] evaluated the corrosion performance of three white irons and three stainless steels with TMP applications in a solution of dissolved chloride at a concentration of 1000 ppm. The pH was adjusted to 3 to match that of typical refiner plate environments. It was particularly interesting that the results parallel those of the cavitation erosion testing. The stainless steels had much higher corrosion resistance than the white irons. This difference was attributed directly to the Cr/C ratio, with the materials of the highest Cr/C ratio being the most corrosion resistant. He also noticed that the corrosion was generally in the form of localized pitting.

Service Performance Rating. Rating of plate alloys based on performance in service is difficult due to the complexity and diversity of the refining conditions. The plate performance varies widely from individual mills [19] and may be specific to the mill and the wood species being used. From an extensive survey of TMP installations

[116], the plate life increased from Ni-hard to stainless steel to high chromium white iron. Leask [8] reported that Ni-hard has the least plate life (300-600 h) followed by high alloy white irons (500-1200 h), and stainless steels (800-1800 h). According to Wasikowski [18], the stainless steels on average run 48% longer than the white irons. Table 3 [17] shows some plate alloy performance ratings on a qualitative basis and without details of refining conditions. Clearly, the high chromium white irons and stainless steels with carbon contents of about 1% and above were shown to be the most wear resistant but Ni-hard and stainless steels with very low carbon levels were the worst. Thompson and Garner [19] showed that the relative performance of these alloys depends strongly on the environmental corrosivity since the wear resistance of the Ni-hard can be greatly improved by raising the white water pH to near-neutral values. Mihelich et al. [38] extended Ni-hard plate life by increasing dilution water pH. To date, however, no one has quantitatively measured plate serration, pitting, or bar rounding damage in terms of plate alloy or wood species.

2.4.2. Plate Material Development

TMP operations depend strongly on the refining ability and the working life time of the refiner plates which are largely determined by the plate material. However, nearly all conventional plate alloys were not particularly designed for TMP applications but simply adapted from other industries regardless of the plate working conditions, damage mechanisms, and service requirements. To date, only a few papers have mentioned the development of new plate materials including cast alloys and surface coatings, but no common viewpoint has been formed.

Cast Alloys. Frazier et al. [16] suggested that a plate alloy for optimum service life should have high hardness, little or no preferred orientation, fine dispersed carbides in preference to massive carbides, and a fine grain size. Clayton et al. [36] recommended four new plate alloys for refiner trials: hypereutectic white iron, heat

resistant tool steel, high carbon stainless steel, and sensitization-resistant TiC stainless steel. However, none of these ideas has been put into practice and no new plate alloy has been developed. Most experiments focused on modifying the existing plate alloys by heat treatment. Thompson et al. [19] reduced the abrasion rate of some as-received plates by heat treating to eliminate residual austenite and produce a fully martensitic matrix, but they suggested that the residual austenite content should be optimized for sufficient alloy toughness. As reported by Thompson [21], the cavitation resistance of plates increased with their hardness which could be enhanced by heat treatment, and additional matrix hardness might be obtained by eliminating retained austenite and forming appropriate secondary carbides during tempering. Kettunen [37] observed that during refining, the plates were often polished towards a mirror surface from which the pulp fibrillation suffers. Thus he considered slight continuous corrosion to be necessary to keep the tooth surface sufficiently rough, which could be achieved by balancing the Cr/C ratio and/or alloying the steel with elements causing hard precipitates. However, his idea may not be applicable since a continuous corrosion will also expedite the bar leading edge damage and cause even more refining problems. In summary, it is unwise to confine the plate material development to existing cast alloys because heat treatment has only a limited effect, while new alloy design may also be unnecessary as only the plate surface layer is utilized in refining. Also, it seems very difficult for a plate made by cast alloy to maintain a rough, continuously corroded bar top without damaging bar edges during refining.

Surface Coatings. Surface engineering has been considered a more fruitful avenue despite some potential developments in conventional plate alloys [2]. Some people have tried to improve the refining performance by using various surface coating techniques. Kettunen [37] used coating techniques to solve the polishing problem in RMP refiner. His laboratory tests on chemical vapor deposited (CVD) TiC and TiN coatings revealed substantial decrease in wear rate, and the practical refining tests confirmed the disappearance of the polishing effect in the TiC coated plates. His work

is clearly of importance for TMP refiner material design due to the similarity between RMP and TMP. Dahlqvist [117] tried to reduce plate wear by increasing carbide contents in the plate surface layer. The plates were detonation-gun coated with WC so that the bar edges become more wear resistant. These plates were run in a primary refiner up to 3500 hours and still maintained a good quality level. He also conducted trials with coating material containing TiC on the plate surface. Clayton et al. [17] confirmed the potential of laser surface alloying for the plate application and predicted an ample scope for further optimization of existing alloys through surface engineering. Frazier [9] indicated that localized hardening of the inlet by flame spraying may reduce the severe cavitation damage in breaker bar zone, if the coatings remain bonded to the plate metal in the hot, acidic refiner environment. Although these results or suggestions were based on different surface coating techniques, they may all indicate that the surface coatings are very promising in TMP refiner applications. This is because the coatings can modify plate surface roughness and surface metallurgy simultaneously, thereby improving both refining effect and plate life without changing the bulk plate alloy.

2.5. PLASMA SPRAYING

Based on the preceding review, the current TMP refiner plates need to be modified to improve both energy transfer and pulp quality. As only the working surface of the refiner plates is of importance to TMP refining, it is unnecessary to optimize the material of the whole plate because the plate cost may increase. More importantly, for plates made out of cast alloys an improved plate metallurgy may not necessarily lead to a qualified surface topography during service and vice versa, while in fact both of them are required for better refining effects. It may not be wise, therefore, to spend a lot of effort and money for new plate alloy design. Instead, surface engineering seems to be a much more fruitful way, as it can effectively modify the material and texture of a component's working surface at the same time, which are just what the TMP refiner plate requires.

Surface engineering refers to any technique which can modify the working surface of a component. As shown in Figure 2.26, there are a number of surface engineering methods which in general can be classified into two families: surface treatment and surface coating. In the surface treatment processes, the surface microstructure and/or chemistry is changed including hard facing, vapor deposition, and many other miscellaneous techniques. In the surface coating processes, however, a material is added to the surface, such as microstructural treatment, diffusion treatment, and implantation treatment. Of all these techniques, plasma spraying is one of the more versatile and has been successfully used in many applications where a wear or corrosion resistant coating is required. Due to very high particle velocity and temperature provided by the plasma jet, superior coating quality can be obtained which may lead to much improved plate damage resistance during service. Many coating properties can also be conveniently changed by adjusting various deposition parameters. As the plasma spraying can apply a wide range of materials in both wire and powder forms, the plate damage resistance may be easily modified according to different plate deterioration environments and refining requirements. The feedstocks, whether in wire or in powder form, can be deposited in various sizes so the plate surface texture may be effectively tailored for a longer pulp residence time and better energy transfer. In addition, plasma spraying can deposit more materials in a given time than many other surface engineering methods and therefore has a higher process efficiency. Thus, this technique seems of great potential for TMP refiner applications.

2.5.1. Process Fundamentals

Spraying Process. Plasma spraying involves two separate processes: plasma/particle interactions (melting) and particle/substrate interactions (solidification). It can be classified into air plasma spraying (APS), low pressure plasma spraying (LPPS), and vacuum plasma spraying (VPS). As shown in Figure 2.27, a DC electric arc is struck from a high-frequency arc starter between a central electrode (cathode) in the torch

and a water-cooled nozzle (anode), while a stream of inert gases (either Ar or N₂, sometimes with the addition of H₂ or He) is passed through this arc. This results in dissociation and ionization of the gases, producing a high-temperature plasma stream from the gun nozzle. A plasma is essentially an ionized gas containing electrons, ionized gas atoms, and atoms or molecules of the plasma forming gas. The spraying material, usually in powder form, is fed into the plasma flame by a carrier gas which is usually the same as the primary plasma gas, where it melts and gains high velocity due to high plasma kinetic energy and is propelled to the substrate. In many cases, wire can be used as feedstock alone or together with powders, as shown in Figure 2.28, resulting in larger molten particles in the flux and therefore thicker splats in the coating layer. A number of process variables must be controlled to obtain a good spray deposit, which are related to power supply, gas, feedstock, substrate, and spray parameters (Figure 2.29). The quality of the coatings, as defined by porosity and strength, tends to improve when increasing the overall energy of the system (thermal plus kinetic) [118].

Spraying Materials. The high temperature (up to 16,000 °C) of the plasma jet can melt any known material, including metals, carbides, or oxides. Thus, plasma spraying has the widest range of materials of any spraying process. The powder size is usually in the range of about 30 to 100 μm. Spraying materials fall into four different families: metals, alloys, ceramics, and cermets. The conventional metals vary from softer materials such as aluminum, copper, and zinc for corrosion applications to hard ones like tungsten for wear applications. Other commonly used metal consumables are iron, nickel, molybdenum, and chromium. The typical alloys include nickel-, cobalt-, and chromium-based alloys. They are usually hardfacing materials and have very good wear resistance. Ceramics are inorganic nonmetallic materials including metallic compounds (carbides, nitrides, borides, or silicides) and nonmetallic compounds (oxides or nonoxides). Conventional ceramic materials used are aluminum oxide (Al₂O₃), chromium oxide (Cr₂O₃) or mixture of chromia and silica (Cr₂O₃-SiO₂). Cermets are composite materials composed of ceramics and a metal intimately bonded together. The

most popular cermet consumable used in plasma spraying is cobalt-bonded tungsten carbide (WC-Co). This material is the counterpart of the familiar cemented carbides that are widely used in cutting tools or other wear components. Ceramics and cermets are generally much harder than metals and alloys, being potentially abrasion-resistant.

Coating Structure. The major morphology features of plasma coatings are lamellar structure, unmelted particles, microstructure, and porosity [119]. As depicted in Figure 2.30, the bulk of the cross section is composed of plate-like lamellae or splats parallel to the substrate surface. These splats result from the impact of molten or semimolten particles. As the impacting particles may split, the average splat volume, about 5 μm thick and 10 to 50 μm in diameter [120], may be smaller than that of the initial powder which usually has a diameter of 30 to 100 μm [61]. Due to rapid cooling, many coatings form columnar grains within the splat in one or two layers normal to the substrate surface; some coatings are noncrystalline and others have a thin amorphous layer next to the substrate followed by crystalline structure. The composition may change owing to evaporation of component(s) in an alloy, decomposition of a gas, or reaction with the atmosphere. Major coating structure parameters are porosity, splat size and shape, and the size, shape, and content of oxide and carbide. Kingswell et al. [121] attributed the coating properties to the strength of individual splats, the cohesion between them, and the size, shape, and distribution of any pores in the coating. For a given feedstock, the resulting coating structure may be substantially changed by adjusting other deposition variables.

2.5.2. Physical Properties

Major physical properties for the plasma coatings include porosity, density, hardness, cohesion, and surface roughness. As the properties of the coatings may strongly affect the resulting wear behavior, it is essential to know their influencing factors before discussing the coating's wear performance. It is important to note,

though, that many research results reported and mentioned here are specific to the type of equipment used and are only generally applicable.

Porosity. Pores in plasma coatings generally exist between the splats or between the splat and the substrate. Some researchers [122-123] reduced the coating porosity by using high current, high feed rate, short spray distance, high primary gas flow, or high secondary gas flow, while others related the porosity to deposition parameters like injection angle [124], powder size [125], or traverse rate [124]. These results may indicate that inadequate powder melting and powder speed are the major sources of porosity. For a given substrate, if the powders are well melted and accelerated, the coating will be built up splat by splat with little porosity. Non-water-cooled substrates have also been found beneficial to porosity reduction [126], probably because a higher substrate temperature will allow the solidified splats to remain plastic for a longer time so that newly arrived particles can remove many of the pores by producing plastic deformation in the deposited layer. Lowered coating porosity was also reported after post-deposition treatments like HIP (hot isostatic pressing) [127] or tempering [126], and this may be attributed to plastic deformation and/or enhanced diffusion at higher temperatures.

Density. Density and porosity are not the same thing. Porosity refers to the volume fraction of voids in the coating structure while density is defined as the mass per unit coating volume. The densities of plasma coatings are usually less than their theoretical values due to the presence of many pores and oxides. Willen [128] suggested that a fast and hot plasma will form the best splats to produce a dense coating and Bartnik et al. [129] reported that porosity, which influences at most the coating quality, correlated strongly with coating density. Smith and Mutassim [130] investigated the effect of plasma arc power, plasma arc gas type and flow rate, plasma gun nozzle size, chamber pressure, and post-deposit heat treatment on deposit density. Angers et al. [131] increased the coating density by decreasing pressure. No significant influence of

spray angle between 45° and 90° on density was found [132], while it was noted that increasing powder feed rate would decrease coating bulk density [133]. Kawase et al. [102] increased the coating density by reducing the spray distance. Smith et al. [135] reported that VPS deposited denser coatings than APS. All these results imply that the density can be increased by well melting and accelerating the powders along with substantially reducing their oxidation during spraying.

Hardness. Obviously the coating hardness is largely determined by the hardness of original feedstock, being usually proportional to the contents of hard particles like tungsten carbides [136]. For a given powder composition, however, the hardness of plasma coatings may be considerably affected by various deposition variables. Hardness is therefore not an intrinsic property for the plasma coatings. As coating hardness can increase significantly with reducing porosity [137], most methods effective for porosity reduction should also be beneficial to hardness and this has been confirmed by various studies. For instance, the coating hardness has been raised using shorter spray distance [138-140] or higher current [122,141], while both have been proved to be effective in porosity reduction. Some other deposition parameters can also affect the coating hardness, probably still by altering the porosity, which include powder feed rate, gas flow, and substrate temperature. Some post-spraying heat treatments, such as HIP [127], autempering [142], and solution treatment [143], can also remarkably enhance the coating hardness. However, a hardness reduction has been reported at higher substrate temperature [144], higher tempering temperature [143], or after sintering treatment [145], which may all be attributed to the relief of residual stresses.

Cohesion. Cohesion refers to the bonding between the splats within the deposit, and it can be roughly reflected by various strength properties of the coatings. The cohesion is usually anisotropic because of the layered structure in the plasma deposit. As the as-sprayed coatings may contain considerable residual stresses induced both during and after the spraying process, post-deposition heat treatments are usually necessary to

substantially relieve these stresses for a better cohesive bonding of the coatings. For example, Smith and Mutasim [130] obtained higher cohesive strengths after heat treatment. Similarly, using annealing Sampath et al. [146] increased ductility of single phase alloy coatings and the fracture strength of two phase alloy coatings. The cohesion of coatings can also be inversely influenced by their porosity. Steffens [125] attributed the poor compressive strength and fracture strength to higher coating porosity. Kuroda et al. [147] reduced the fracture stress by increasing spray distance, and related it to the change in the temperature and velocity of sprayed powders. As both the temperature and velocity of the particles have been related to coating porosity, it appears that any methods which can reduce porosity may also be very beneficial to the coating's cohesion.

Surface Roughness. As an important physical property to the plasma coatings, surface roughness is the major measure of their working surface topography. Although there are many surface roughness parameters, roughness average (R_a) is the most commonly used which is defined as the arithmetic mean of the deviations of the roughness profile from the mean line. Some researchers have related the coating roughness to various influencing factors. Surface roughness increase was obtained when using small spray distance, large powder size, high current, low primary gas flow and decreased powder feed rate [114,148]. As reported by Lugscheider et al. [149], surface roughness of coatings depended on the type and composition of the alloys and the plasma system. Nicoll [150] correlated the coating roughness to substrate surface roughness and the degree of fusion and flow of the selected powder. Mann et al. [101], moreover, found a decrease in coating roughness after sintering and attributed it to the softening of coatings during sintering. Although no conclusions can be drawn from these results, it may be inferred that the coating surface roughness is determined largely by the size and shape of the splats or by the substrate roughness if the coating is very thin.

2.5.3. Wear Performance

A number of papers have been published on plasma sprayed coatings. Most of the studies, however, were carried out to investigate the correlations of various process variables with the resultant coating physical properties. A few papers can be found in the literature which have discussed the wear performance of the plasma deposits, but no systematic work has been done and no general viewpoint has been formed. With many process parameters affecting the coating quality, it is often difficult to conclude whether the wear data of the coatings have reflected their material nature or not. Also, in wear tests the repeatability errors for a given type of plasma coating are usually much higher than its cast alloy counterpart. Thus, the wear behavior evaluation for plasma coatings may not be meaningful without identifying the deposition parameters and the resulting structure characteristics.

Abrasion Performance. The abrasion resistance of cast alloys usually increases with their hardness, and such a relationship shall also be true for plasma coatings. For a number of oxide, carbide and metallic coatings, however, Scholl and Clayton [114] found no general correlation between hardness and abrasion rate. This is understandable because the plasma coatings can differ drastically in structure characteristics due to too many deposition variables involved, and such a relationship may exist only within a small group rather than over a wide range of coatings. Some authors have confirmed the validity of this relationship for several given groups. Heimann et al. [151] showed an abrasion resistance increase of alumina-titania coatings with the microhardness. Slavin and Nerz [152] optimized abrasion behavior of WC-Co deposits when a high volume fraction of tungsten carbides was present, which can be attributed to the higher coating hardness provided by a higher carbide content. Pores have also been found detrimental to coating abrasion performance. Ito et al. [127] reported that due to many pores and inadequate bonding between splats the WC-Co coatings had higher wear rate than the cemented carbides. Moreover, reduced abrasion rates for some as-sprayed coatings have been obtained after austempering [142] or HIP [127]. From above, the abrasion behavior

of plasma coatings may be determined mainly by the presence of hard phase(s), the porosity, and the post-spraying treatment.

Erosion Performance. Few erosion tests have been reported on the plasma coatings, but similar results have been shown by different authors. Taylor et al. [153] found a strong correlation of density with microhardness and erosion rate. Rangaswamy and Herman [154] attributed superior erosion behavior to high carbon content, small mean free path and high density in the coatings they examined. Chou et al. [123], studying Al_2O_3 and $\text{Cr}_3\text{C}_2/\text{NiCr}$ coatings, reported that increasing current and secondary gas flow led to lower porosity and reduced blast erosion damage. Nerz et al. also noticed that coating erosion resistance increased with hardness and with reducing porosity [137], and the coatings with hard chromium carbides embedded in a metallic matrix had excellent high temperature erosion behavior [155]. Based on these studies, it seems that the erosion damage of plasma coatings can be reduced in a way very similar to abrasion. That is, the erosion resistance can be improved by the presence of very hard phases, the reduction in porosity, and the increase in hardness. However, two parameters, mean free path and matrix hardness, should be noted as they may respectively affect erosion damage and abrasion damage in different ways. In erosion tests, the abrasive can enter the matrix between the hard particles more easily and have a much greater impact energy than in abrasion. Thus, a smaller mean free path and a relatively soft matrix could be more beneficial to erosion resistance than to abrasion behavior.

Cavitation Erosion Performance. Many papers have discussed the cavitation erosion behavior of various materials, but only a few involved plasma coatings. Bhat et al. [156] related cavitation erosion of coatings to intersplat bonding, and considered it essential to obtain a dense, low porosity oxide-free deposit to reduce damage rate. Asahi et al. [157] also correlated the cavitation damage to bond strength. Guo et al. [158] attributed the improved cavitation behavior of WC-Co coatings to reduced porosity, larger WC grain size, and increased metal binder content. Guo and Herman [159], in

a study of the cavitation erosion of Tribaloy coatings, showed that damage decreased with coating density but increased with the extent of oxidation. Mann et al. [101] found that sintering could drastically reduce damage rate of as-sprayed coatings but adding WC to metallic coatings would not decrease the cavitation erosion. All these results, although obtained in different situations, have highlighted one common denominator: splat-to-splat bonding. In these studies, increasing binder content, minimizing oxidation, reducing porosity, and using sintering might all have improved the intersplat bonding, while using larger WC size clearly reduced the interface total. All these methods led to a decreased damage rate. As in cast alloys, the areas like grain boundaries or carbide-matrix interfaces are always preferentially cavitation eroded, the alloy interfaces are considered a problem. In plasma coatings, however, the intersplat bonding is even worse than the phase-to-phase bonding in cast alloys. Thus, increasing interface bonding and reducing interface area will reduce cavitation erosion of the coatings considerably. Adding hard components like WC into the coatings, however, could not reduce damage probably because in cavitation erosion no hard abrasives are encountered as in abrasion.

Table 2.1. Properties of North American Pulpwoods [1]

SPECIES	FIBER LENGTH (mm)	FIBER DIAMETER (μ m)	WOOD DENSITY (lb/ft ³)
SOUTHERN REGION			
Longleaf Pine	4.9	35-45	41
Shortleaf Pine	4.6	35-45	36
Loblolly Pine	3.6	35-45	36
Slash Pine	4.6	35-45	43
NORTHEAST REGION			
Black Spruce	3.5	25-30	30
White Spruce	3.3	25-30	26
Jack Pine	3.5	28-40	30
Balsam Fir	3.5	30-40	25
NORTHWEST REGION			
Douglas Fir	3.9	35-45	34
Western Hemlock	4.2	30-40	29
Redwood	6.1	50-65	25
Red Cedar	3.5	30-40	23
HARDWOODS			
Aspen	1.04	10-27	27
Birch	1.85	20-36	38
Beech	1.20	16-22	45
Oaks	1.40	14-22	46
Red Gum	1.70	20-40	34

Table 2.2. Typical Compositional Ranges For Plate Alloys [17]

Alloy Type	% C	% Cr	% Si	% Mn	% Ni	% Cu	% Mo
Ni-Hard I	3.0/3.6	1.4/4.0	0.5/0.8	1.3 max	3.0/5.0	---	1.0 max
15-3	2.4/3.6	14/18	1.0 max	0.5/1.5	0.5 max	1.2 max	1.0/3.0
20-2-1	2.0/3.2	18/23	1.0 max	0.5/1.5	1.5 max	1.2 max	1.5 max
25Cr	2.3/3.0	23/28	1.0 max	0.5/1.5	1.5 max	1.2 max	1.5 max
440C	0.85/1.2	15/18	1.0 max	0.5/1.5	---	---	1.0 max
17-4 PH	0.07 max	15/18	1.0 max	0.7 max	3.5/4.5	2.5/3.2	---

Table 2.3. Qualitative Service Performance of Refiner Plate Alloys [17]
(Estimated relative performance ranked 1 to 6 with 1 the best)

Alloy Type	Corrosion	Wear	Impact	Serration
Ni-Hard I	6	4	4	2
15-3	5	3	-	-
20-2-1	4	3	4	4
25Cr	3	2	4	5
440C	3	3	3	4
17-4PH	1	6	1	6

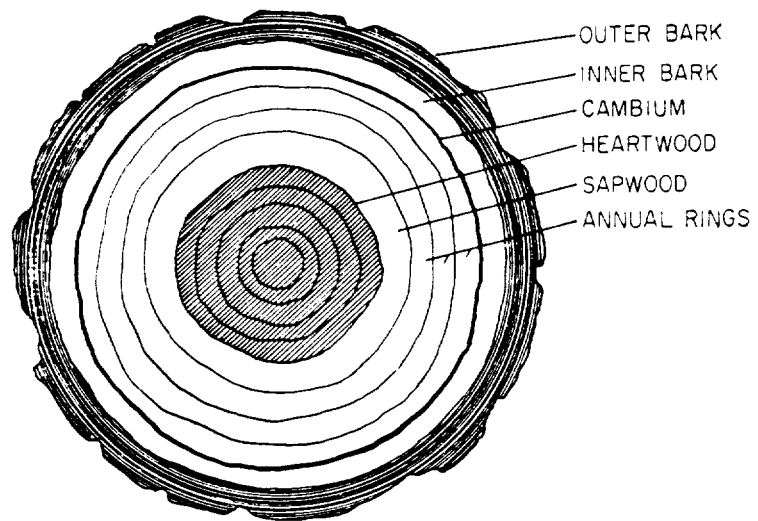


Figure 2.1. Cross-sectional sketch of a mature stem [1].

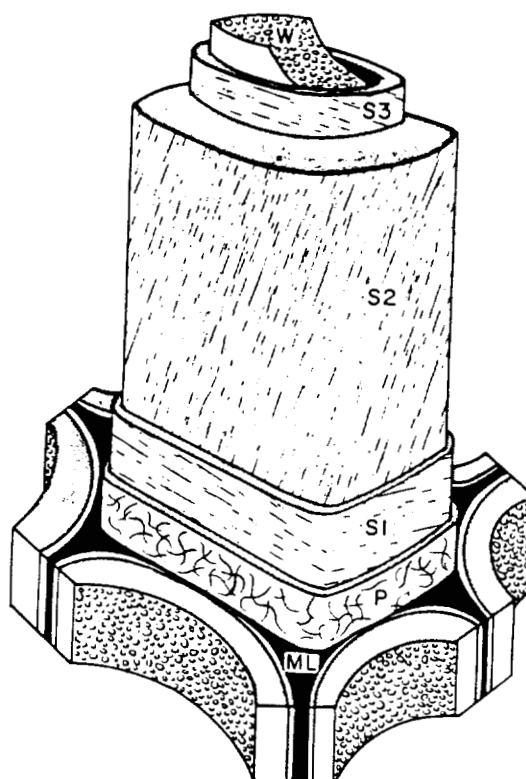


Figure 2.2. Cell wall organization [6].

- W: Warty layer;
- S3: Innermost layer of the secondary wall;
- S2: Middle layer of the secondary wall;
- S1: Outer layer of the secondary wall;
- P: Primary wall;
- ML: Middle lamella.

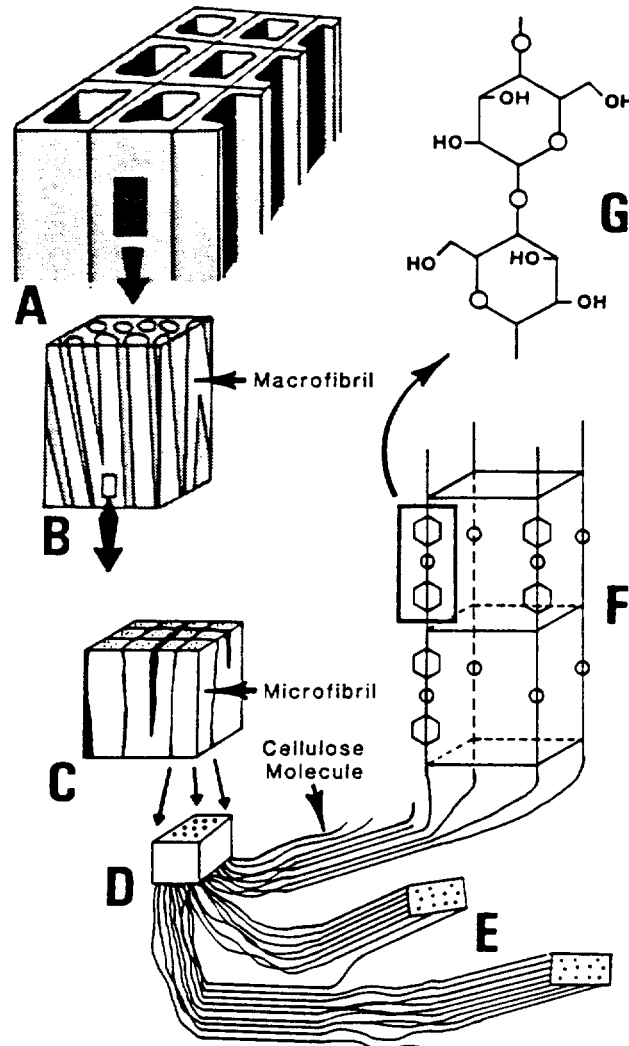


Figure 2.3. Microscopic and submicroscopic structure of cellulose [7].

- A. Transverse/longitudinal view of several wood fibers.
- B. Portion of a fiber S2 layer.
- C. Portion of a macrofibril.
- D. Cross-section of a single microfibril.
- E. Region of a microfibril where the cellulose chains exhibit a high degree of order.
- F. Organization of cellulose molecules into a series of "unit cells".
- G. A cellobiose unit - two adjacent glucose residues connected by an oxygen atom.

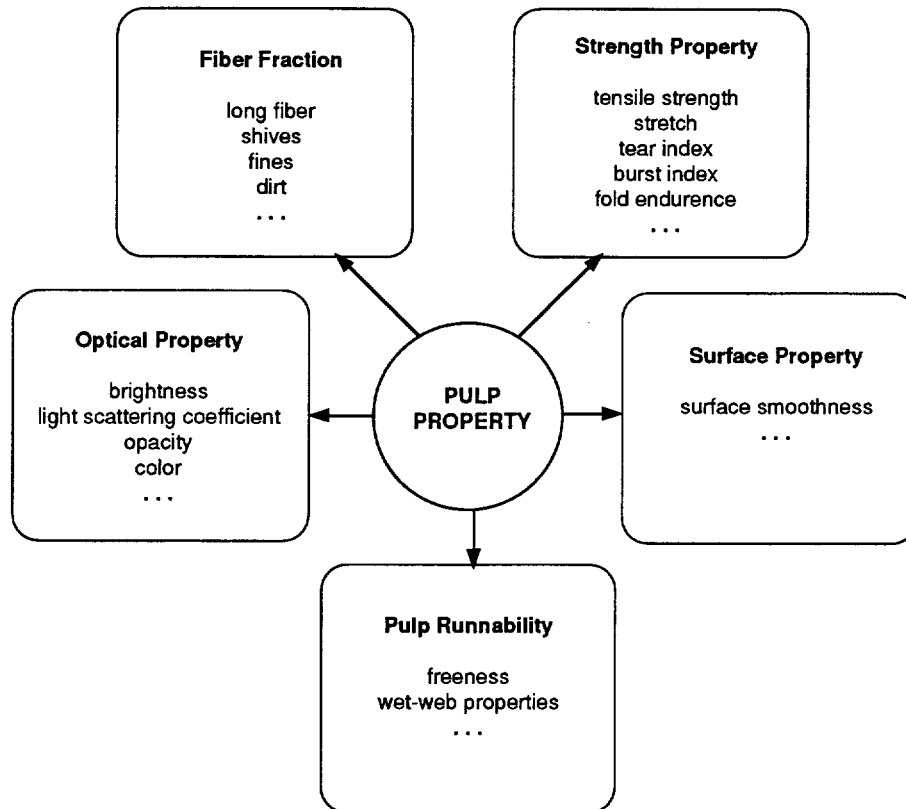


Figure 2.4. Pulp properties.

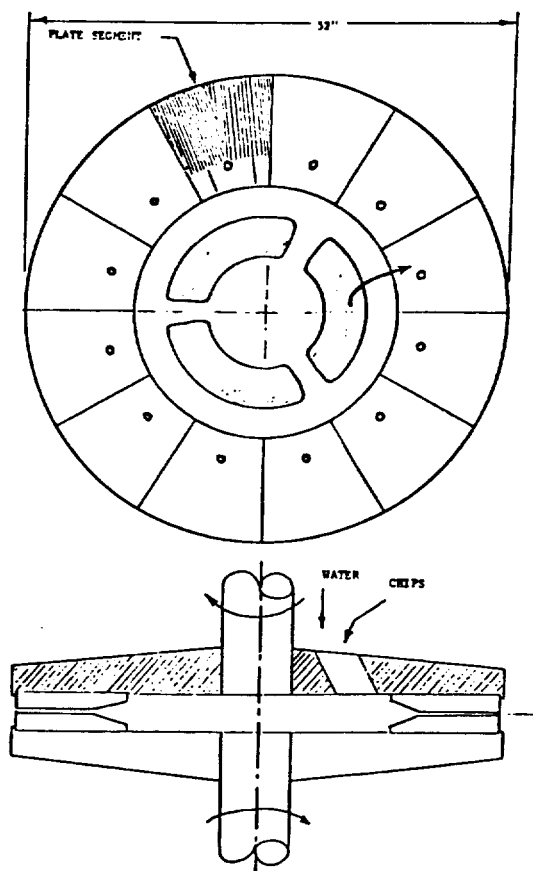


Figure 2.5. TMP refiner system [9].

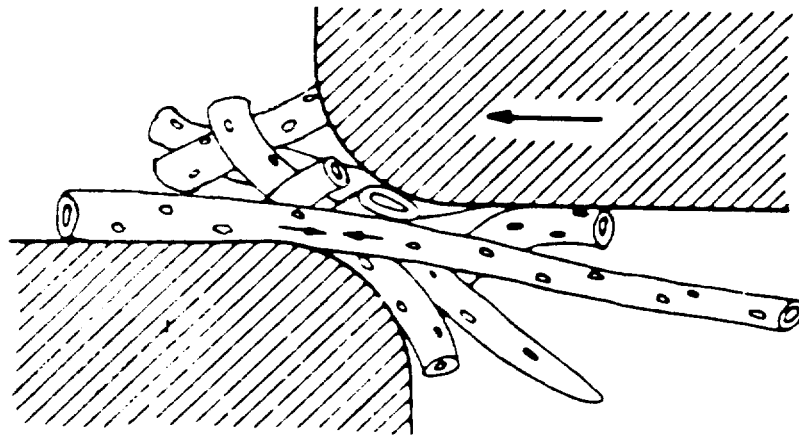


Figure 2.6. Fiber-to-fiber and fiber-to-metal contact during refining [1].

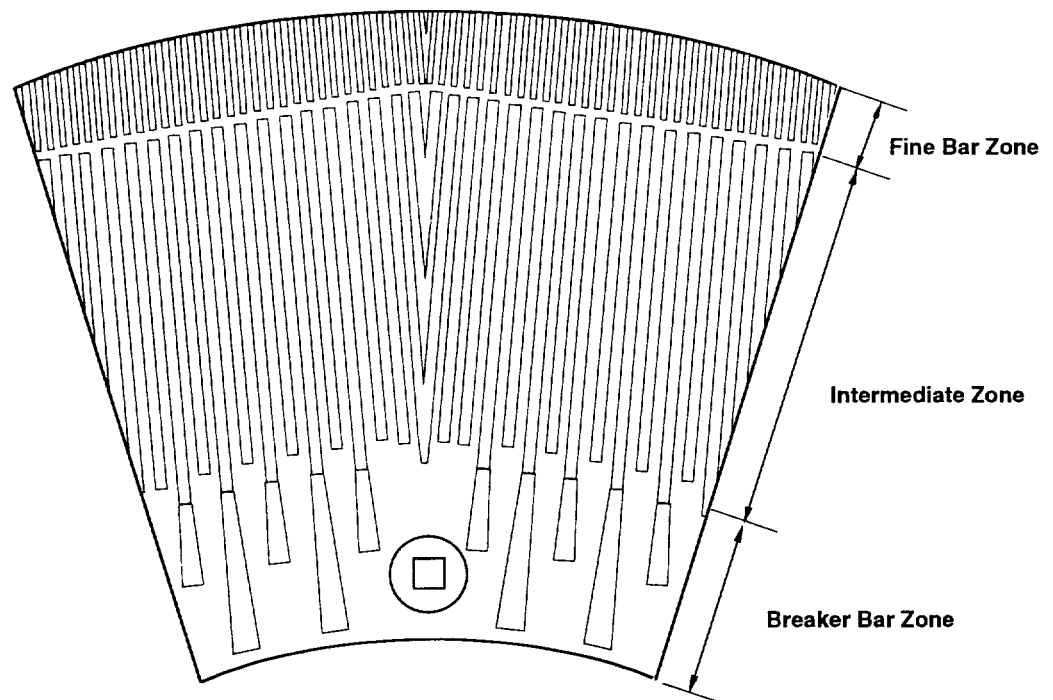


Figure 2.7. A typical TMP refiner plate.

$$SR = \frac{H}{ROOT}$$

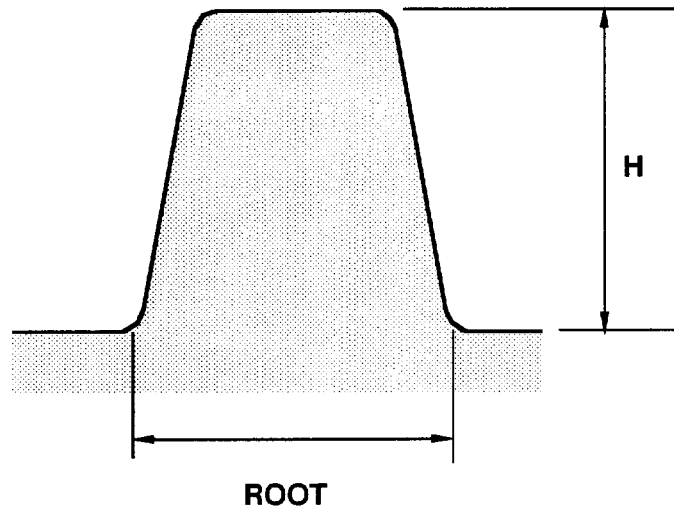


Figure 2.8. Bar strength ratio [14].

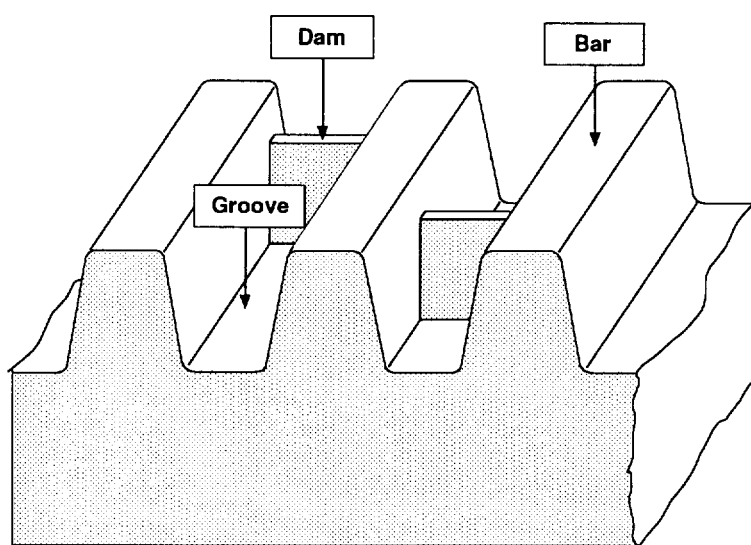


Figure 2.9. Bars, grooves, and dams.

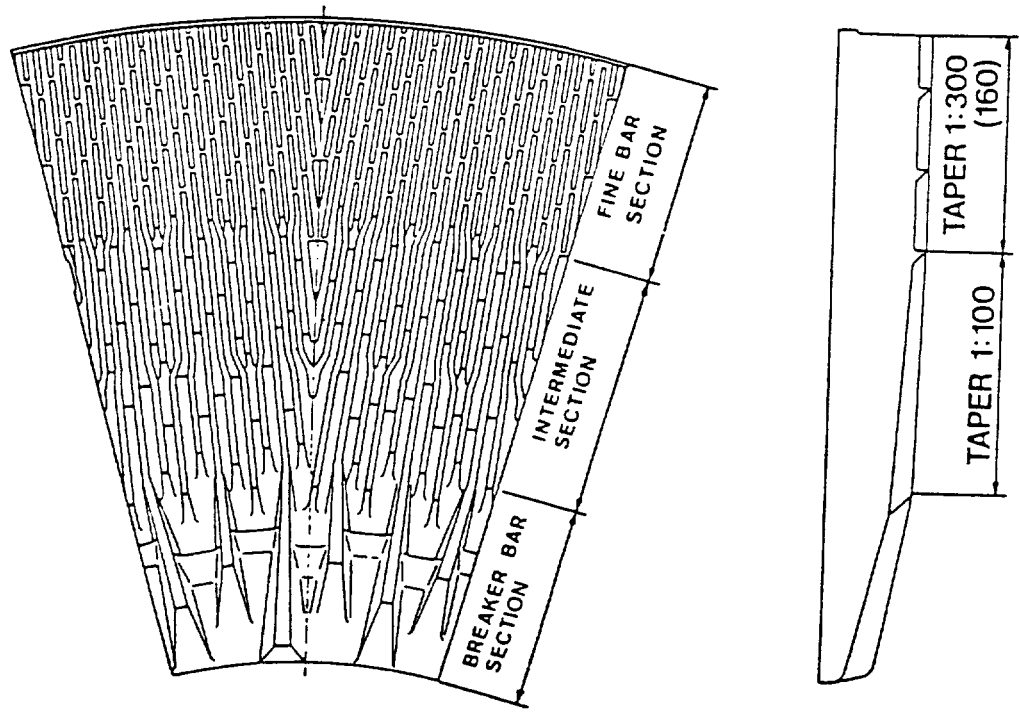


Figure 2.10. Plate taper [8].

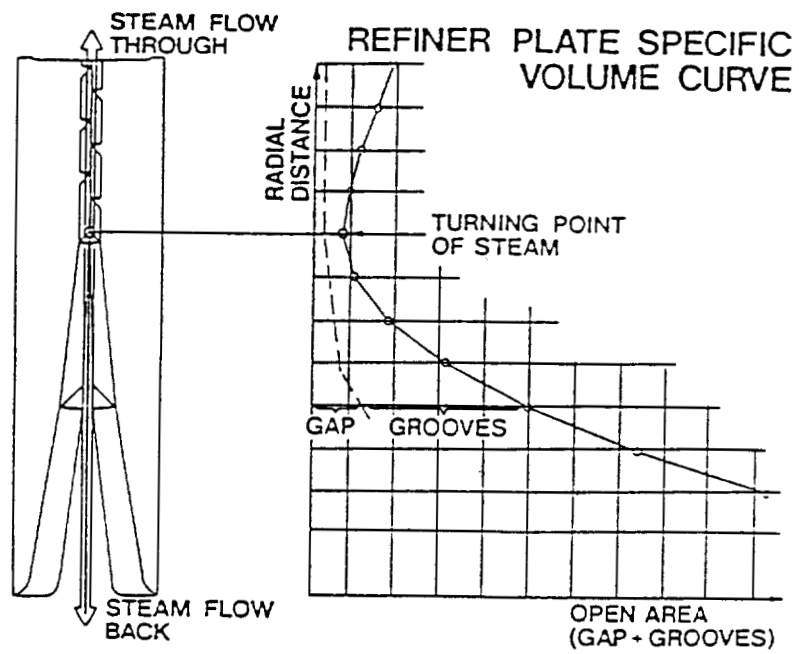


Figure 2.11. Refiner plate specific volume curve [8].

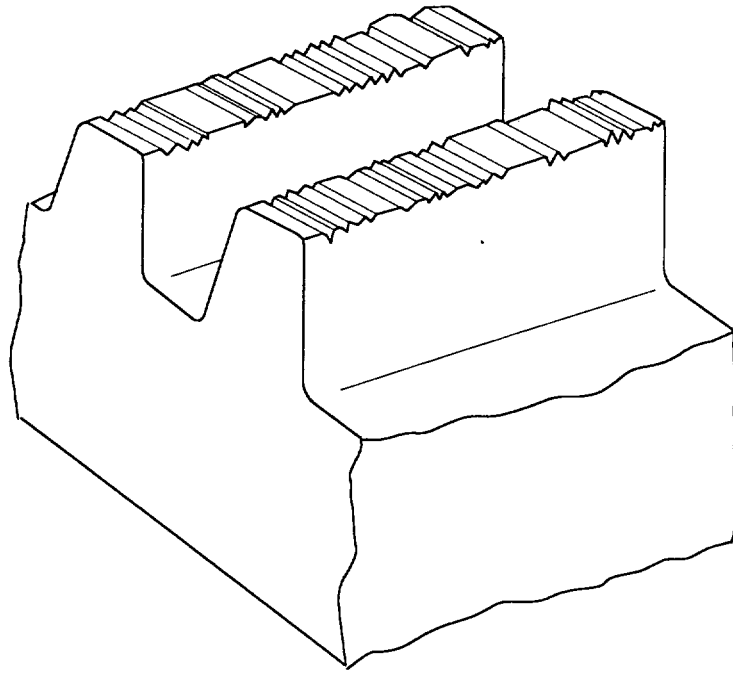


Figure 2.12. Serration damage.

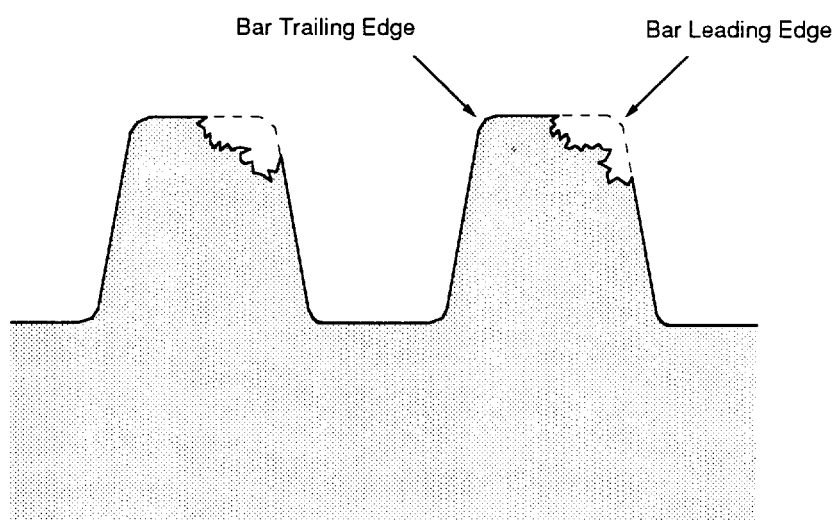


Figure 2.13. Pitting damage.

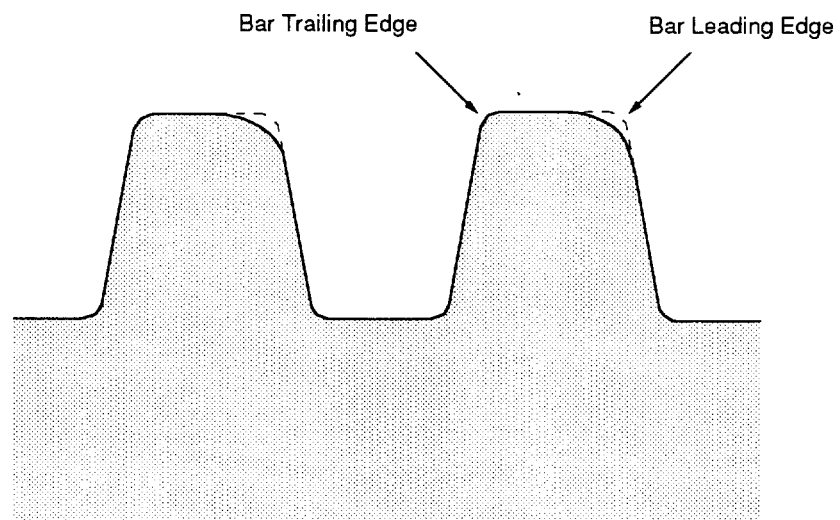


Figure 2.14. Bar rounding damage.

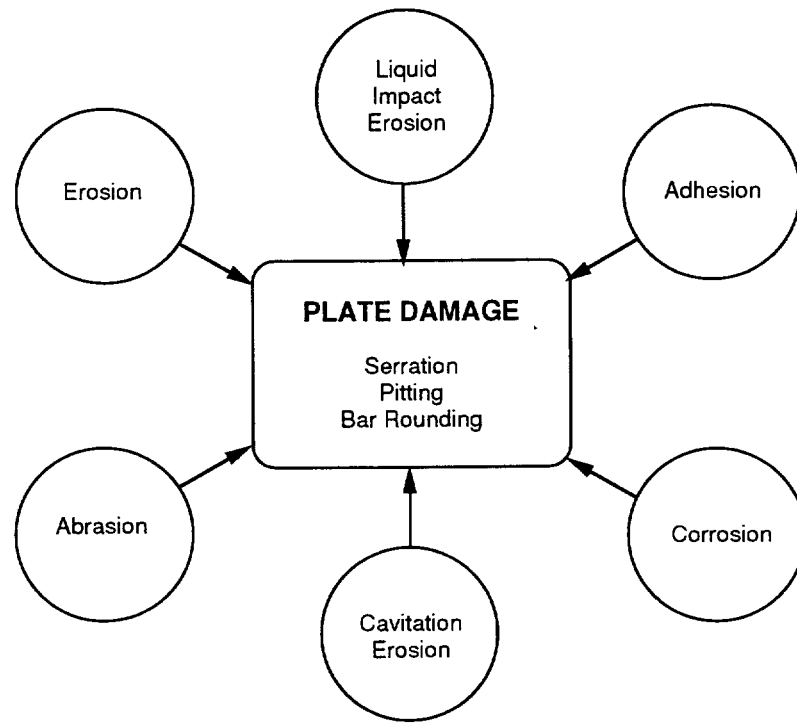


Figure 2.15. Plate deterioration modes and mechanisms.

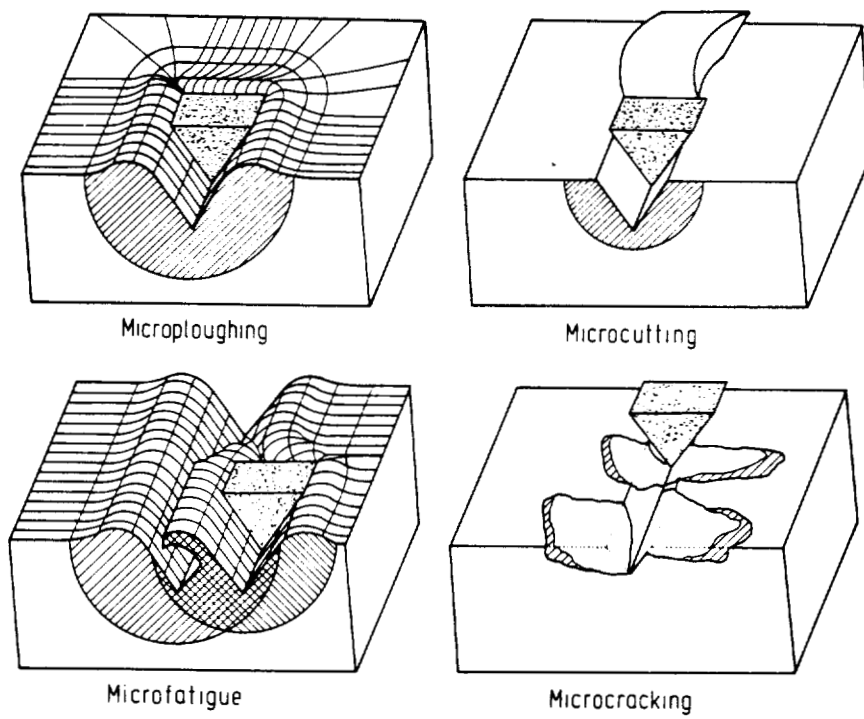


Figure 2.16. Physical interactions between abrasives and surface of material in abrasion [47].

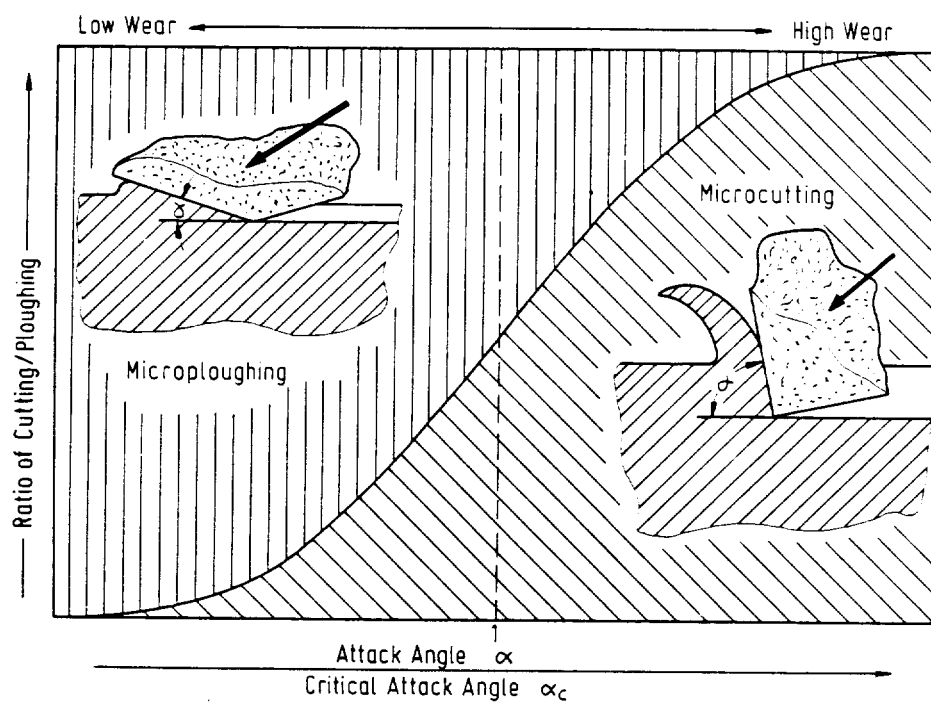
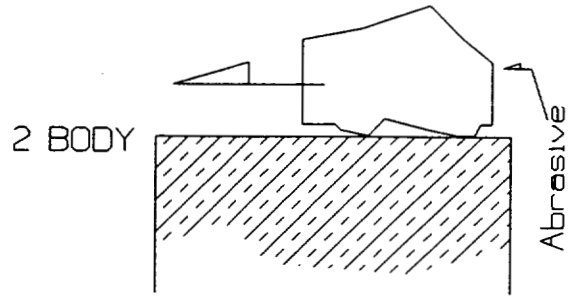
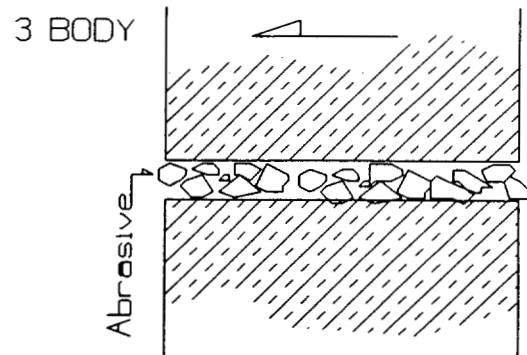


Figure 2.17. Ratio of microcutting to microploughing as a function of the ratio of the attack angle α to the critical attack angle α_c [47].



(a)



(b)

Figure 2.18. Two-body abrasion (a) and three-body abrasion (b).

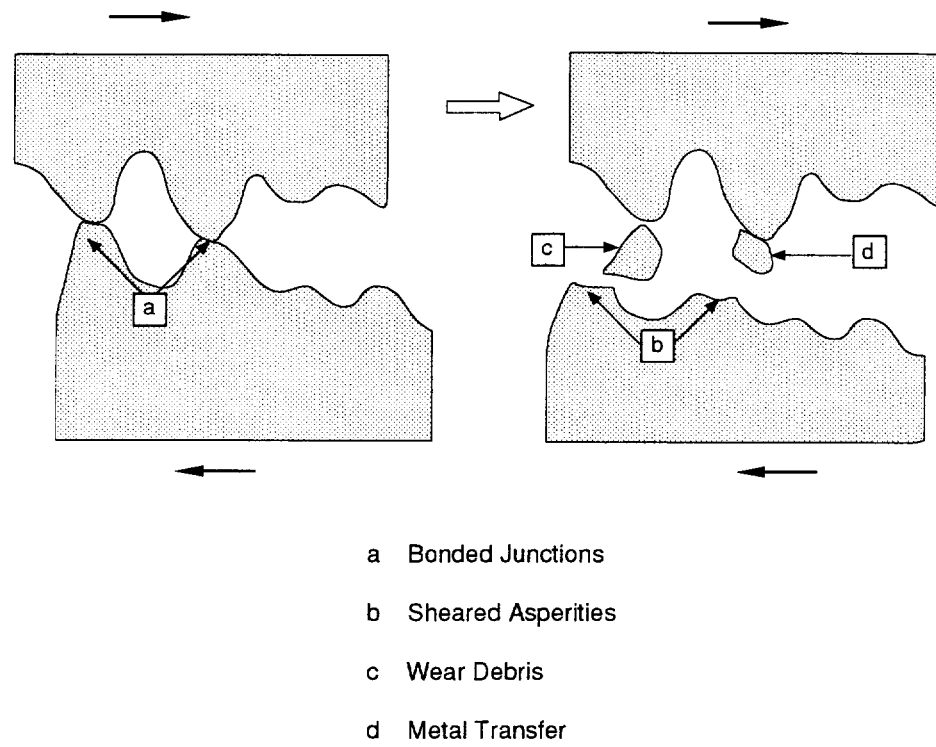


Figure 2.19. Asperity bonding, asperity rupture, metal transfer, and debris formation in adhesion.

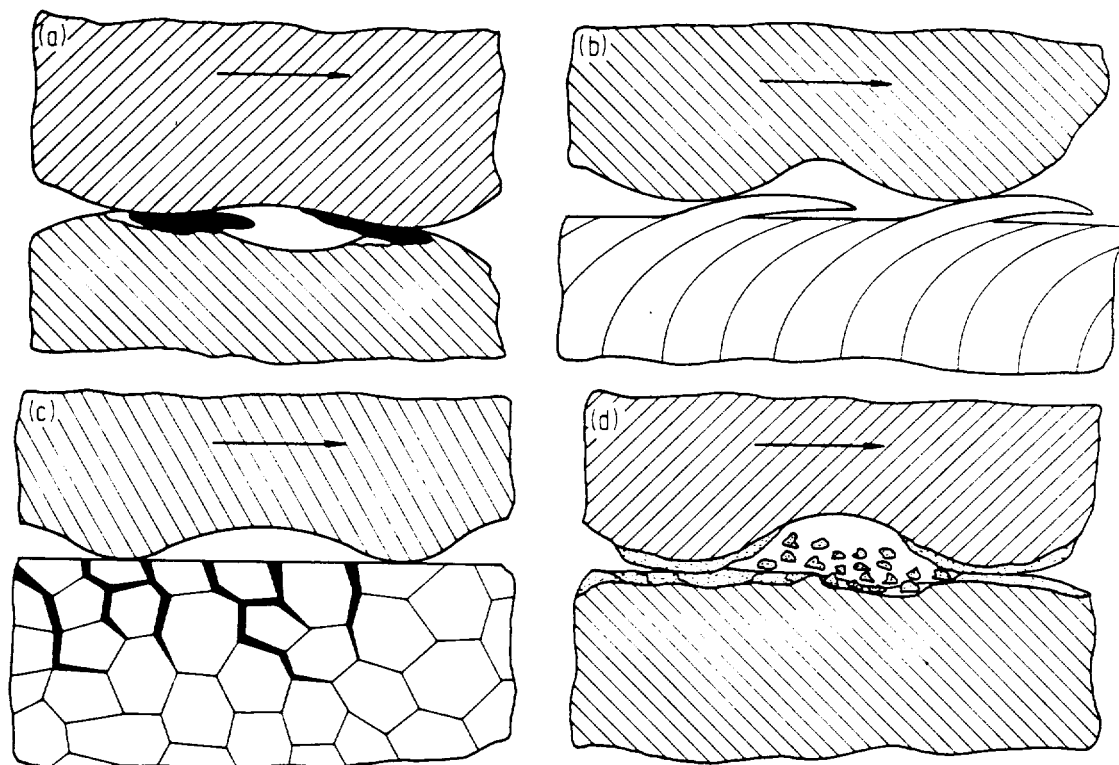


Figure 2.20. Mechanisms of wear during sliding contact [47].

- (a) Adhesive junctions, material transfer and grooving.
- (b) Surface fatigue due to repeated plastic deformation on ductile solids.
- (c) Surface fatigue results in cracking on brittle solids.
- (d) Tribochemical reaction and cracking of reaction films.

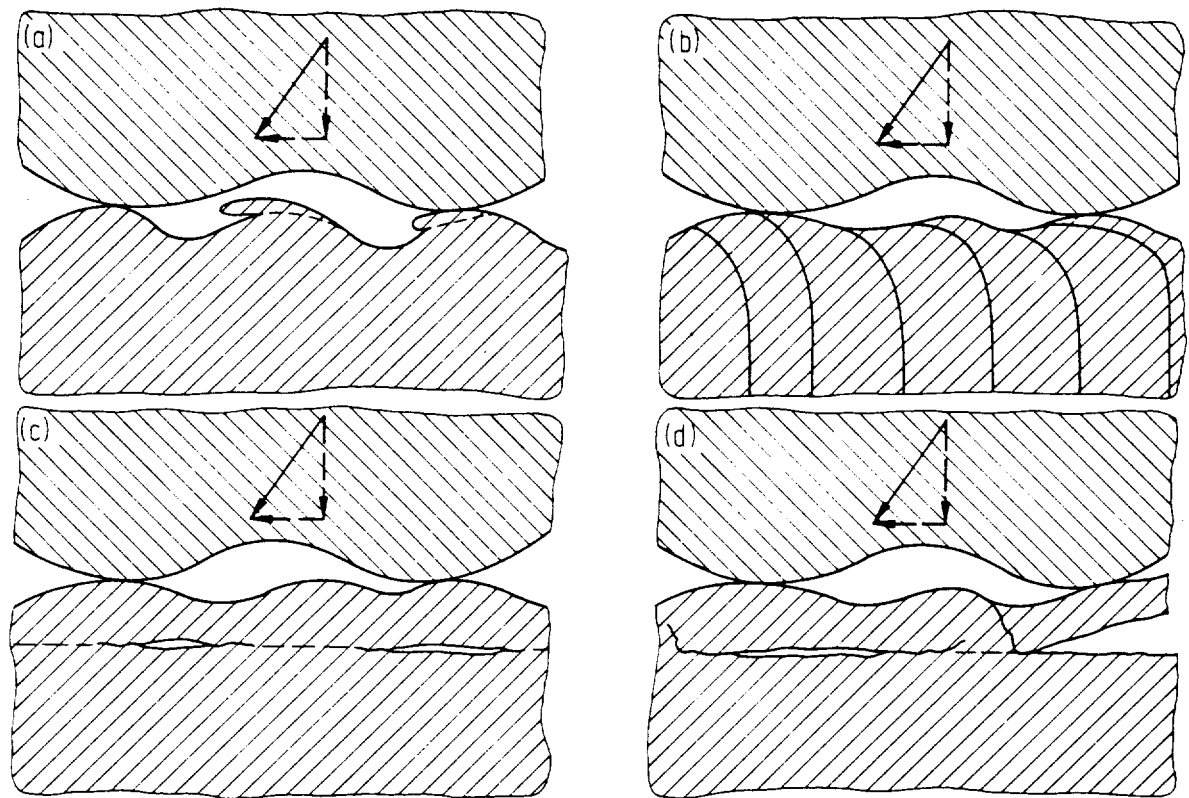
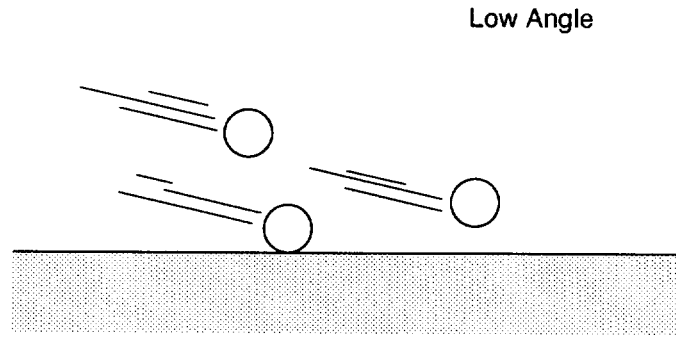
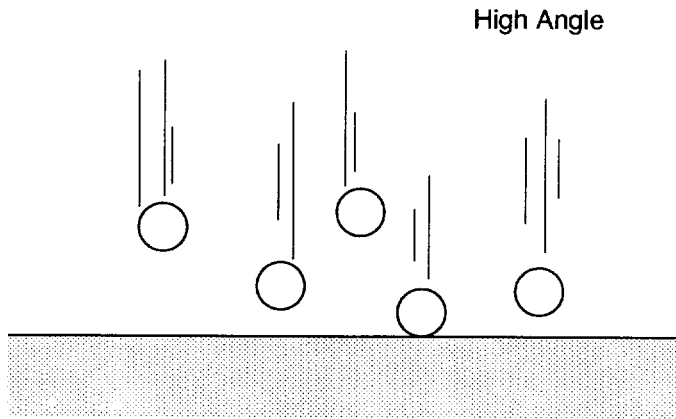


Figure 2.21. Formation of wear sheets due to delamination [47].

- (a) Smoothing of the softer surface.
- (b) Strain accumulation below the surface.
- (c) Initiation of subsurface cracks.
- (d) Formation of sheet-like wear particles.



(a)



(b)

Figure 2.22. Low angle erosion (a) and high angle erosion (b).

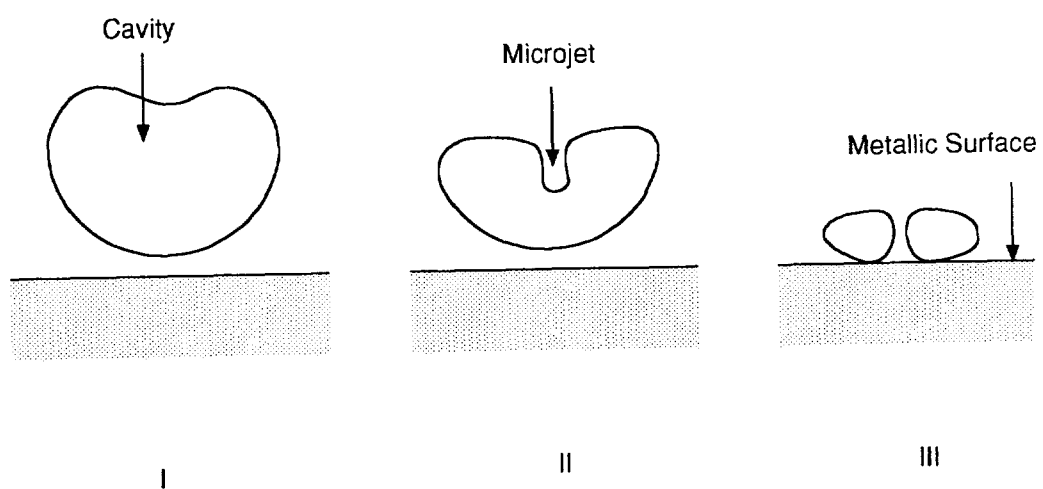
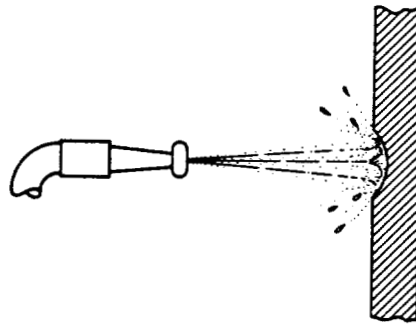
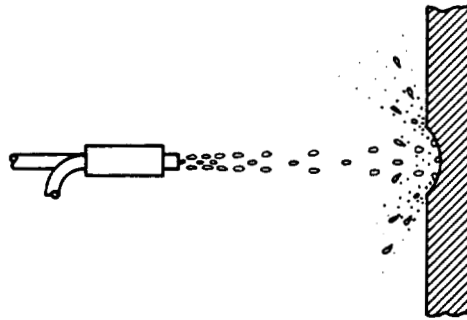


Figure 2.23. Schematic representation of successive stages of nonsymmetrical cavity collapse with microjet impingement against a metallic surface [78].



(a)



(b)

Figure 2.24. Schematic of liquid impingement erosion by liquid jet (a) or drop (b) [61].

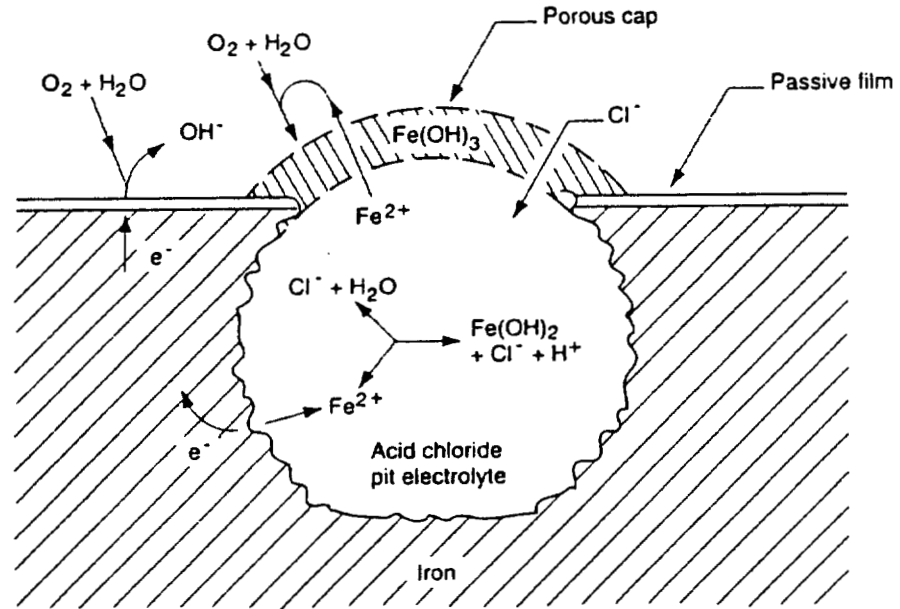


Figure 2.25. Schematic of pitting corrosion processes at an actively growing pit in iron [109].

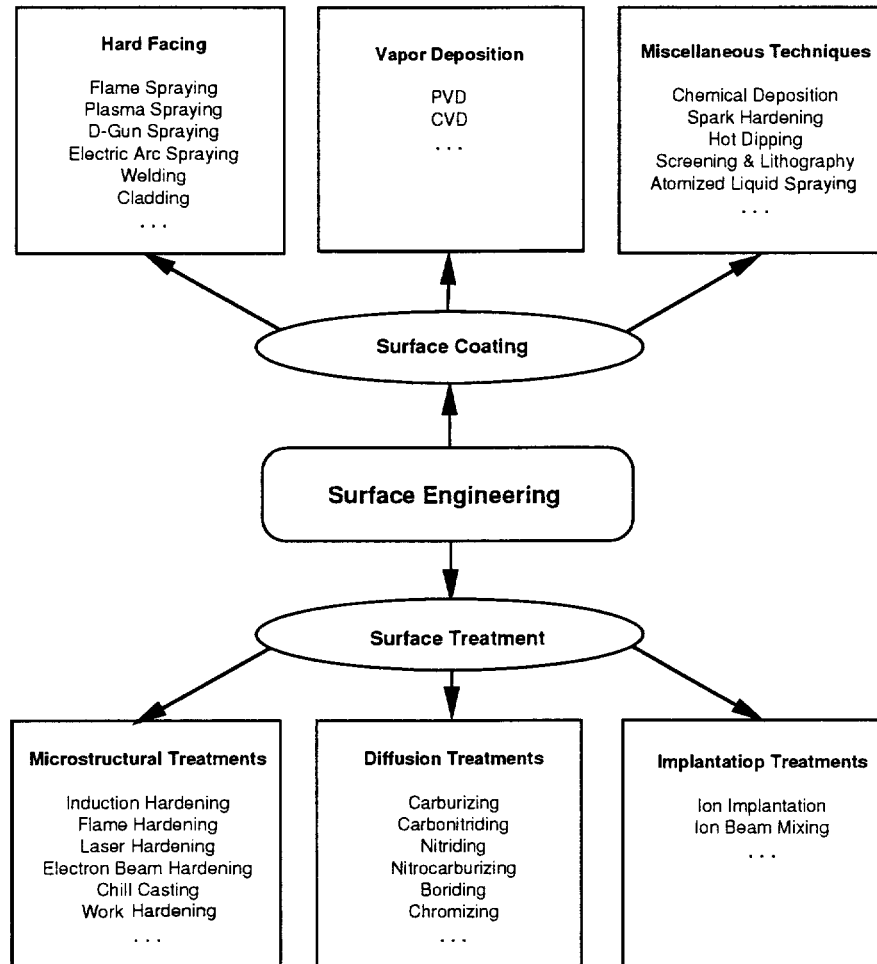


Figure 2.26. Surface engineering.

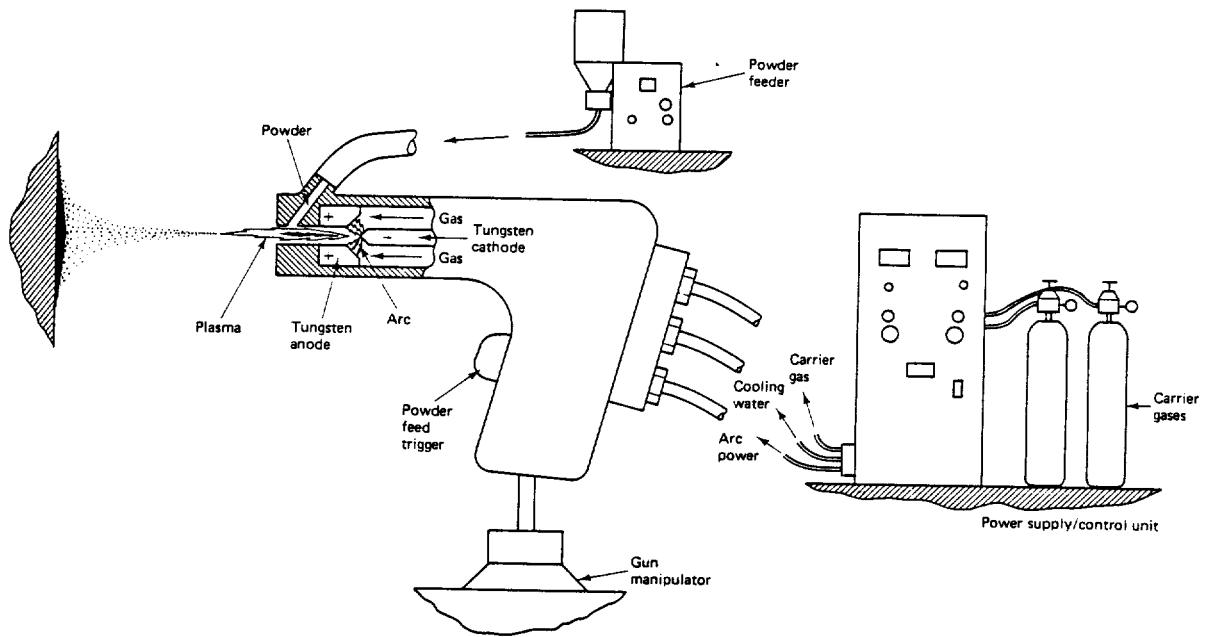


Figure 2.27. Plasma spraying process [61].

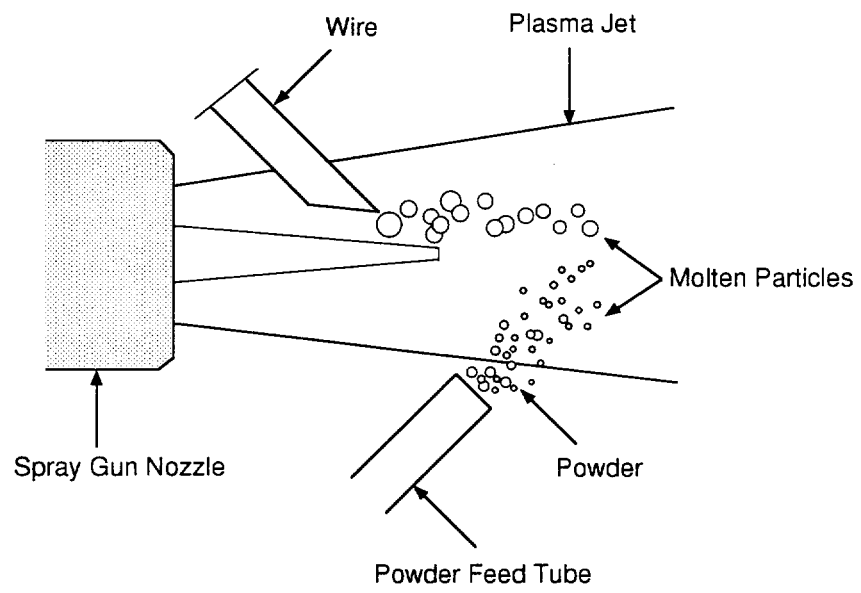


Figure 2.28. Wire feed and powder feed.

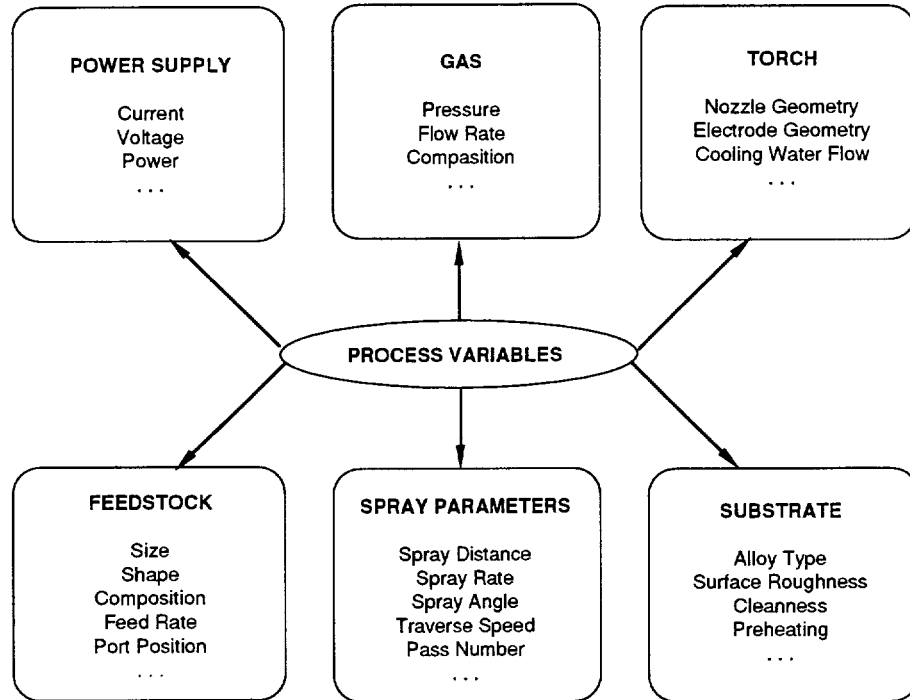


Figure 2.29. Plasma spraying process variables.

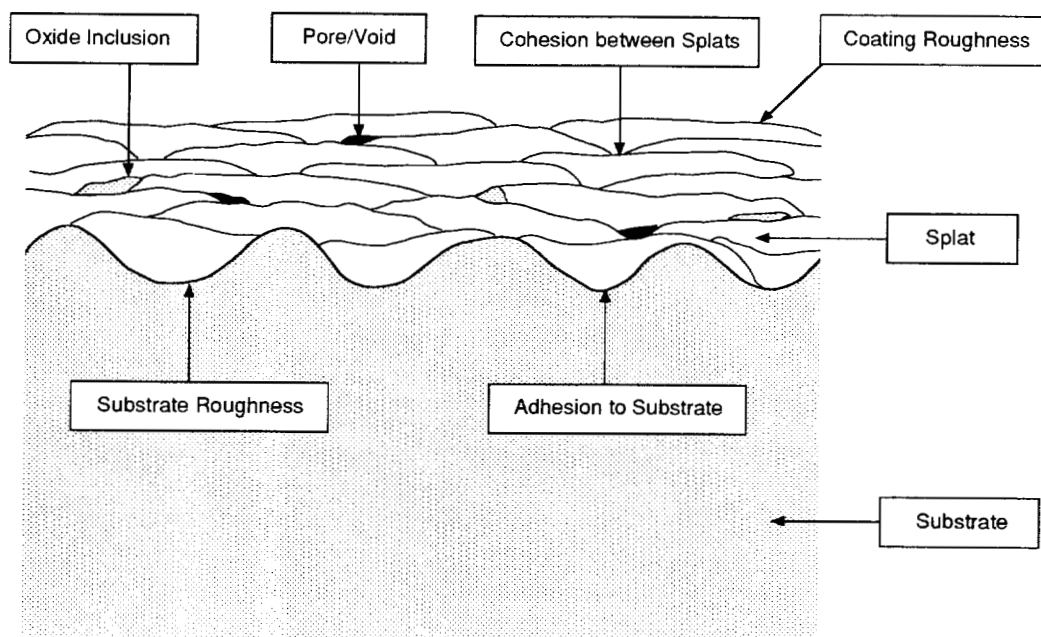


Figure 2.30. Cross-section of plasma coating.

CHAPTER 3 EXPERIMENTAL

3.1. PLATE FAILURE ANALYSIS

3.1.1. Interrupted Mill Trials

The interrupted mill trials were conducted in a Bauer 485, counter rotating, primary refiner. The refiner was usually run at a constant 6 MW and the feed rate and dilution water were adjusted to accommodate different wood species. The primary stage was chosen for the trials to reduce the incidence of plate clashing. Two types of plate alloys were tested, C20 and S17, representing 20-2-1 white iron and 440C stainless steel respectively. In the first four trials, a series of C20 plates were run for different durations with white wood chips, as shown in Table 3.1. In the first trial, plates were run for 147 hours, just long enough to achieve their break-in and therefore the expected optimum performance. As plate changes are normally scheduled after approximately 1000 hours of service, the 147-hour-trial represented 15% of typical full plate life. The following three trials were carried out for 550, 772, and 1166 hours, representing roughly 50, 75, and 100% of full life. The fifth experiment was also a full life test with white wood but the plate alloy was S17 stainless steel. The last trial involved running C20 plates to 100% life with Douglas fir.

3.1.2. Plate Damage Examination

For each mill trial, one plate was sectioned to obtain the specimens needed for

the failure analysis. From Figure 3.1, the specimens were cut from three general locations in the breaker bar, the intermediate bar, and the fine bar zone. As shown in Figure 3.2, the surface and subsurface (via cross-section) for each plate were examined by SEM and optical microscopy. Therefore two sets of specimens were prepared. Specimens approximately 20×20 mm, containing the plate bars, were sectioned by water cooled abrasive cutoff saws from the plates. The specimens were cleaned using a soft bristle brush with soap and water in conjunction with an ultrasonic bath. The specimen surfaces were then examined in the SEM with 20 KV and 11-20 mm working distance. The specimens cut for subsurface observations were mounted by a Leco PR-30 mounter with Extec black phenolic powder, ground and polished, etched with 4% nital and then examined in a Nikon Epiphot inverted metallurgical microscope. The subsurface examination emphasized cross-sections parallel to the plate rotation direction.

3.1.3. Plate Damage Measurements

As no "standard" methods can be found to quantify plate damage, appropriate methodology and measurements were developed. Bars and grooves constitute the plate surface. In used refiner plates the bars are often severely serrated, pitted, or edge rounded but the grooves retain their original shapes. In this work, therefore, the surface damage measurements focused only on the plate bars.

As depicted in Figure 3.3, using a transparency printed with a grid, the serrated and pitted plate surface area fractions were roughly determined. The bar rounded area fraction, however, was negligibly small since bar rounding seldom covers a wide range of the bar top. The maximum bar rounded width (Figure 3.4), therefore, was used to represent the bar rounding damage degree while the mean bar rounded width was much more difficult to determine. As refining proceeds, serrated and pitted areas may overlap each other. Thus, serrated zone width and pitted bar leading edge fraction may be the better measures for serration and pitting, respectively. The former is defined as the

length from the plate periphery to the end of the severely serrated zone (Figure 3.5), while the later is the ratio of the total pitted bar leading edge length to the total original one (Figure 3.6).

It should be noted that both bar rounding and pitting occurred primarily along the bar leading edges. As a result, the two types of damaged areas can overlap. Since the pitting damage usually occurred late in the plate life, the pitted areas will replace some of the bar rounded ones as plate service continues, which can be reflected by the monotonic increase in pitted bar leading edge fraction. Thus, in the late plate life the measured maximum bar rounded width value may not be the real one as a substantial percentage of the rounded bar leading edges can be overlapped by pitted areas. Even late in the plate life, however, the pitting damaged areas are still discontinuous along the bar leading edges (Figure 3.6), while the profiles of bar rounded areas along the leading edges are usually continuous (Figure 3.4). Despite the presence of several pitted areas, the maximum bar rounded width can still be roughly estimated from the profiles of bar rounded areas, thereby being a good measure of the plate bar rounding damage.

For heavily serration damaged plates the surface plastic deformation and work hardening were quantified. The surface deformation in the serrated areas was characterized by measuring the thickness of the severely deformed layer and the maximum surface displacement. As shown in Figure 3.7, such a layer can be easily detected from the metallographic cross-sections of the serrated plates, because in either C20 or S17 plates many eutectic carbides which are oriented roughly normal to the plate surface could be deformed and cracked along with the matrix in the plate moving direction. The degree of work hardening induced by serration damage was reflected by the matrix microhardness increase in the heavily deformed surface layer. The bulk hardness of the alloys was determined by a Wilson Rockwell Hardness Tester, while the matrix hardness and carbide hardness were examined using a Knoop indenter with 25 g

load and 15 second loading time. Each hardness value was the average of over twenty measurements, with the standard deviation also being calculated and listed.

3.2. PLATE MATERIAL EVALUATION

3.2.1. Plate Alloys

Alloy Composition. Eight different refiner plate alloys were examined. They can be divided into two families. The cast white iron family included three alloy groups: Ni-hard, 20-2-1, and 25 Cr white irons. The martensitic stainless steel family included cast 440C and cast 17-4PH. With some alloys, Ni-hard, 20-2-1, and 440C, there are two types of alloys which had basically the same compositional range but different microstructures and hardness levels. These alloys were produced by different companies with different heat treatment methods. The specimens of five alloys, including C80, C30, C20, C15, and 17-4PH, were cut from large used refiner plates. The NH, C25, and S17 alloy specimens, however, were obtained from small cast coupons so their microstructures were relatively finer. All alloys were tested in the as-received conditions, with their compositional ranges being listed in Table 3.2.

Alloy Characterization. The microstructures of the plate alloys were examined with a Nikon inverted metallograph at a magnification of 400 times. The specimens were prepared by first grinding with a series of sand papers up to 800 grit, and then polished by 5 μm and 0.05 μm alumina abrasives. Before the metallographic examination, the polished 17-4 PH steel specimen was etched by Villela's reagent (5 ml HCl, 1 g picric acid, and 100 ml ethanol), while other plate alloys were etched with a 10% nital. For some carbide-containing alloys, including the 20-2-1 and Ni-hard irons, the carbide volume fractions were measured by using an image analyzer. For each specimen ten measurements were taken to obtain the mean value. The bulk hardness of the alloys was evaluated by the Wilson Rockwell Hardness Tester, with each reported value being the

average of more than ten measurements. The microhardness for both matrix and carbide were determined by using a Knoop indenter with 25 g load and 15 second loading time, with each hardness value being the average of at least ten measurements. Secondary dendritic arm spacing, which is an indicator of the fineness of the as-cast alloy structure, was determined approximately by using a scaled objective lens in the Nikon metallograph at a magnification of 200 or 400 times (Figure 3.8).

3.2.2. Plasma Coatings

Coating Deposition. To obtain a general picture of the effect of deposition parameters on the microstructure, microhardness, surface roughness and wear performance, 33 plasma coatings, covering 17 groups of materials, were deposited by a 200 KW Plazjet plasma-spray system. The spray gun, which is schematically shown in Figure 3.9, was operated at 400-450 volts and 300-350 amperes. Nitrogen was used as the primary gas at 250 slpm with a supply gas pressure of 200 psi. When needed, hydrogen was used as the secondary plasma forming gas at 50 slpm with a supply pressure of 200 psi. Annealed 1020 and 1060 steel coupons (1" × 3" × 1/2") were used as substrates, being washed with soapy water, grit blasted with 40 mesh chilled iron shot, degreased with acetone, and then cleaned in ethanol immediately to spraying. Grit blasting can efficiently clean substrate surfaces and increase the surface roughness of the coupons to be sprayed so that the bonding between the coating and the substrate is improved. The samples were held in either a water-cooled fixture or a graphite fixture and coatings deposited by multiple passes. Power level, gas flow rates, and powder feed rates were maintained relatively constant for all coatings deposited. Powder gas pressure was held constant at 15 psi while feed rate was varied between 7.5 and 10 rpm, depending on the powder type. The powder was fed by a Plasmadyne Rotohopper powder feeder, being injected into the plasma at 90° for oxide materials and 60° for carbide powders. Spray distance and powder size were the major variables to modify the coating roughness. The former was changed from 100 to 250 mm while the latter

varied within the range of powders available. Tables 3.3 and 3.4 show the powder compositions, sizes, and physical properties for the 17 groups while Table 3.5 lists the deposition parameters for all 33 coatings.

Coating Characterization. The coating specimens were sectioned and mounted as depicted in Figure 3.10, ground through 800 grit sandpaper and then polished with 5 μm and 0.05 μm alumina abrasives. All coatings were examined in the as-sprayed and unetched condition. Coating porosity was evaluated by the image analyzer. As shown in Figure 3.11, surface roughness parameter R_a is defined as the arithmetic mean of the deviations of the roughness profile from the mean line. By using a Mitutoyo SurfTest 401 analytical profilometer with associated analyzer and recorder, R_a was obtained from at least ten measurements being made in non-parallel traverses on each specimen. The thickness of a coating was determined by using the Nikon metallograph. Microhardness values of the coatings were obtained on transverse sections through the coatings using a Knoop indenter with 100 g load, with each hardness value being the average of at least ten measurements. For some coatings the mean splat thickness values were measured using a scaled objective lens with the Nikon metallograph. The coating density was estimated from the powder densities and powder composition.

3.2.3. Wear Testing

The wear behavior of both the plasma coatings and conventional refiner plate alloys was evaluated in three types of wear tests: abrasion, erosion, and cavitation erosion. Before testing, the cast alloy specimens were ground with sandpapers while all coatings were tested directly in the as-sprayed condition. Each cast alloy's behavior was determined from just one specimen, while each coating's was the average of up to six specimens. A tool steel, D2, was used as the reference to evaluate the wear data reproducibility. The weight loss of all specimens was measured by a balance with a sensitivity of 0.0001 g. The worn surfaces and subsurfaces were examined respectively

by SEM and optical microscope. The worn surface roughness values for cavitation eroded specimens were also determined.

Abrasion Testing. Abrasion behavior was evaluated by using a dry-sand-rubber-wheel (DSRW) test machine (ASTM G65), illustrated in Figure 3.12, which produces low stress abrasion. By means of a lever arm, the specimen was loaded against a 227 mm rubber rimmed steel wheel rotating at 200 rpm with 130 Newtons of load. A sand feeding apparatus fed abrasive at a rate of 250-350 g/min, and a counter was used to measure the number of wheel revolutions. The rotation of the wheel is such that its working face moves in the direction of the abrasive flow. The abrasive used was 50-70 mesh rounded Ottawa silica sand, being introduced between the test specimen and the rotating wheel. The total test duration of each specimen was 1200 revolutions or approximately 1000 meters, with the weight loss of the specimen measured every 200 revolutions. The first 400 revolutions, however, were used as the running-in period during which the weight loss was not counted in calculating the wear resistance. The total weight loss was plotted against the total path length and the abrasion behavior was represented by weight loss per unit path length.

Erosion Testing. Erosion behavior of materials was examined using a multiple capacity erosion test machine schematically shown in Figure 3.13. This rig can erode a specimen surface with either high velocity water (50 - 100 m/s) or high velocity steam (over 100 m/s) with entrained abrasive particles, producing water sand erosion (WSE) and steam sand erosion (SSE), respectively. The erodant used was 50-70 mesh rounded Ottawa silica, being fed at a rate of 30 g/min. The impingement angle was 90°. In WSE tests, the stand-off distance between the nozzle exit and the specimen was 0.5 inch (6.3 mm) while the nozzle was 3/8 inch (9.5 mm) in diameter. Each specimen was weighed after 400 g of erodant was used, with four iterations of the process but the first one as the running-in period. In SSE tests the procedure was similar except weight loss was measured after every 50 g of erodant were consumed, the stand-off distance was 0.5

inch (12.7 mm), and the nozzle diameter was 1/8 inch (3.2 mm). The total weight loss was plotted versus the total amount of abrasive used and the wear behavior was evaluated by weight loss per unit amount of erodant.

Cavitation Erosion Testing. An ultrasonic vibratory system was used to generate repeated cavitation near the specimen inside a vessel filled with deionized water, shown in Figure 3.14. The power supply converted conventional 50/60 Hz line current to 20 KHz electrical energy and provided it to the converter by which the electrical energy was changed to mechanical vibratory energy. The booster determined the amplitude of the vibrations while the horn and the consumable tip was used to transmit the ultrasonic vibrations to the fluid medium. The gap between the tip and the sample surface was 0.04 inch (1 mm) and the power control set at 80%. The temperature of the working liquid was maintained at room temperature by a water jacket surrounding the vessel's outer wall. The test duration for each alloy specimen was 14 hours with the weight loss measured every two hours with the first 4 hours being the running-in period. For each coating specimen, the test duration was 2 hours with the weight loss measured every 15 minutes but the first 30 minutes being the running-in period. The wear behavior was represented by weight loss per unit time.

Table 3.1. Interrupted Mill Trials

Trial No.	Plate Alloy	Service Time (hrs)	Plate Life (%)	Wood Species
1	C20 (20-2-1)	147	15	White Wood
2	C20 (20-2-1)	550	50	White Wood
3	C20 (20-2-1)	772	75	White Wood
4	C20 (20-2-1)	1166	100	White Wood
5	S17 (440C)	1165	100	White Wood
6	C20 (20-2-1)	950	100	Douglas Fir

Table 3.2. Plate Alloy Compositions

Alloys		% C	% Si	% Mn	% Cr	% Mo	% Ni	% Cu
Ni-Hard	NH	3.0/3.6	0.5/0.8	1.3 max	1.4/4.0	1.0 max	3.0/5.0	-
	C80	3.0/3.5	0.5/0.8	0.4/0.8	1.9/3.2	-	3.5/5.0	-
20-2-1	C30	2.0/3.2	1.0 max	0.5/1.5	18/23	1.5 max	1.5 max	1.2 max
	C20	3.0/3.3	0.5/0.8	0.6/0.9	20/21	1.8/2.2	0.4 max	0.8/1.2
25Cr	C25	2.4/2.8	0.5/0.8	0.6/0.9	25/27	0.3 max	0.4 max	0.4 max
440C	C15	0.9/1.2	1.0 max	0.5/1.5	15/18	1.0 max	-	-
	S17	0.9/1.2	1.0 max	0.5/1.5	15/18	1.0 max	-	-
17-4PH	17-4PH	0.07 max	1.0 max	0.7 max	15/18	-	3.5/4.5	2.5/3.2

Table 3.3. Powder Compositions and Sizes

Family	Group	Sample#	Powder Composition	Powder Size (μm)
Alloys	Fe-Mo-C	1 - 3	82%Fe, 15%Mo, 3% C	- 90 + 10
	Ti-Alloy	4	Proprietary Wire	n.a.
	Ni-Cr-Si-Fe-B1	5 - 6	78.4%Ni, 12.5%Cr, 3%Fe, 3.7%Si, 2.4%B	- 105 + 15
	Ni-Cr-Si-Fe-B2	7 - 8	73.9%Ni, 14.5%Cr, 4.3%Fe, 4.3%Si, 3%B	- 105 + 15
	IN625-Cr ₃ C ₂	9	IN-625 Wire + Cr ₃ C ₂	- 105
Ceramics	Al ₂ O ₃ -TiO ₂	10 - 16	87%Al ₂ O ₃ , 13%TiO ₂	- 45 + 10
	Cr ₂ O ₃ -SiO ₂ -TiO ₂	17 - 18	92%Cr ₂ O ₃ , 5%SiO ₂ , 3%TiO ₂	- 90 + 10
Cermets	Cr ₃ C ₂ -WC-TiC-Ni-Mo	19	62%Cr ₃ C ₂ , 25%WC, 5%TiC, 4%Ni, 3%Mo	- 45 + 5
	W-C-Co1	20	12%Co, 4%C, 2%Max Fe, bal. W	- 105 + 75
	W-C-Co2	21	12%Co, 4%C, 2%Max Fe, bal. W	- 75 + 45
	WC-Co1	22	89%WC, 11%Co	- 45 + 15
	WC-Co2	23	91%WC, 9%Co	- 45 + 15
	Cr ₃ C ₂ -WC-TiC-Ni-Mo-C1	24 - 25	62%Cr ₃ C ₂ , 25%WC, 5%TiC, 4%Ni, 3%Mo, 1%C	- 105 + 15
	Cr ₃ C ₂ -WC-TiC-Ni-Mo-C2	26 - 27	62%Cr ₃ C ₂ , 25%WC, 5%TiC, 4%Ni, 3%Mo, 1%C	- 45 + 5
	WC-Cr ₃ C ₂ -Ni1	28 - 29	70%WC, 24%Cr ₃ C ₂ , 6%Ni	- 45 + 5
	WC-Cr ₃ C ₂ -Ni2	30 - 31	70%WC, 24%Cr ₃ C ₂ , 6%Ni	- 125 + 45
	Cr ₃ C ₂ -Ni-Cr	32 - 33	75%Cr ₃ C ₂ , 20%Ni, 5%Cr	- 105 + 15

Table 3.4. Powder Physical Properties [120,160]

Powders		Melting Point (°C)	Density (g/mm ³)	Hardness (kg/mm ²)
Metallic Elements	Fe	1535	7.87	200
	Mo	2610	10.22	300
	Ni	1450	8.91	210
	Cr	1900	7.19	600
	Co	1495	8.80	230
	W	3380	19.25	500
Nonmetallic Elements	B	2300	2.34	2600
	Si	1410	2.33	800
	C	3550	2.27	very soft
Alloys	Ti Alloy	1660	4.43	250
	Inconel 625		8.44	
Oxides	Al ₂ O ₃	2049	3.98	2100
	TiO ₂	1840	4.25	1100
	Cr ₂ O ₃	2330	5.21	1300
	SiO ₂	1705	2.20	550-750
Carbides	Cr ₃ C ₂	1895	6.68	1800
	TiC	3160	4.92	2800
	WC	2627	15.8	2100

Table 3.5. Deposition Parameters

Family	Group	Sample #	Voltage/Current (Volts/Amps)	Spray Energy (KW)	Spray Distance (mm)
Alloy	Fe-Mo-C	1	425/300	127.5	100
	Fe-Mo-C	2	425/300	127.5	150
	Fe-Mo-C	3	425/300	127.5	200
	Ti-Alloy	4	400/400	160.0	200
	Ni-Cr-Si-Fe-B1	5	420/350	147.0	200
	Ni-Cr-Si-Fe-B1	6	420/350	147.0	150
	Ni-Cr-Si-Fe-B2	7	420/350	147.0	200
	Ni-Cr-Si-Fe-B2	8	420/350	147.0	150
	IN625-Cr ₃ C ₂	9	400/400	160.0	200
Ceramic	Al ₂ O ₃ -TiO ₂	10	450/325	146.3	100
	Al ₂ O ₃ -TiO ₂	11	400/350	140.0	200
	Al ₂ O ₃ -TiO ₂	12	400/350	140.0	150
	Al ₂ O ₃ -TiO ₂	13	400/350	140.0	100
	Al ₂ O ₃ -TiO ₂	14	425/300	127.5	100
	Al ₂ O ₃ -TiO ₂	15	425/300	127.5	150
	Al ₂ O ₃ -TiO ₂	16	425/300	127.5	200
	Cr ₂ O ₃ -SiO ₂ -TiO ₂	17	400/350	140.0	200
	Cr ₂ O ₃ -SiO ₂ -TiO ₂	18	400/350	140.0	150
Cermet	Cr ₃ C ₂ -WC-TiC-Ni-Mo	19	420/350	147.0	200
	W-C-Co1	20	400/350	140.0	150
	W-C-Co2	21	400/350	140.0	200
	WC-Co1	22	400/350	140.0	200
	WC-Co2	23	400/350	140.0	250
	Cr ₃ C ₂ -WC-TiC-Ni-Mo-C1	24	420/350	147.0	200
	Cr ₃ C ₂ -WC-TiC-Ni-Mo-C1	25	420/350	147.0	150
	Cr ₃ C ₂ -WC-TiC-Ni-Mo-C2	26	420/350	147.0	200
	Cr ₃ C ₂ -WC-TiC-Ni-Mo-C2	27	420/350	147.0	150
	WC-Cr ₃ C ₂ -Ni1	28	425/350	148.8	150
	WC-Cr ₃ C ₂ -Ni1	29	425/350	148.8	200
	WC-Cr ₃ C ₂ -Ni2	30	425/350	148.8	150
	WC-Cr ₃ C ₂ -Ni2	31	425/350	148.8	200
	Cr ₃ C ₂ -Ni-Cr	32	400/350	140.0	200
	Cr ₃ C ₂ -Ni-Cr	33	400/350	140.0	150

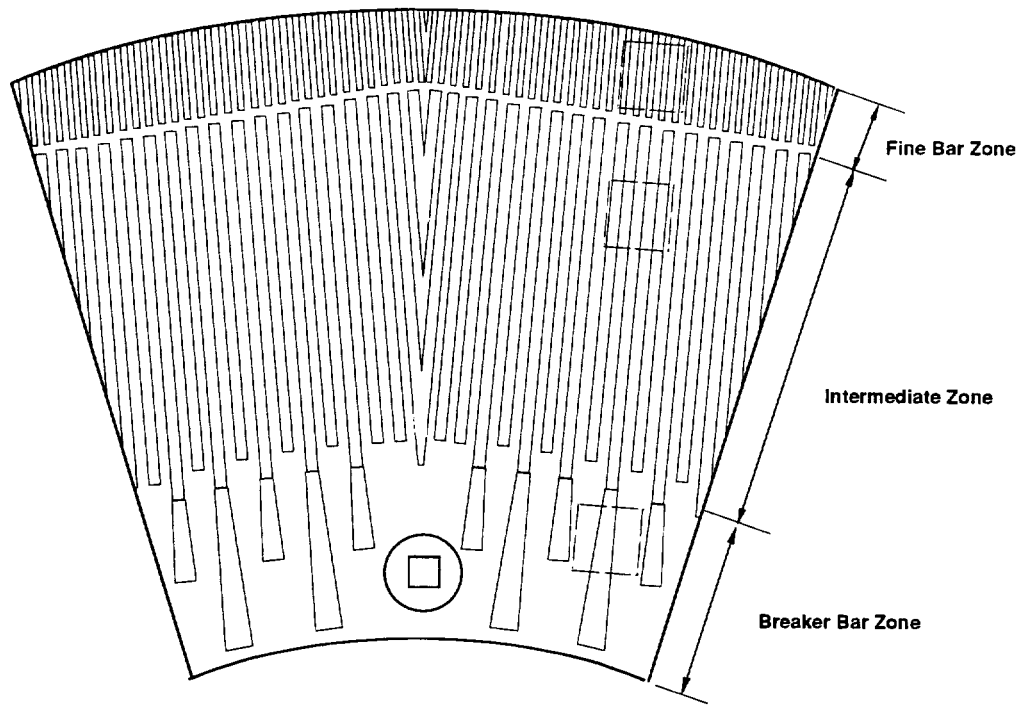


Figure 3.1. Sectioning of specimens from damaged plate.

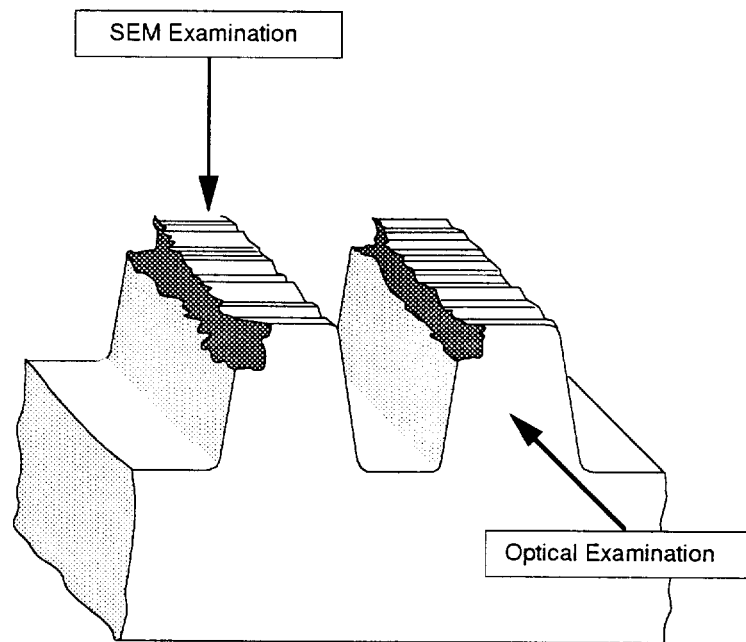


Figure 3.2. Surface examination and subsurface examination.

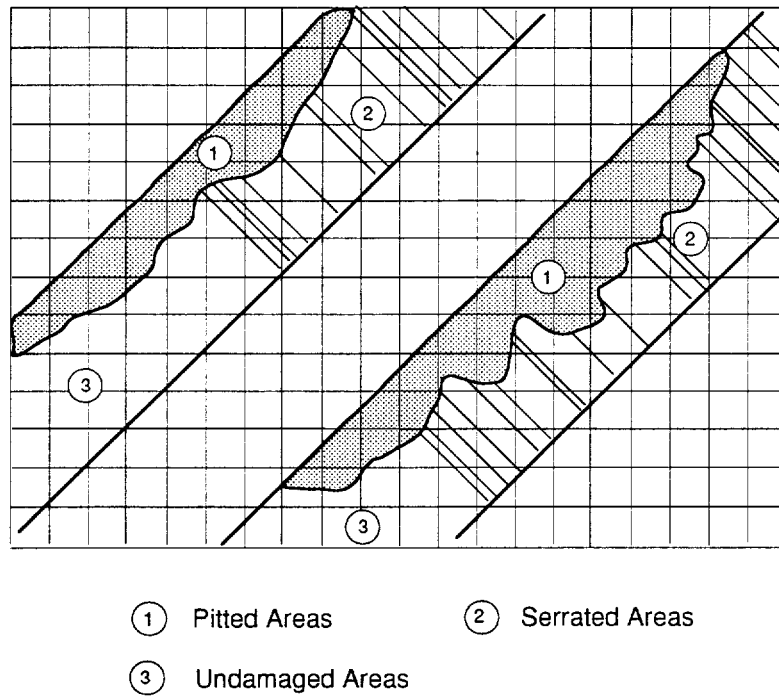


Figure 3.3. Serrated area fraction and pitted area fraction.

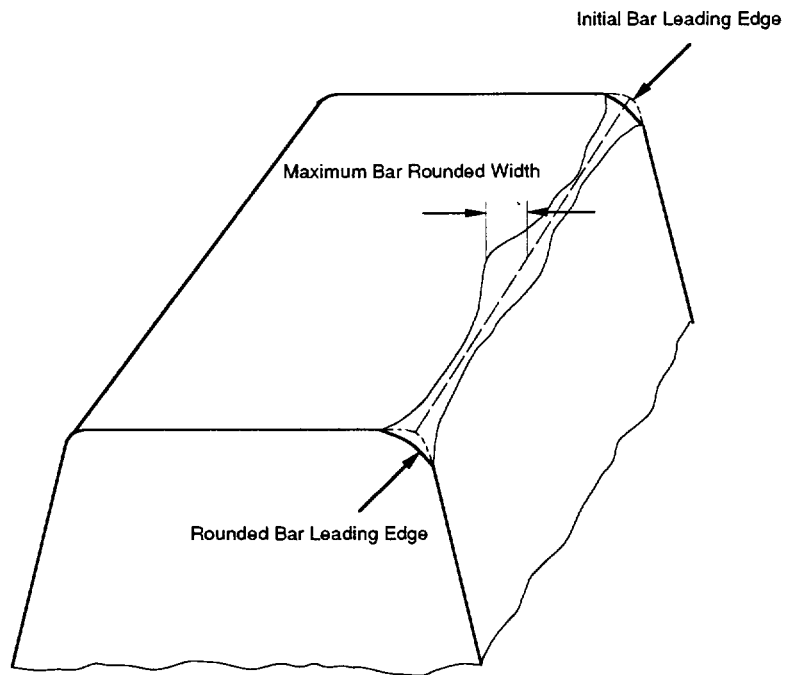


Figure 3.4. Maximum bar rounded width.

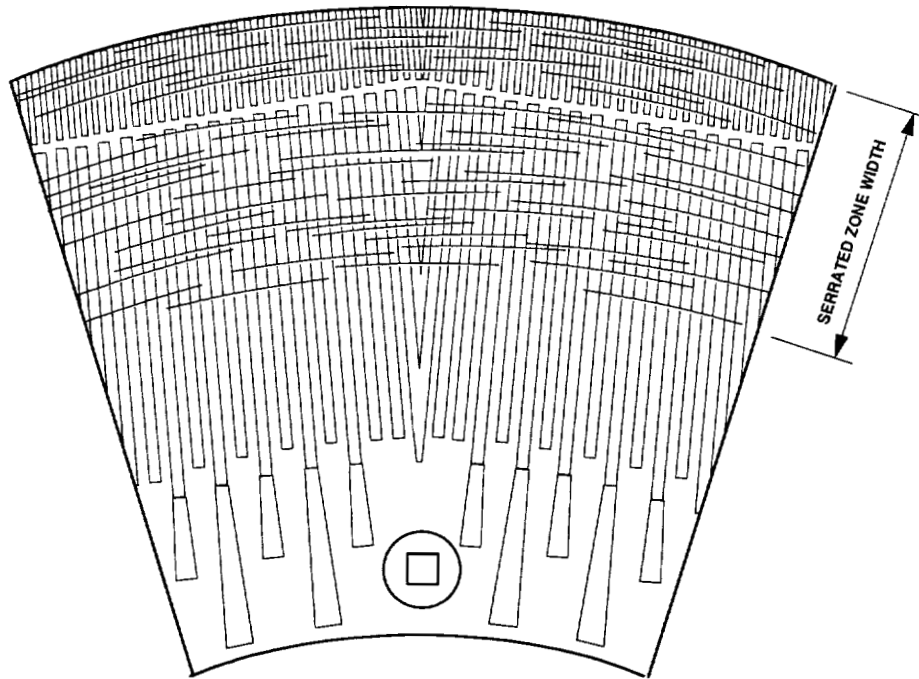


Figure 3.5. Serrated zone width.

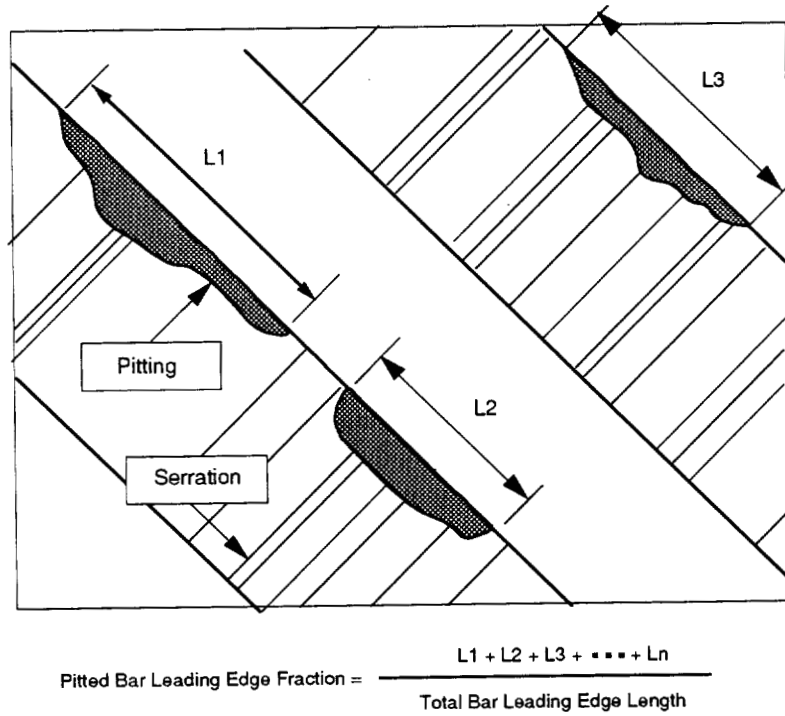


Figure 3.6. Pitted bar leading edge fraction.

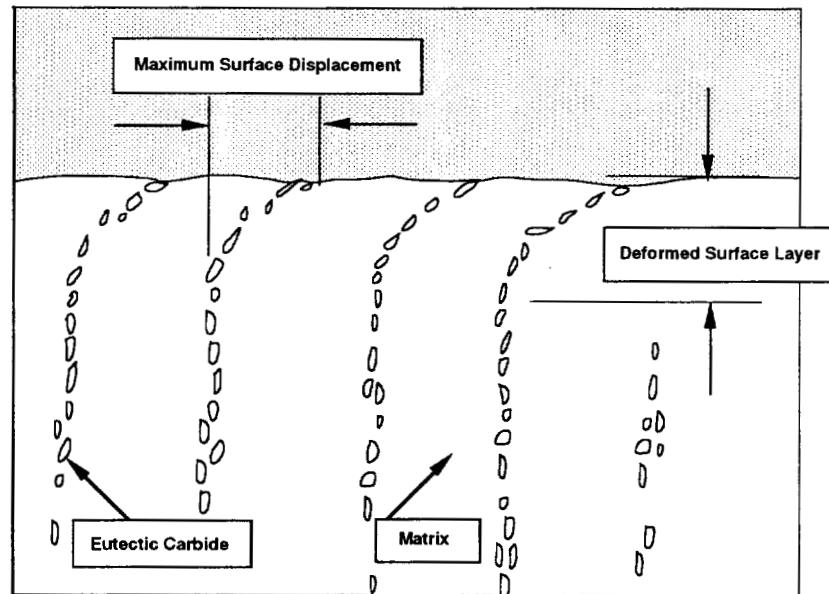


Figure 3.7. Maximum surface displacement and deformed surface layer thickness.

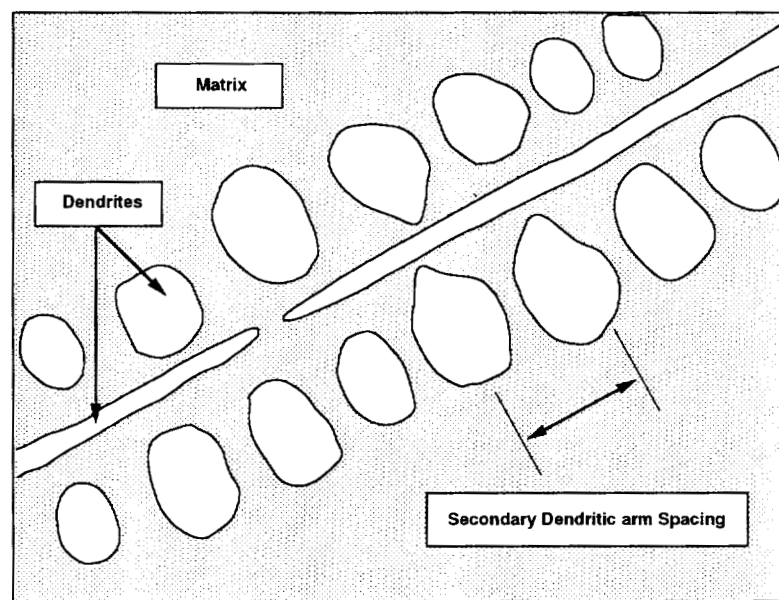


Figure 3.8. Secondary dendritic arm spacing.

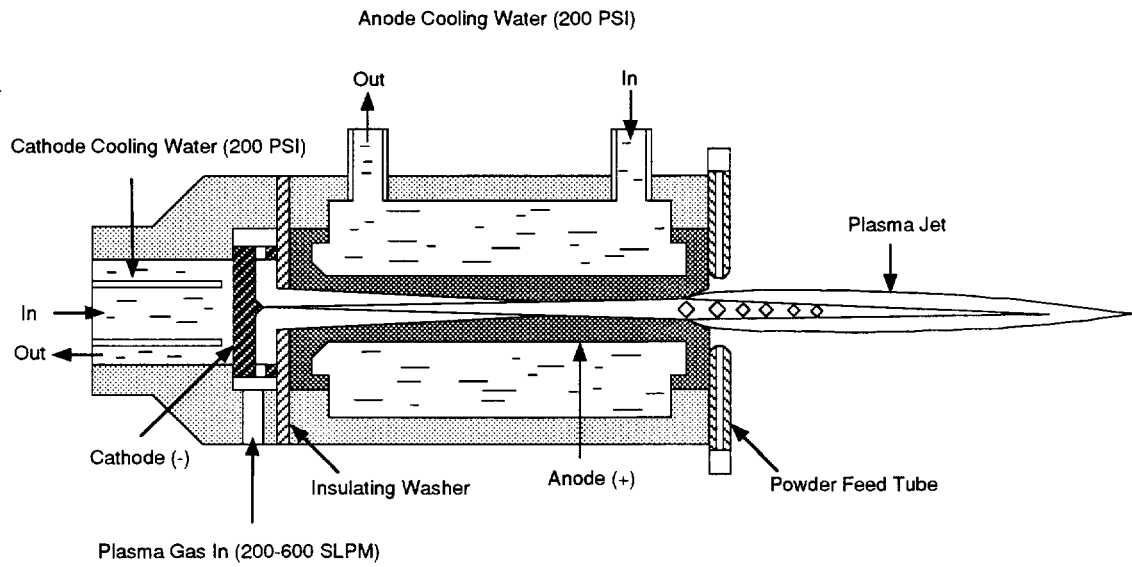


Figure 3.9. Schematic of the spray gun.

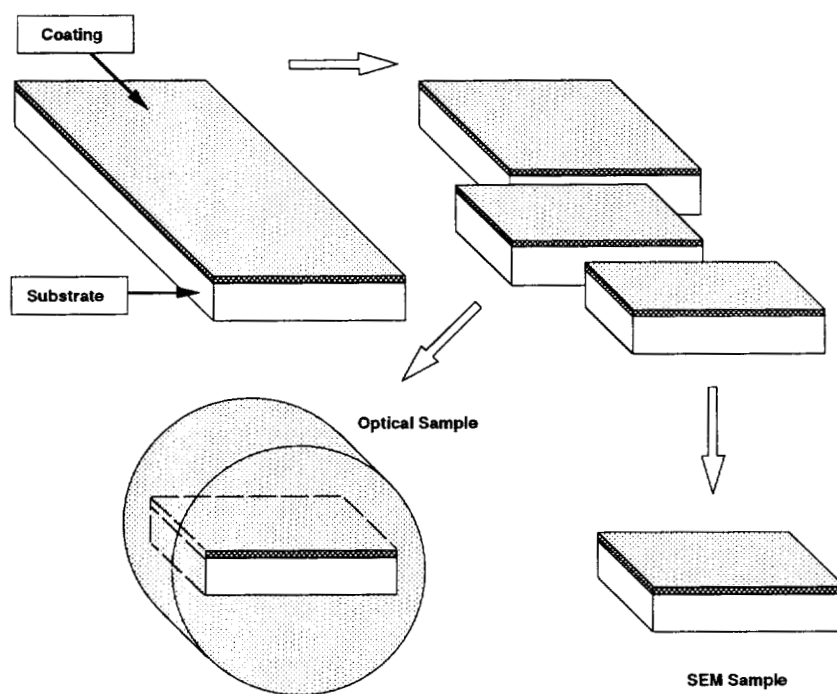


Figure 3.10. Metallographic coating specimen.

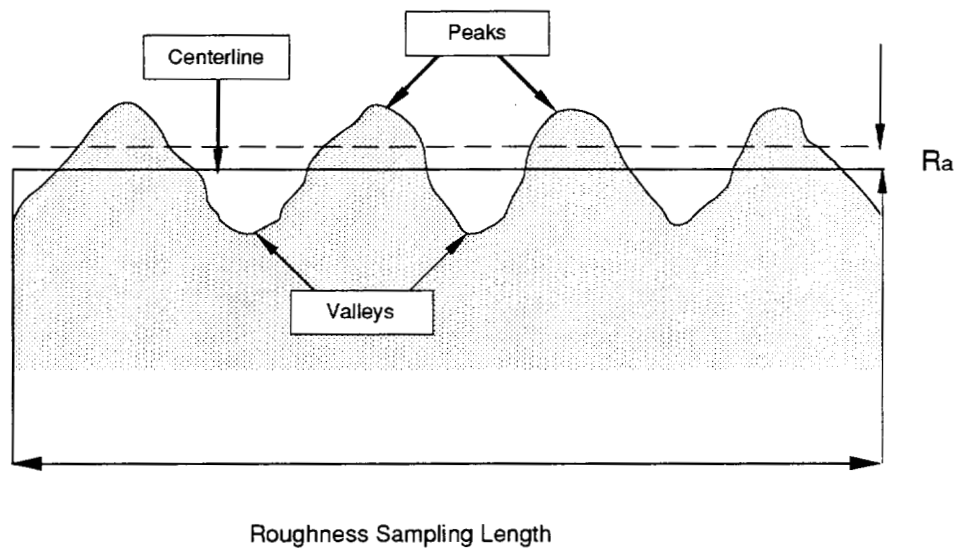


Figure 3.11. Roughness average - R_a .

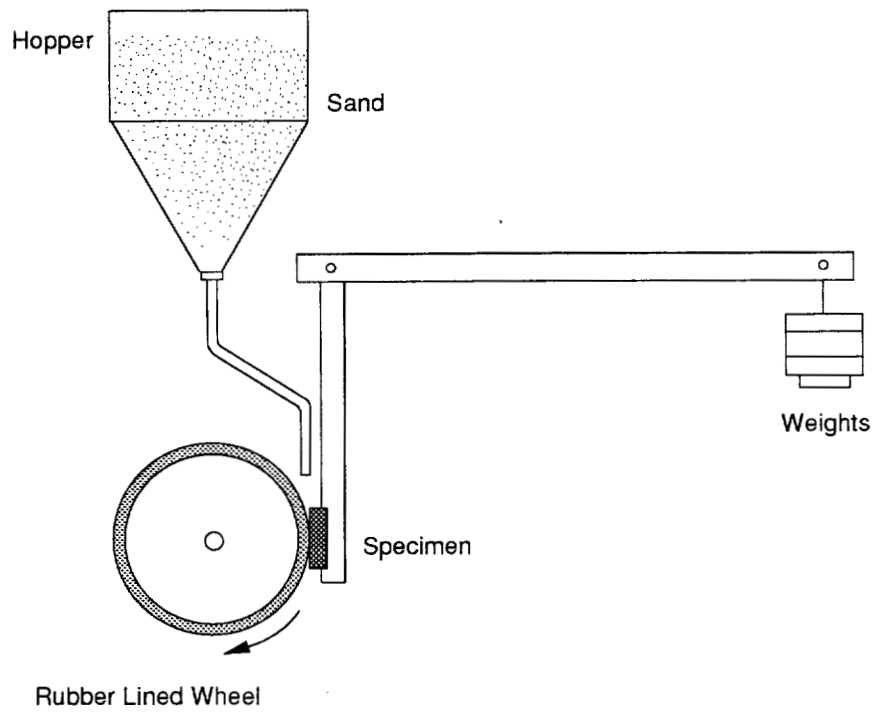


Figure 3.12. Schematic of abrasion test.

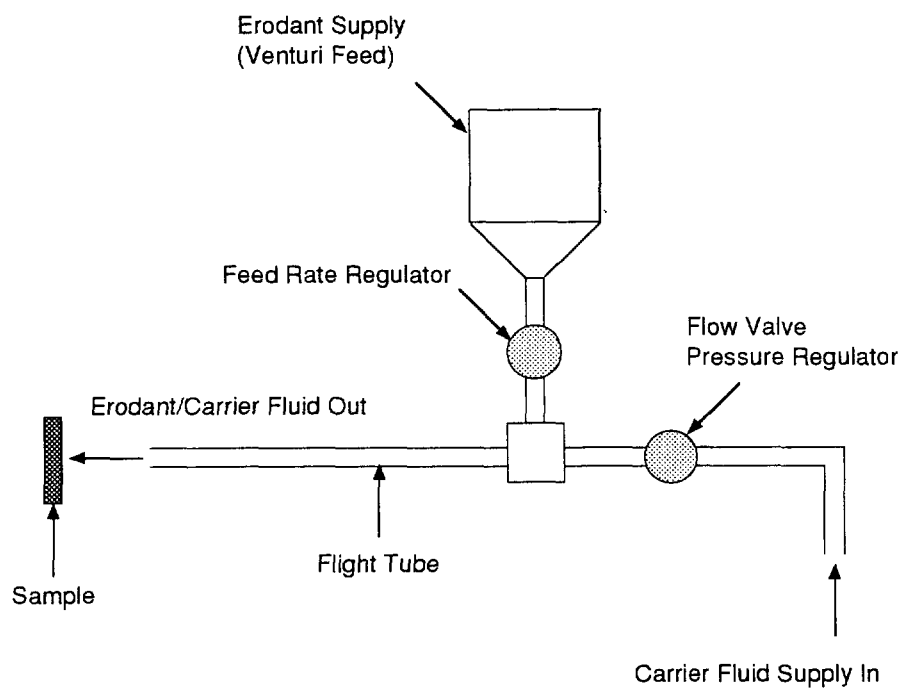


Figure 3.13. Schematic of erosion test.

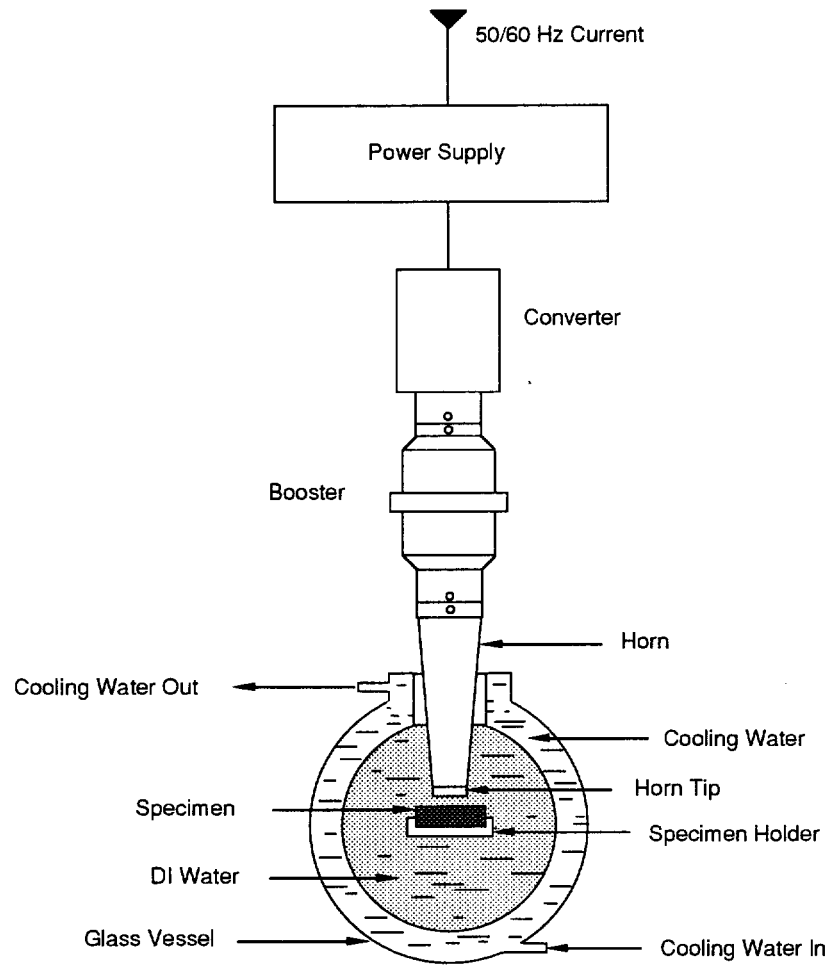


Figure 3.14. Schematic of cavitation erosion test.

CHAPTER 4 RESULTS

4.1. PLATE DAMAGE MEASUREMENT

4.1.1. Serration Damage

Table 4.1 shows some characteristics for the heavily serrated plates removed from Trials 4 and 5. It is obvious that after 100% working life severe plastic deformation occurred in the serrated surface layers for both C20 (20-2-1 white iron) and S17 (440C stainless steel) plates. The S17 steel plates, however, experienced a higher degree of surface deformation because they exhibited a deeper deformed surface layer than the C20 iron plates. It can also be seen from Table 4.1 that the S17 steel, although containing a much smaller percentage of carbides than the C20 white iron, was higher in bulk hardness, mainly because its matrix was tempered martensitic instead of austenitic. For both types of plates, however, a substantial work hardening was detected in the heavily serrated areas based on the fact that the matrix microhardness had increased considerably in the plastically deformed surface layers.

Table 4.2 presents the serrated surface area fractions for all six mill trials. Clearly, serration damage initiated primarily from plate periphery, extending towards the intermediate zone as refining proceeded. Under all conditions, however, only the refining zone could be serrated, while the breaker bars were completely free from any serration damage. This may indicate that serration is caused mainly by plate clashing because the two opposing rotating disks can only touch each other in the refining zone.

Compared to intermediate bar zone, moreover, the fine bar zone was much more severely serration damaged.

As service continued, the total serrated area fraction increased first and then decreased slightly after 75% of plate life, Table 4.2. This is due mainly to the development of pitting damage in the refining zone. Therefore, the serrated zone width, instead of the serrated area fraction, should be a better measure for serration damage degrees. Serration did increase with service time, and the S17 alloy experienced less serration damage than C20 plates after 100% working life when using the same wood stock (Table 4.3).

4.1.2. Pitting Damage

Comparing Table 4.4, which shows the pitted area fraction, with Tables 4.2 and 4.3, it is obvious that pitting occurred later than serration but could extend to all three plate zones. After 50% of working life, the plate surface was still not severely pitted. From the results of 4th, 5th, and 6th mill trials, after 100% life the fine bar zones for both C20 and S17 plates had fully deteriorated. That is, 100% of the fine bar zone had been either serrated or pitted. However, there were still many undamaged areas in the intermediate or breaker bar zones even after 100% life. According to Table 4.4, in each of the three plate zones the pitted area fraction increased with service time. As in the refining zone the pitted areas and serrated regions may overlap each other, the pitting damage degrees may not be satisfactorily reflected by the pitted area fraction.

The pitted bar leading edge fraction, a better indicator of the pitting damage, is shown in Table 4.5. From the results of 1st through 4th mill trials, the pitting damage increased with the plate working life. In addition, as shown in Table 4.5 the S17 steel plates experienced much less pitting damage than the C20 iron plates after 100% of their service life when using the same feed stock, indicating that the 440C steel is more pitting

resistant than the 20-2-1 iron. The C20 plates were more severely pitted in the 6th trial than in the 4th one. In the 6th mill trial, the feed stock was Douglas fir instead of white wood so that the dilution water was increased approximately 5% which may induce more pitting damage. For the plates made from the same alloy, therefore, the pitting damage could be considerably influenced by operational adjustments during refining.

4.1.3. Bar Rounding Damage

As illustrated in Table 4.6, the maximum bar rounded width increased with plate service time. After 100% working life, the S17 alloy plates exhibited much more bar rounding damage than the C20 plates when using the same wood stock, which indicated that the 20-2-1 white iron was more bar rounding resistant than the 440C stainless steel. Based on the data of 4th and 6th mill trials listed in Table 4.5, after 100% service life Douglas fir could result in much more bar rounding damage than the white wood on the C20 plates. This may imply that pulpwood played a significant role in the process of bar rounding. Douglas fir is one of the most commonly used softwoods in TMP refining, while the white wood refers primarily to all other Northwest softwoods but Douglas fir. From Table 2.1 [1], the Douglas fir and the white wood differ considerably in wood density, with the former being much denser. Thus, it might be hypothesized that a higher wood density would cause more bar rounding damage. Similarly, Wang [161] has also reported that mechanically stronger wood led to greater wear to steel woodcutting tools than mechanically weaker wood.

4.2. PLATE DAMAGE OBSERVATION

4.2.1. Serration Damage

On a macroscale only deep circumferential grooving can be seen in the severely serrated plates. Microscopically, however, the serrated surface can be divided into two

types of regions, a "smooth region" and a "rough region", based on whether most eutectic carbides were flush with or protruded above the matrix.

The surface features of the smooth regions for C20 plates are shown in Figures 4.1 through 4.3, with the arrows representing the plate moving directions. As shown in Figure 4.1, many microscopic grooves parallel to the plate moving direction can be found which constituted the very deep circumferential grooves on a macroscale. There were also many long deep cracks normal to the plate motion. In addition, the serrated surface could also be severely smeared by deformed material. In cross-sections of the "smooth regions", Figure 4.2, observed deformation was in the plate rotation direction while many cracks were generally parallel to the plate surface. Both matrix and carbides were fractured and deformed (Figures 4.2a-b), with some decohesion between the matrix and carbides (Figures 4.2c-d). In some locations of the "smooth regions", the long parallel grooves were deep and with sharp edges (Figure 4.3a), while the rest of the "smooth regions" were generally flat and smooth (Figure 4.3b). The carbides, which were basically flush with the matrix, either retained their original shapes or were fractured and spalled, without being edge rounded. Except for the long parallel grooves, there were a few dents and scratches with varied orientations in the matrix. Figures 4.3c-d show the very flat and smooth serrated surfaces more clearly. The carbides were either flush with the matrix or cracked and spalled off. All these characteristics may be attributed to plate clashing during refining.

In contrast, the "rough regions" were considerably different from the "smooth regions" in damaged surface features. Figures 4.4 and 4.5 respectively show the surface and subsurface characteristics in the rough regions for the C20 plates. As depicted by Figure 4.4, in the "rough regions" the long parallel grooves had basically disappeared while the matrix was covered predominantly with numerous dents and short scratches with various orientations. In these places, the carbides protruded well above the preferentially grooved matrix, with their edges being rounded and slightly deformed.

These eutectic carbides could also be fractured, while severe carbide spalling was not found. In addition, there were no clear signs of sliding contact in the "rough regions" such as serious surface deformation, smearing, melting, cracking, and spalling. These characteristics can be seen more clearly from the cross-section photos of the "rough regions" (Figure 4.5). The eutectic carbides, especially the sides towards the plate moving direction, had been well edge rounded. Most carbides were able to stand well proud of the matrix and some of them had been fractured but seldom spalled off. The matrix seemed to be protected by the protruding carbides to a certain degree. Severe subsurface deformation, cracking and spalling were absent.

Similarly, the "smooth regions" and "rough regions" can also be observed in heavily serrated surfaces of the S17 stainless steel plates, and the damaged surface features in either type of regions were basically comparable with those found in the C20 high chromium white iron plates. Figure 4.6 shows the characteristics in the "smooth regions" of serrated S17 plates. Numerous long parallel grooves in the plate moving direction can be found, with severe surface layer cracking and spalling also present. Again, there were few dents and short scratches with varied orientations in these regions. The severe surface cracking can also be seen from the cross sections of these regions, as shown by Figure 4.7. The cracks could be either surface or subsurface ones, and all developed preferentially along the eutectic carbide/dendrite interfaces. As revealed by Figure 4.7d, the serrated subsurface had been heavily deformed in the direction of plate motion. In addition, it is evident that both cracking and deformation were much more serious in the serrated S17 plates than in the C20 plates.

Like the C20 plates, the serrated S17 steel plates also showed "rough regions" wherever the long parallel grooves were absent. These areas, as displayed by Figure 4.8a, were covered with numerous dents and short grooves or scratches with varied orientations. Moreover, the eutectic carbides, although much smaller in size and volume fraction than those in the C20 white iron plates, were able to protrude above the heavily

scratched matrix and were obviously edge rounded (Figures 4.8b-c). Figure 4.8d shows some cracks along the eutectic carbide-matrix interfaces, while the cracking damage seems much less than that in the "smooth regions". In general, there were no any signs of severe surface deformation, spalling, and melting in these regions.

More interestingly, in the "smooth regions" of both the 20-2-1 and the 440C alloy plates, a surface layer of white color was observed on the serrated bar tops near the bar trailing edges. As depicted by Figure 4.9, these surface layers appear to be extensive material flow induced by severe plastic deformation with probable additional surface melting and/or phase transformation. After etching, no structural features were visible except for some tiny pores. These layers were therefore etch-resistant and very similar to the "white layers" found by many investigators on sliding wear damaged ferrous surfaces [63-67,162]. In addition, surface temperature flashes and extensive cyclic deformation, the two key factors determining the formation of the "white layers" [68], are clearly available in the serrated "smooth regions". As a result, the surface layers shown in Figure 4.9 appear to be the "white layers" defined in the ASM Handbook [69], and the presence of "white layers" in these areas indicates that sliding wear played a significant role in the serration damage process of the refiner plates.

4.2.2. Pitting Damage

Pitting damage occurred primarily along the bar leading edges. Figures 4.10 shows many pits in the heavily pitted areas of the C20 iron plates. These pits were generally not very large in size but quite deep, and were present in both refining zone (Figure 4.10a) and breaker bar zone (Figure 4.10b). The cross-section pictures clearly show that these pits developed predominantly along the eutectic carbide-matrix interfaces (Figures 4.10c-d).

The pitting damage process can be illustrated by Figure 4.11. First, small cracks normal to the plate surface were initiated along the interface between the matrix and the eutectic carbides (Figure 4.11a). Then, as the matrix near the carbides was preferentially attacked, the dendrite near the cracks was edge rounded and the surrounding carbides were removed so that pits were produced (Figure 4.11b). Due to the presence of many pits, as shown in Figure 4.11c, the dendrite lost the support from the surrounding eutectic structure and finally spalled out. It is evident from Figure 4.11d that the pitting damage continued at the bottom of the pit by developing new cracks along the adjacent eutectic/matrix interface structures.

Like the C20 plates, the S17 alloy plates experienced a very similar pitting damage process which can be seen in Figure 4.12. Again, the pit could initiate and develop in various directions but always along the eutectic structure interfaces, as revealed by Figures 4.12a-b. Due to the preferential damage of the eutectic structures, the dendrites were left unsupported and vulnerable to removal. Figure 4.12c shows a big pit left by the spalled dendrite. After the dendrite spalling, as shown by Figure 4.12d, new cracks were produced at the bottom of the pit to continue the pitting damage. Thus, on a microscale the plate pitting damage is very localized, although it can occur on a large scale macroscopically.

Some pit bottoms along the bar leading edges for both C20 and S17 alloy plates are shown in Figure 4.13. There were always numerous eutectic carbides at the pit bottoms, which demonstrates again that the material spalling during pitting occurred predominantly along the eutectic structures between the dendrites. In both refining zone and breaker bar zone of the S17 steel plates, as depicted by Figures 4.13c and 4.13d, the bar leading edges were always covered with many eutectic carbides which were left by the spalled dendrites.

Figure 4.14 displays the preferential damage process during pitting near the eutectic structures along the bar leading edges more clearly. Initially, only the interfaces between the carbides and the matrix were slightly attacked, as shown in Figure 4.14a. Then as depicted by Figure 4.14b the damage spread to both the dendrites and the matrix within the eutectic structures. Figure 4.14c shows that the dendrite edges and the matrix in the eutectic areas had been further damaged, leaving the eutectic carbides unsupported. Finally, all eutectic materials were completely removed and the unsupported dendrite was ready to spall off (Figure 4.14d).

As displayed in Figure 4.15, for both C20 and S17 alloy plates, whether in breaker bar zone, fine bar zone, or in intermediate zone, the heavily pitted bar leading edges exhibited almost the same surface features. That is, both the eutectic structures between the dendrites and the dendrite edges were always preferentially damaged, leaving the dendrites without sufficient support and ready to spall off. This may imply that for both C20 and S17 alloy plates the pitting damage in all three zones was actually caused by very similar mechanisms.

For the heavily pitting damaged C20 alloy plates, many crack networks can be clearly seen at the cavity bottoms either in the intermediate zone (Figure 4.16a) or in the fine bar zone (Figure 4.16b). From the metallographic cross-sections, as revealed by Figures 4.16c and d, many thin cracks, which appeared to be fatigue cracks, were present in the austenite matrix near the pit bottoms. These cracks might be used as the evidence to support that the plate pitting damage was actually a fatigue failure process.

4.2.3. Bar Rounding Damage

As the plate service proceeds, the maximum bar rounded width increases. However, the total rounded bar leading edge length will decrease because pitted areas, which are also distributed mainly along the bar leading edges, can gradually replace the

rounded bar rounded areas. As a result, "pure" bar rounding damage is more easily observed in the early stages of plate life.

As shown in Figures 4.17a-c, in all three plate zones the rounded C20 plate bar leading edges displayed basically the same surface features when using white wood as the feed stock. That is, numerous dents and short scratches with varied orientations distributed on the surface in the matrix regions, while the eutectic carbides, showing heavily rounded edges, protruded well above the preferentially grooved matrix. Figure 4.17d demonstrates that the C20 plates run with Douglas fir exhibited similar surface features on the rounded bar leading edges.

On the rounded bar leading edge, Figure 4.18a, the eutectic carbides were generally free from any scratches and dents although the matrix had been heavily grooved. Figure 4.18b shows some pits in the severely bar rounded areas which obviously resulted from carbide spalling. Similarly, for the S17 plates the matrix areas on the rounded bar leading edges were also covered with a lot of grooves and scratches with various orientations. As shown in Figures 4.18c-d, the carbides, although had smaller size and lower hardness than those of C20 alloy, could still stand above the matrix and were obviously edge rounded. It should be noted, moreover, that for either C20 or the S17 alloy plates no clear signs of severe surface deformation, cracking, and spalling are visible in the bar rounded areas.

4.3. WEAR TESTING OF PLATE ALLOYS

4.3.1. Alloy Characterization

Alloy Microstructure. The microstructures of the eight plate alloys tested are shown in Figures 4.19 and 4.20, and their compositions have been listed in Table 3.2.

As depicted in Figures 4.19a and 4.19b, both NH and C80 alloys, which belong to the Ni-hard white iron group, contained continuous interdendritic carbide networks and transformed austenitic matrix. Based on its morphology and microhardness, the matrix for either of the two Ni-hard materials should contain martensite and retained austenite. Also, the NH specimen exhibited a finer solidified structure than the C80 simply because it was obtained from small coupons instead of a large, thick, refiner plate.

Figures 4.19c and 4.19d show the microstructures of two 20-2-1 alloys, C20 and C30. Both were composed of eutectic M_7C_3 carbides which were present in the form of isolated islands rather than continuous networks. The matrix of both alloys remained austenitic. Compared to the C20 iron, the C30 alloy had a finer microstructure, that is, smaller secondary dendritic arm spacing and carbide thickness.

Due to non-equilibrium cooling many eutectic carbides also formed in the two 440C stainless steels, C15 and S17, Figures 4.20a and b, as in the white irons. These steels, however, had much smaller carbide volume fractions because of their lower carbon contents. The carbides, moreover, were much finer than those of the white irons, existing mainly in interdendritic regions. As different heat treatments were used, the S17 steel had a fully austenitic matrix while the C15 alloy appeared to have a tempered martensitic one. It is also obvious that the C15 had a much coarser dendritic structure than the S17 material.

As can be seen from Figure 4.20c, the 25Cr white iron, C25, was similar to the 20-2-1 alloys in microstructure. Its M_7C_3 carbides, however, were much finer and longer or, in other words, had a higher length-to-width ratio. This is possibly because the increased chromium content changed the morphology of the M_7C_3 eutectic carbides. Like the 20-2-1 alloys, the C25 also had a fully austenitic matrix.

Figure 4.20d depicts the microstructure of the 17-4 PH steel tested, which is very similar to that of a typical austenitized and tempered 17-4PH cast alloy shown in the Metals Handbook [163]. The structure consists of elongated pools of ferrite in a tempered martensitic matrix. The knoop hardness values for the ferrite and the matrix are approximately 370 and 470, respectively.

Alloy Characteristics. Table 4.7 shows some characteristics of the plate alloys investigated. The carbide volume fraction values for different alloys in a given group are not very different. In a given group, the alloys had very similar carbide hardness, implying that these carbides were of the same type. The carbides in the 20-2-1 group were much harder than those in the 25 Cr although both were of the M_7C_3 type. As their hardness values fell in between, the carbides of 440C steels must also be of the M_7C_3 type. In contrast, the carbides in Ni-hard irons had the lowest hardness as their type was M_3C instead of M_7C_3 . For either Ni-hard or 20-2-1 group, the matrix hardness was also at the same level. For the 440C group, however, the C15 alloy had a substantially harder matrix than the S17, indicating that their matrices should be mainly martensitic and austenitic, respectively. From Figure 4.21, the alloy bulk hardness can be better correlated with matrix hardness rather than the carbide hardness. Also, based on Table 4.7 the secondary dendritic arm spacing of alloys in a given group could be doubled, which means that the alloys even in the same group may vary significantly in structure fineness due to different solidification conditions.

4.3.2. Laboratory Wear Testing

The wear test results of plate alloys are displayed in Table 4.8. There was no appreciable relationship between the alloy hardness and their wear behavior in any of the three wear tests. Of all materials examined, the 17-4 PH stainless steel, which contained no eutectic carbides, behaved worst in all three wear tests. In general, the white irons had better abrasion performance but lower cavitation erosion resistance than the 440C steels, but all these alloys varied little in erosion behavior. The materials in a given

group exhibited similar abrasion and erosion rates, while they differed significantly in cavitation erosion performance. For Ni-hard group, finer dendritic structures corresponded to higher cavitation damage rate, while an opposite trend was observed for alloys in the 20-2-1 or 440C groups. The matrix type of the 440C alloys may also influence their cavitation erosion resistance as the martensitic matrix usually contains more interfaces and less working hardening ability than the austenite.

4.3.3. Worn Surface Examination

Abraded Surfaces. As shown in Figures 4.22 and 4.23, on the DSRW abraded surfaces of various plate alloys there were many long parallel grooves, while short grooves and scratches with varied orientations were absent. Comparing Figure 4.22 with 4.23, the abrasion grooves on the 440C and 17-4PH stainless steel surfaces appear to be relatively deeper than those found in the 20-2-1 and Ni-hard white irons. Obvious carbide protruding, edge rounding, cracking, and spalling were not present in all cases. The damaged surfaces were generally flat and smooth. Although the abraded surface features are to some extent like those found in the "smooth regions" of the heavily serrated plates, no significant surface deformation and surface cracking can be seen from either the abraded surfaces or the cross-sections.

Eroded Surfaces. There were many dents and short grooves with various orientations on the water sand eroded specimen surfaces, as illustrated in Figures 4.24 and 4.25. Local plastic deformation can often be observed near the dents or scratches, but severe surface cracking and surface spalling were not found (Figures 4.25c-d). Again, as in the DSRW abrasion tests, no evident carbide protruding, edge rounding, cracking and spalling were observed. However, the erosion damaged specimen surfaces appeared to be rougher than the abraded ones. After the erosion tests, all plate materials, whether white irons or stainless steels, exhibited very similar worn surface features,

which is consistent with the fact that these alloys were not substantially different in erosion damage resistance.

Cavitation Eroded Surfaces. Under low magnifications, Figure 4.26, many pits can be seen on the cavitation eroded surfaces. These pits were different in size and shape probably because they were in different development stages. By examining these pits under higher magnifications, Figure 4.27, it is clear that they initiated primarily from the eutectic structure areas, with many microcracks near the eutectic carbide/matrix interfaces being also present. As shown in Figures 4.28a and b, the eutectic regions between the dendrites were preferentially attacked. From Figures 4.28c and d, the dendrites could slightly protrude above the eroded specimen surface. In addition, dendrite edge rounding occurred as the dendrite surfaces adjacent to the eutectic areas had also been preferentially attacked while their internal regions remained basically undamaged (Figures 4.28c-d). All these features are basically the same as those found in the heavily pitted refiner plates.

4.4. WEAR TESTING OF PLASMA COATINGS

4.4.1. Coating Characterization

Coating Microstructure. Figures 4.29 through 4.31 show the microstructures of some groups of plasma coatings listed in Table 3.3. Many alloy coatings, such as Fe-Mo-C, Ni-Cr-Si-Fe-B, and Ti-alloy, exhibited a thin layered structure built up by a series of overlapping pancakes, which is typical for plasma sprayed materials (Figure 4.29). Also, there were few pores and cracks so that the coating deposits were basically solid. In contrast, for most cermet and ceramic coatings like $\text{Cr}_2\text{O}_3\text{-SiO}_2\text{-TiO}_2$, W-C-Co, WC-Co, and WC- $\text{Cr}_3\text{C}_2\text{-Ni}$, the thin-layered structure could not be clearly seen while very high percentages of pores and microcracks were present (Figures 4.30-4.31). The reason for the substantial difference in the coating structure may be related to various deposition

parameters which were not well optimized. For example, powder melting point may affect the coating microstructures considerably. From Tables 3.3 and 3.4, the powders used to make metallic alloy coatings had much lower melting points than those used in ceramics or cermets. Thus, for a given deposition energy the metallic alloy particles could be well melted during spraying and plastically deformed into thin pancakes upon impacting the substrate. Conversely, the powders of high melting points, like tungsten carbide, could not be melted and deformed easily during spraying, thereby leading to more pores and microcracks in the deposits. Also, a larger powder size would lead to greater average splat thickness or smaller coating interface area (Figure 4.29). Of all materials deposited, the Ti-alloy coatings (Figure 4.29d) had the largest average splat size, mainly because they were produced from proprietary wire feedstock rather than powders.

Coating Characteristics. Some coating characteristics are listed in Table 4.9. All ceramic and cermet materials had substantially higher hardness than the metallic alloy coatings, due primarily to the presence of sufficient amount of very hard carbides and/or oxide particles which are harder than most metallic powders. There was also a general tendency for the coatings deposited at shorter working distances to be harder (Figure 4.32). The density values listed were estimated from the powder composition and the densities of the components involved. While not accurate, these density values are good estimates to roughly compute the volume loss rate of coatings during wear testing. Owing to the additions of tungsten or tungsten carbide particles, most cermets were much higher in density than the alloy or ceramic coatings examined in this work. Some ceramics such as $\text{Al}_2\text{O}_3\text{-TiO}_2$ and $\text{Cr}_2\text{O}_3\text{-SiO}_2\text{-TiO}_2$ had very low density due to the presence of various oxides.

The alloy coatings were generally much higher in surface roughness than the ceramic and cermet materials, which was consistent with the alloy coatings being deposited with a larger powder size and, therefore, composed of thicker splats. From

Table 3.3 and 4.8, it is obvious that the coating surface roughness tended to increase with the original powder size. The Ti-alloy coatings had the highest surface roughness value of all materials deposited, primarily as the Ti-alloy feed material was wire rather than powder particles. As shown in Figure 4.33, in general a shorter spray distance led to higher R_a values. This may be because a longer distance can allow the powders to fully melt, while a fully melted particle can vaporize rapidly during spraying and, more importantly, fracture upon impacting the substrate. Also, when powder composition and spray distance were held constant, the coating surface roughness increased with powder size (Figure 4.34).

Table 4.10 compares the characteristics of two groups of coatings, Fe-Mo-C and WC-Co, which were selected to further investigate the correlations of the coating properties with their wear performance. For each given group six specimens were sprayed in different batches. As the spraying processes used were only nominally the same, the variations of coating properties between batches could be induced by fluctuations in deposition parameters. Clearly, the WC-Co coatings were substantially harder but also much more porous than the Fe-Mo-C materials. For both groups of coatings, as shown in Figure 4.35, the microhardness decreased with increasing porosity. When the porosity is high, thus, the coating microhardness obtained may not be a true result of the deposited material. From Figure 4.36, the surface roughness of Fe-Mo-C coatings roughly increased with their average splat thickness, which was in accordance with the fact that a larger powder size usually led to a higher R_a value.

4.4.2. Wear Testing of Coatings

The influence of the coating's deposition parameters on the wear behavior can be inferred by comparing Tables 3.3-3.5 and Table 4.11. As stated earlier, for a given coating group, when other variables remained the same a longer spray distance usually led to a lower hardness (Figure 4.32). In most cases, for a given coating group, the

abrasion rate increased with the spray distance, no matter which type of abrasive was used (Figure 4.37). Therefore, the abrasion resistance of a given group of coatings was usually proportional to their hardness. By comparing the results for WC-Cr₃C₂-Ni1 and WC-Cr₃C₂-Ni2 groups, it can be found that a larger powder size led to better cavitation erosion behavior (Figure 4.38). The improved coating cavitation erosion performance may result from the increased splat size or reduced coating interface area owing to using larger powder size. In all of the solid particle erosion tests, no evident correlations can be found between the coating's wear rate and deposition parameters.

To select the coating materials with best wear behavior, the volume loss rates of all coating groups were calculated from Table 4.11 and listed in Table 4.12. Unfortunately, no one group of coatings behaved best for all six types of wear tests and the relative performance ranking of these coating groups was drastically different from one wear test to another. By further examining the wear data, however, it can be seen that some metallic alloy coatings had better cavitation erosion behavior and some cermet materials had superior abrasion resistance, while their erosion rates were not significantly different. The Fe-Mo-C coatings behaved excellently in cavitation erosion and very good in other wear tests, while the WC-Co materials behaved excellently in abrasion and very good in other tests. According to the plate failure analysis, abrasion and a pitting process similar to cavitation erosion (depending on the location on the plate) played the leading roles in refiner plate deterioration. Therefore, these two groups of coatings were redeposited for further evaluation.

Table 4.13 displays the wear behavior of the two groups of coatings. For each group, neither abrasion nor erosion performance changed significantly, while the cavitation erosion rate doubled in some cases. The WC-Co coatings generally behaved better than the Fe-Mo-C materials in all three wear tests. As shown in Figure 4.39, for either coating group the abrasion behavior can be correlated with their cavitation erosion performance, but there seemed no relationship between erosion and abrasion rates.

From Figure 4.40, it appears that the coating's cavitation erosion rate decreased rapidly with increasing coating hardness. As the coating hardness depended considerably on porosity (Figure 4.35), for both groups of coatings tested, the cavitation erosion behavior was in fact influenced by coating porosity instead of hardness, Figure 4.41. However, no significant correlations can be found between the porosity and the erosion or abrasion performance (Figures 4.41-4.42).

It can be seen in Figure 4.43 that the cavitation erosion resistance for both groups of coatings increased with their initial surface roughness. As the initial surface roughness R_a was roughly proportional to the mean splat thickness (Figure 4.36), the cavitation erosion behavior was actually improved by increasing the mean splat thickness or reducing the interfaces between splats, as shown in Figure 4.44, which was consistent with the fact that a smaller interface area in cast alloys would also lead to less cavitation erosion damage.

The mean volume loss rates of the two groups of coatings were calculated from Table 4.13 and shown in Table 4.14, with the wear rates of the plate alloys being also presented. It is obvious that the WC-Co coatings behaved superior to the Fe-Mo-C materials in all three wear tests, especially in the abrasion tests. Unfortunately, according to Figures 4.45 and 4.46, the plasma coatings were much inferior to all plate alloys in both cavitation erosion and erosion performance. In the DSRW abrasion tests, however, the WC-Co coatings were more wear resistant than all plate alloys, and the Fe-Mo-C materials behaved worse than the white irons but much better than the stainless steels, as revealed by Figure 4.47.

4.4.3. Worn Surface Examination

Abrasion. The abrasion damaged plasma sprayed coatings displayed worn surface features very similar to those seen in the plate alloys. For both Fe-Mo-C and

WC-Co coatings, as shown by Figure 4.48, the DSRW abraded surfaces were covered with numerous long parallel grooves, but few short grooves and scratches with varied orientations were present. In addition, no substantial surface deformation occurred. The damaged surfaces were basically flat and smooth, while many cracks can be seen from either the worn surfaces or the cross-sections.

Erosion. Like the plate alloys, the eroded surfaces for the Fe-Mo-C and WC-Co coatings were basically the same. Many dents and short scratches with various orientations distributed on the eroded surfaces (Figures 4.49a-b), and the cross-sections of the eroded coatings were also alike (Figures 4.49c-d). Again, in addition to local plastic deformation adjacent to the dents, scratches, and grooves, severe surface deformation in the coating layer was not found. Moreover, substantial surface cracking and spalling were absent.

Cavitation Erosion. Figure 4.50 shows many deep pits on the cavitation eroded coating surfaces, and these pits, which usually had high depth-to-diameter ratios, were similar to those found in the pitting damaged refiner plates or the laboratory cavitation damaged plate alloy specimens. Many cracks surrounding these pits can also be found (Figure 4.50b), and the cross-section photos of the cavitation eroded coatings revealed severe microcracking at the bottoms of these pits (Figures 4.50c-d).

Table 4.1. Characteristics for Plates Removed from Trials 4 and 5

Plate Characteristics		100% life C20 Whitewood (Trial 4)	100% life S17 Whitewood (Trial 5)
Bulk Hardness	(HRC)	49.6 ± 0.7	54.0 ± 1.1
Carbide Hardness	(Knoop 25g)	1273.1 ± 62.3	1180.1 ± 71.2
Matrix Hardness	(Knoop 25g)	305.4 ± 24.3	461.5 ± 22.5
Deformed Layer Matrix Hardness	(Knoop 25g)	449.4 ± 32.8	579.1 ± 29.0
Deformed Layer Thickness	(μm)	20.5 ± 4.0	45.0 ± 10.0
Maximum Surface Displacement	(μm)	17.5 ± 4.0	77.0 ± 15.4

Table 4.2. Serrated Bar Top Surface Area Fraction

Plate Zones	Serrated Area Fraction (%)					
	15% life C20 Whitewood (Trial 1)	50% life C20 Whitewood (Trial 2)	75% life C20 Whitewood (Trial 3)	100% life C20 Whitewood (Trial 4)	100% life S17 Whitewood (Trial 5)	100% life C20 Douglas fir (Trial 6)
Fine Bar	28.9	100	95.1	80.9	73.4	31.4
Intermediate	0	32.9	58.5	60.2	46.9	52.3
Breaker Bar	0	0	0	0	0	0
Total	5.6	42.6	59.5	58.7	52.9	43.4

Table 4.3. Serrated Zone Width

Mill Trial	15% life C20 Whitewood (Trial 1)	50% life C20 Whitewood (Trial 2)	75% life C20 Whitewood (Trial 3)	100% life C20 Whitewood (Trial 4)	100% life S17 Whitewood (Trial 5)	100% life C20 Douglas fir (Trial 6)
Serrated Zone Width (mm)	10	80	120	130	100	140

Table 4.4. Pitted Bar Top Surface Area Fraction

Plate Zones	Pitted Area Fractions (%)					
	15% life C20 Whitewood (Trial 1)	50% life C20 Whitewood (Trial 2)	75% life C20 Whitewood (Trial 3)	100% life C20 Whitewood (Trial 4)	100% life S17 Whitewood (Trial 5)	100% life C20 Douglas fir (Trial 6)
Fine Bar	0	0	4.9	19.1	26.6	68.6
Intermediate	0	0	1.9	7.5	0	28.3
Breaker Bar	0	2.8	5.8	73.8	7.7	9.7
Total	0	0.3	3.0	18.3	6.2	34.8

Table 4.5. Pitted Bar Leading Edge Length Fraction

Plate Zones	Pitted Bar Leading Edge Fractions (%)					
	15% life C20 Whitewood (Trial 1)	50% life C20 Whitewood (Trial 2)	75% life C20 Whitewood (Trial 3)	100% life C20 Whitewood (Trial 4)	100% life S17 Whitewood (Trial 5)	100% life C20 Douglas fir (Trial 6)
Fine Bar	0	3.3	19.0	69.7	42.5	84.4
Intermediate	0	1.4	13.5	38.9	1.4	88.3
Breaker Bar	0	5.0	8.9	92.1	7.1	29.7
	-----	-----	-----	-----	-----	-----
Total	0	2.3	14.8	52.6	14.4	82.4

Table 4.6. Maximum Bar Rounded Width

Mill Trial	15% life C20 Whitewood (Trial 1)	50% life C20 Whitewood (Trial 2)	75% life C20 Whitewood (Trial 3)	100% life C20 Whitewood (Trial 4)	100% life S17 Whitewood (Trial 5)	100% life C20 Douglas fir (Trial 6)
W (mm)	0	0.51	1.01	1.04	2.16	2.34

Table 4.7. Characteristics of Plate Alloys

Alloys		Bulk Hardness (HRC)	Carbide Hardness (Knoop 25g)	Matrix Hardness (Knoop 25g)	Secondary Dendritic Arm Spacing (μm)	Carbide Volume Fraction (%)	Cr/C
White Irons	NH	57.8 ± 0.8	944.9 ± 48.6	483.4 ± 19.7	27.1 ± 5.8	28.2 ± 1.3	0.8
	C80	57.5 ± 1.0	966.6 ± 78.3	477.0 ± 33.5	54.1 ± 9.4	32.2 ± 2.1	0.8
	C30	50.5 ± 1.2	1354.9 ± 70.4	357.2 ± 18.0	22.2 ± 3.5	26.2 ± 2.1	7.9
	C20	49.8 ± 0.9	1393.2 ± 60.4	356.0 ± 18.1	42.3 ± 7.0	24.6 ± 2.2	6.5
	C25	49.5 ± 0.9	1166.3 ± 66.6	438.5 ± 18.1	20.0 ± 4.2	21.2 ± 1.0	10.0
Stainless Steels	C15	57.2 ± 0.2	1249.0 ± 60.3	671.5 ± 12.2	51.3 ± 4.7	3.8 ± 0.6	15.7
	S17	34.1 ± 0.9	1232.0 ± 84.8	322.3 ± 19.1	25.0 ± 2.9	3.5 ± 0.8	15.7
	17-4PH	42.0 ± 0.7	-	472.7 ± 18.2	-	-	-

Table 4.8. Wear Rate of Plate Alloys

Alloys		Abrasion Rate (mg/km)	Erosion Rate* (mg/kg)	Cavitation Erosion Rate (mg/hr)
White Irons	NH	59.7	4.42	0.62
	C80	61.5	4.48	0.41
	C30	45.5	3.65	0.37
	C20	55.5	4.50	0.87
	C25	71.4	3.92	0.08
Stainless Steels	C15	327.0	4.29	0.22
	S17	357.5	4.31	0.05
	17-4PH	786.4	6.24	1.60

* Water sand erosion with 50-70 mesh silica sand.

Table 4.9. Coating Characteristics

Family	Group	Sample #	Thickness (mm)	Hardness (HK ₁₀₀)	Density* (g/cm ³)	Ra (μm)
Metallic Alloys	Fe-Mo-C	1	0.42	633	8.1	25.7
	Fe-Mo-C	2	0.49	701	8.1	14.8
	Fe-Mo-C	3	0.26	628	8.1	10.1
	Ti-Alloy	4	0.37	340	4.5	27.4
	Ni-Cr-Si-Fe-B1	5	0.29	747	8.3	11.1
	Ni-Cr-Si-Fe-B1	6	0.32	805	8.3	14.1
	Ni-Cr-Si-Fe-B2	7	0.24	778	8.1	11.6
	Ni-Cr-Si-Fe-B2	8	0.35	823	8.1	15.7
	IN625-Cr ₃ C ₂	9	0.42	325	5.0	18.4
Ceramics	Al ₂ O ₃ -TiO ₂	10			3.3	5.0
	Al ₂ O ₃ -TiO ₂	11	0.08	991	3.3	8.3
	Al ₂ O ₃ -TiO ₂	12	0.29	1103	3.3	6.5
	Al ₂ O ₃ -TiO ₂	13		1514	3.3	9.4
	Al ₂ O ₃ -TiO ₂	14	0.30	1190	3.3	10.4
	Al ₂ O ₃ -TiO ₂	15	0.30	1102	3.3	7.1
	Al ₂ O ₃ -TiO ₂	16	0.31	985	3.3	5.5
	Cr ₂ O ₃ -SiO ₂ -TiO ₂	17	0.16	1259	5.1	8.1
	Cr ₂ O ₃ -SiO ₂ -TiO ₂	18	0.25	1476	5.1	7.5
Cermets	Cr ₃ C ₂ -WC-TiC-Ni-Mo	19	0.14	848	8.4	4.0
	W-C-Co1	20	0.91	1942	17.1	12.6
	W-C-Co2	21	0.44	1082	17.1	8.3
	WC-Co1	22	0.12	1262	15.0	11.0
	WC-Co2	23	0.05	916	15.2	5.5
	Cr ₃ C ₂ -WC-TiC-Ni-Mo-C1	24	0.05	1064	9.0	6.2
	Cr ₃ C ₂ -WC-TiC-Ni-Mo-C1	25	0.18	1348	9.0	8.6
	Cr ₃ C ₂ -WC-TiC-Ni-Mo-C2	26	0.09	1076	9.0	5.7
	Cr ₃ C ₂ -WC-TiC-Ni-Mo-C2	27	0.27	1270	9.0	8.7
	WC-Cr ₃ C ₂ -Ni1	28	0.16	822	13.2	3.7
	WC-Cr ₃ C ₂ -Ni1	29	0.08	938	13.2	3.8
	WC-Cr ₃ C ₂ -Ni2	30	0.08	1146	13.2	6.6
	WC-Cr ₃ C ₂ -Ni2	31	0.08	739	13.2	4.8
	Cr ₃ C ₂ -Ni-Cr	32	0.35	849	7.2	10.8
	Cr ₃ C ₂ -Ni-Cr	33	0.48	935	7.2	11.7

* Estimated values.

Table 4.10. Characteristics of Two Groups of Coatings

Specimen		Coating Thickness (mm)	Surface Roughness R_a (μm)	Coating Hardness (Knoop 100g)	Splat Thickness (μm)	Coating Porosity (%)
Fe-Mo-C	I	0.62	11.44 ± 0.20	549.6 ± 36.3	6.33 ± 0.99	1.02 ± 0.43
	G	0.70	12.12 ± 0.51	584.5 ± 31.2	7.73 ± 1.29	0.59 ± 0.26
	K	0.70	12.87 ± 0.42	592.6 ± 43.4	7.22 ± 1.28	0.72 ± 0.34
	D	0.77	12.37 ± 0.09	594.8 ± 29.9	7.18 ± 1.05	0.55 ± 0.30
	B	0.60	13.48 ± 0.48	594.5 ± 15.8	8.62 ± 1.38	0.46 ± 0.19
	E	0.80	13.56 ± 0.74	656.2 ± 37.3	9.35 ± 1.37	0.34 ± 0.11
WC-Co	AE	1.36	6.20 ± 0.21	1050.8 ± 70.6		2.81 ± 0.67
	AH	1.35	5.78 ± 0.18	1041.9 ± 44.8		3.87 ± 0.97
	AA	0.97	5.58 ± 0.13	978.3 ± 35.8		4.79 ± 0.97
	AD	1.34	5.65 ± 0.15	1011.3 ± 66.5		4.34 ± 0.96
	AG	1.41	5.36 ± 0.27	985.8 ± 51.5		5.81 ± 1.24
	AC	0.79	5.32 ± 0.11	864.2 ± 36.8		6.38 ± 1.28

Table 4.11. Comparison of Coating Wear Behavior by Samples

Group	Sample #	DSRW (SiO ₂) (mm ³ /km)	DSRW (Al ₂ O ₃) (mm ³ /km)	WSE (SiO ₂) (mm ³ /kg)	WSE (Al ₂ O ₃) (mm ³ /kg)	SSE (Al ₂ O ₃) (mm ³ /kg)	CE (DI Water) (mm ³ /hr)
Fe-Mo-C	1	17.7	233.3		18.2	220.1	0.56
Fe-Mo-C	2	16.3	200.7	12.2	20.8	194.9	0.98
Fe-Mo-C	3	25.7	309.0	11.0	20.4	184.6	1.23
Ti-Alloy	4	71.3	666.0	4.9	10.0	79.1	2.52
Ni-Cr-Si-Fe-B1	5	80.9	304.7	23.1	34.5	209.6	3.39
Ni-Cr-Si-Fe-B1	6	79.6	365.2	25.7	36.1	524.8	4.12
Ni-Cr-Si-Fe-B2	7	56.3	265.0	21.7	24.1	150.7	1.44
Ni-Cr-Si-Fe-B2	8	28.3	252.5	27.5	42.3	540.2	5.25
IN625-Cr ₃ C ₂	9	49.1	315.9	4.4	9.5	82.2	1.22
Al ₂ O ₃ -TiO ₂	10	10.2	820.0				
Al ₂ O ₃ -TiO ₂	11	137.3		21.4	36.8	347.9	
Al ₂ O ₃ -TiO ₂	12	52.1	164.4	18.9	38.3	451.2	
Al ₂ O ₃ -TiO ₂	13	12.5	101.2				
Al ₂ O ₃ -TiO ₂	14	40.5	71.4	19.1	39.1	512.7	2.45
Al ₂ O ₃ -TiO ₂	15	13.9	106.6	18.0	35.3	369.1	3.39
Al ₂ O ₃ -TiO ₂	16	234.5	152.2	18.9	38.2	440.6	
Cr ₂ O ₃ -SiO ₂ -TiO ₂	17	14.2	202.7	20.2	38.5	473.7	
Cr ₂ O ₃ -SiO ₂ -TiO ₂	18	6.7	202.7	11.6	29.5	615.7	
Cr ₃ C ₂ -WC-TiC-Ni-Mo	19	16.2	142.4	11.4	21.4	204.6	3.27
W-C-Co1	20	3.6	25.2	10.5	25.4	240.2	
W-C-Co2	21	3.9	146.1	12.4	19.4	423.7	
WC-Co1	22	8.1	45.0	10.3	16.1	182.1	5.71
WC-Co2	23	6.7	80.2	7.5	12.8	143.8	5.11
Cr ₃ C ₂ -WC-TiC-Ni-Mo-C1	24	112.8		12.7	24.7	250.0	
Cr ₃ C ₂ -WC-TiC-Ni-Mo-C1	25	16.2	265.6	17.4	32.3	360.7	
Cr ₃ C ₂ -WC-TiC-Ni-Mo-C2	26	75.3		14.6	28.3	277.8	
Cr ₃ C ₂ -WC-TiC-Ni-Mo-C2	27	5.4	132.1	15.7	26.8	253.8	6.85
WC-Cr ₃ C ₂ -Ni1	28	44.2	572.3	25.5	43.5	367.1	18.00
WC-Cr ₃ C ₂ -Ni1	29	77.9	689.0	21.8	39.7	408.2	31.70
WC-Cr ₃ C ₂ -Ni2	30	12.4		14.3	25.5		
WC-Cr ₃ C ₂ -Ni2	31	76.8	635.4	16.4	31.6	506.2	16.05
Cr ₃ C ₂ -Ni-Cr	32	8.4	81.3	19.1	29.6	244.2	7.43
Cr ₃ C ₂ -Ni-Cr	33	6.7	56.9	15.9	23.9	209.4	

Table 4.12. Comparison of Coating's Wear Behavior by Groups

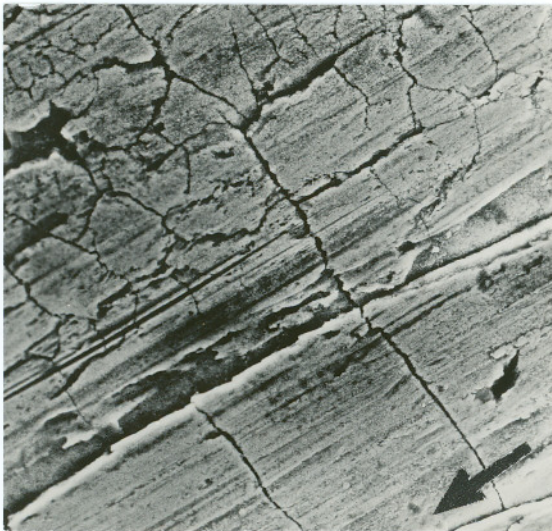
Family	Group	Sample#	DSRW (SiO ₂) (mm ³ /km)	DSRW (Al ₂ O ₃) (mm ³ /km)	WSE (SiO ₂) (mm ³ /kg)	WSE (Al ₂ O ₃) (mm ³ /kg)	SSE (Al ₂ O ₃) (mm ³ /kg)	CE (DI Water) (mm ³ /hr)
Alloys	Fe-Mo-C	1 - 3	19.4	271.1	8.4	15.7	160.7	0.8
	Ti-Alloy	4	71.2	664.5	4.9	10.0	78.9	2.5
	Ni-Cr-Si-Fe-B1	5 - 6	80.5	336.2	24.5	35.5	368.6	3.8
	Ni-Cr-Si-Fe-B2	7 - 8	42.1	257.5	24.5	33.1	343.8	3.3
	IN625-Cr ₃ C ₂	9	49.1	315.9	4.4	9.5	82.2	1.2
Ceramics	Al ₂ O ₃ -TiO ₂	10 - 16	68.5	233.8	19.1	37.2	420.5	2.9
	Cr ₂ O ₃ -SiO ₂ -TiO ₂	17 - 18	10.5	203.5	15.9	34.2	546.9	8.9
Cermets	Cr ₃ C ₂ -WC-TiC-Ni-Mo	19	16.3	143.3	11.5	21.6	205.8	3.3
	W-C-Co1	20	3.6	25.2	10.6	25.4	240.3	-
	W-C-Co2	21	3.9	146.2	12.4	19.4	423.9	7.3
	WC-Co1	22	8.0	44.9	10.3	16.1	181.7	5.7
	WC-Co2	23	6.8	80.3	7.5	12.8	144.1	5.1
	Cr ₃ C ₂ -WC-TiC-Ni-Mo-C1	24 - 25	64.2	264.4	15.0	28.4	303.7	7.0
	Cr ₃ C ₂ -WC-TiC-Ni-Mo-C2	26 - 27	40.1	131.5	15.1	27.4	264.6	10.7
	WC-Cr ₃ C ₂ -Ni1	28 - 29	61.0	630.5	23.7	41.6	387.7	24.8
	WC-Cr ₃ C ₂ -Ni2	30 - 31	44.6	635.4	15.4	28.5	506.2	16.0
	Cr ₃ C ₂ -Ni-Cr	32 - 33	7.9	73.5	17.6	26.8	227.8	7.5

Table 4.13. Wear Rate of FeMoC and WC-Co Coatings

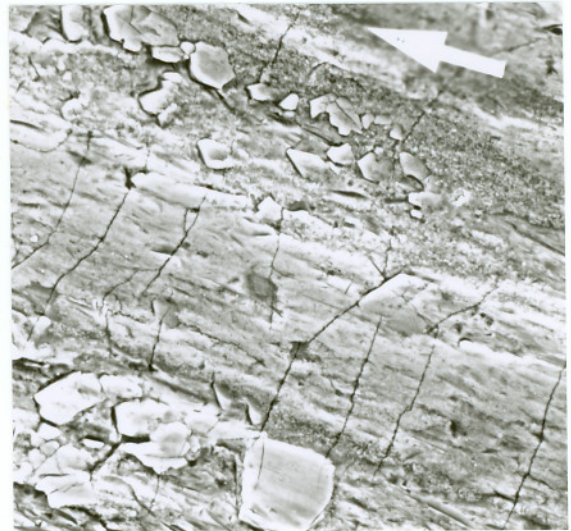
Specimen		Abrasion Rate (mm ³ /km)	Erosion Rate (mm ³ /kg)	Cavitation Erosion Rate (mm ³ /hr)
Fe-Mo-C	I	20.0	2.73	2.50
	G	19.9	2.48	1.76
	K	18.8	2.52	1.64
	D	18.7	2.35	1.48
	B	19.0	2.73	1.47
	E	17.8	2.64	0.91
WC-Co	AE	4.01	2.20	1.04
	AH	3.74	2.28	1.46
	AA	3.99	2.45	1.57
	AD	3.72	2.10	1.58
	AG	3.67	2.37	1.75
	AC	3.51	2.22	2.24

Table 4.14. Volume Loss Rate of All Materials Tested

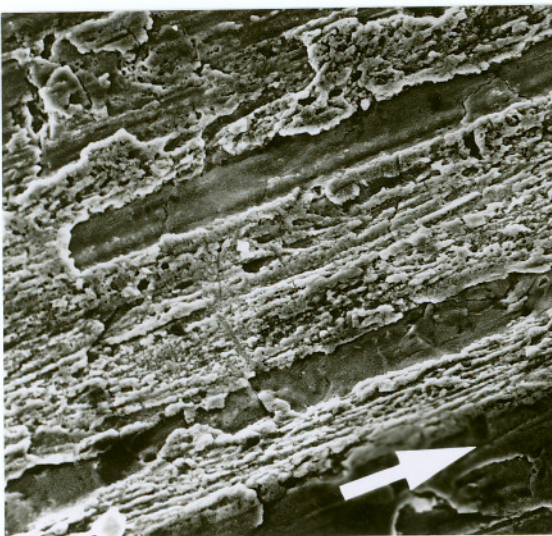
Materials		Abrasion Rate (mm ³ /km)	Erosion Rate (mm ³ /kg)	Cavitation Erosion Rate (mm ³ /hr)
Plasma Coatings	WC-Co	3.8	2.27	1.60
	Fe-Mo-C	19.0	2.58	1.63
White Irons	NH	8.0	0.59	0.083
	C80	8.2	0.60	0.055
	C30	6.1	0.49	0.049
	C20	7.4	0.60	0.116
	C25	9.5	0.52	0.011
Stainless Steels	C15	41.9	0.55	0.028
	S17	45.8	0.55	0.006
	17-4PH	99.5	0.79	0.203



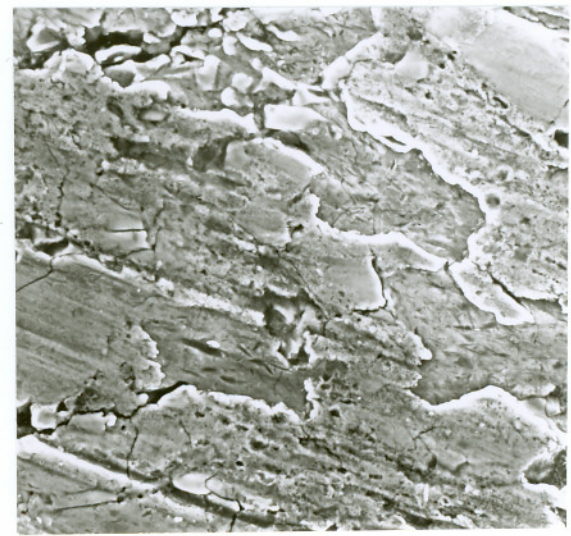
(a) 600X



(b) 800X



(c) 600X

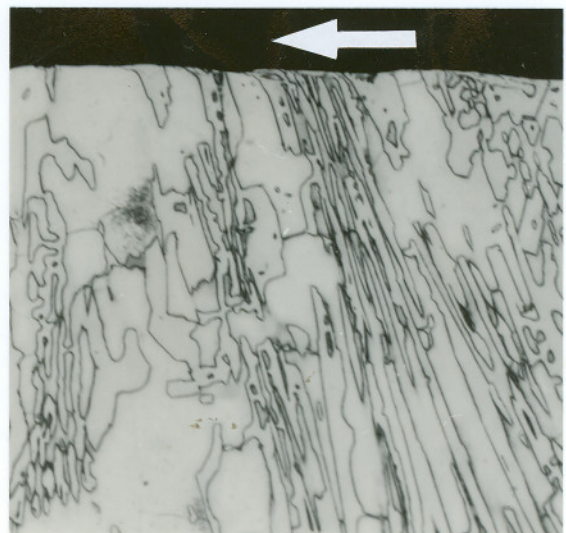


(d) 700X

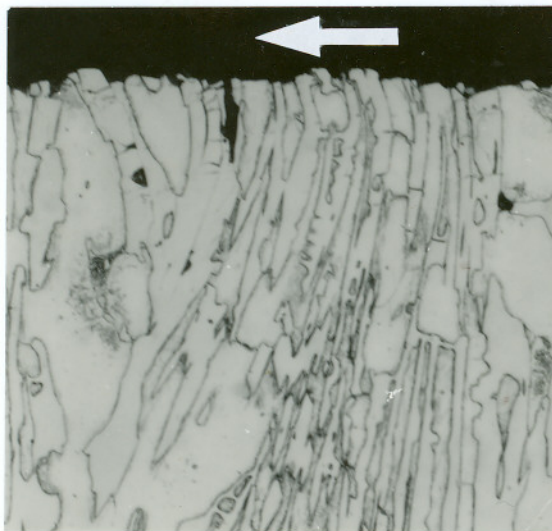
Figure 4.1. Serrated surfaces in the "smooth regions" for C20 plates.



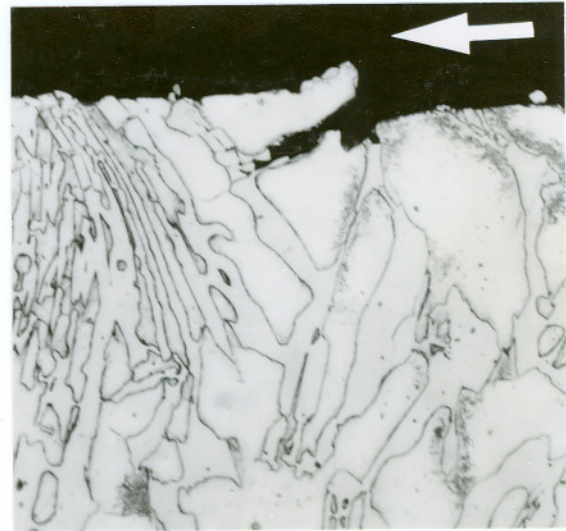
(a) 400X



(b) 400X

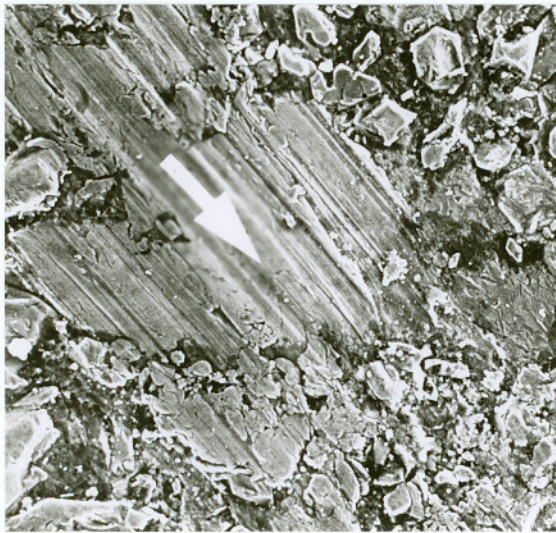


(c) 400X

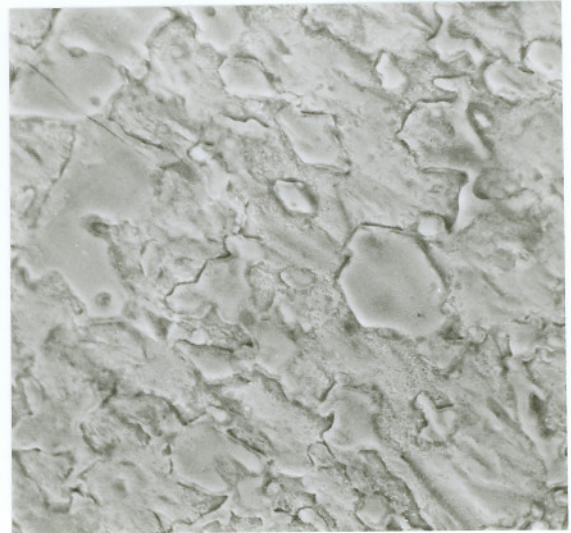


(d) 400X

Figure 4.2. Serrated subsurfaces in the "smooth regions" for C20 plates.



(a) 1000X



(b) 1000X

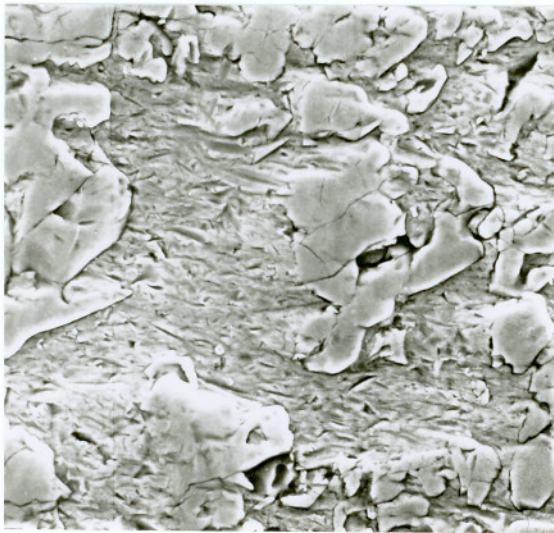


(c) 400X

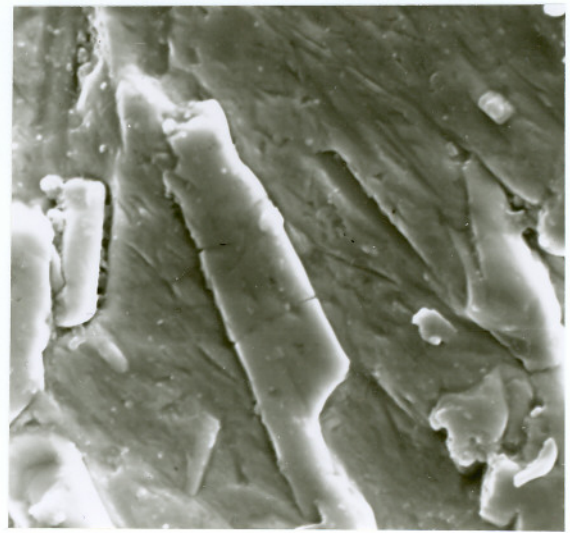


(d) 400X

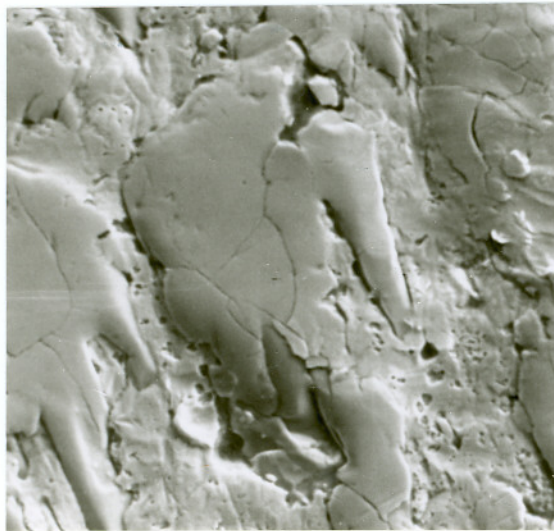
Figure 4.3. Serrated surfaces (a-b) and subsurfaces (c-d) in the "smooth regions" for C20 plates.



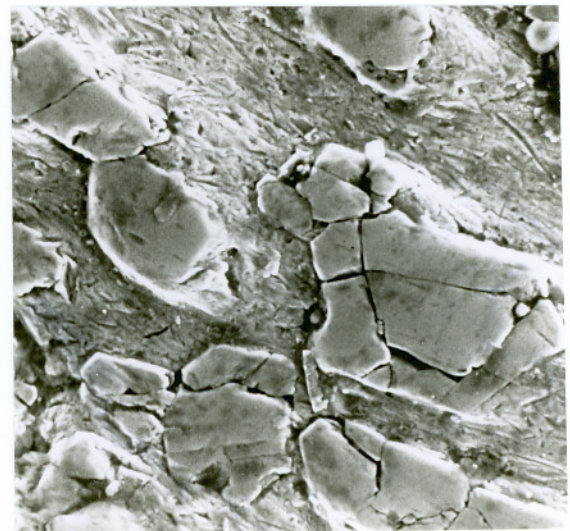
(a) 1000X



(b) 2000X

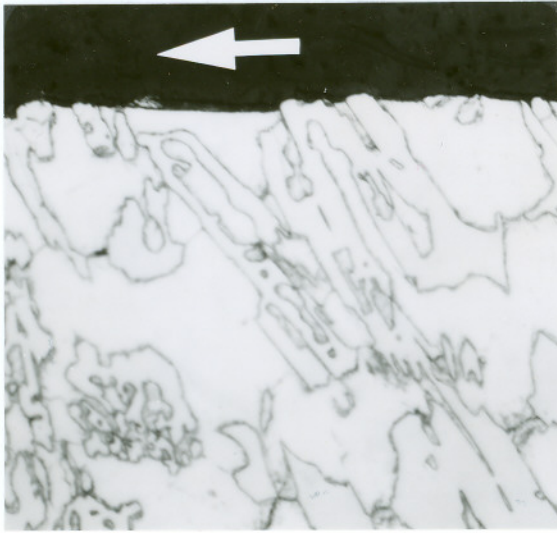


(c) 2000X

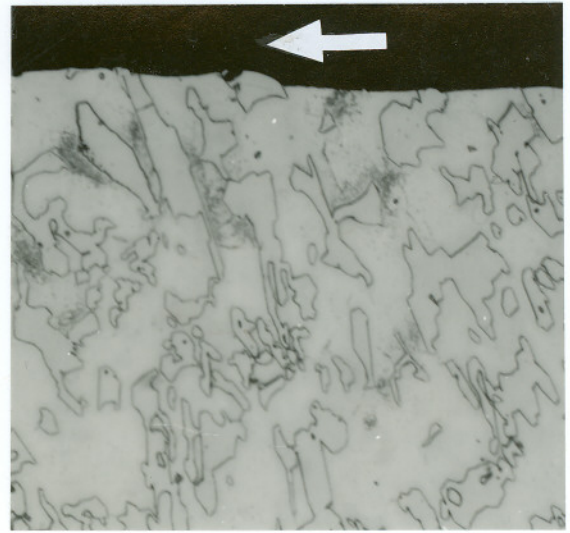


(d) 2000X

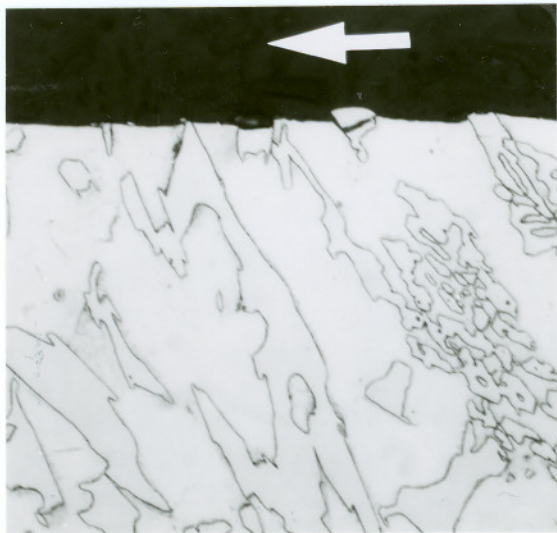
Figure 4.4. Serrated surfaces in the "rough regions" for C20 plates.



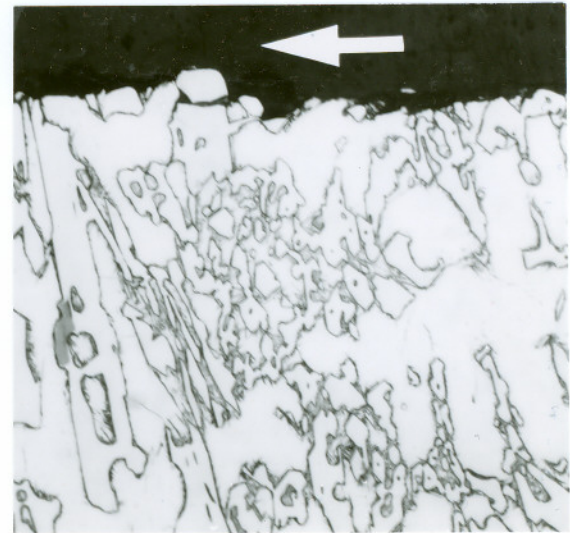
(a) 400X



(b) 400X



(c) 400X

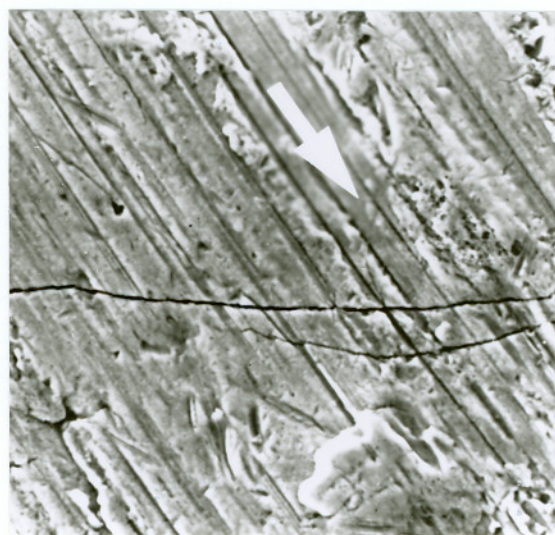


(d) 400X

Figure 4.5. Serrated subsurfaces in the "rough regions" for C20 plates.



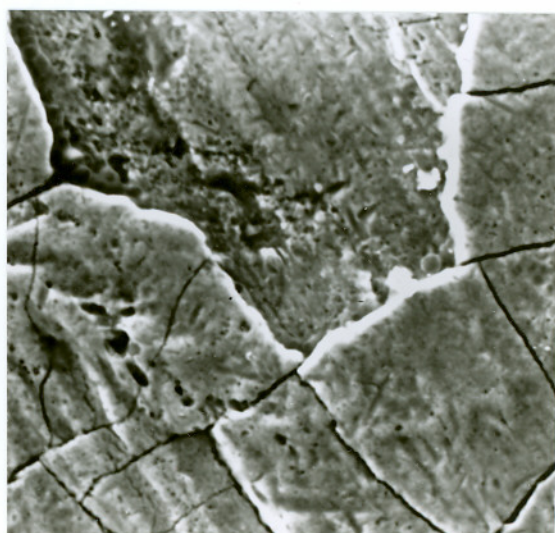
(a) 1000X



(b) 1000X

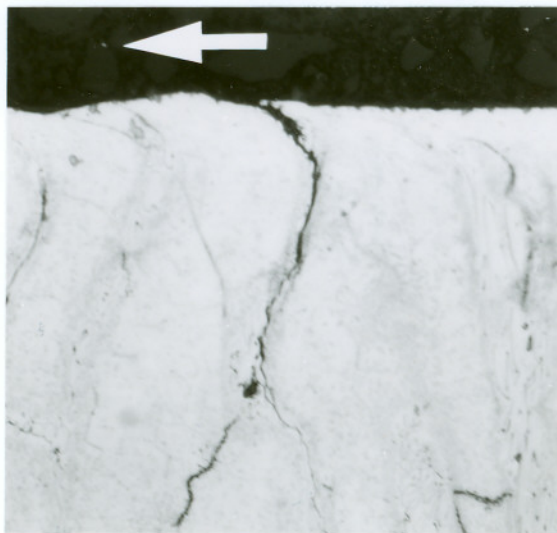


(c) 300X

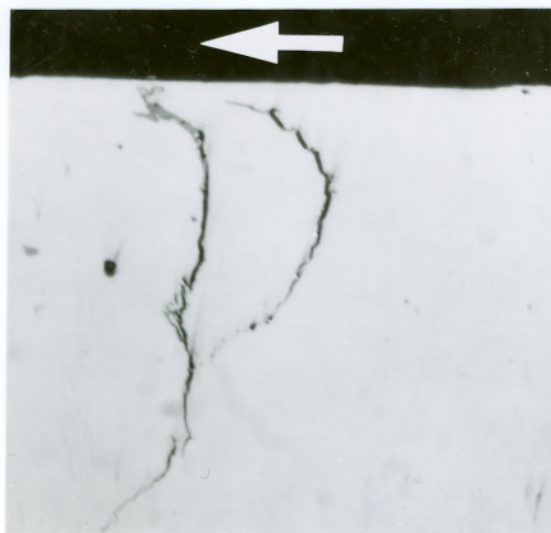


(d) 1000X

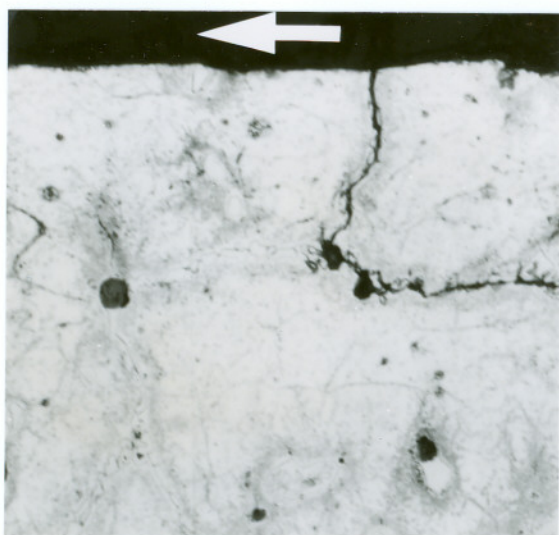
Figure 4.6. Serrated surfaces in the "smooth regions" for S17 plates.



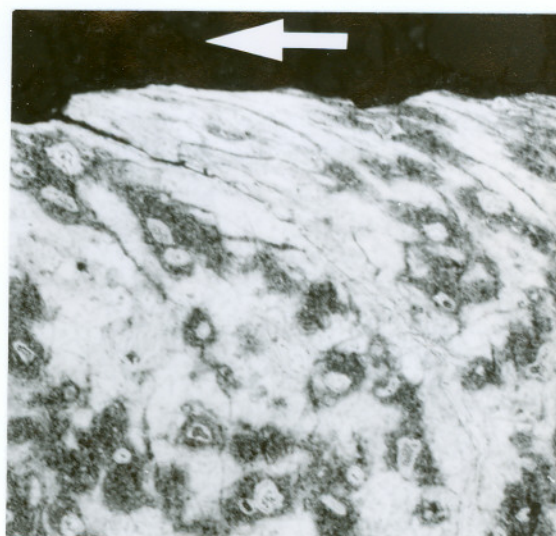
(a) 400X



(b) 400X

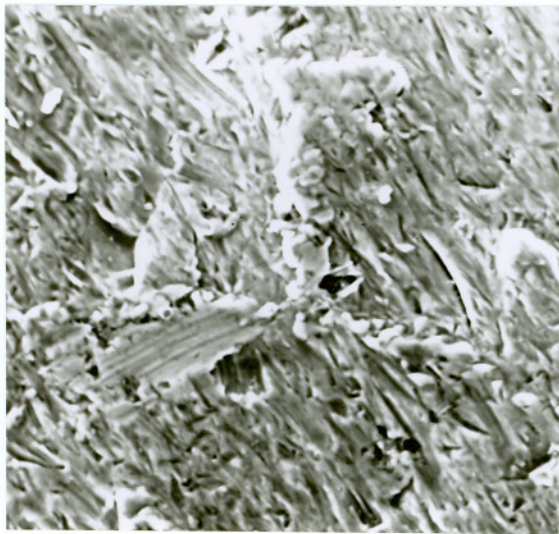


(c) 400X

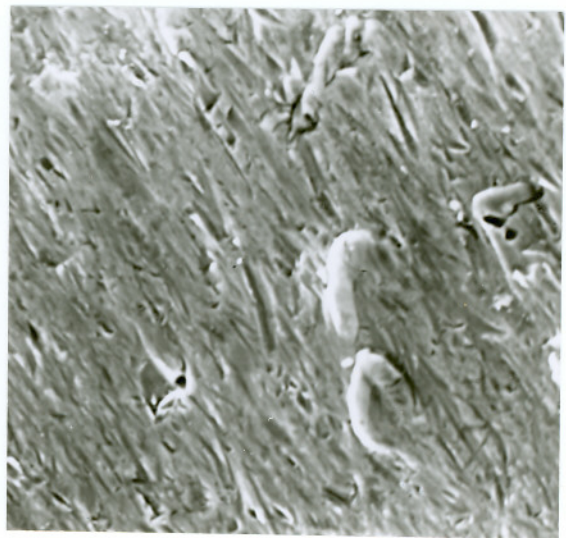


(d) 400X

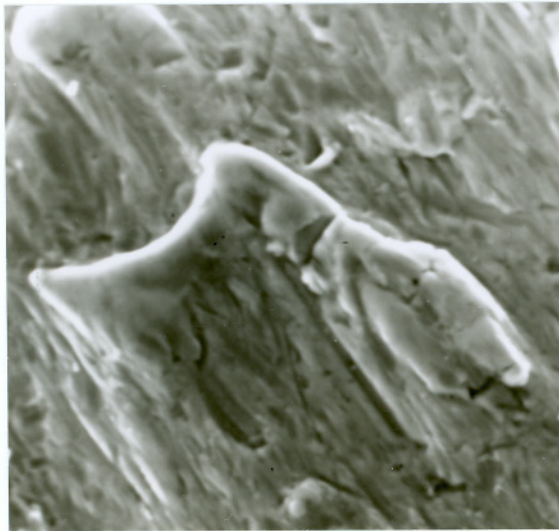
Figure 4.7. Serrated subsurfaces in the "smooth regions" for S17 plates.



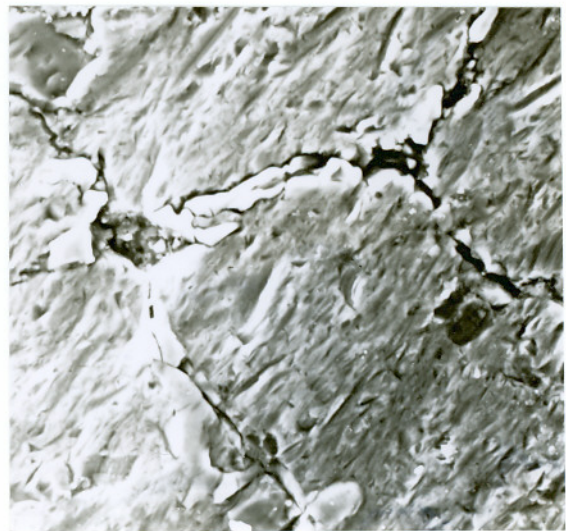
(a) 1200X



(b) 1000X

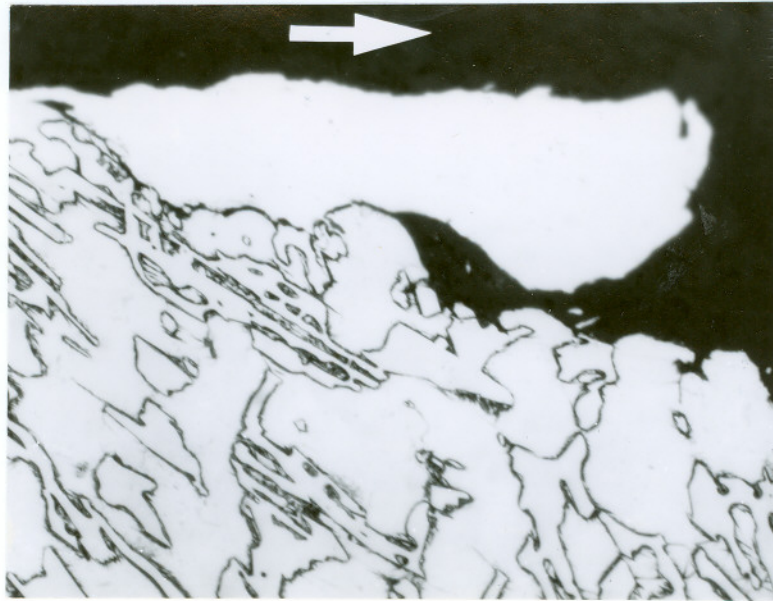


(c) 2000X

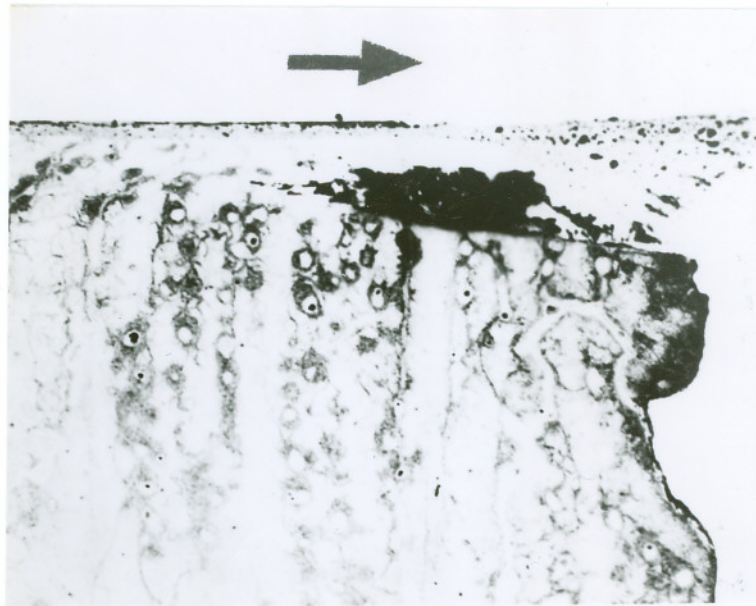


(d) 1000X

Figure 4.8. Serrated surfaces in the "rough regions" for S17 plates.

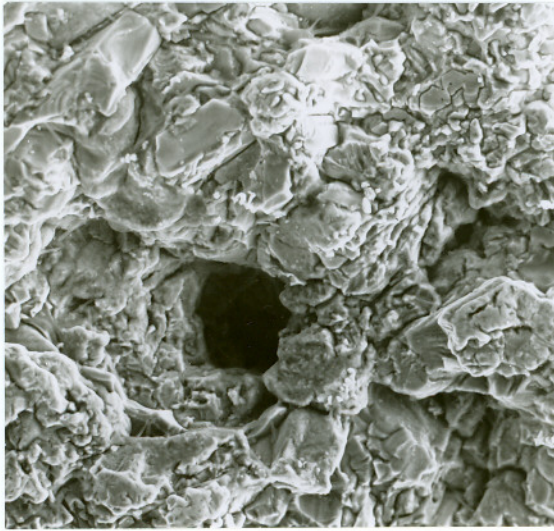


(a) 20-2-1 Plate 400X

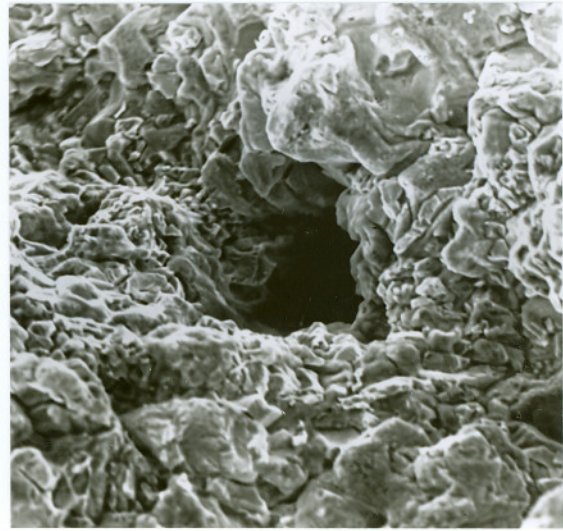


(b) 440C Plate 160X

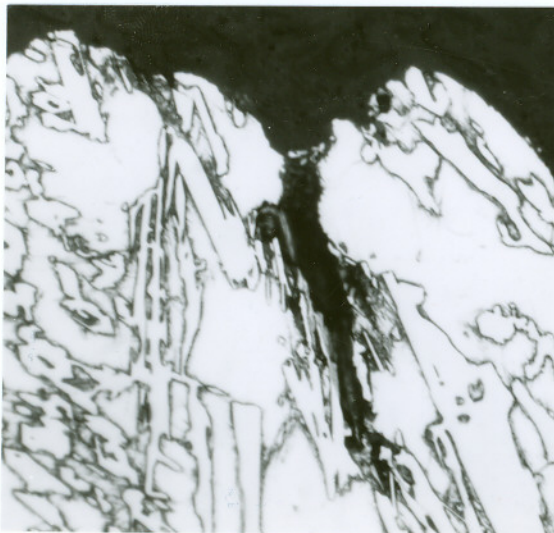
Figure 4.9. White surface layers near the bar trailing edges in the "smooth regions".



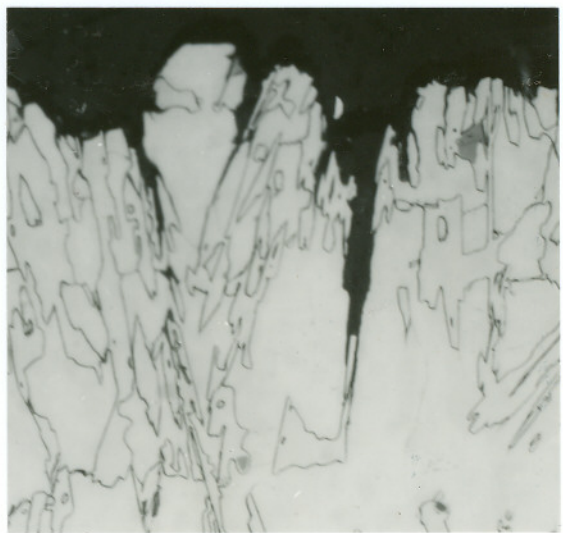
(a) Intermediate Zone 500X



(b) Breaker Bar Zone 1000X

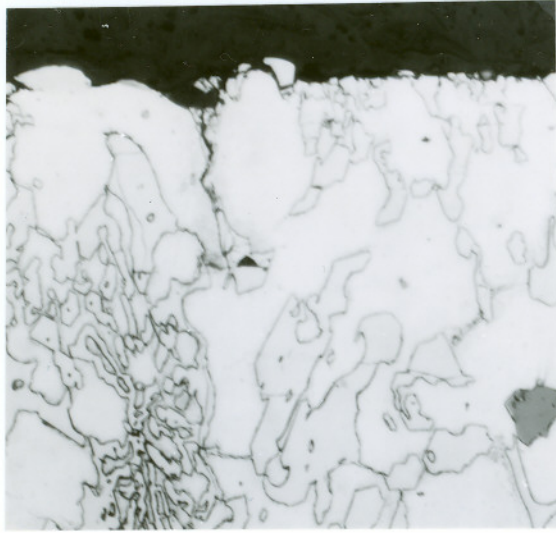


(c) Fine Bar Zone 400X

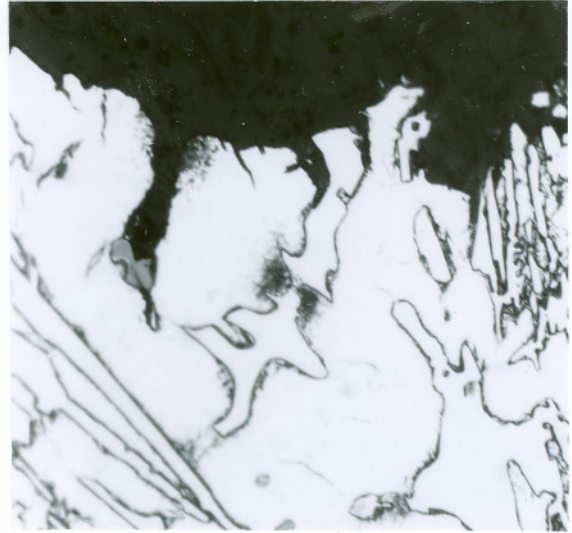


(d) Fine Bar Zone 1000X

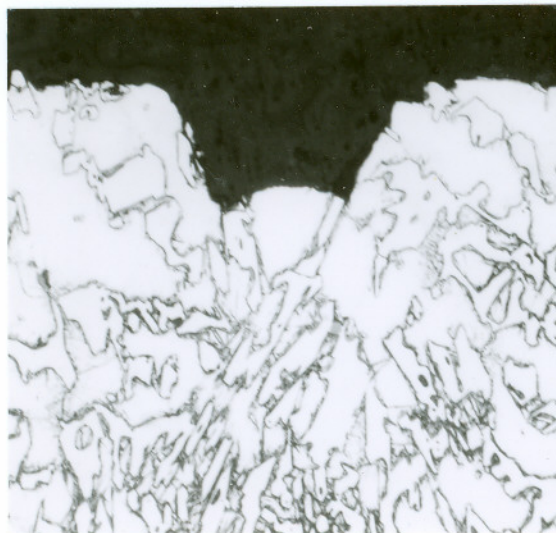
Figure 4.10. Deep pits in the pitted bar leading edges of the C20 plates.



(a) 400X



(b) 400X

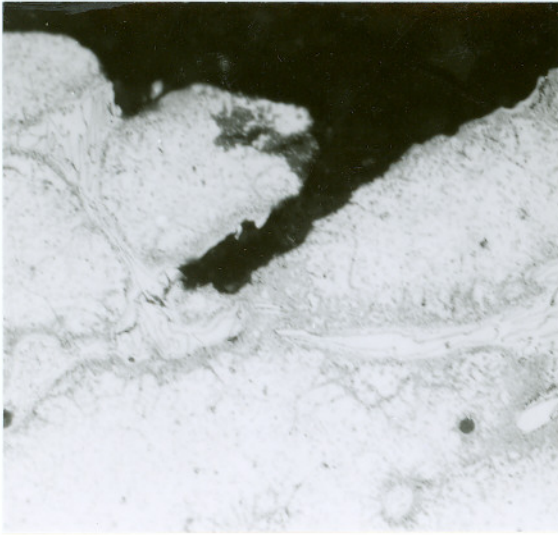


(c) 400X



(d) 400X

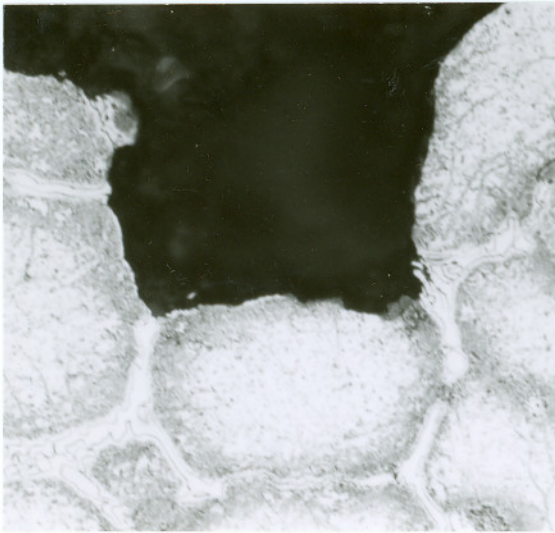
Figure 4.11. Pitting damage process in the bar leading edges of the C20 plates.



(a) 400X



(b) 400X



(c) 400X

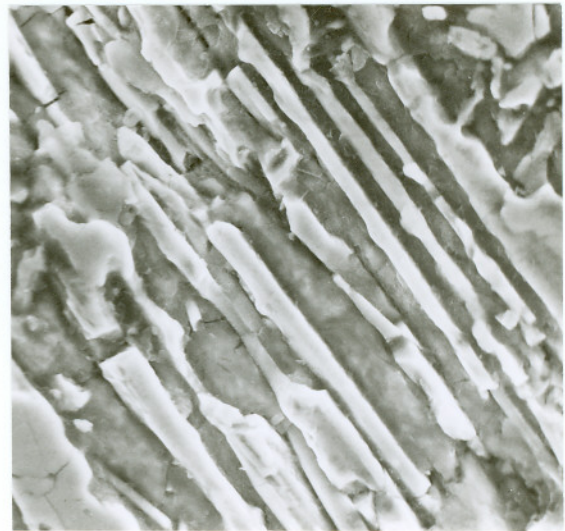


(d) 200X

Figure 4.12. Pitting damage process in the bar leading edges of the S17 plates.



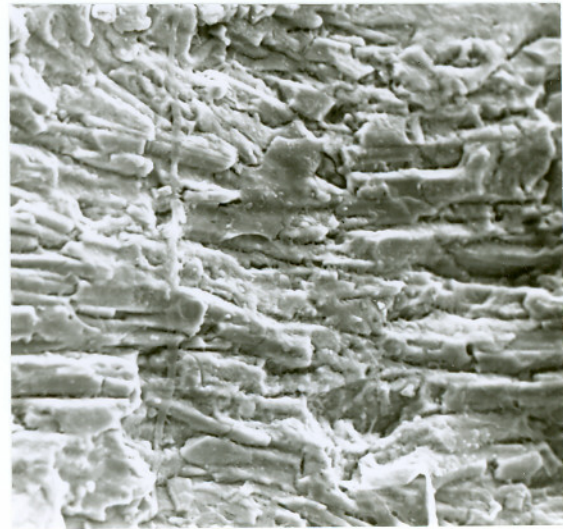
(a) Fine Bar Zone 400X



(b) Intermediate Zone 1000X

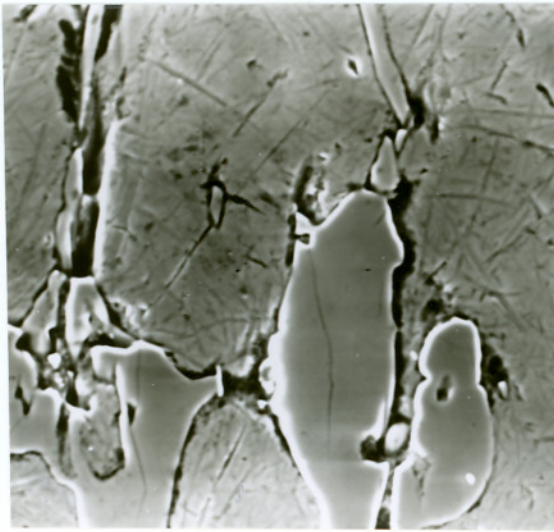


(c) Fine Bar Zone 1000X

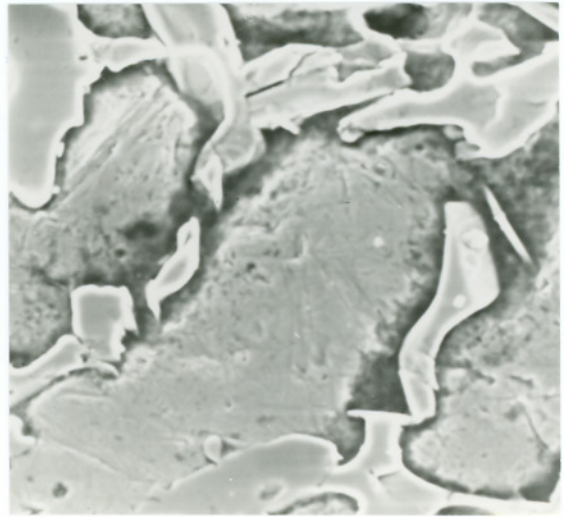


(d) Breaker Bar Zone 1000X

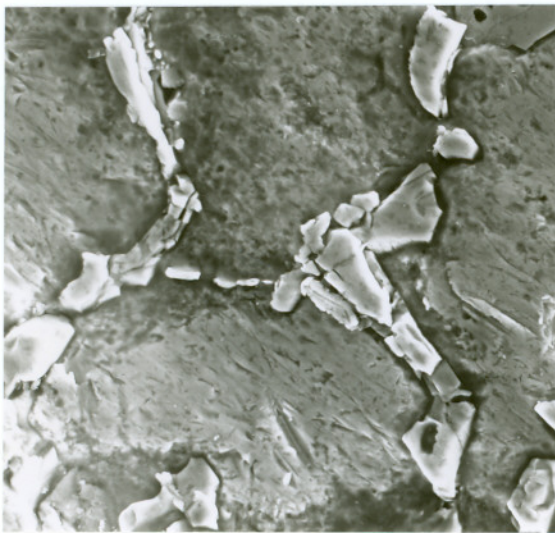
Figure 4.13. Carbides at the pitted bar leading edges of C20 (a-b) and S17 (c-d) plates.



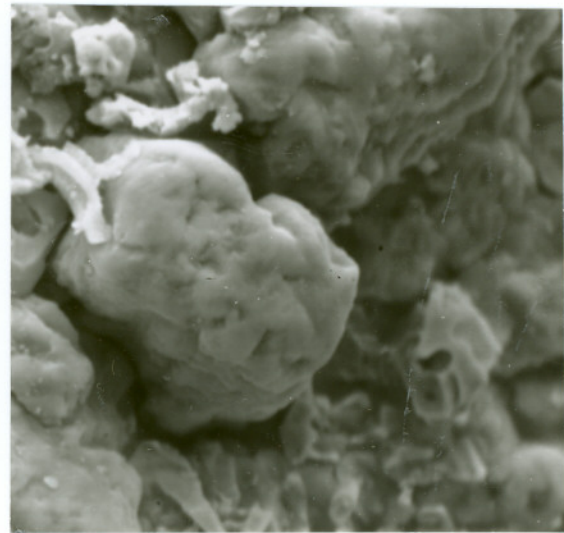
(a) 4th Trial, Breaker Bar Zone 1000X



(b) 4th Trial, Breaker Bar Zone 1000X

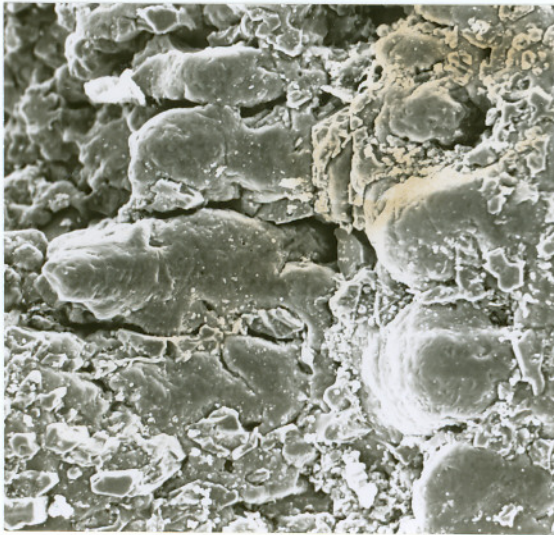


(c) 3rd Trial, Intermediate Zone 900X

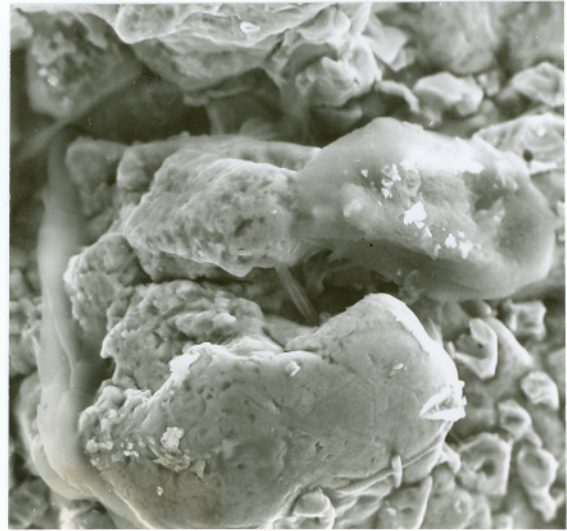


(d) 3rd Trial, Breaker Bar Zone 1500X

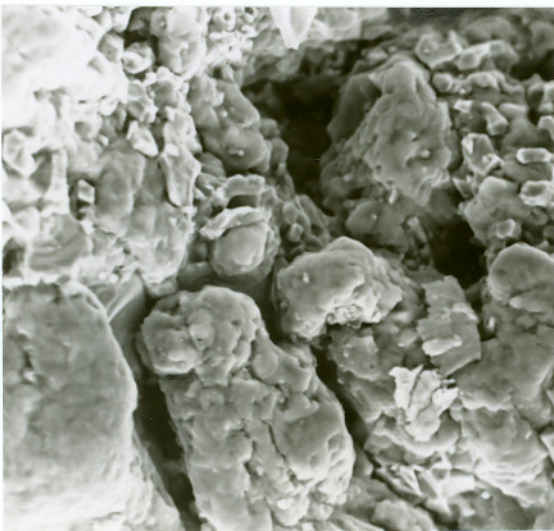
Figure 4.14. Pitting process on the pitted C20 plate bar leading edges.



(a) Fine Bar Zone 500X



(b) Intermediate Zone 1000X



(c) Breaker Bar Zone 900X

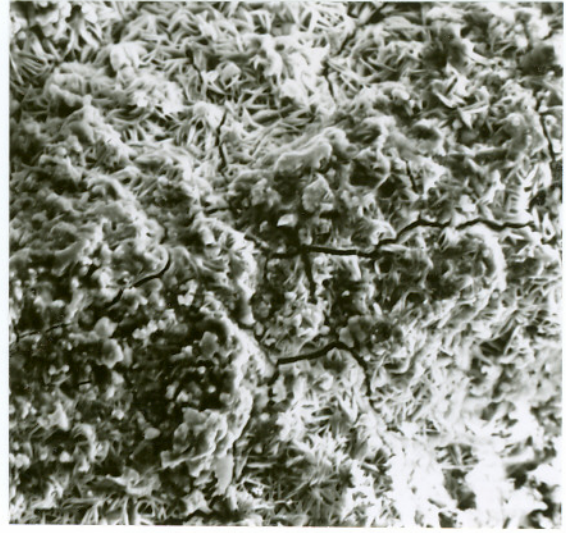


(d) Fine Bar Zone 600X

Figure 4.15. Pitted bar leading edges of C20 plates (a-c) and S17 plates (d).



(a) Intermediate Zone 1600X



(b) Fine Bar Zone 1500X



(c) Fine Bar Zone 400X

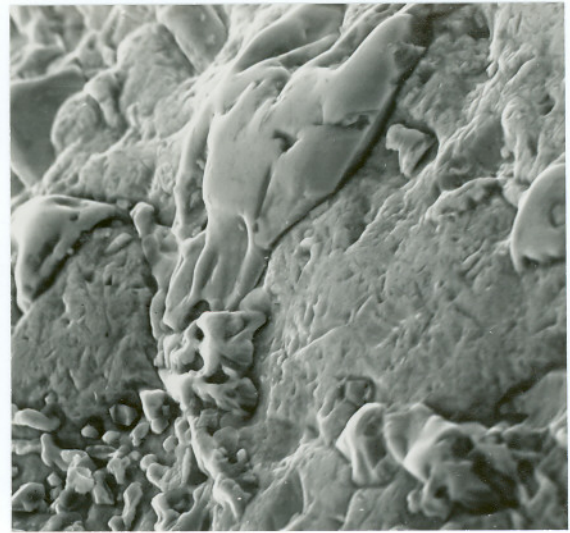


(d) Fine Bar Zone 400X

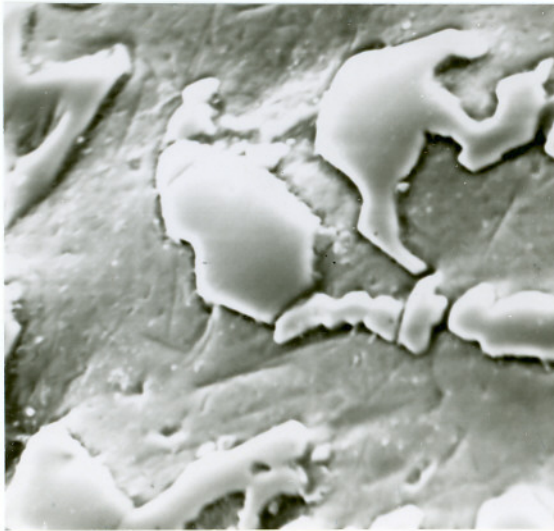
Figure 4.16. Fatiguelike cracks on the pitted C20 plate bar leading edges.



(a) Fine Bar Zone 1500X



(b) Intermediate Zone 1000X



(c) Breaker Bar Zone 2000X

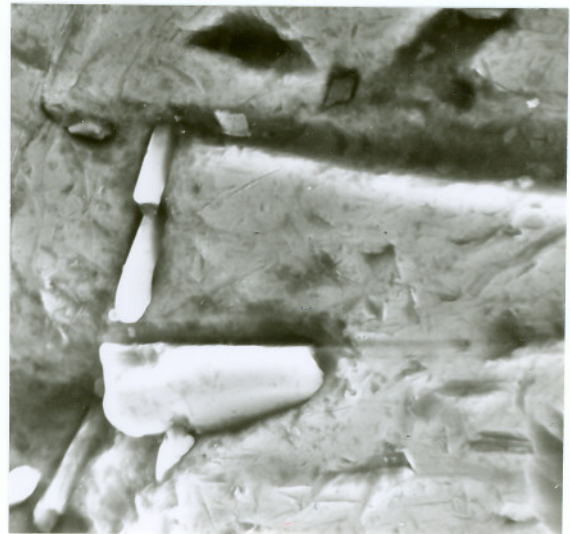


(d) Intermediate Zone 2000X

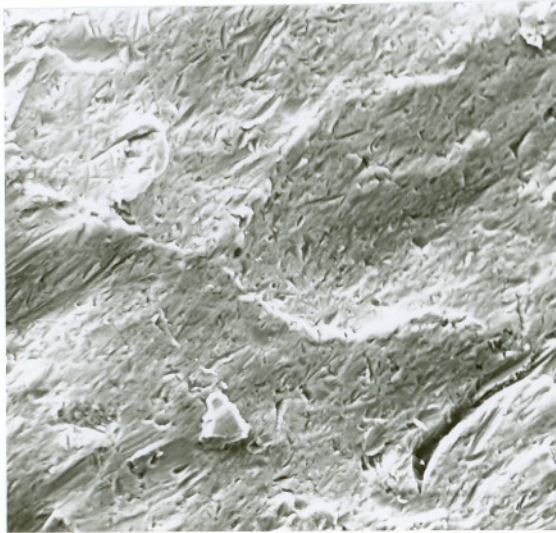
Figure 4.17. Rounded bar leading edges of C20 plates with whitewood (a-c) and Douglas fir (d).



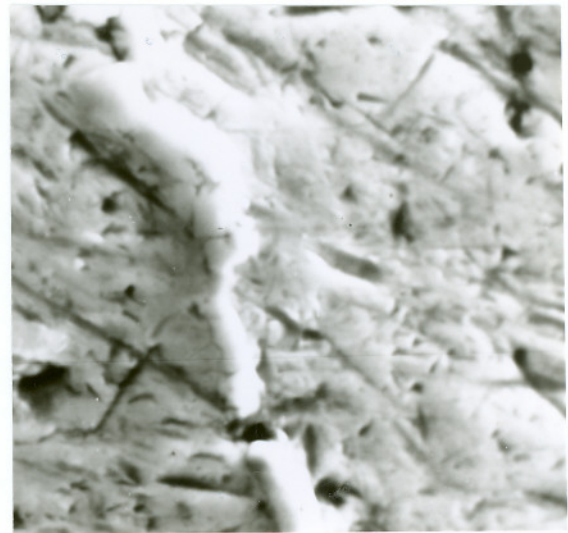
(a) Fine Bar Zone 5000X



(b) Intermediate Zone 3000X

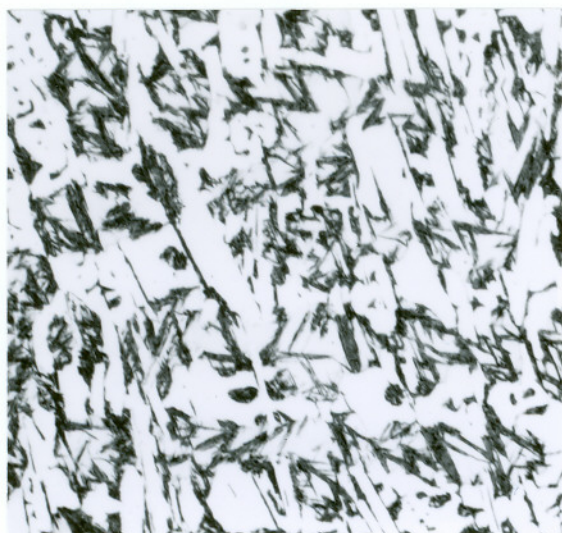


(c) Intermediate Zone 500X



(d) Intermediate Zone 3000X

Figure 4.18. Rounded bar leading edges of C20 plates (a-b) and S17 plates (c-d).



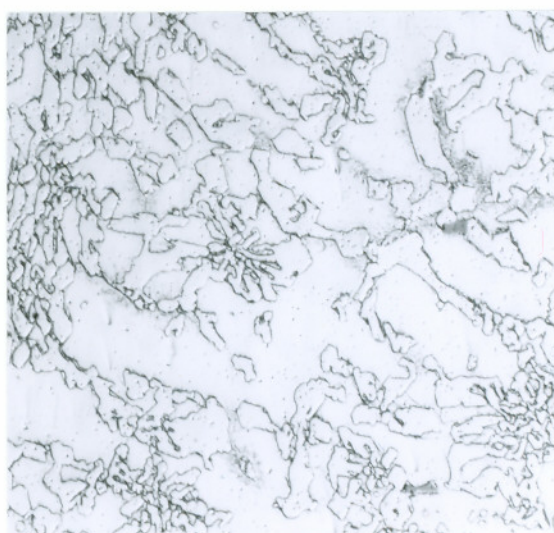
(a) NH 400X



(b) C80 400X



(c) C20 400X

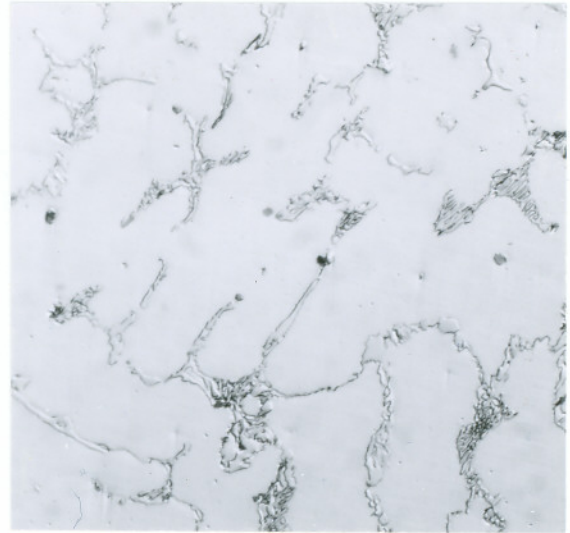


(d) C30 400X

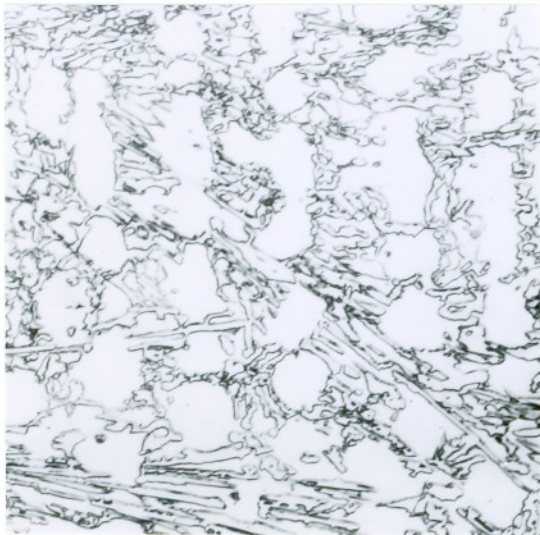
Figure 4.19. Microstructures of plate alloys: (a-b) Ni-hard white irons (eutectic M_3C carbides plus martensite); and (c-d) 20-2-1 high chromium white irons (eutectic M_7C_3 carbides plus austenite).



(a) C15 400X



(b) S17 400X

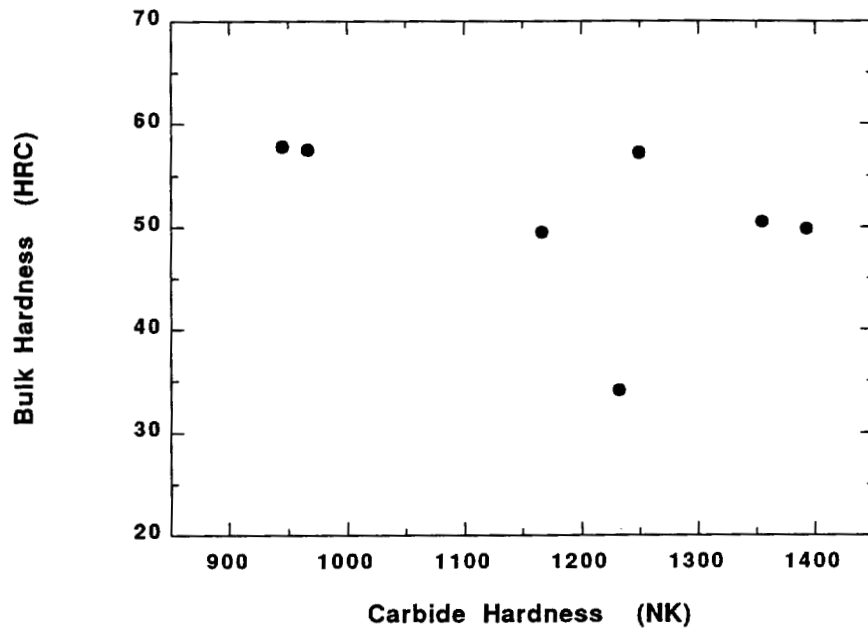


(c) C25 400X

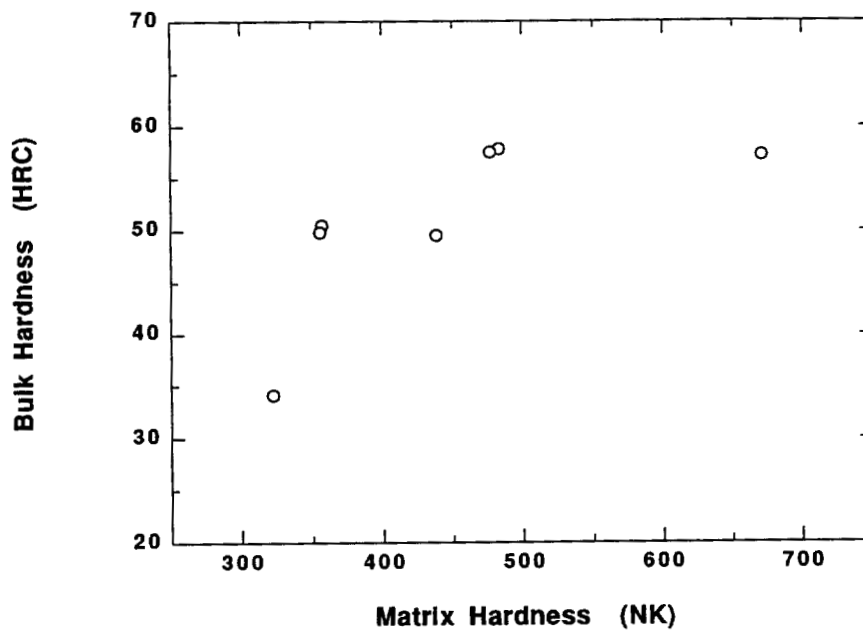


(d) 17-4PH 400X

Figure 4.20. Microstructures of plate alloys: (a) 440C stainless steel (eutectic carbides plus martensite); (b) 440C stainless steel (eutectic carbides plus austenite); (c) 25Cr iron (eutectic M_7C_3 carbides plus austenite); and (d) 17-4 PH stainless steel (ferrite pools in martensite matrix).

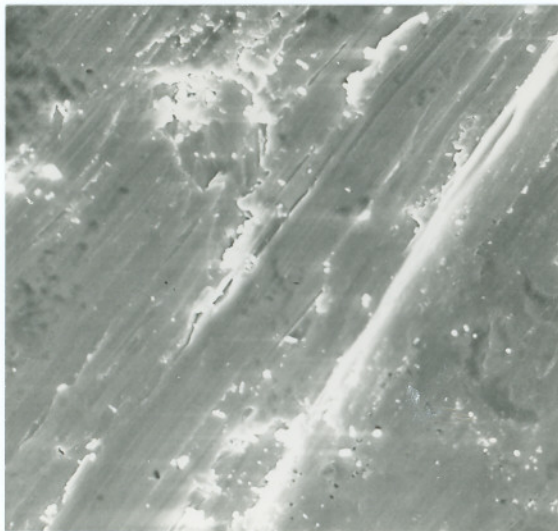


(a)



(b)

Figure 4.21. Plate alloy bulk hardness versus carbide hardness (a) and matrix hardness (b).



(a) C20 2000X



(b) C20 400X

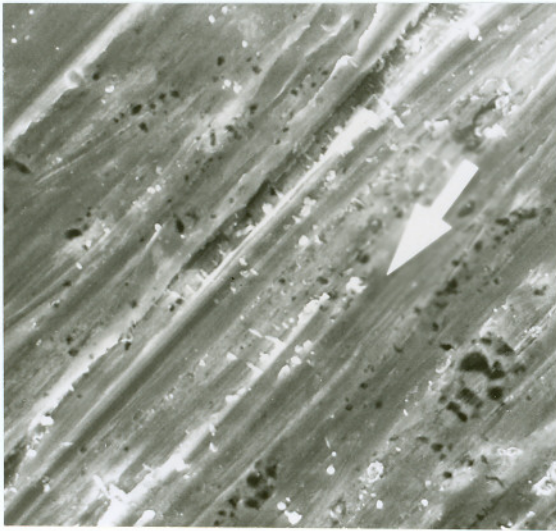


(c) C80 1000X

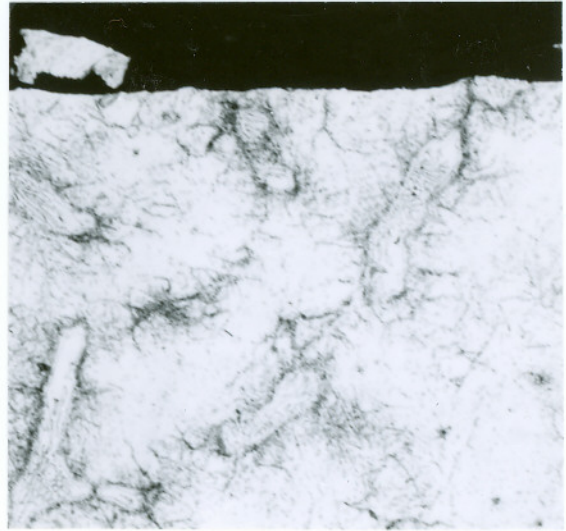


(d) C80 400X

Figure 4.22. DSRW abraded surfaces of 20-2-1 iron (a-b) and Ni-hard iron (c-d).



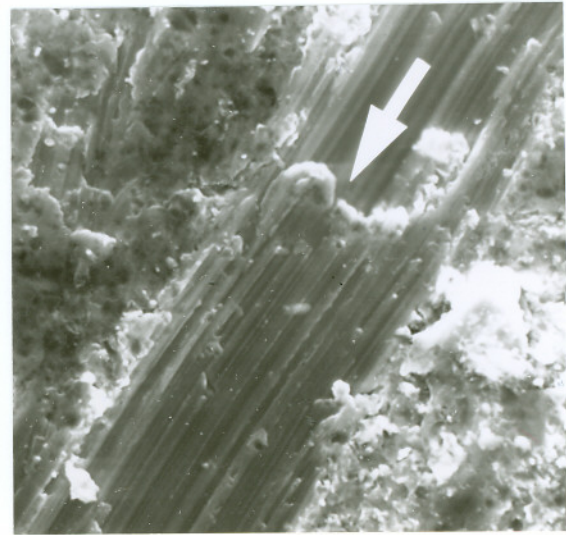
(a) C15 2000X



(b) C15 400X

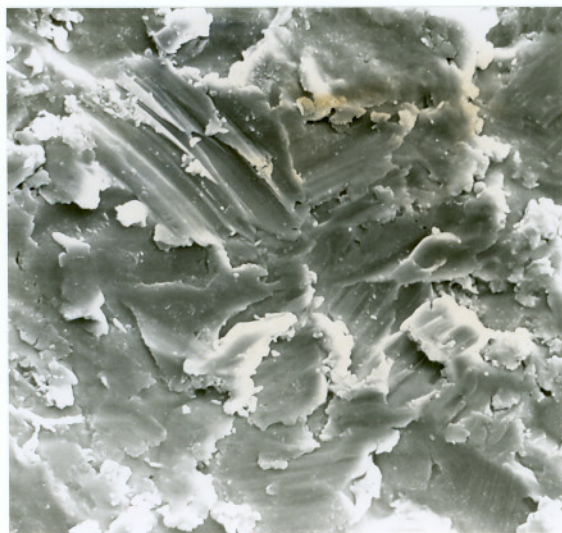


(c) 17-4 PH 3000X



(d) 17-4 PH 3000X

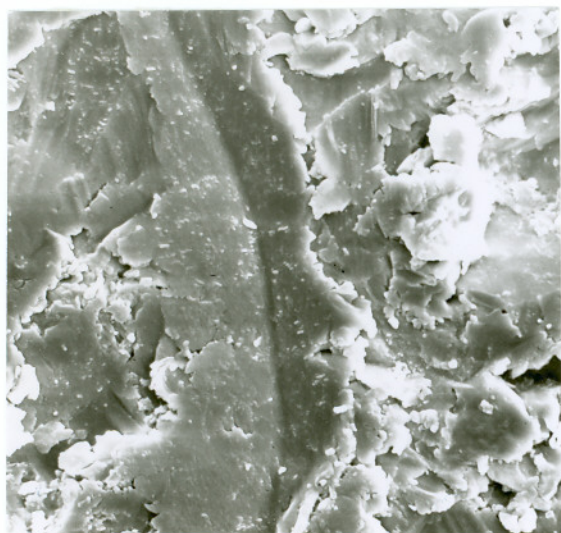
Figure 4.23. DSRW abraded surfaces of 440C steel (a-b) and 17-4 PH steel (c-d).



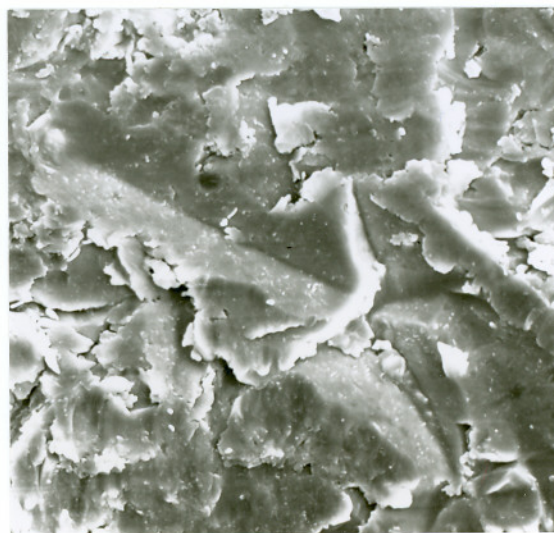
(a) NH 2000X



(b) C20 2000X

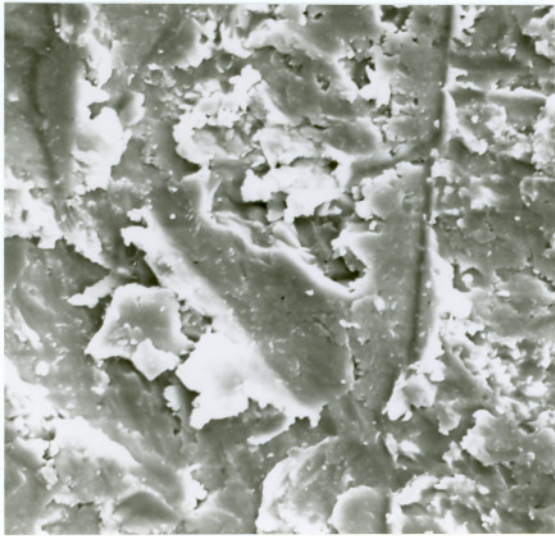


(c) C25 2000X

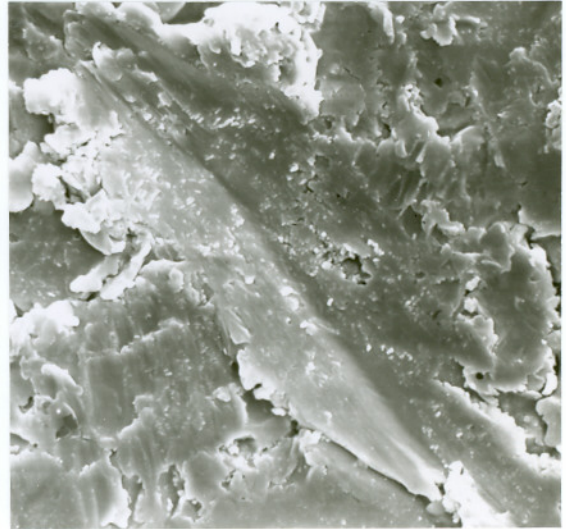


(d) 17-4 PH 2000X

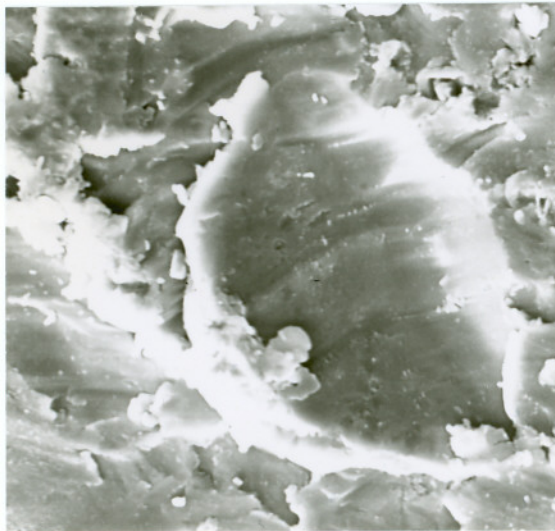
Figure 4.24. Eroded plate alloy surfaces.



(a) S17 2000X



(b) C15 2000X



(c) NH 3000X

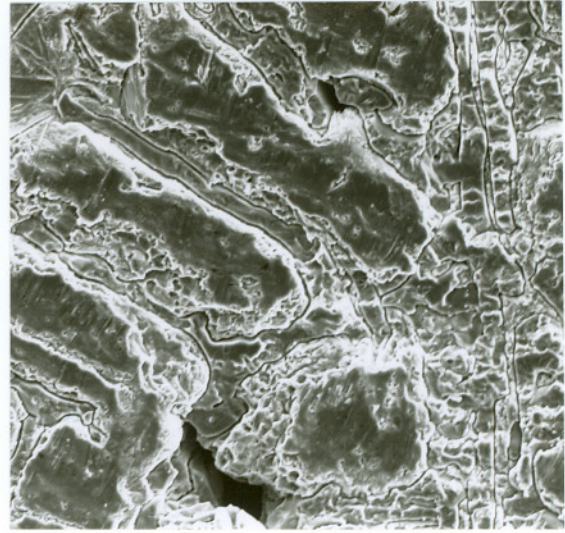


(d) 17-4 PH 2000X

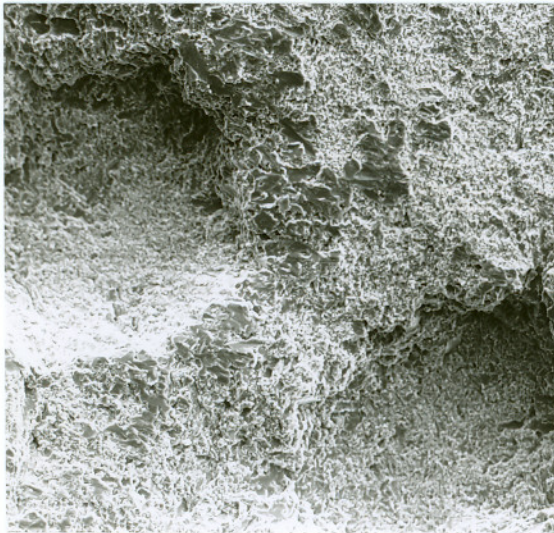
Figure 4.25. Eroded plate alloy surfaces.



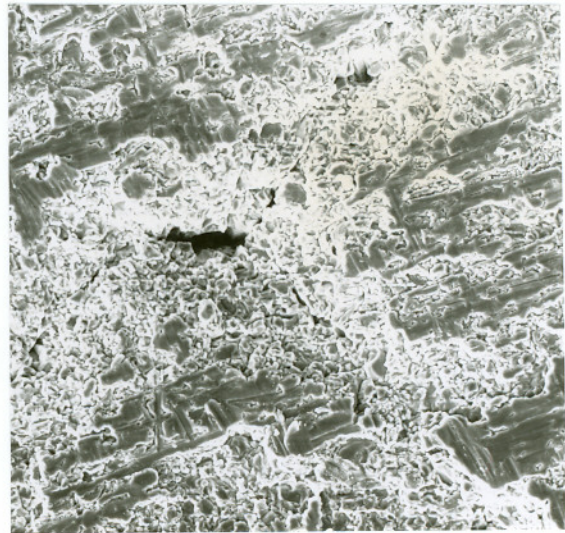
(a) C20 300X



(b) C80 500X

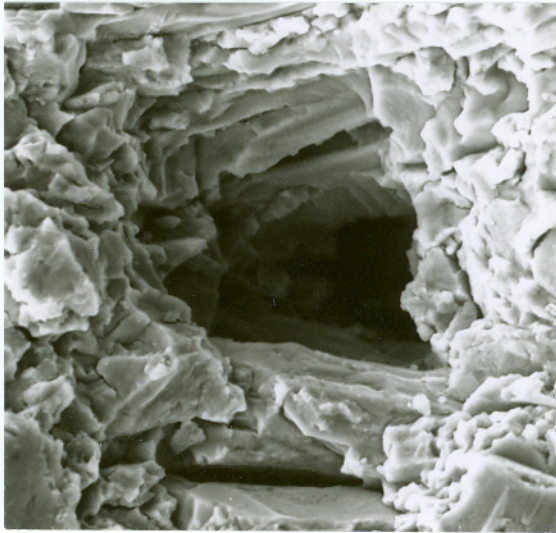


(c) 17-4 PH 200X

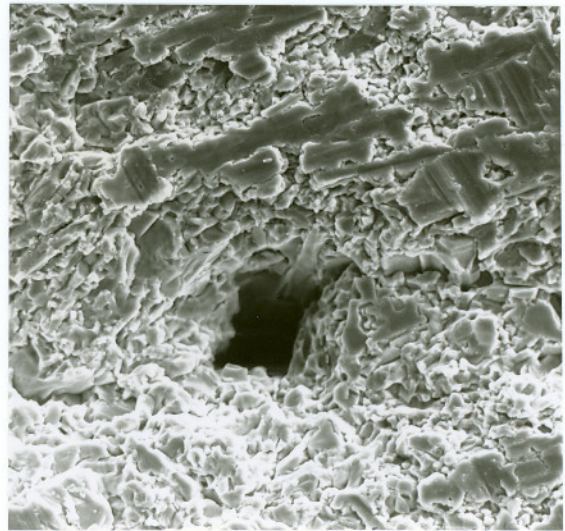


(d) C25 500X

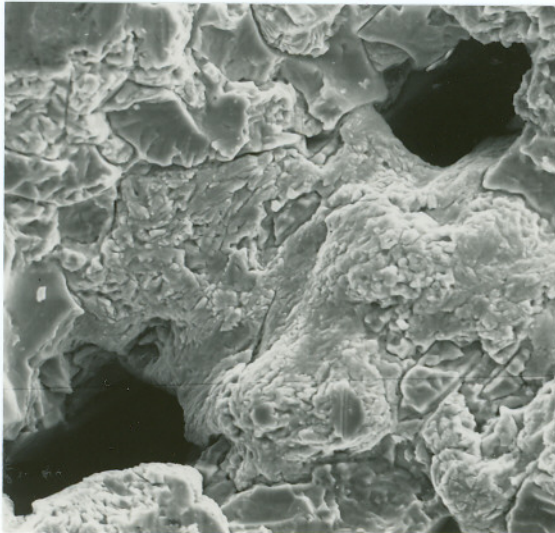
Figure 4.26. Various pits on the cavitation eroded alloy surfaces.



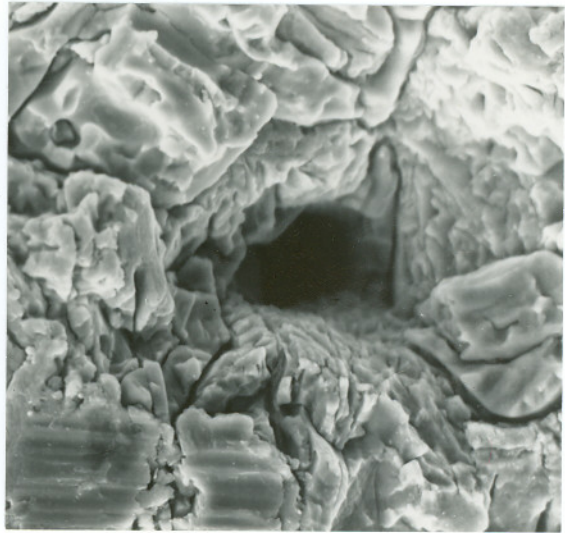
(a) C30 2000X



(b) C25 1000X

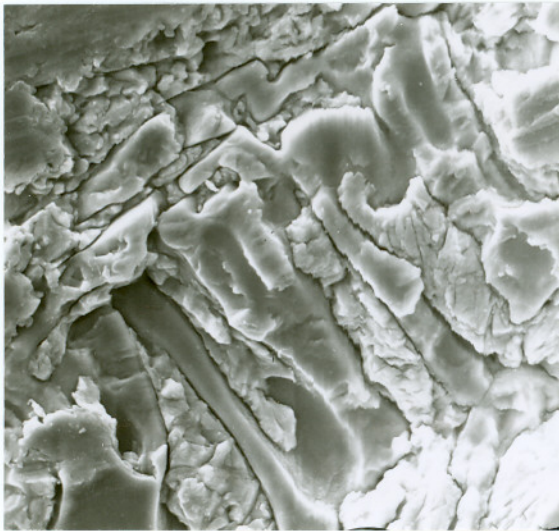


(c) C80 1000X

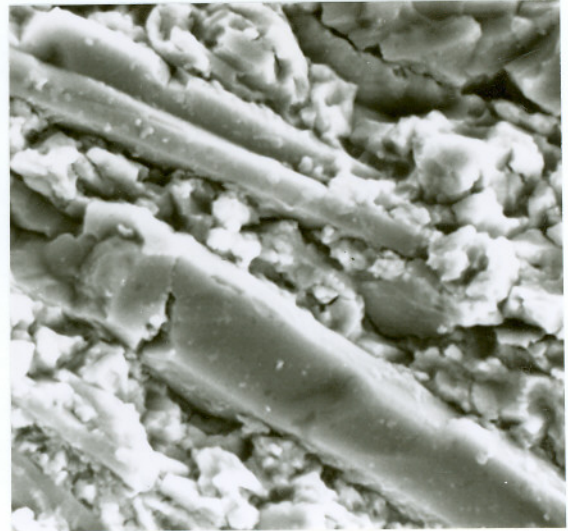


(d) NH 2000X

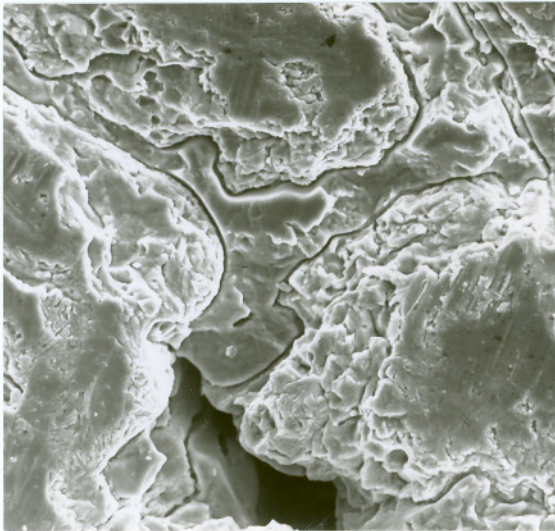
Figure 4.27. Various pits on the cavitation eroded alloy surfaces.



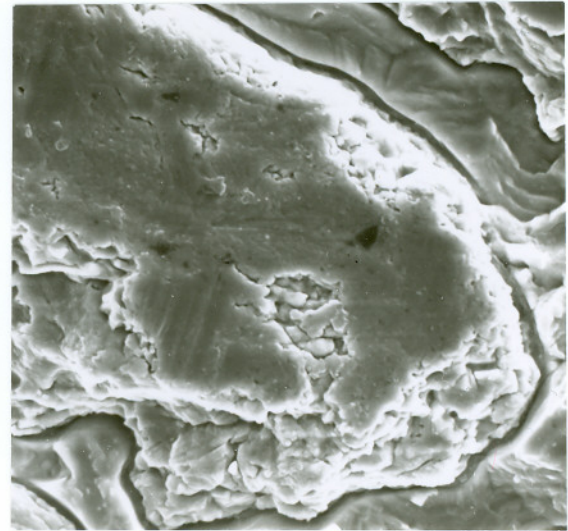
(a) NH 2000X



(b) C30 4000X

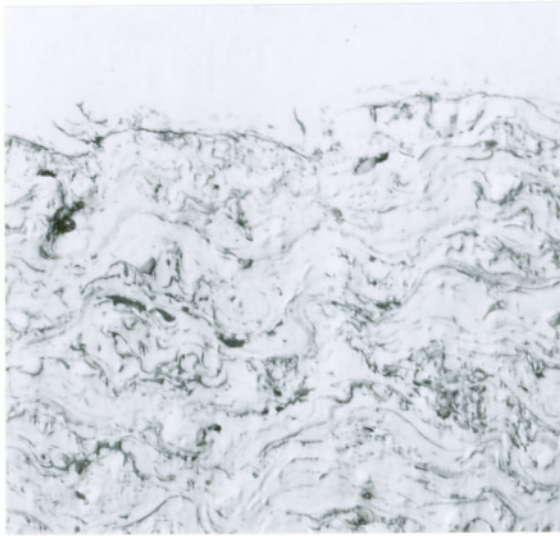


(c) C80 1000X

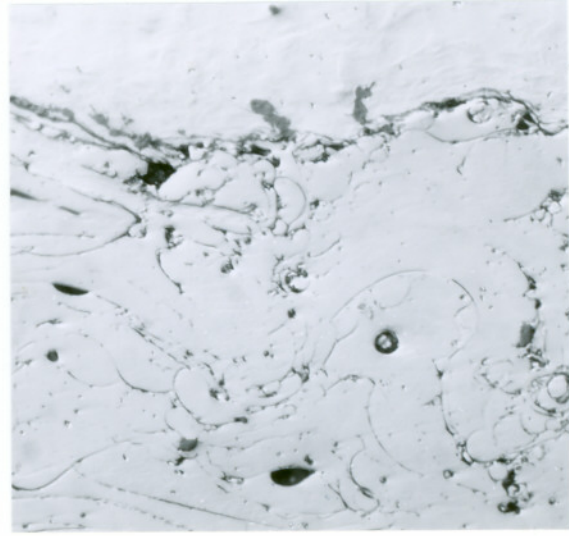


(d) C80 2000X

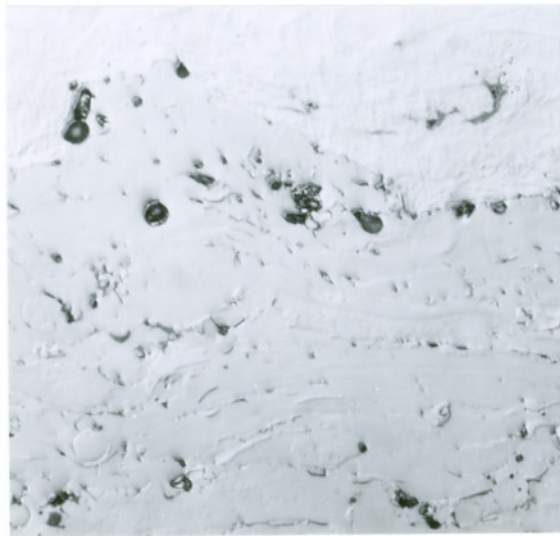
Figure 4.28. Cavitation eroded surfaces of various plate alloys.



(a) Fe-Mo-C 400X



(b) Ni-Cr-Si-Fe-B1 400X

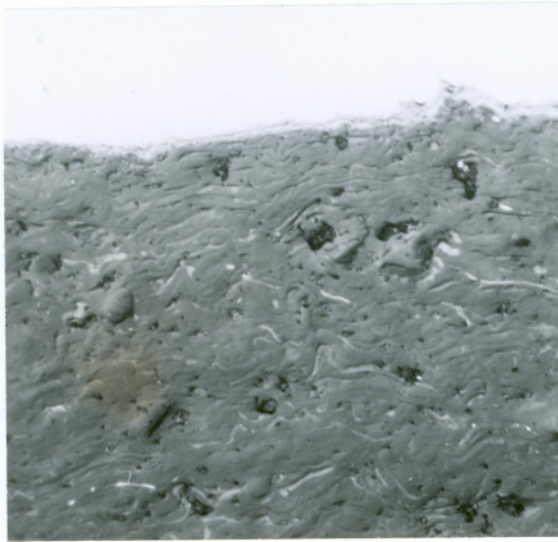


(c) Ni-Cr-Si-Fe-B2 400X



(d) Ti-Alloy 400X

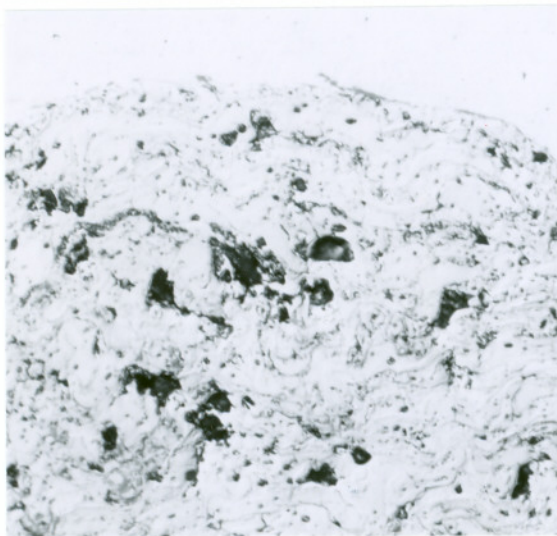
Figure 4.29. Microstructures of alloy coatings.



(a) $\text{Al}_2\text{O}_3\text{-TiO}_2$ 400X



(b) $\text{Cr}_2\text{O}_3\text{-SiO}_2\text{-TiO}_2$ 400X



(c) $\text{Cr}_3\text{C}_2\text{-WC-TiC-Ni-Mo-C}_2$ 400X

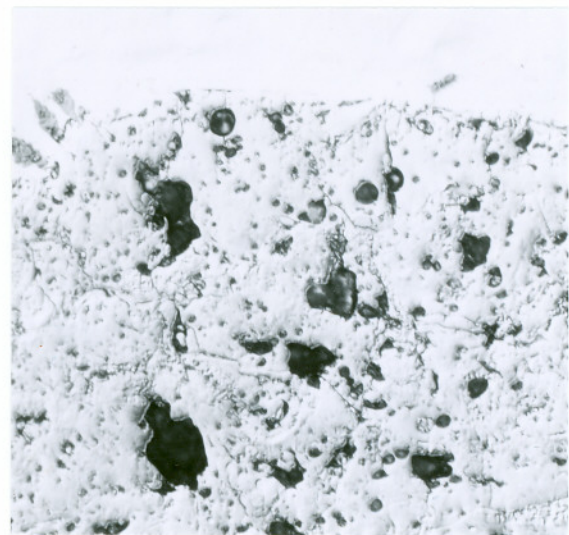


(d) $\text{Cr}_3\text{C}_2\text{-Ni-Cr}$ 400X

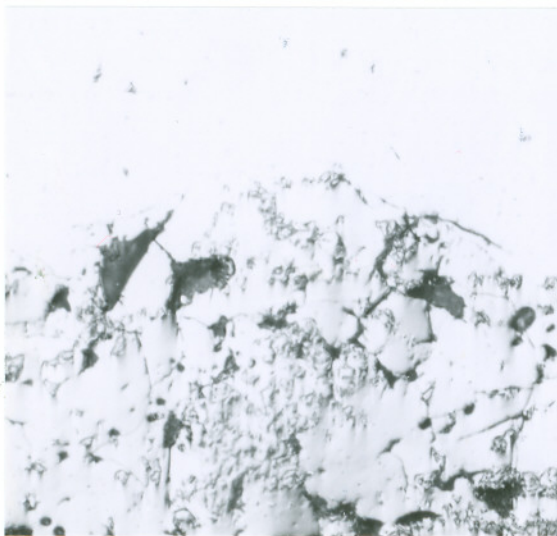
Figure 4.30. Microstructures of ceramic coatings (a) and cermet coatings (c-d).



(a) W-C-Co1 400X



(b) W-C-Co2 400X



(c) WC-Co1 400X



(d) WC-Co2 400X

Figure 4.31. Microstructures of cermet coatings.

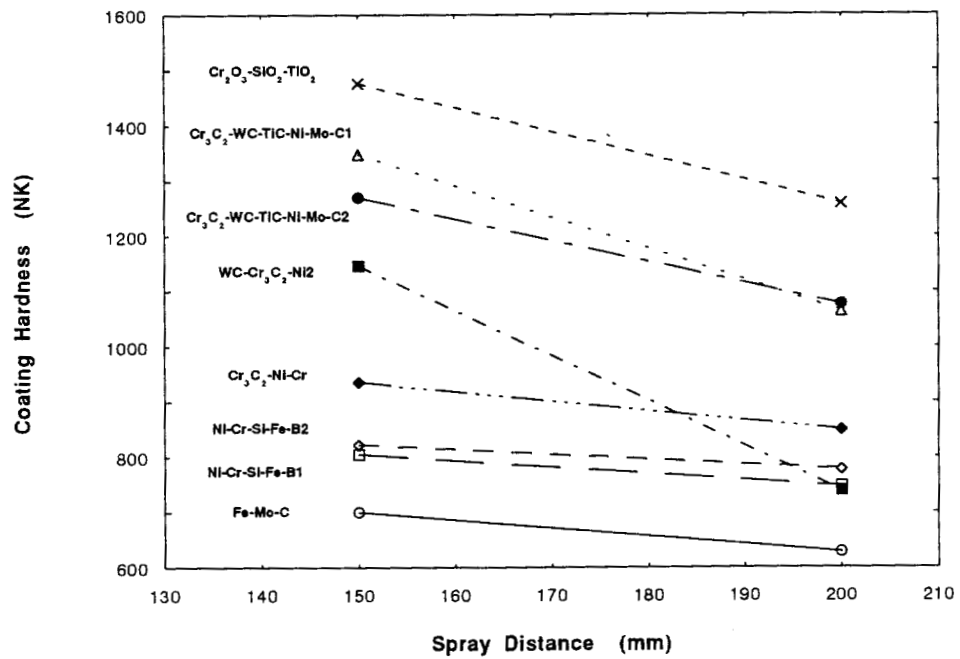


Figure 4.32. Coating hardness versus spray distance.

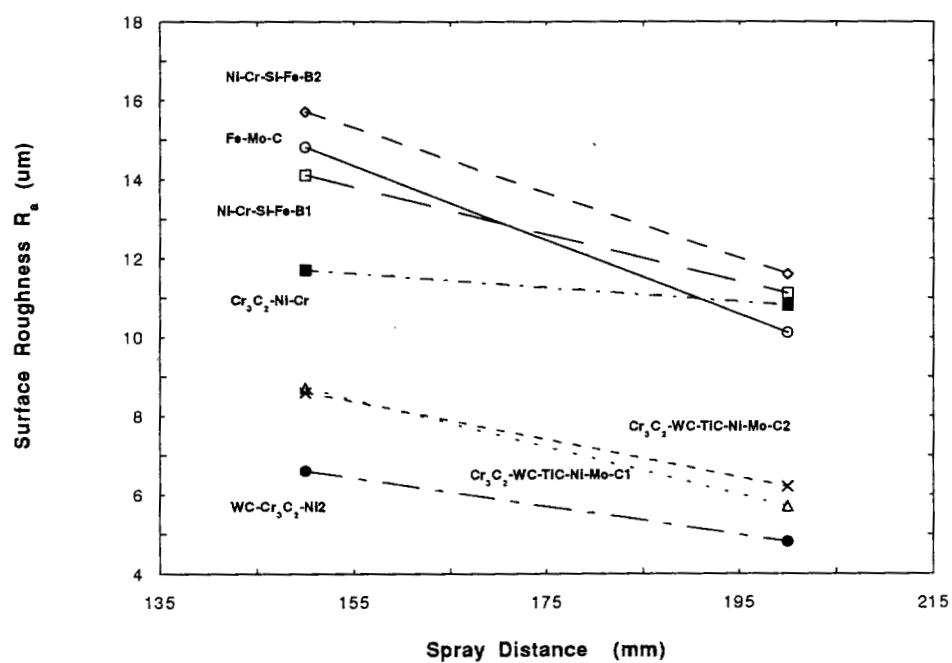


Figure 4.33. Coating surface roughness versus spray distance.

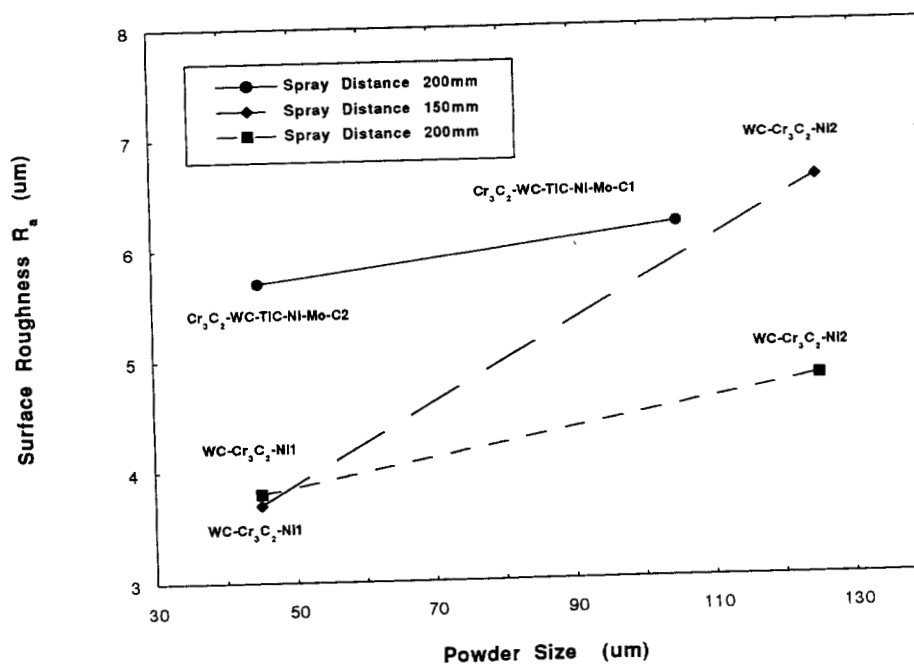
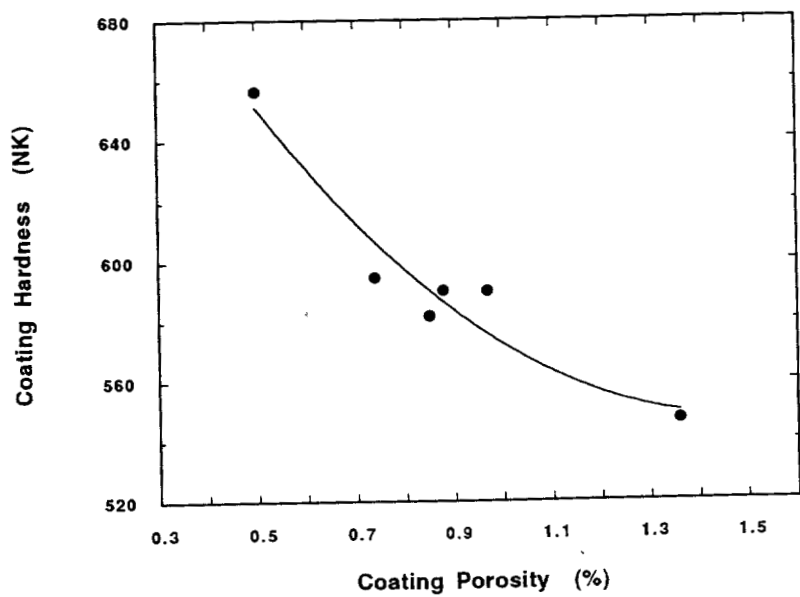
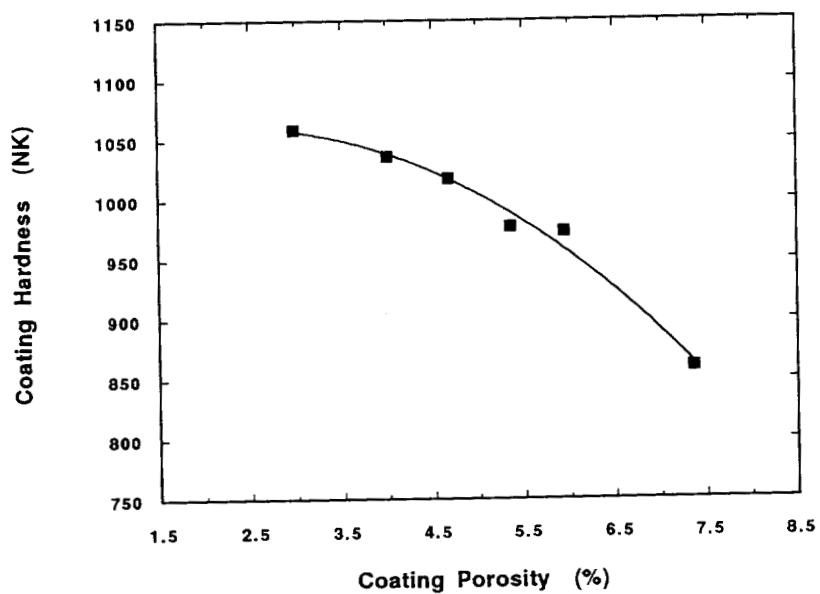


Figure 4.34. Coating surface roughness versus powder size.



(a) Fe-Mo-C coatings.



(b) WC-Co coatings.

Figure 4.35. Hardness versus porosity for Fe-Mo-C (a) and WC-Co coatings (b).

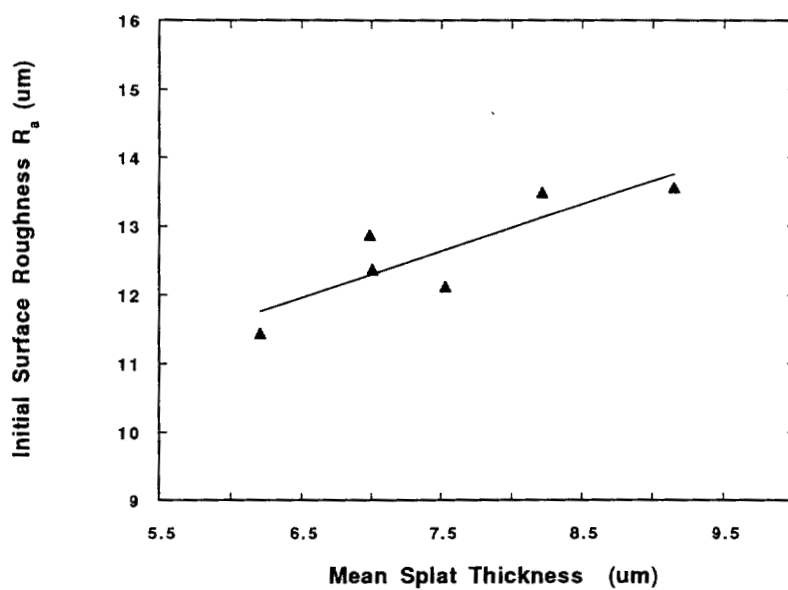
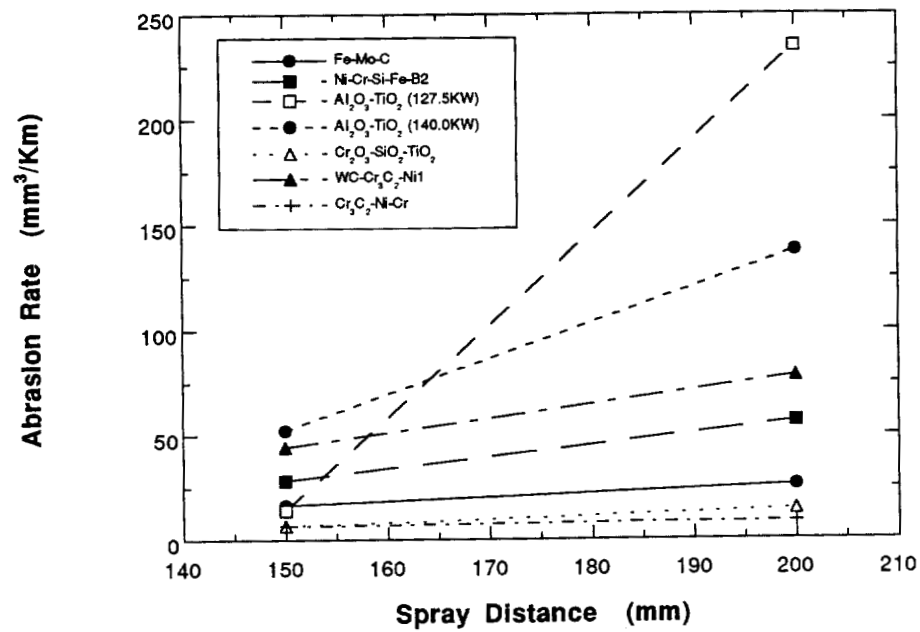
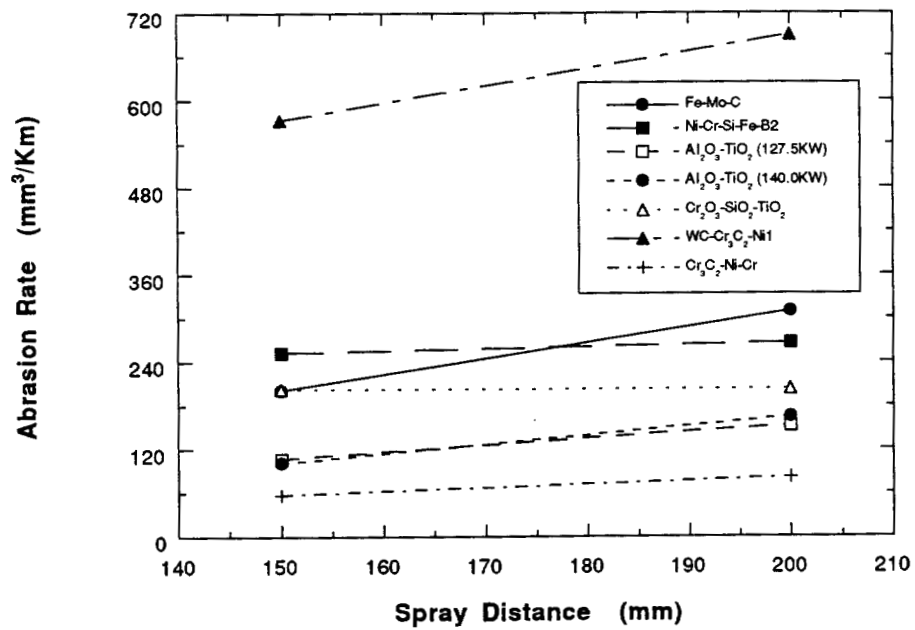


Figure 4.36. Surface roughness versus splat thickness for Fe-Mo-C coatings.

(a) SiO₂.(b) Al₂O₃.Figure 4.37. Abrasion rate versus spray distance (a) SiO₂ and (b) Al₂O₃.

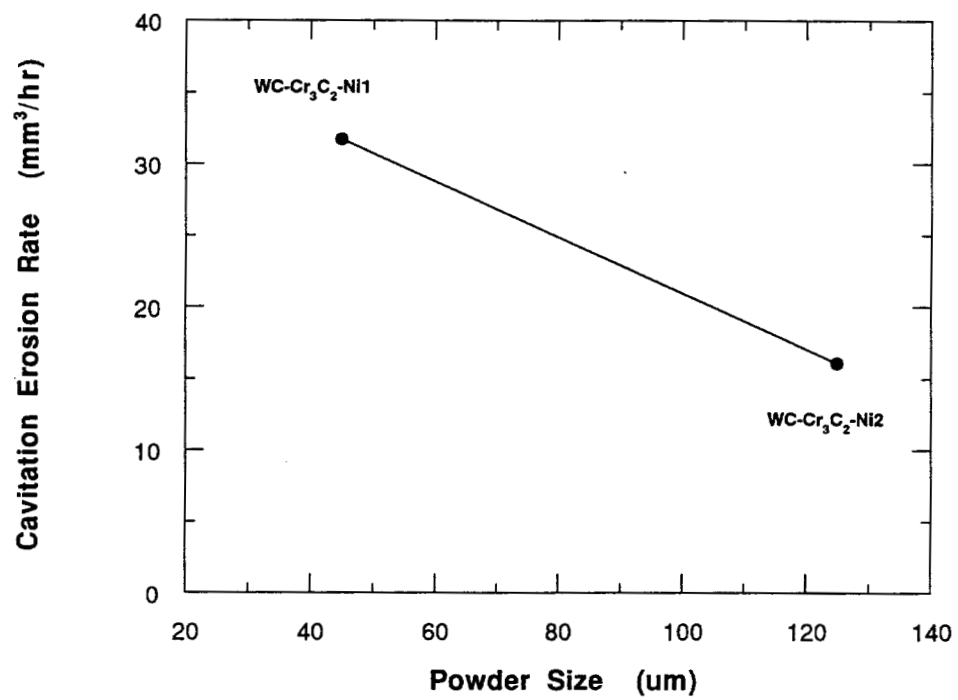
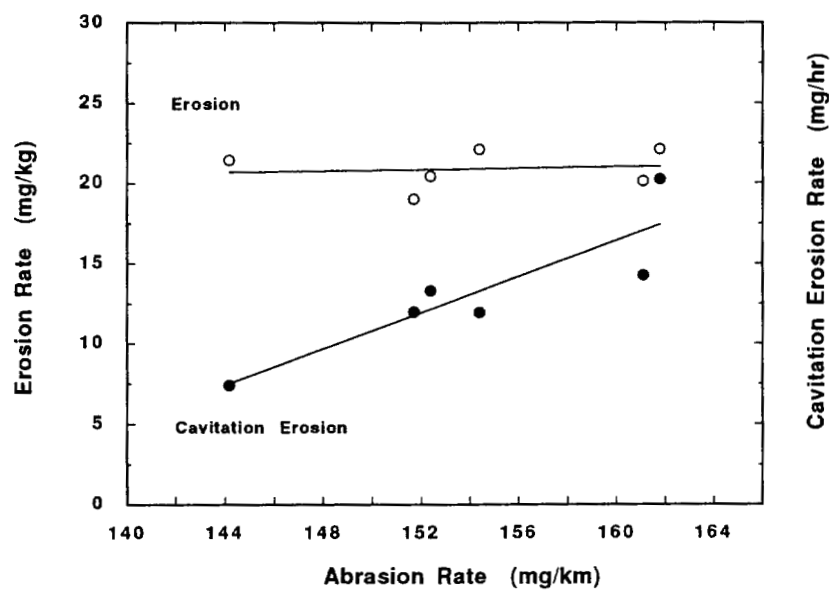
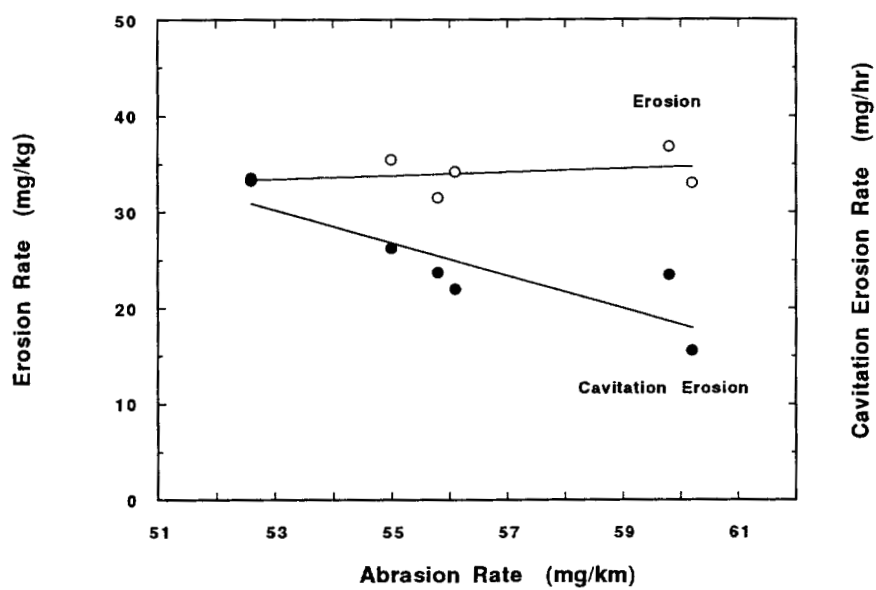


Figure 4.38. Cavitation erosion rate versus powder size.

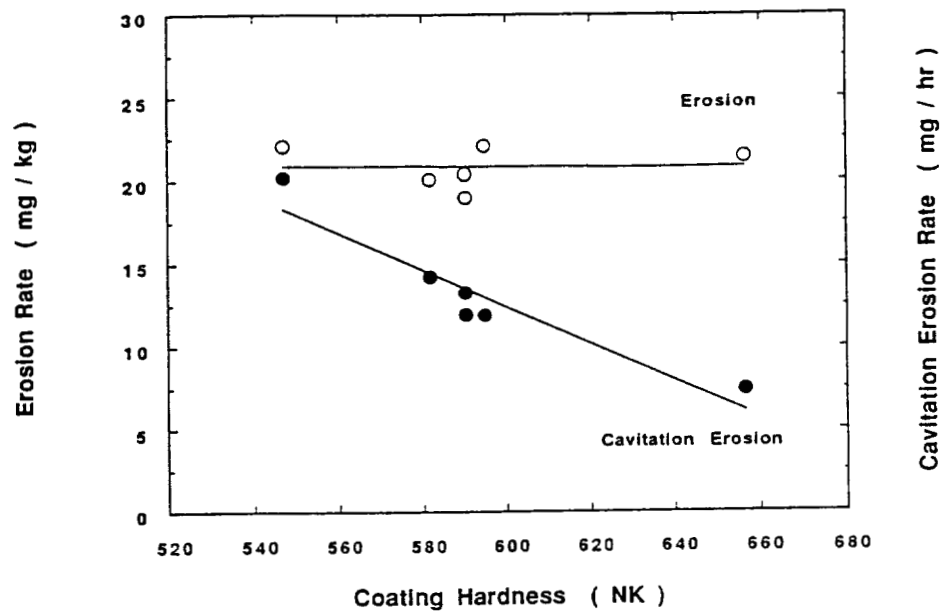


(a) Fe-Mo-C coatings.

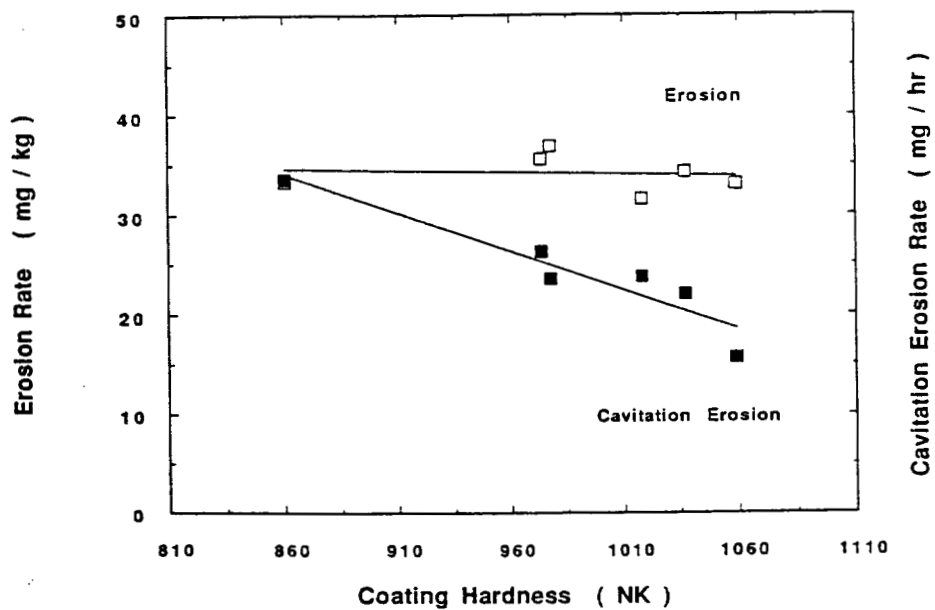


(b) WC-Co coatings.

Figure 4.39. Correlations of abrasion rate with erosion and cavitation erosion rates.

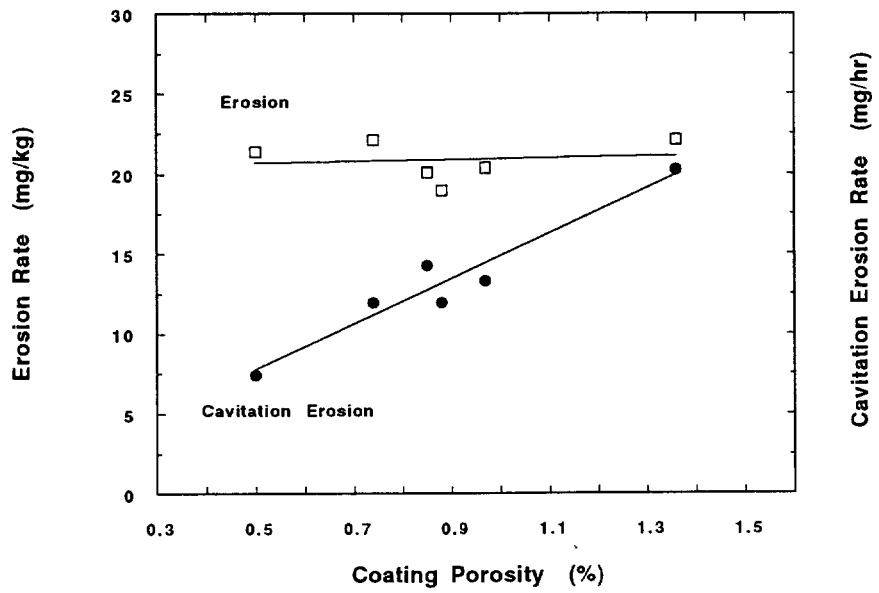


(a) FeMoC coatings

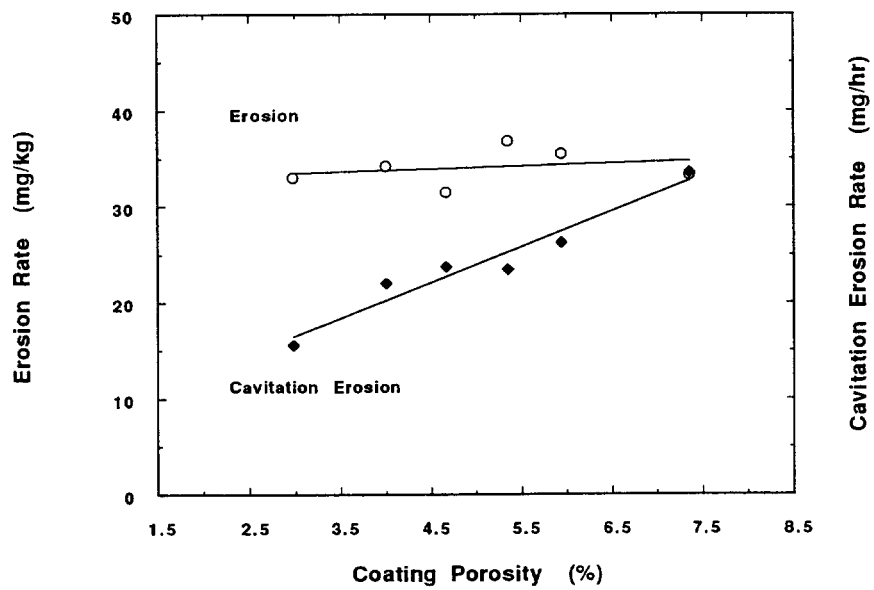


(b) WC-Co Coatings.

Figure 4.40. Erosion and cavitation erosion rates versus coating hardness.

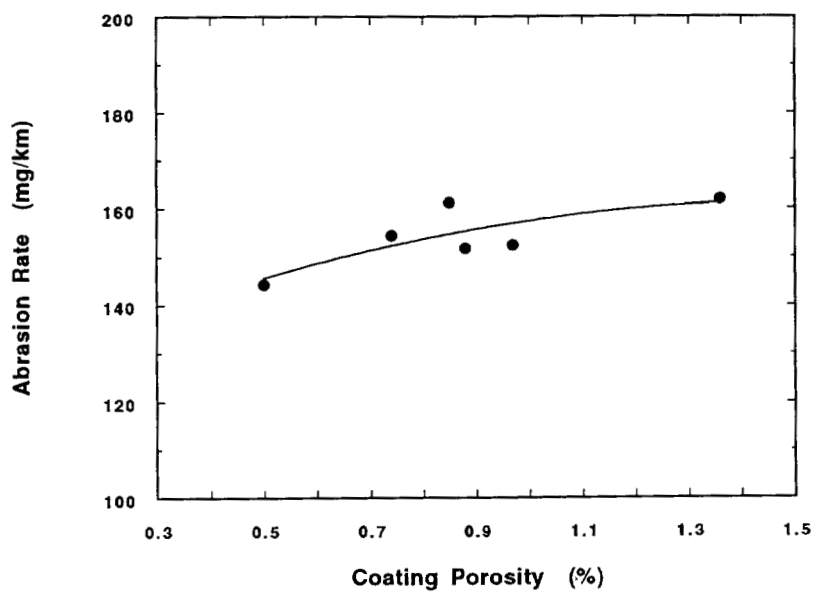


(a) Fe-Mo-C coatings.

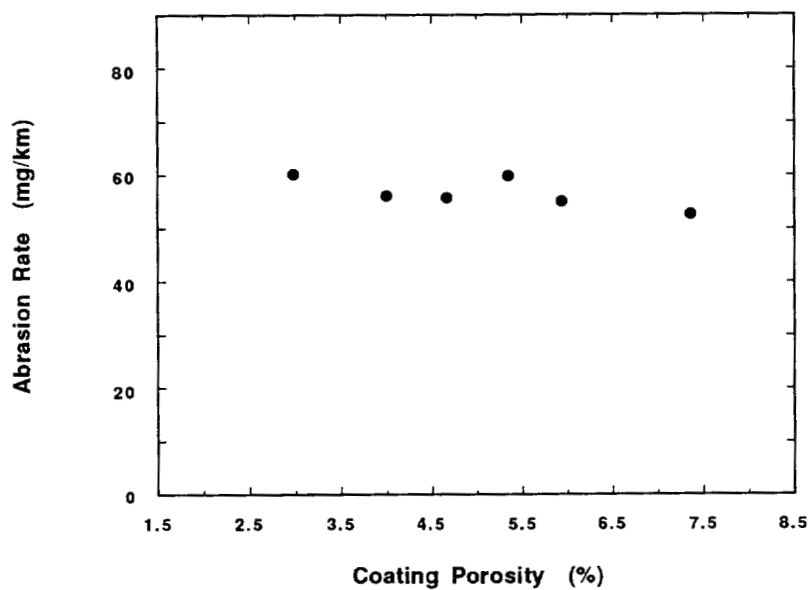


(b) WC-Co coatings.

Figure 4.41. Erosion and cavitation erosion rates versus coating porosity.

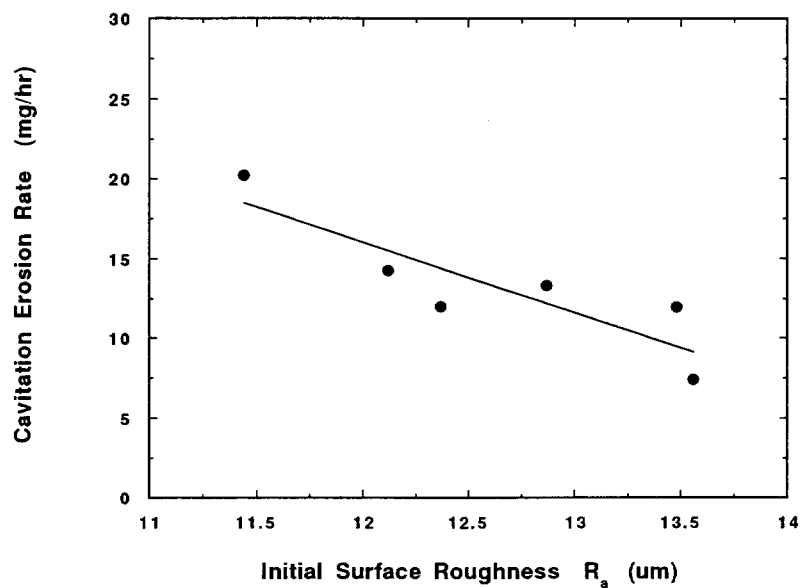


(a) Fe-Mo-C coatings.

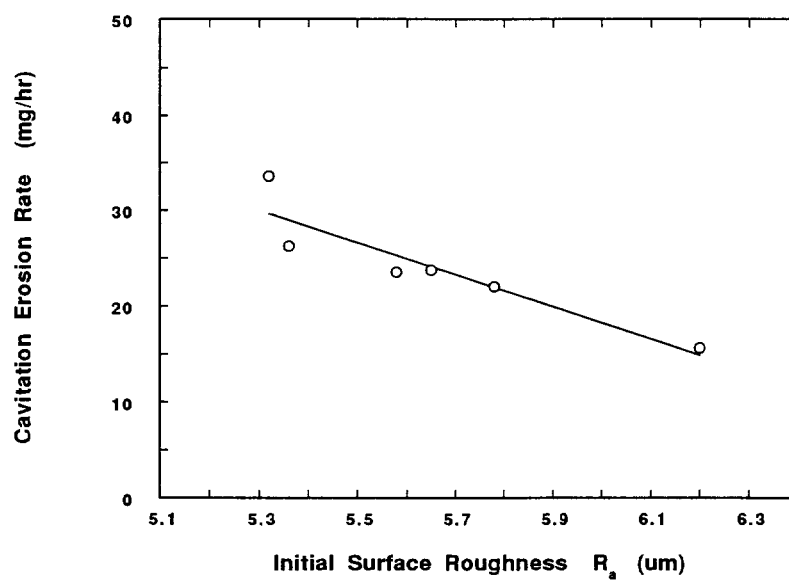


(b) WC-Co coatings.

Figure 4.42. Abrasion rate versus coating porosity.



(a) Fe-Mo-C coatings.



(b) WC-Co coatings.

Figure 4.43. Cavitation erosion rate versus surface roughness.

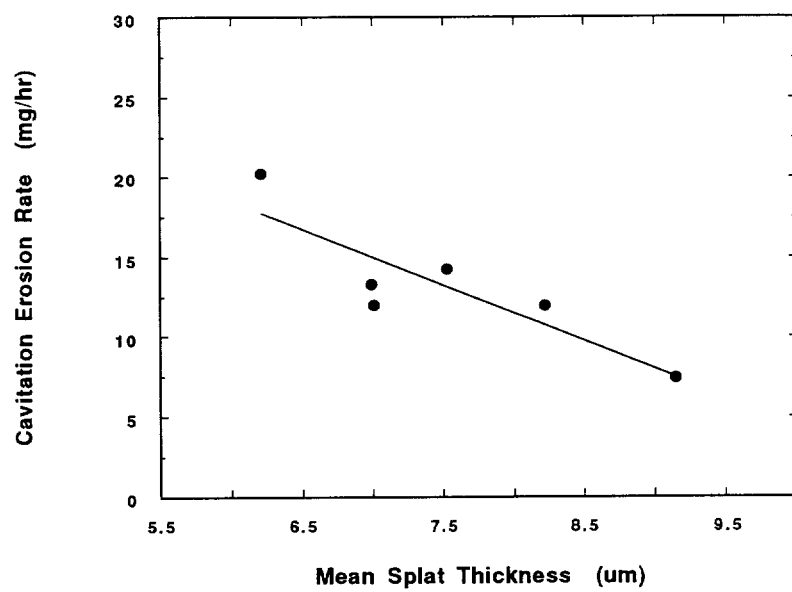


Figure 4.44. Cavitation erosion rate versus splat thickness for Fe-Mo-C coatings.

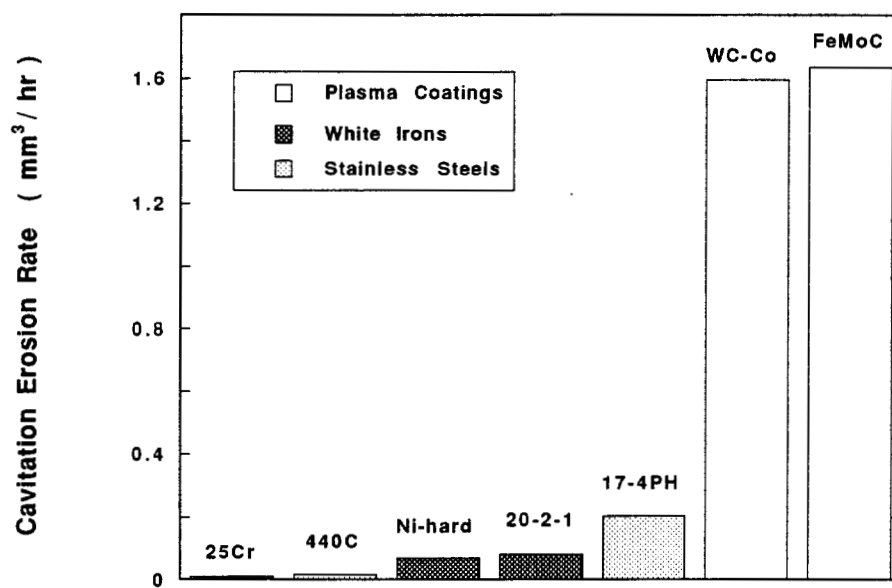


Figure 4.45. Comparison of cavitation erosion rate.

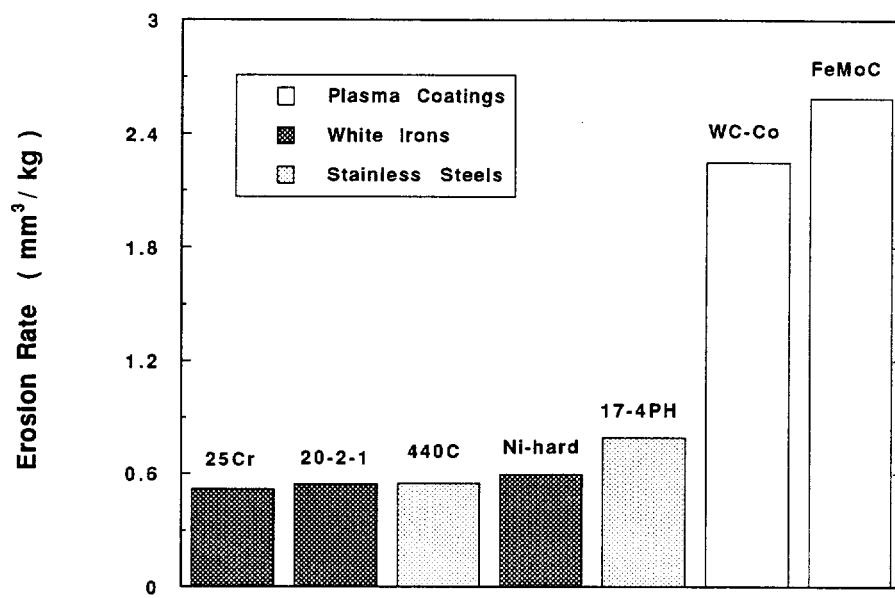


Figure 4.46. Comparison of erosion rate.

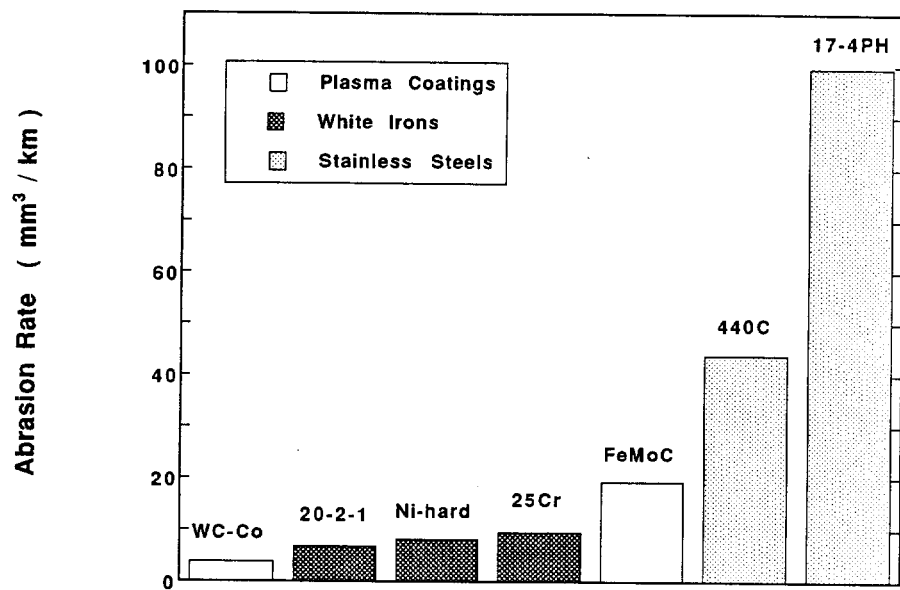
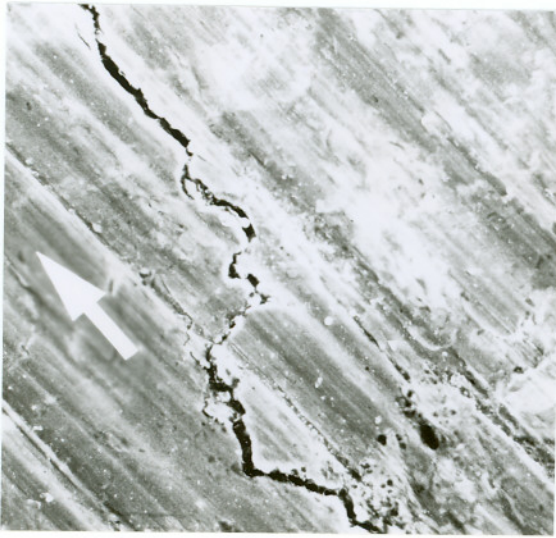
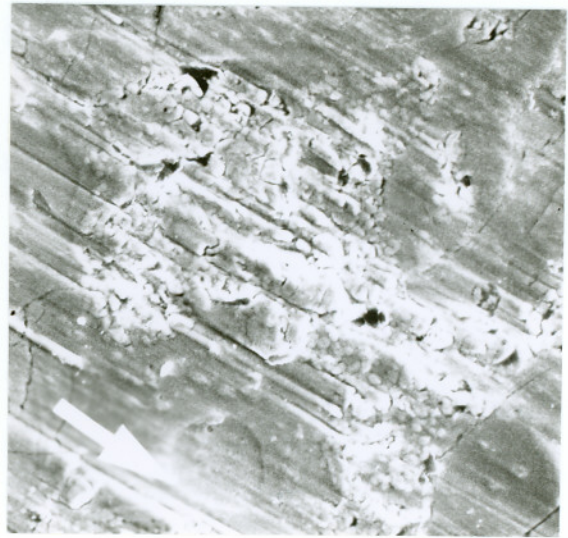


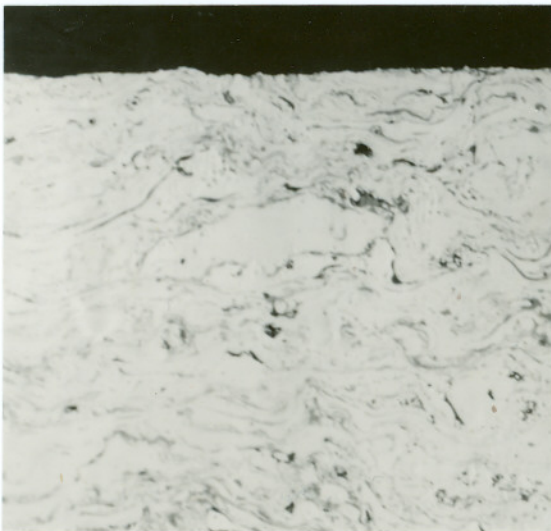
Figure 4.47. Comparison of abrasion rate.



(a) Fe-Mo-C 1000X



(b) WC-Co 2000X

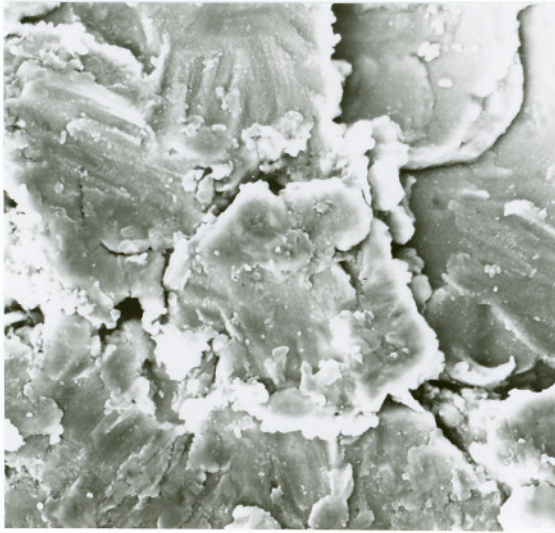


(c) Fe-Mo-C 400X

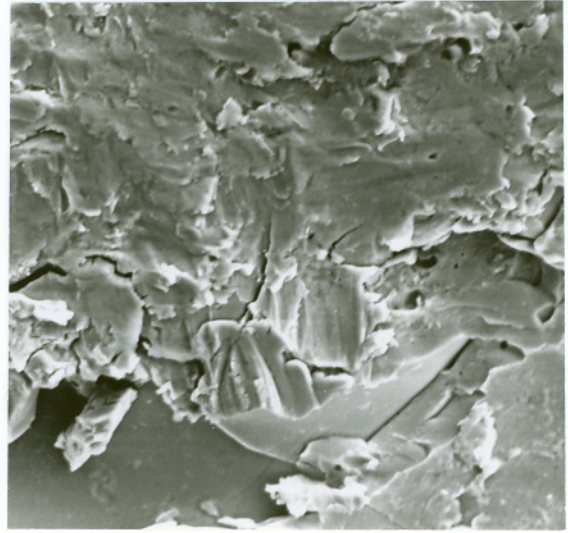


(d) WC-Co 400X

Figure 4.48. Abraded coating surfaces.



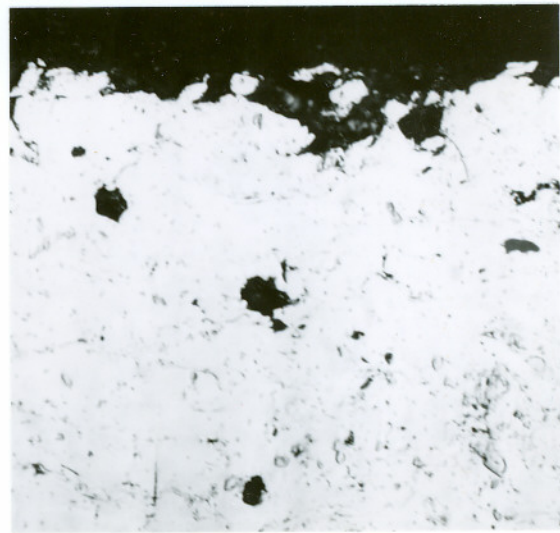
(a) Fe-Mo-C 2000X



(b) WC-Co 2000X

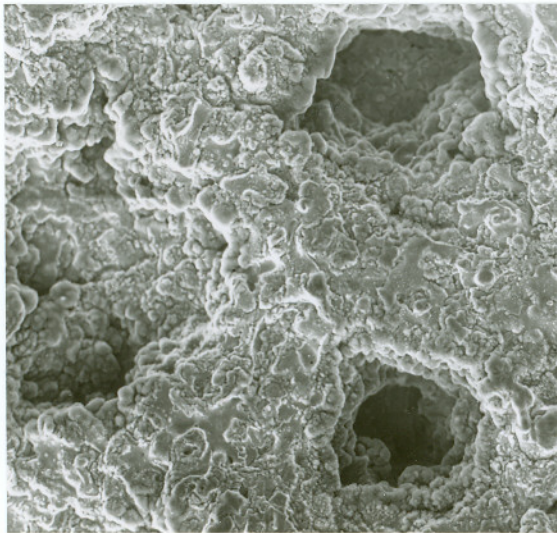


(c) Fe-Mo-C 400X

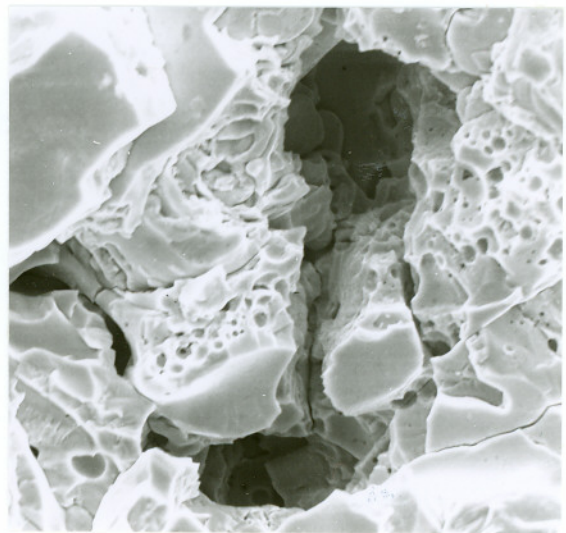


(d) WC-Co 400X

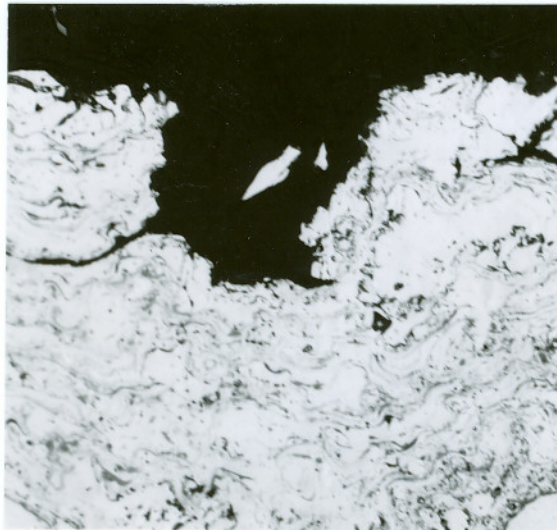
Figure 4.49. Eroded coating surfaces.



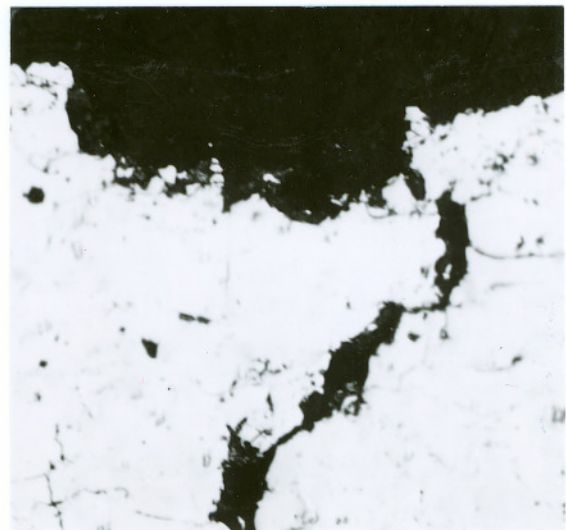
(a) Fe-Mo-C 200X



(b) WC-Co 2000X



(c) Fe-Mo-C 400X



(d) WC-Co 400X

Figure 4.50. Cavitation eroded coating surfaces.

CHAPTER 5. DISCUSSION

5.1. PLATE FAILURE ANALYSIS

Based on the results obtained from the interrupted mill trials, it can be concluded that serration, pitting, and bar rounding were the three major failure modes contributing to plate deterioration. The three modes were in turn governed by various wear mechanisms, playing very different roles in the surface damage of different plate zones or locations. Being influenced by service time, plate alloy, and feed stock, the plate deterioration is a process during which the three forms of damage may interact or overlap, and vary considerably in both extent and distribution. Thus, the plate deterioration is a complex process which must be investigated in terms of many variables such as plate zone, service time, plate alloy, and wood species.

5.1.1. Serration Damage

Origin of Serration. From the surface damage measurements and observations conducted on the used plates removed from the interrupted mill trials, serration damage originated undoubtedly from plate-to-plate contact during refining. This can be demonstrated by both macroscopic and microscopic evidence. On a macroscale, the severe circumferential surface grooving was always present and it was obviously related to direct metal-to-metal contact. Microscopically, many distinct signs of plate clashing have been observed, including material smearing and long parallel microgrooving on the

serrated plate surfaces, plastic deformation in the direction of plate rotation, work hardening, cracking, and spalling in the severely deformed subsurface layers, as well as the presence of "white layer". All these findings are attributable to severe mechanical actions during refining rather than any form of corrosion damage. As a result, the localized corrosion theory proposed by Rideout et al. [110] is unlikely to be applicable for most of the serration problems encountered in TMP refiners. Instead, the plate serration damage can be attributed primarily to nothing but the plate clashing.

Distribution of Serration. Based on the mill trial results, serration damage distributed mainly on the bar tops of the refining zone. It initiated from the plate periphery and extended towards the plate midsection as service continued, but never exceeded the refining zone. Compared to the intermediate bars, the outer part of the fine bars were not only serrated preferentially but also more severely. Such serration damage distribution may be explained by the characteristics of the disk refiner set-up, as schematically shown in Figure 5.1. Because of large centrifugal forces at high rotational speed, the two disks, especially their outer parts, will deflect away and cause unwanted premature pulp escape from the refiner. Thus, at rest the disks are usually mounted as shown in Figure 5.1(a). When at speed, they become more parallel due to substantial centrifugal forces, Figure 5.1(b). The plates are also ground into a specific taper so that they will run flat in the refining zone when the pulp is introduced and a load is applied, Figure 5.1(c). Serration is therefore expected to occur preferentially in the fine bar zone whenever the pulp mat is interrupted, insufficient, or unable to support the applied load.

Formation of Circumferential Grooving. Visual inspection can always reveal deep circumferential grooving on the heavily serrated plates. The formation of the grooves may be schematically illustrated by Figure 5.2. On a microscale the plate surfaces are not perfectly smooth due to the presence of many asperities. During plate clashing, each plate could cut or plough its counterpart's surface by using its own asperities, Figure 5.2(b). Many spalled carbides and entrained sand particles, as well as

the metal chips removed from the plate surface layers, might not move out of the refiner immediately. Instead, they could embed into one plate surface and cut the other, Figure 5.2(c). Many ridges caused by serration had very sharp edges and could also contribute to the circumferential grooving, as shown in Figure 5.2(d). Due to substantial surface work hardening caused by plate clashing, which has been confirmed by the data listed in Table 4.1, these asperities, metal chips and ridges would be expected to be much harder than the bulk plate material, being effective to groove the plate surface along with the sand and carbide particles like small machine tools. Adhesion could also have played a significant role in this process due to many signs of surface material transfer, smearing, and melting.

"Smooth Region" and "Rough Region". As indicated earlier, microscopically the heavily serration damaged plate surface can be divided into two types of regions, a "smooth region" and a "rough region", based on whether most eutectic carbides were flush with the matrix, as depicted in Figure 5.3. In the "smooth regions", Figure 5.3(a), the serrated surface was basically smooth and flat, especially when viewed from the cross-sections parallel to the plate moving direction. A number of long parallel microgrooves were visible, but few short grooves and scratches with various orientations in the matrix can be found. Severe surface deformation, cracking, and spalling were also present. The carbides were cut, deformed, or fractured along with the matrix, but never protruded above the matrix and edge rounded. Conversely, from Figure 5.3(b), in the "rough regions" the long parallel microgrooves were generally absent while numerous dents and short disorderly scratches occurred in the matrix. The serrated surface appeared to be relatively rough as most carbides were able to stand well above the preferentially scratched matrix. These protruded carbides could be edge rounded but seldom grooved. Carbide deformation and fracturing would occur, but their degrees were much smaller than in the "smooth regions". No substantial surface deformation and cracking were found in the "rough regions".

The formation of the two different regions may be described schematically by Figure 5.4. During plate clashing, as the "machine tools" on one plate were under high stress and were hard enough to effectively attack both matrix and carbides on its counterpart, the resulting serrated surfaces tended to be microscopically "smooth" and the carbides, which were fractured and deformed, would be flush with the matrix. After the clashing, the two disks were separated again by a sufficiently thick pulp mat so that the long parallel microgrooves in the "smooth regions" were abraded or eroded and finally removed. As the short scratches in the matrix varied in orientations, the abrasive particles must be loose, resulting in abrasion and/or erosion instead of sliding wear. Being under relatively lower stress due to the presence of a thick pulp mat, the abrasives would not easily cut the carbides like the "machine tools" in the "smooth regions". Instead, they preferentially scratched the matrix material, letting the carbide edges rounded and well protruding above the matrix but seldom fractured and deformed. Thus, the serrated plate surface became microscopically "rough".

Once another round of plate clashing occurs, the "rough" region could be changed back to a "smooth" one again, and new microgrooves were produced. In a given serrated area, the two types of regions might alternate many times until the bar height loss became substantial. As a heavily serrated plate might not have a perfectly flat surface, the two types of regions could coexist in different places at a given time. A "smooth" region indicates that the plate clashing occurred recently while a "rough" one means that the plate-to-plate contact had not occurred for some long time. During the early stages of refining, many machining grooves were still visible in the non-serrated regions, while in the late plate life these grooves were removed and the non-serrated regions became very similar to the "rough regions" in surface features. It can be inferred that the "smooth regions" and the "rough regions" were induced under clashed operation conditions and normal operation conditions, respectively. Here the "normal condition" does not necessarily mean the absence of bar rounding and pitting damage, and it only excludes the presence of direct plate-to-plate contact. Thus, it seems that the

"smooth regions" were the result of sliding wear at high speeds and loads causing thermal effect, while the "rough regions" were caused by abrasion and/or erosion.

Serration Mechanisms. From the preceding analysis, the serration process may be briefly described as follows. When plate clashing occurred, due to very high stress and rotational speed many surface asperities could be severely deformed, welded together, and then fractured, causing heavy adhesion between the two contacting metallic surfaces. Simple asperity adhesion occurred very early in the serration process. Once debris was generated from the microscopic asperity or junction fractures, abrasion could take over as the prevailing wear mode. Many asperities, fractured junctions, spalled carbides, and entrained sand particles would produce severe abrasion damage. As most microgrooves were oriented unidirectionally and no dents or random scratches were found, the abrasives were basically embedded on one plate surface and caused two-body self abrasion. Owing to continuous cutting or plowing actions, many ridges with sharp edges were formed and they could well be work hardened, joining other abrasives to "machine" the plate surfaces and expedite the serration process. When normal refining operations resumed, the serrated areas would be abraded and/or eroded, with abrasives loose causing randomly oriented short grooves. Due to a thick pulp mat, the stress applied on the abrasives was much lower than during plate clashing, and the corresponding plate damage was also greatly reduced. Thus, the serration damage was caused mainly by sliding wear or a combination of adhesion and two-body abrasion during plate clashing. The three-body abrasion and/or erosion during normal refining operations helped to extend the serrated zone towards the plate midsection by reducing the bar height, while they played only minor roles in the serration process.

Service Time Effect. As shown in Table 4.3, the serration damage for the C20 alloy plates worked with white wood increased rapidly with service time. This is understandable because plate clashing could occur frequently during service, while due to high rotational speed and working load even a transient plate-plate contact might cause

heavy serration damage. Thus, plate serration increased with service time and was by no means an uncommon damage mode as it occurred in all plates removed from the mill trials, even the plates after 15% service life. Although the serration damage increased with service time, the serration rate was generally decreased. From Table 4.3, about 60% of the total serration damage occurred during the first half of the plate life while more than 90% of the damage had formed after 75% of working life, which was in consistent with the fact that the serration is most severe during start-up of an installation [10]. The reduced serration rate could be ascribed primarily to less chances for plate clashing late in the plate life due to substantial bar height loss in the serrated zone. Thus, an appropriate plate taper seems critical for serration damage reduction.

Plate Alloy Effect. After 100% working life, the C20 (20-2-1) plates experienced much more serration damage than the S17 (440C) ones when using the same wood stock, which is not only demonstrated by the serrated zone width data listed in Table 4.3, but also noticeable by visual inspection of the serrated plates, with the C20 plates exhibiting much deeper circumferential grooving. As both types of plates were basically the same in working condition and configuration, only plate material accounted for the difference in serration damage degree. From Table 4.1, the S17 steel could be deformed more easily than the C20 iron. For the C20 plates, therefore, less plastic deformation would occur on the asperities, metal chips, or the sharp ridges which served as the "machine tools". As a result, these protuberances could retain their original sharp edges to cause sliding wear. On the contrary, for the S17 plates these protuberances might be well deformed and lose their sharpness during clashing, producing much less circumferential grooving. Eutectic carbides in these alloys might also be responsible for the difference in serration damage degree. Compared to S17 steel, the C20 white iron contained eutectic carbides of larger size, higher hardness, and greater volume fraction, thereby leading to more sliding wear during plate clashing.

Wood Species Effect. The serration damage was also found to be affected by wood species. The wood stock could not play a major role in the circumferential grooving during plate-to-plate contact, but it might help to extend the serrated zone by expediting the bar height loss during normal refining operations. The sooner the bars lose their height the sooner the serrated zone extended. The serrated zone width for the C20 plates associated with Douglas fir is found to be greater than that with whitewood (Table 4.3), and macroscopic examination also indicated that the plates worked with Douglas fir suffered a more severe bar height loss in the refining zone. Therefore, a faster extension of serrated zone, or a heavier serration damage, can be confirmed for the plates worked with Douglas fir. The reason why Douglas fir caused more damage during the normal operations is still unknown, but it may be related to the wood density. Wood species, no matter how dense they are, can seldom cut or groove a metallic surface directly. Due to the higher wood density, however, the Douglas fir fibers were more difficult to deform than the whitewood fibers when loaded, and they could transfer more load to the abrasives held against a plate surface, thereby causing more wear loss, Figure 5.5. It is hypothesized that this caused the C20 plates worked with Douglas fir to exhibit more serration damage than with the whitewood.

5.1.2. Pitting Damage

Distribution of Pitting. According to the mill trial results listed in Tables 4.4 and 4.5, pitting damage occurred in both the refining zone and the breaker bar zone. It was, however, most severe along the bar leading edges, although the bar tops near the leading edges were also attacked. During refining, the bar leading edges usually experience much higher working loads than other areas on the plate surface such as the grooves and the bar trailing edges. As a result, the preferential pitting damage near the bar leading edges was clearly attributable primarily to some type of mechanical action rather than corrosion. The bulk bar tops, although also bore a very high working load, were basically free from serious pitting probably because serration, a more severe plate

damage mode, dominated the bar top surface deterioration. The distribution of pitting damage was also dependent on the service time. For the C20 plates worked with whitewood, from Table 4.4, after 15% plate life no appreciable damage occurred, while over 80% of the total pitting damage was produced in the final quarter of the service life. In contrast to the serration problem discussed above, therefore, the pitting damage occurred usually late in the plate life.

Formation of Cyclic Stress. As pitting damage occurred late in the plate life, it might have involved a rather long incubation time during which the bar leading edges were repeatedly deformed and work hardened by cyclic stress. Such a stress could be induced via a local fluid pressure pulse and/or steam pressure pulse generated during bar crossings. Figure 5.6 shows schematically the local pressure pulse near a moving bar leading edge as a function of the relative position of this bar to the plate bars on another disk. The local pressure would increase as two bars got closer but decrease when they separated again, attaining its minimum when this bar's trailing edge met another bar's leading edge and maximum when the leading edges of two bars met together. For the refiner system shown in Figures 2.5 and 2.7, the total number of fine bars on each disk was 768 (12 plates with each having 64 fine bars). If each disk rotated at 1500 rpm, the relative rotational speed would be 3000 rpm. Thus, every minute the stress cycles imposed on each bar could be more than 2.3×10^6 . If one microcrack was initiated per minute by fatigue or another mechanism, in a given location up to 6×10^4 cracks might be produced after 1000 hour service, sufficient to cause severe pitting damage. As the plate surface examination did reveal many small cracks in the heavily pitted areas, the pitting could be a fatigue initiated damage process.

Pulp Effect. Without pulp or a fluid medium, the bar crossings would generate no pressure wave in the refiner nor cyclic stress on the bar leading edges. Therefore, the stress cycles could only be imposed on the plate bars via some type of medium, either wood stock, liquid, or steam available in the refiner. The wood fibers, although

usually plenty in amount in the refiner during refining, were unlikely to play the major role in producing the stress cycles and damaging the bar leading edges, especially when the leading edges had been well destroyed. This can be justified from two aspects. First, if the pressure pulses generated during bar crossings were imposed to the plate bars mainly through wood fibers, many abrasive particles could also be held against the bar leading edges by wood stock to cause abrasion and/or erosion damage. In fact, dents, grooves, and scratches were not observed in the severely pitted areas. Second, if pitting damage was induced mainly by imposing the pressure wave via wood stock, the honey-combed pitting appearance and the high pit depth/diameter ratio can not be explained. This is because the wood stock under very high stress would easily crush all thin peaks in the heavily pitted regions but hardly enter any tiny pits to further deepen them. Thus, the effect of wood particles on plate pitting, although it can not be ruled out, seems to be very minor, especially when the leading edges had crumbled away.

Water Effect. As the wood stock would contribute little to the pitting process, the liquid in the refiner was a major candidate to induce plate pitting by causing cyclic stresses on the plate bars. In the breaker bar zone, liquid was undoubtedly available because large amounts of feed water were introduced through the refiner inlet to adjust the pulp consistency, which is defined as the weight percentage of pulp in a pulp and water mixture. The refining zone, however, is generally thought to contain only steam and wood pulp. As the disks rotate very fast under high working load, a large amount of heat is generated by the severe mechanical actions from disks, raising the temperature inside the refiner up to 140° C so that all dilution water will be vaporized in the refining zone. This assumption may not be true. First, as the disks rotate rapidly, the water may stay in the refining zone for less than half a second, having no enough time to fully evaporate into steam before moving out of the refiner along with pulp. Also, condensation of steam within the refiner is a possible source of water [20]. More importantly, as any pulp has a certain consistency or, in other words, contains some liquid water, it is true that the water in the pulp will be squeezed out when compressed

by the refiner bars [10]. Despite severe water evaporation, therefore, a certain amount of water may still be available in the form of liquid jets or drops in the refining zone to cause pitting damage.

Cavitation Erosion and Liquid Impingement Erosion. As water is thought to have played an important role in producing the cyclic stress on the bar leading edges to cause pitting, cavitation erosion and liquid impingement erosion must be considered since they are the only common wear modes induced by liquid. Thus, the pressure wave inside the refiner generated by bar crossings could be changed into cyclic stress and imposed on the bar leading edges by water through either bubble collapse or liquid impact, causing cavitation erosion and liquid impingement erosion, respectively. Such an assumption can be convincingly demonstrated by at least three pieces of evidence. First, the heavily pitted plates and the laboratory cavitation eroded specimens were very similar in surface features. That is, on a macroscale the damaged surfaces always exhibited a honey-combed appearance, while microscopically many tiny pits with very high depth/diameter ratios were present. Second, for different plate alloys the performance rankings for pitting damage and for cavitation erosion were similar (Figure 5.7). Third, both types of erosion have been widely defined as fatigue-initiated failure processes. In the severely pitted areas many fatiguelike cracks were observed (Figures 4.16a and d). As the two types of erosion are considered sufficiently similar processes and can produce undifferentiated worn surfaces, either or both of them were able to result in the plate pitting damage.

Pitting Corrosion. Beaudry [111] has related the plate wear to pitting corrosion, and reported a severe pitting corrosion damage for Ni-hard plates at pH's below 4.5. Laliberte [113] also claimed that pitting corrosion could occur on stainless steel plates, particularly in mills with high concentration of chloride. Similarly, from Jones [109], the stainless alloys containing chromium and nickel are most likely to be pitting corroded, especially in neutral-to-acid solutions with chloride. As the typical wet

refining environment is acidic [9,21,37], the effect of pitting corrosion on plate pitting may not be ruled out in most cases. With mechanical actions such as cavitation erosion going on, it seems that pitting corrosion could only play a minor role in the plate pitting process. Thompson [21], however, has reduced the laboratory cavitation erosion rate of plate alloys by up to 100 times through changing the solution from mild acid (pH 4.5) to neutral (pH 7). Hence, pitting corrosion may strongly accelerate the plate pitting process, especially when the wet environment's pH is close to 4.5. For the current interrupted mill trials, however, pitting corrosion has not been proved to be present because the wet refining environment was not monitored during trials, and based on the used plates it is difficult to differentiate pitting corrosion from plate pitting as both can produce many deep cavities and result in a honey-combed appearance.

Breaker Bar Zone Pitting. The breaker bar zone pitting can be attributed primarily to cavitation erosion because large amounts of water was introduced from the refiner inlet. When two breaker bars move apart, the local liquid pressure near the bar trailing edges could be greatly reduced comparing with the bulk water pressure, as shown in Figure 5.8. Once the local pressure of the liquid was below its vapor pressure, many bubbles would be generated. As the next two bars draw closer, the local liquid pressure in this region would increase drastically, resulting in bubble collapse near the bar leading edges. Thus, the bubbles usually formed near the bar trailing edges but collapsed along the bar leading edges due to repeated local liquid pressure fluctuations. As homogeneous bubble formation inside the liquid needs a higher nucleation energy to overcome the bubble's surface energy, the bubbles usually form heterogeneously on some existing nucleation sites such as wood fibers or bar surfaces. Although liquid impingement erosion has also been related to the breaker bar zone pitting [14,16,21], it would not play a significant damaging role in the breaker bar zone where the plate tangential velocity is well below 100 m/s which is usually not enough to cause any severe liquid impingement damage. It was therefore cavitation erosion that accounted mainly for the breaker bar zone pitting.

Refining Zone Pitting. Unlike the breaker bar pitting, there is no general agreement on the cause of the refining zone pitting [21]. Although some researchers [14,18,20] have correlated it with both cavitation erosion and liquid impingement erosion, their assumptions may be strongly challenged, because in general only pulp and steam are believed present in the refining zone owing to severe water evaporation.

As analyzed earlier, however, despite the evaporation a certain amount of water might still be available in the refining zone in the form of liquid jets or drops. The water could be squeezed out from the pulp, condensed from the steam, or even directly transferred from the breaker bar zone. Due to severe mechanical actions during refining, the temperature inside a refiner could be as high as 140 °C. The surface temperature of the refiner plates would be even higher because of the repeated metal-to-metal contacts during plate clashing. As schematically shown in Figure 5.9, if water were present on the plate surface, it would be always flashing to steam due to the refiner operating temperature, generating many bubbles due to water evaporation in the refining zone. On encountering pulp or liquid impact during bar crossings, these bubbles would be under high pressure and then collapse, leading to cavitation damage.

On the other hand, for a refiner shown in Figure 2.5, if each disk rotated at 1500 rpm and was 1.32 m in diameter, a water drop moving with one disk near the plate periphery could impact the plate bars on another disk with a tangential velocity over 200 m/sec, causing liquid impact damage. This hypothesis may be strongly challenged since such a velocity seems not enough to cause severe liquid impingement erosion, and more importantly, the disk gap during refining is usually around 0.5 mm which would limit the water drop size and produce no liquid impact damage. As indicated by Brunton et al. [106], however, at moderate velocities such as in the region of 200 m/s, a single drop may produce no visible damage while a large number of repeated impacts will cause erosion of the solid. If each plate had 64 fine bars and all bars were covered with some water, a given fine bar could be liquid impacted up to 38400 times per minute which

should be large enough to cause some damage. Also, from Field et al. [107], if a drop is oscillating it is the largest radius of curvature that a drop can reach at the impact surface, rather than the drop size, that determines the damage degree. Thus, although the plate gap was less than 1 mm, the actual drop radius of curvature could be much larger (Figure 5.10). As a result, the refining zone pitting may also be affected by liquid impingement erosion. Moreover, stress corrosion might also have contributed to the pitting damage process due to the stresses in plates resulted from residual stress and/or high speed rotation.

According to the mill trial results, the pitted surfaces in all plate zones were difficult to differentiate both visually and microscopically. A honey-combed appearance could always be seen on a macroscale. Microscopically, a number of deep pits formed preferentially in the eutectic areas, especially near the carbide/matrix interfaces, with many fatiguelike cracks being present near the pit bottoms. In addition, the pitting performance rankings for the 440C steel and the 20-2-1 alloy in three plate zones were also similar (Figure 5.11). All these similarities may imply that the pitting throughout the plate surface could have a common deterioration mechanism or be acted upon by similar stress cycles. Thus, based on the nature of TMP refining and the mill trial results, the possibility of cavitation erosion and liquid impingement erosion in refining zone may not be ruled out. However, more experimental work still needs to be done to confirm the presence of cavitation erosion and/or liquid impingement erosion, to detect other possible mechanisms such as pitting corrosion and stress corrosion, and to determine the major damaging mechanism in the refining zone pitting process.

Preferential Pitting in the Eutectic Areas. From the mill trial results, the pitting damage in all plate zones always initiated at the matrix/eutectic carbide interfaces. In other words, the eutectic areas were always preferentially damaged. These surface features were very similar to those of cavitation eroded specimens. Such a phenomenon is still not well understood, but it might be related to the chromium depletion and

preferential work hardening in the matrix near the eutectic carbides. Due to carbide formation, the matrix near the carbides could be heavily sensitized, or chromium-depleted. As the wet environment in TMP refining is usually acidic, the plate pitting would be accelerated in the sensitized areas owing to their reduced corrosion resistance. On the other hand, pitting damage could be related to a cyclic stress induced by bar crossings. In general, however, little impact energy imposed on the carbides can be absorbed to cause deformation. Most of the energy, instead, was directly transferred to the nearby matrix. Thus, the matrix in the eutectic zones would absorb more impact energy and be more liable to be work hardened than in the bulk dendritic areas, leading to easier fatigue crack generation and development. Although these hypotheses need to be tested by further studies, we may conclude that reducing chromium depletion and carbide/matrix interface area would be beneficial to plate pitting resistance.

Plate Alloy Effect. After 100% life the S17 (440C) plates experienced much less pitting damage than the C20 (20-2-1) ones, Table 4.5. The reason for this trend is still unclear, but four factors might account for it. As shown by Figures 4.2 and 4.6, the S17 stainless steel was much smaller in average carbide size and carbide volume fraction than the C20 white iron, so the matrix near the eutectic carbides would tend to be less severely chromium depleted, thereby leading to reduced preferential pitting damage in the chromium depleted zones. Secondly, although both alloys had similar chromium contents, the C20 iron should have lower average chromium level in the matrix than the S17 steel as its higher carbide volume fraction would cause more chromium depletion in the matrix. Third, owing to its higher capability of deformation which can be shown in Table 4.1, the matrix of S17 steel was able to absorb more impact energy from bubble collapse and/or liquid impact before being work hardened, leading to slower fatigue crack initiation and propagation. Finally, as the S17 alloy had smaller carbide size and volume fraction, its matrix in the eutectic zones or the chromium depleted zones would be fatigue damaged more slowly due to less impact energy transferred from nearby eutectic carbides. Although these hypotheses need more experimental work to further confirm,

it may be safe to say that 440C stainless steel will have much better pitting resistance than a 20-2-1 alloy.

Service Time Effect. Based on the interrupted mill trial results, pitting damage on the refiner plates depended heavily on service time. As revealed by Table 4.5, like the serration damage, the plate pitting increased with service time for the C20 plates worked with white wood. Unlike the serration rate, however, the pitting damage rate increased, instead of decreased, as refining proceeded. After 15% working life, there was no any appreciable pitting damage in any of the three plate zones, while over 70% of the total pitting damage accumulated in the final quarter of the plate life. This means that pitting damage usually occurred late in the plate life, or in other words the pitting process had involved a rather long incubation period. Therefore, it implies that the plate pitting is induced primarily by a cyclic stress and is basically a fatigue-initiated failure process. In addition, it can be inferred from the mill trial results that pitting damage may not seriously influence the TMP refining actions during the first half of the plate life. In the second half or especially in the final quarter of the service life, however, much more attention must be paid to plate pitting, because it has been indicated that heavy pitting in the refining zone can cause poor pulp quality [21].

5.1.3. Bar Rounding

Surface Features. The surface features of the rounded bar leading edges were very similar to those of the "rough regions" on the serrated bar tops. That is, no severe surface deformation and cracking were found. The eutectic carbides were standing above the matrix and edge rounded, and the matrix was covered with numerous dents, grooves and scratches with various orientations. Thus, the failure mechanisms in these two types of areas seem to be similar. However, there were still some differences in the surface features. The degrees of both the protrusion and edge rounding of the carbides were greater than those in the "rough regions" of the serrated surfaces. Also, in the "rough

regions" the carbides were severely fractured and spalled, while along the rounded bar leading edges little carbide cracking and spalling could be observed. All these may be due to the different working conditions in the two types of areas. Unlike the bar tops, the bar leading edges would generally experience little plate clashing during refining. As a result, the carbides in the bar rounding damaged areas would seldom be fractured and spalled off although they were more protruding above the matrix than those in the "rough regions" of the serrated areas. Due to the dents, grooves and scratches in varied orientations, therefore, the bar rounding damage could be attributed mainly to abrasion and/or erosion.

Silica Particles. To cause abrasion and/or erosion, a certain amount of abrasive must be available in the refiner. Many authors have proposed that silica sand (SiO_2) or grit entrained in the wood chips plays a major role in bar rounding damage of refiner plates [12,19-20,37,111], but the evidence available can not satisfactorily support this assumption. The extensive bar rounding damage could be produced if there was a sufficient amount of abrasive in the wood stock, while in fact after water cleaning there is little debris left in the wood chips. The silica sand, if really present, would only make up an extremely small percentage of the refining stock and could not play a leading role in the extensive bar rounding. Additionally, from Table 5.1, the silica is comparable with the $(\text{Fe,Cr})_7\text{C}_3$ in Vicker hardness. Thus, the silica would usually be able to cut both matrix and M_7C_3 carbide, which has been confirmed by the DSRW abrasion results (Figure 4.22). In the bar rounding damaged areas, however, only matrix grooving was observed while the carbides were basically free from any scratches and grooves. Moreover, if the bar rounding damage did result mainly from the silica particles, the absence of bar leading edge matrix grooving in the early stages of plate life can not be explained, since the hard abrasive content in the wood stock should be constant during the entire refining process. It is therefore reasonable to infer that the matrix grooving and bar rounding was caused primarily by something other than the entrained silica particles or other hard abrasives.

Metal Debris. During refining, it has been hypothesized that metal debris could be produced by serration and pitting from the plate bars and mixed into the pulp. The broken carbides (Figures 4.5c-d), cracked surface layers (Figures 4.6c-d), and unsupported dendrites (Figure 4.14d) were all potential metal debris, while the pits shown in Figures 4.11c and 4.12c indicate that metal chips had been produced. As the metal debris might well outnumber the entrained sand particles, they could make up the major part of the abrasives causing bar rounding. For a double disk refiner with each disk rotating at 1500 rpm and if the pulp residence time is one half second, a single metal chip could damage each plate bar up to 25 times. Due to the presence of a pulp mat, the metal chips would not be under very high stress when potentially damaging the bars. The debris would be in general softer than the carbides and would not directly cut them, but could damage the protruded carbides, especially the carbide edges, through a microfracturing process, leading to carbide edge rounding. Also, these debris could be harder than the bulk matrix due to severe plastic deformation and work-hardening and would preferentially groove the matrix. When refining begins, the plates are not heavily serrated or pitted such that very few metal debris were available in the refiner to cause bar rounding. As service continued, more and more debris were produced and might expedite the bar rounding process. While a plausible hypothesis, there is little direct evidence of such behavior, much like the presence of silica in the wood chips and pulp. Thus, more research work needs to be done to experimentally confirm it.

Wood Species. Although it has been reported that uncontaminated paper fibers cause little wear when sliding or rubbing against steel [57], wood stock must contribute to the bar rounding damage process to some extent. Direct evidence of "abrasion" of metals by wood materials is lacking and the literature is also quite lean on the entire topic of wear by soft abrasives. Under classical abrasive wear theory, the abrasive must be at least as hard as the counterface. As a result, the wood particles cannot directly groove and scratch the plate surface. However it can be easily pictured how the wood fibers would be responsible for transferring the high working load in the refiner

whenever plate-to-plate contact was absent. Thus, the wood stock could indirectly deform, work harden, or groove the matrix by forcing the metal debris or sand particles (if such debris were present) against the moving plate surfaces. As the wood chips played a significant part in the bar rounding process, their density must influence the damage rate considerably. Wood species with higher density are usually of thicker cell walls and smaller lumen sizes, thereby exhibiting lower flexibility and compressibility when sheared or compressed. During refining, therefore, denser wood species would absorb less mechanical energy than the ones with lower densities. Most of the working load imposed on the denser wood chips could be directly transferred to the refiner plates to cause bar rounding damage. These arguments can be well supported by the interrupted mill trial results. As shown in Table 4.6, the bar rounding damage was doubled when the C20 plates worked with Douglas fir instead of white wood, and wood density was a major difference between the two mill trials with the Douglas fir having a higher density.

Plate Alloy Effect. As indicated in Table 4.6, the C20 (20-2-1) plates revealed much better bar rounding resistance than the S17 (440C) ones when both worked with whitewood. This may be attributed primarily to their difference in microstructure. Compared to the S17 stainless steel, the C20 white iron had a greater eutectic carbide volume fraction but a smaller mean free path between the carbides. Under a certain working load, as a result, metal debris or sand particles of given sizes would not easily cut into the matrix of the C20 alloy because of the presence of numerous hard carbides. In other words, the eutectic carbides in C20 iron could effectively prevent the matrix from preferential grooving or scratching damage, while the carbides in the S17 steel were not sufficient enough to protect its matrix. The lower matrix hardness and carbide hardness for the S17 alloy might also have contributed to its higher bar rounding damage rate. On the other hand, the carbides of the C20 alloy were usually more firmly supported by the matrix because they in general had much larger size than those of the S17 steel, resulting in less severe carbide spalling under the attack of various types of

abrasive particles and therefore the superior bar rounding damage resistance.

Service Time Effect. As shown in Table 4.6, for the C20 plates worked with whitewood, the bar rounding damage was proportional to service time but the damage rate was not a constant over the entire plate life. After 15% working life, no appreciable bar rounding was found, while almost 100% damage was produced during the next 60% plate life. In the final quarter of service life, basically no new bar rounding damage was developed. Therefore, unlike either serration or pitting damage, the bar rounding seems most severe in the middle plate life. This trend may be related to two factors, that is, the abrasive content and the stress condition. The entrained sand or grit particles would not change very much in content during refining, if the feed stock remained constant. Thus, this effect can be ruled out. From the mill trial results, over 80% of the total serration damage occurred in the middle 60% plate life (Tables 4.3), while over 70% of the total pitting damage occurred in the final quarter of the plate life (Table 4.5). As refining continued, therefore, the metal debris content in the pulp would increase considerably due to increased serration/pitting damage. On the other hand, however, the working stress imposed on the bar leading edges could reduce rapidly with increasing service time due to the sharpness loss of the bar edges. In the beginning although a higher stress was present the amount of abrasive particles would be insufficient, while late in the plate life although abrasive content was higher the working stress would be substantially reduced. Thus, the highest bar rounding rate would occur in the middle plate life when both working stress and abrasive content were sufficiently high.

Damage Mechanisms. From the analyses presented above, the bar rounding process may be summarized as follows. The bars are rounded by abrasion and/or erosion. The abrasive may be metal debris removed from plate surface and sand particles entrained in the wood chips. These particles could directly scratch the matrix in the bar rounded areas. When plate service began, little bar rounding occurred as not many metal debris were available. In the later stages of plate life, the bar rounding rate

decreased greatly since the working load imposed on the rounded bar leading edges became smaller. The wood stock could not cut the plate surface directly, but might indirectly groove the matrix by forcing the abrasive particles against the rotating plates. Also, by transferring the high working load to the bar leading edges, the wood stock could help to spall off some cracked or unsupported carbides, dendrites, and surface layers. For different plate alloys, the similar performance rankings (Figure 5.12) in mill trials and laboratory tests might also imply the correlation between bar rounding and abrasion. Due to the presence of solid particles, the high steam pressure inside the refiner, the high rotational speed of disks, and many dents and short random grooves on the bar rounded areas, erosion might also contribute to bar rounding. Therefore, the bar rounding damage may essentially be an abrasion and/or erosion process.

5.2. PERFORMANCE EVALUATION

5.2.1. Wear Performance of Plate Alloys

Relevance of Wear Testing. From the results of the laboratory wear tests and the mill trials, the plate alloys ranked in the same order in both cavitation erosion test and observed pitting damage, with the surface features of cavitation eroded specimens and the pitted plates being similar. Also, similar rankings were obtained in DSRW abrasion testing and in observed bar rounding damage, though the surfaces of the laboratory abraded samples appeared to be different from those of the bar rounded leading edges. For example, on abraded surfaces the carbides were flush with the matrix and cut by abrasives along with the matrix, while in the bar rounded areas the carbides stood well above the preferentially grooved matrix and were edge rounded. Additionally, the grooves were long and parallel in the abraded samples but short and disorderly on the rounded bar leading edges. These differences, however, may be attributed primarily to different patterns of motion and hardnesses of abrasive particles in the two processes. In bar rounding process most solid particles were relatively soft and loose, being able to

move both tangentially and radially under influence of the high rotational speed and steam pressure. In DSRW tests, however, the silica particles were very hard and could only move along the rotation direction of the wheel, grooving both carbides and matrix unidirectionally. Hence, bar rounding and the DSRW wear were essentially caused by the same mechanism: abrasion. As a result, the laboratory tests, especially the cavitation erosion and DSRW abrasion tests, were relevant to the damage environment of the refiner plates and could be used together to predict the durability of various plate materials in TMP refining.

Abrasion Performance. Based on the DSRW abrasion test results, no correlation between material hardness and wear rate can be found for various plate alloys examined, Figure 5.13. It seems, therefore, that bulk hardness is not a universal measure of the abrasive wear performance of very different alloys. Further examination of Figure 5.13 reveals that even for a given group of alloys the proportional relationship between bulk hardness and abrasion resistance may not be obvious. As a result, it could be the microstructure, rather than the bulk hardness, that most significantly influences the alloy abrasion rate. In general, the white irons behaved much better than the stainless steels in abrasion tests mainly because of their much higher eutectic carbide volume fractions. The 20-2-1 alloys exhibited the best abrasion behavior since their carbides were not only very high in volume fractions but also harder than those in other carbide-containing plate alloys tested (Table 4.7). In the 440C steel group, the S17 alloy exhibited lower abrasion rate than the C15 alloy primarily because the former's matrix was martensitic instead of austenitic and much higher in hardness. The 17-4PH stainless steel behaved much poorer than all plate alloys tested, possibly due to the absence of eutectic carbides and the presence of ferrite pools.

Erosion Performance. In water-sand-erosion, the wear rate for different plate materials tested, especially for carbide-containing alloys, varied much less than in the DSRW abrasion tests. It is easy to imagine that high chromium white irons should be

more erosion resistant than stainless steels due to the presence of large amounts of very hard eutectic carbides. The experimental results, however, have shown that these two groups of plate alloys behaved similarly in erosion performance. This may be explained by the nature of the solid particle erosion testing. In DSRW abrasion tests, the abrasive particles slide over the sample surface at a linear velocity of about 2.4 m/s, while in water sand erosion they impact directly on the specimen with a velocity of 50 - 100 m/s. Thus, the hard eutectic carbides would be much more easily fractured and spalled off in erosion than in abrasion tests, being unable to effectively protect the matrix from further damage. Under the impact of high-velocity solid particles, the beneficial effect of hard eutectic carbides on wear resistance could be greatly reduced. As a result, in water sand erosion these two groups of materials behaved very similarly.

Cavitation Erosion Performance. From the laboratory test results, for a given group of carbide-containing alloys the cavitation damage rate increased with the phase interface area. For example, in the Ni-hard group the NH alloy had a smaller dendrite size than the C80 iron, which reflected a smaller carbide size and finer matrix so that the total interface area was greater and the cavitation erosion rate was higher. This trend was reversed for the 440C group since the C15 steel, which had a larger dendrite size than the S17 alloy, exhibited a much higher damage rate. This is due mainly to the difference in matrix structure. Being used in an as-cast state, the Ni-hard group had a smaller dendrite size which represented more interfaces. The two 440C steels, however, were heat-treated and their dendritic size can only reflect the coarseness of the carbides but not the matrix. Although larger in dendritic arm spacing, the C15 steel had a martensitic matrix instead of an austenitic one so that it had more matrix interfaces than the S17 alloy, leading to a greater interface area and a higher damage rate. Thus, the proportional correlation of the interface area with the cavitation erosion rate is still valid for the 440C steels. Also, the martensitic matrix usually has a higher hardness and lower deformation ability than the austenite so that the fatigue crack development would be easier as cavitation erosion is basically a fatigue failure process.

In addition, the alloy Cr/C ratio seemed also significant to the cavitation erosion behavior of alloys. From Figure 5.14, for different carbide-containing alloys the cavitation damage rate reduced with increasing the Cr/C ratio when the secondary dendritic arm spacing was roughly constant. This may be because a higher Cr/C ratio will increase the matrix chromium concentration which may in turn reduce the sensitization near eutectic carbides. Therefore, a lower cavitation damage rate may be related to a reduced chromium depletion near the carbides due to higher alloy Cr/C ratio. For the 20-2-1 group, C30 alloy was finer in microstructure but lower in cavitation erosion rate than the C20 iron, while this does not necessarily mean that cavitation damage could sometimes decrease with increasing total interface area. The C30 and C20 irons, although similar in carbide volume fraction, were very different in Cr/C ratio which might have played a significant role in controlling the cavitation erosion rate. As the C30 had higher Cr/C ratio than the C20 iron, its better cavitation erosion behavior could be ascribed to reduced matrix chromium depletion near the carbides due to increased matrix chromium content. It is predictable, therefore, that if the Cr/C ratio remained constant, the C20 iron, instead of the C30, would exhibit more damage as it had a coarser microstructure and therefore a greater interface area. Hence, the cavitation damage could be reduced by reducing the interface area, improving the deformation ability, and increasing the Cr/C ratio.

Plate Damage and Plate Alloys. From the mill trials and laboratory wear tests, it can be concluded that the bar rounding and pitting behavior of plate alloys can be roughly reflected by their abrasion and cavitation erosion resistances, respectively. Serration was caused primarily by plate clashing and its damage rate could not be easily predicted by simply using these conventional wear tests, while the alloy's deformation ability might serve as a good measure. Among the alloys tested, the 17-4 PH steel is clearly not competitive in TMP refiner applications as it performed worst in all three wear tests. Compared to the 440C steels, the 20-2-1 and Ni-hard irons had superior abrasion performance but much poorer cavitation erosion behavior, as well as potentially

lower serration damage rate. The 25Cr iron, however, had the advantages of both 20-2-1 and 440C groups as it behaved very well in all three wear tests, being promising to exhibit satisfactory refining performance. When plate bar rounding is the major concern of TMP refining, therefore, high chromium white irons with higher carbide volume fraction and hardness should be used preferentially as they are usually the most abrasion resistant. In contrast, if the pitting damage and serration damage are the major factors limiting the plate performance, 440C steels will be more advantageous owing to their superior cavitation erosion resistance and deformation ability. If all three types of plate damage have to be minimized, the 25 Cr iron is of advantage.

Plate Alloy Optimization. In summary, the optimized plate alloy shall have a sufficiently high Cr/C ratio and contain a certain amount of eutectic carbides of medium size and spacing distributed in a fully austenitic matrix. A certain amount of eutectic carbides can efficiently resist the attack of hard abrasives and protect the matrix, leading to lower abrasion and erosion rates. The average carbide spacing should also be controlled. A smaller carbide spacing can provide a better bar rounding resistance by well protecting the matrix from abrasion and/or erosion, while may greatly promote the pitting process due to increased eutectic carbide/matrix interfaces. A fully austenitic matrix has superior cavitation erosion behavior because of few interfaces present, low serration damage rate due to sufficient deformation ability, and sufficient abrasion resistance due to high work-hardening ability. Unlike a martensitic matrix, moreover, the austenite structure usually contains few secondary carbides so that its matrix chromium depletion caused by carbide formation will be less severe, leading to improved cavitation erosion resistance. The alloy Cr/C ratio is needed to be high to ensure satisfactory abrasion and erosion resistances by transforming continuous M_3C networks into harder and isolated M_7C_3 carbides. More importantly, a high Cr/C ratio is very beneficial to cavitation erosion performance due possibly to increased matrix chromium content which may reduce matrix chromium depletion.

5.2.2. Wear Performance of Plasma Coatings

Abrasion Performance. Based on the DSRW wear test results, the abrasion behavior of plasma sprayed coatings, especially when using a silica abrasive, was determined primarily by coating hardness which is a function of both powder composition and spray distance. The coatings of different compositions differed drastically in hardness, and the coatings deposited by harder powder particles generally exhibited better abrasion performance. For a given coating group of the same powder composition, reducing spray distance could greatly increase the coating hardness and therefore the abrasion resistance. The abrasive wear rate, however, seemed not susceptible to coating porosity. Some cermet coatings behaved very well in abrasion tests despite their substantially high porosity. For example, the W-C-Co1 and W-C-Co2 coatings, although very high in porosity levels (Figures 4.31a-b), had the lowest abrasion rates among all plasma coatings tested when using SiO₂ abrasives (Table 4.12). For a given coating group such as WC-Co, if powder composition and spray distance remained constant the abrasion rate changed very little although the porosity had been doubled, as indicated by Figure 4.40. This may be attributed to the presence of very hard phases like tungsten carbides in these coatings. The beneficial effect of the very hard phases on the abrasion behavior was so great that it had fully offset the detrimental influence of pores. Similarly, other coating properties such as splat size and surface roughness also had little effect on the abrasion behavior of plasma coatings.

Erosion Performance. Similar to the plate alloys, no matter what type of abrasive was used, the plasma coatings varied much less in water-sand-erosion tests than in DSRW abrasion tests. Some metallic alloy coatings and cermets performed better in erosion tests than other plasma deposits. The lower erosion rates of these alloy coatings was possibly because of their better deformation and work-hardening ability under the impact of high-velocity solid particles, while the cermet coatings obtained their superior erosion behavior due primarily to the presence of very hard carbides. Unlike the

situations in DSRW abrasion testing, however, the cermet coatings were no longer the most wear resistant in erosion tests. Instead, they became inferior to many alloy coatings such as Fe-Mo-C, Ti-alloy and IN625-Cr₃C₂. When the abrasive particles impacted directly on, instead of merely sliding over, the sample surface, the coating's brittleness could play a much greater role in the wear damage process. As the cermet coatings are usually more brittle than the metallic alloy ones, they would be damaged faster in spite of their higher hardness. This is because when the coating deposit is too soft it cannot effectively resist the attack of erodent particles and deeper scratches will be produced on the eroded surface. Conversely, if the coating layer is too hard and brittle, many surface and subsurface cracks, which can drastically expedite the damage process, will be easily induced by the high-velocity erodent particles. To optimize the erosion resistance, therefore, the coating hardness must be maintained at a medium level. For a given coating group, a shorter spray distance generally resulted in a higher hardness and therefore a lower erosion rate, like in the DSRW abrasive wear tests. However, the erosion behavior seemed to be insensitive to other coating properties including porosity and splat thickness, as shown in Tables 4.10 and 4.13.

Cavitation Erosion Performance. Based on the test results, the plasma coatings, like the plate alloys tested, seem to have a major parameter to determine their cavitation erosion resistance: the interface area. As well demonstrated, the cavitation damage initiated preferentially from the interfaces which are usually the weaker areas in a heterogeneous material. The coatings always contained many interfaces since they were constituted of numerous small splats. The presence of carbides and oxides would further increase the coating interface area. Compared to the cast alloys, the coatings are often much higher in percentage of pores and microcracks which also lead to more interfaces, Figure 5.15. As schematically shown by Figure 5.16, when other deposition parameters remain constant the powders with higher melting point and hardness can lead to more pores and microcracks in the coating layer as such powders are easy to solidify but hard to plastically deform even at very high temperature and impact velocity. The test results

have shown that the WC-Co coatings, which were sprayed by powders of high melting points, contained more pores and microcracks than other plasma deposits examined. Like the cast alloys, therefore, the coatings could be much less cavitation damaged when containing fewer interfaces. As the bonding between splats in coatings is generally much poorer than that between grains or different phases in cast alloys, reducing the interface area must be particularly important for the coatings to improve their cavitation erosion performance.

The test results also show that coating cavitation erosion behavior depended on many deposition parameters and coating properties like powder size, porosity, surface roughness, and splat thickness. All these, however, could be reduced to the interface area. For example, it seems to be powder composition that strongly influence the cavitation damage rate as some alloy coatings (Fe-Mo-C, Ti-alloy, and IN625-Cr₃C₂) and some ceramics (Cr₃C₂-WC-TiC and Al₂O₃-TiO₂) behaved much better than others. In fact, these coatings had lower porosity and larger splat size, while both can result in a smaller interface area. From Figure 4.38, there was a trend that larger powder size led to less cavitation damage, and this may also be ascribed to increased splat size or reduced interface area. The Ti-alloy and IN625-Cr₃C₂ coatings, for example, behaved very well in cavitation erosion mainly because they, unlike other deposits, were made by wires instead of powder particles. These wires had much greater diameter than the powders and formed larger splats or fewer coating interfaces (Figure 4.29), thereby leading to lower damage rates. For a given coating group such as Fe-Mo-C, the cavitation erosion resistance improved when increasing coating surface roughness and splat thickness but reducing the porosity (Tables 4.10 and 4.13). A greater porosity would result in more coating interfaces, while a higher surface roughness might be due to a larger mean splat size. Thus, if the coating material was given, all these parameters might be correlated to the same thing: coating interface area.

5.2.3. Optimization of Coating Performance

According to the experimental results, the wear performance of plasma coatings in different laboratory tests depended primarily on their microstructure and properties which were in turn determined by many deposition parameters including powder composition, powder size, spraying distance, spraying energy, and the traverse speed and distance. It can be inferred that these deposition parameters may also significantly influence the performance of plasma coatings in TMP refining. Only when all major deposition parameters have been well optimized, the best performance of the coatings can be obtained and their advantages (or disadvantages) over the conventional cast alloys in TMP refiner applications may be truly reflected. Because there are a great number of variables involved in the plasma spraying and a slight adjustment in one parameter may greatly change the coating's structure and therefore the properties, there shall be an ample room to optimize the deposition process of the coatings in terms of their performance in both laboratory wear and TMP refining.

Powder Composition. Powder composition is very important for coating's performance. Some alloy coatings like Ti-alloy and IN625-Cr₃C₂ had the lowest wear rates in all erosion tests (Table 4.12), simply as they contained very few hard and brittle carbides and had better deformation ability under the severe impact of erodent particles. Their better cavitation erosion behavior can be related to smaller interfacial area as they were deposited by alloy wires instead of powders, while their higher abrasion rates were due possibly to the absence of sufficient carbides. Other alloy coatings such as Fe-Mo-C were also deposited by carbide-free powders, while as their powders contained carbide-forming elements like iron and carbon, during spraying different types of molten powders could meet together and form many carbides like Fe₃C in the coating layer so that the hardness was increased and abrasion resistance was improved. The Fe-Mo-C group, however, had inferior erosion performance compared to the Ti-alloy and IN625-Cr₃C₂ coatings because of the higher hardness and lower deformation ability. Some cermet coatings, such as WC-Co1 and WC-Co2, behaved very well in abrasion as their microstructures were constituted mainly by WC carbides which were much harder than

alloy or other carbide particles. Their higher cavitation erosion and erosion rates were due to higher porosity, more microcracks, and higher brittleness. If the content of hard particles is too high, the abrasion behavior may be excellent but the erosion and cavitation erosion damage will be substantially increased. In contrast, for an alloy coating free from any carbides the erosion and cavitation erosion performance may be excellent but their abrasion rate must be very high. To obtain the best trade-off wear behavior, therefore, the powders must contain a certain percentage of hard components like carbides, or at least some carbide-forming elements, and a sufficient amount of alloy particles of relatively higher plasticity such as cobalt, nickel, and iron.

Powder Size. As another significant factor influencing the performance of plasma coatings, powder size can modify both wear properties and surface topography. Although having little effect on the coating's abrasion and erosion behavior, the powder size could strongly influence the cavitation erosion resistance (Figure 4.38). Since a larger original powder size will lead to a larger average splat thickness, the cavitation erosion performance can be improved due to reduced total area of coating interfaces. It has been demonstrated by the laboratory tests that the Ti-alloy and IN625-Cr₃C₂ coatings, which were deposited by alloy wires, displayed larger splat size, less interfaces, and therefore superior cavitation erosion resistance than those coatings made from powders. On the other hand, it can be seen from the experimental results that the coating surface roughness appeared to increase with original powder size. Hence, plasma spraying the refiner plates with a larger powder size can lead to a rougher plate surface which may be very beneficial to TMP refining efficiency and the resulting pulp quality, because the friction between plate surface and wood particles may increase the pulp residence time. However, the powder size should be controlled within a reasonable range because oversized powder particles may be very difficult to fully melt during spraying and will cause higher porosity and more microcracks in the coating structure.

Spray Distance. Being a major deposition parameter, spray distance played an

important role in determining the coating microstructures and the properties. For a given coating group, the DSRW abrasion resistance, especially when relatively softer abrasives were used, could be considerably improved by reducing the spray distance. This could be due mainly to the increase in coating hardness with closer spray distances. From Figure 5.17, for an argon/hydrogen plasma the temperature and axial velocity decrease drastically with increasing the distance away from the gun. For a given powder composition, therefore, reducing the spray distance from 200 to 100 mm will make a big difference since a shorter spray distance would prevent the fully molten powders from being considerably cooled and slowed before impacting the substrate. The molten particles with higher temperature and velocity would definitely form coating deposit of higher bonding, lower porosity, and less microcracks, thereby leading to higher coating hardness and abrasion resistance. In contrast, reducing spray distance increased erosion rate for a given group of coatings, due mainly to the reduced coating deformation ability as indicated by the increase in hardness. In addition, a decreased spray distance corresponded to an improved cavitation erosion behavior possibly because of increased average splat size or reduced total interface area which can be indicated by the increased surface roughness. As the molten particles may be evaporated to a certain degree before striking the substrate and solidifying on it, a shorter spray distance may lead to a larger splat size by preventing severe evaporation. A lower porosity, which will also reduce the total interfaces, can be obtained under smaller spray distance since the particles can be well deformed at high temperature and velocity. Thus, the coating cavitation erosion resistance were improved by decreasing the spray distance. As a simple but effective method of modifying the coating surface roughness, reducing the spray distance may also improve the TMP refining process by increasing the pulp residence time. However, this distance should not be too short to avoid any substrate melting.

Spray Energy. Based on the coating photomicrographs and wear data, sufficient spray energy (the product of voltage times current) is also essential for coating microstructure and performance. Comparing Figures 4.29-4.31, many alloy coatings.

such as Fe-Mo-C and Ti-alloy, were constituted mainly by thin splats. For some cermet coatings like W-C-Co and WC-Co groups, such a layered structure was not evident since most particles seemed not solidified in the form of thin splats, and there were higher percentages of pores and microcracks. The laboratory tests revealed higher erosion and cavitation erosion rates for the W-C-Co and WC-Co coatings. The spray energy may account for these differences in coating structure and wear property. These coatings, although differed greatly in powder melting point, were deposited by similar spraying energies. Having lower melting points than the tungsten carbides, the alloy powders like iron or cobalt could be easily melted during spraying and deformed into thin splats upon impacting the substrate, and the resulting porosity is very low. Also, due to lower melting points the solidified splats could remain plastic for a long time and would not be easily cracked by the impact of high-velocity particles, leading to less microcracks in both newly-deposited and the solidified splats (Figure 5.18). The total interfaces and therefore the cavitation damage rates were reduced. Thus the deposition of powders with higher melting points needs more spray energy to obtain satisfactory coating structure and wear performance, while a lower spray energy has to be used for those powders with low melting points to avoid unnecessary evaporation and oxidation.

Traverse Speed and Traverse Distance. Traverse speed and traverse distance of the spray gun may be other important deposition parameters for the plasma coatings, especially those made by powders of higher melting points. As shown in Figure 5.19, either higher traverse speed or shorter traverse distance will increase the number of passes per unit time. If this number is high, the coating layers will not only be built up more rapidly, but be subjected to greater heat by the plasma arc plume during spraying. Therefore the splats deposited on the substrate surface may solidify more slowly and remain plastic for a longer time. Under the impact of high-velocity particles, accordingly, the solidified splats can be well deformed without any severe fracturing, leading to reduced amount of pores and microcracks and therefore the interface areas. In addition, as both the coating layer and the substrate are well heated, less residual

stress may be produced in the coating structure due to slower cooling which will cause less thermal cracking. The coating's wear performance, especially the cavitation erosion resistance, may be greatly improved because of reduced total of interfaces. Therefore, higher traverse speed and shorter traverse distance may be particularly beneficial to those coatings deposited from powders of higher melting points.

In summary, many deposition parameters can be further optimized to improve the coating wear performance. Sufficiently hard particles like WC carbides should be added to the powders to obtain a high abrasion resistance, while a certain amount of alloy powders with lower hardness can reduce the erosion and cavitation erosion rates by providing a higher deformation ability. A larger powder size corresponds to a better cavitation erosion behavior because of the reduced coating interface areas caused by increase in mean splat size. A shorter spray distance should be used to increase the pulp residence time by producing a higher coating surface roughness. Also, a smaller spray distance may effectively improve the abrasion resistance by increasing the coating hardness, and improve the cavitation erosion behavior by forming larger splats and reducing the total interface area. In addition, for some coatings, especially those deposited from powders of higher melting points, greater spray energy, higher traverse speed, and smaller traverse distance are needed to increase the erosion and cavitation erosion damage through reducing the contents of pores and microcracks.

5.2.4. Potential of Plasma Spraying in TMP Refining

It is evident from the laboratory wear tests that the plasma coatings are generally inferior to all conventional plate alloys in erosion and cavitation erosion tests, but can exhibit much better abrasion resistance than all cast plate alloys, especially the stainless steels. Therefore the coatings tested might be considered comparable with the cast plate alloys in trade-off wear resistance. As the abrasion and cavitation erosion performances can be correlated mainly to bar rounding damage and pitting damage resistances,

respectively, the coatings, if applied on the refiner plates, might be expected to cause less bar rounding but more pitting damage than the cast alloys. Thus, the plasma spraying techniques might be potentially competitive in TMP refiner applications when bar rounding, instead of pitting damage, is the major concern in plate performance.

As stated earlier, the cavitation erosion resistance of the coatings may be improved by optimizing various deposition parameters such as powder composition, powder size, spray distance, spraying energy, traverse speed, and traverse distance, which can reduce the total interface area by controlling the coating porosity, crack density, and splat size. Due to the nature of plasma spraying, the effect of deposition parameter optimization on the cavitation damage rate may be limited. It is therefore unlikely for the plasma coatings to be as pitting resistant as those cast alloys during refining. However, since most pitting damage formed in the final quarter of plate life while almost all bar rounding damage occurred during the first three quarters of plate life (Tables 4.5 and 4.6), the plasma coatings could be able to stay on the plate surface without being pitted for a long time, thereby effectively improving the bar rounding resistance and the plate performance.

In addition, using plasma spraying techniques the plate surface texture can be modified effectively. The experimental results have shown that the alloy surface roughness can be easily increased by plasma spraying, and the roughness can be adjusted by changing the deposition parameters such as spraying distance and powder size. As the plasma coatings, although still not well optimized yet, can have a comparable trade-off wear resistance with the cast plate alloys tested, it can be predicted that these coatings will be able to stay on the plate surface without being removed rapidly, especially during the early and middle plate life. If the friction between wood particles and the bar top surfaces can be increased due to higher plate surface roughness and sufficient coating durability, the plasma spraying techniques may lead to a longer pulp residence time and therefore improved TMP refining performance.

Table 5.1. Hardness of Abrasives and Second Phases [46]

Material or phase		HV
Matrix	Ferrite	70-200
	Pearlite, alloyed	300-460
	Austenite, low alloy	250-350
	Austenite, high Cr iron	300-600
	Martensite	500-1010
Carbide	Cementite	840-1100
	Chromium carbide (Fe,Cr) ₇ C ₃	1200-1600
	Molybdenum carbide Mo ₂ C	1500
	Tungsten carbide WC	2400
	Titanium carbide TiC	3200
	Boron carbide B ₄ C	3700
Abrasive	Quartz	900-1280
	Corondum	1800
	Silicon carbide	2600
	Diamond	10000

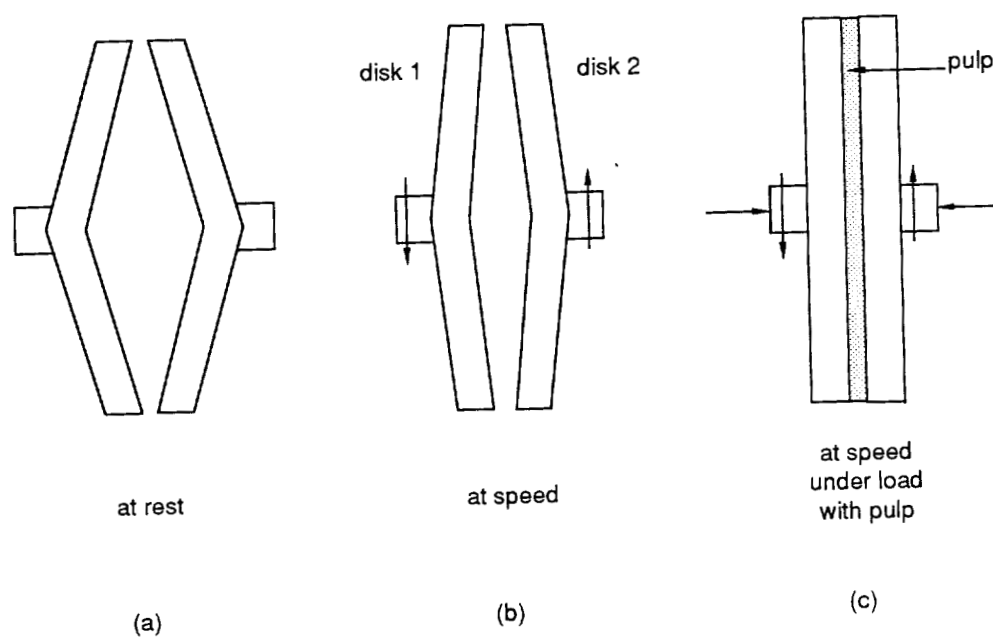


Figure 5.1. Schematic of a disk refiner set-up.

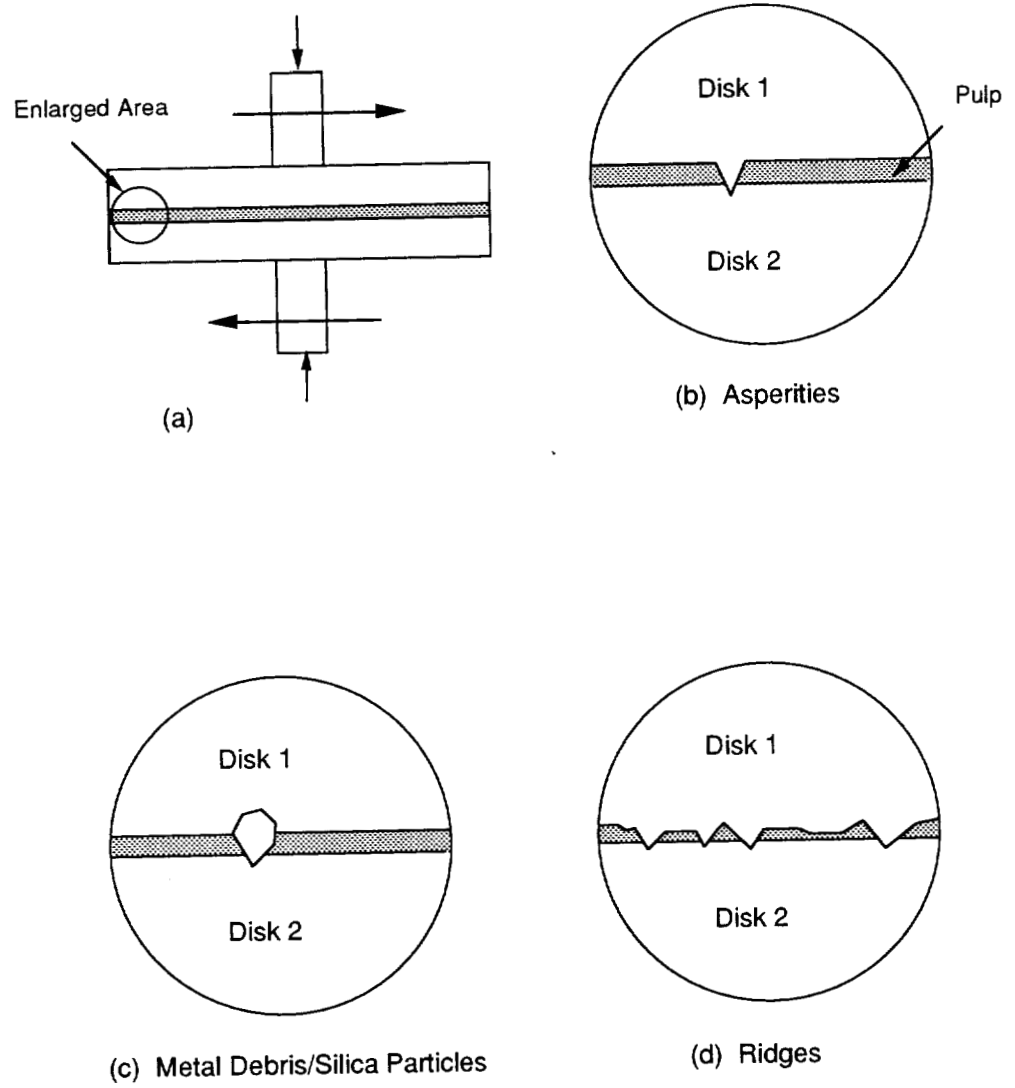
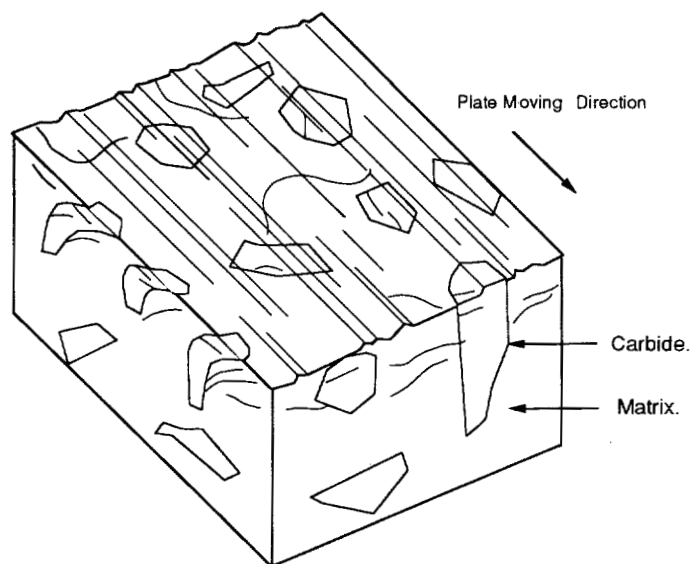
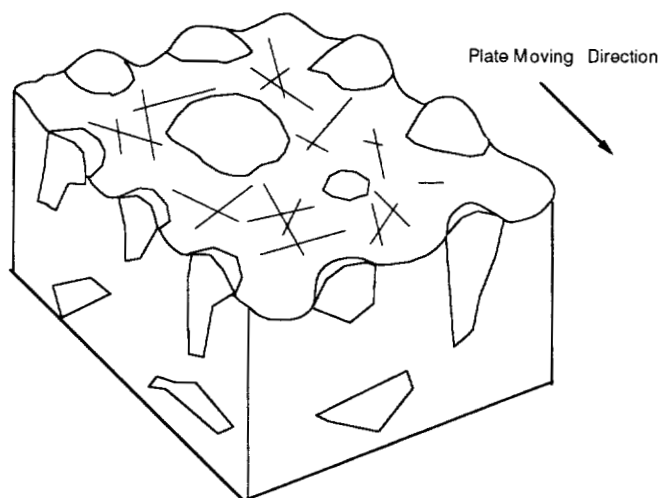


Figure 5.2. Formation of circumferential grooving.



(a) "Smooth region".



(b) "Rough region".

Figure 5.3. "Smooth region" (a) and "rough region" (b).

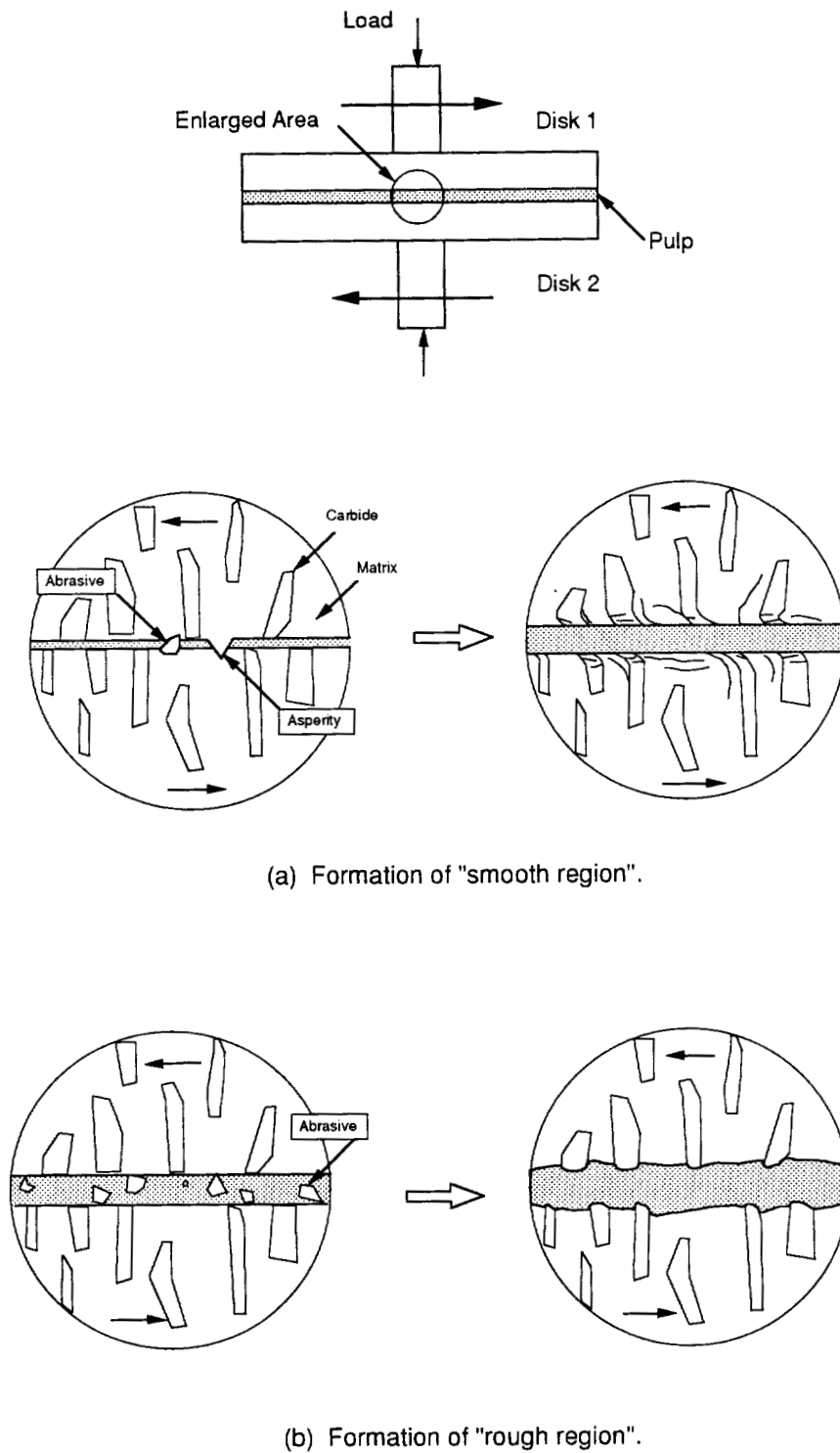
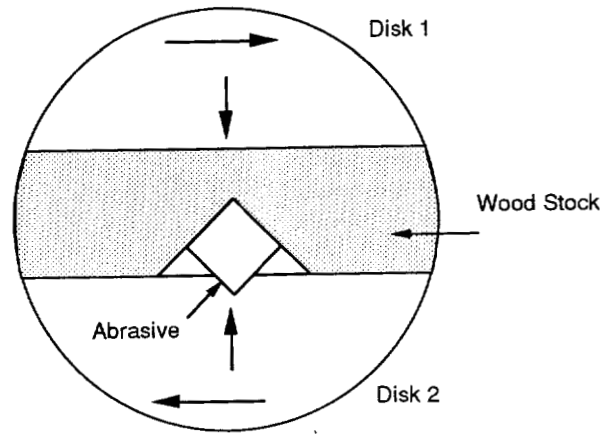
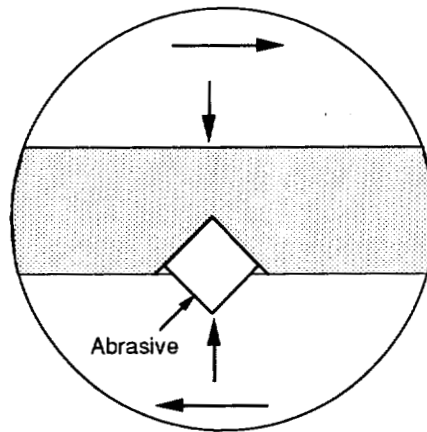


Figure 5.4. Formation of "smooth region" and "rough region".



(a) White wood.



(b) Douglas fir.

Figure 5.5. Wood density and serration damage.

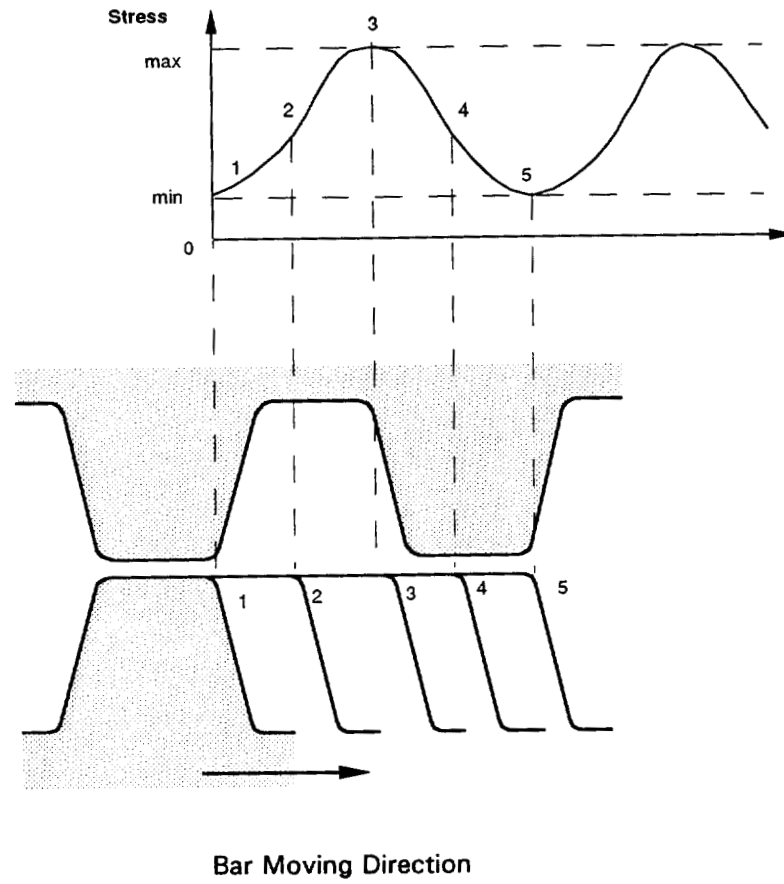
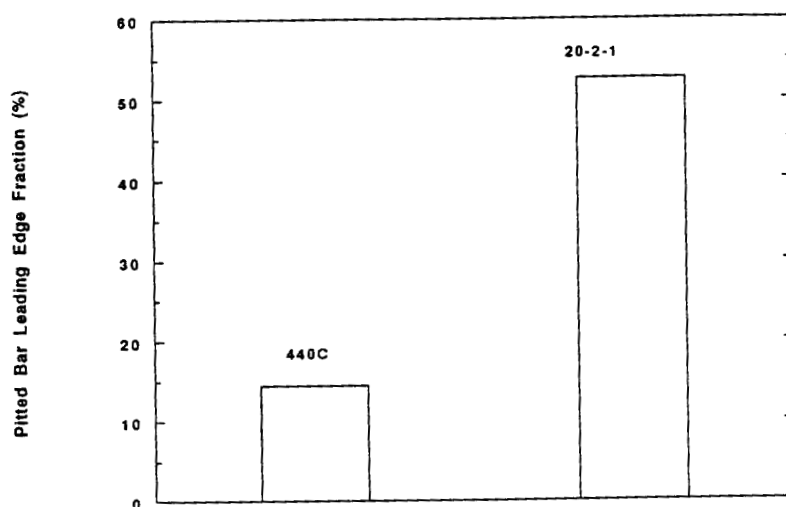
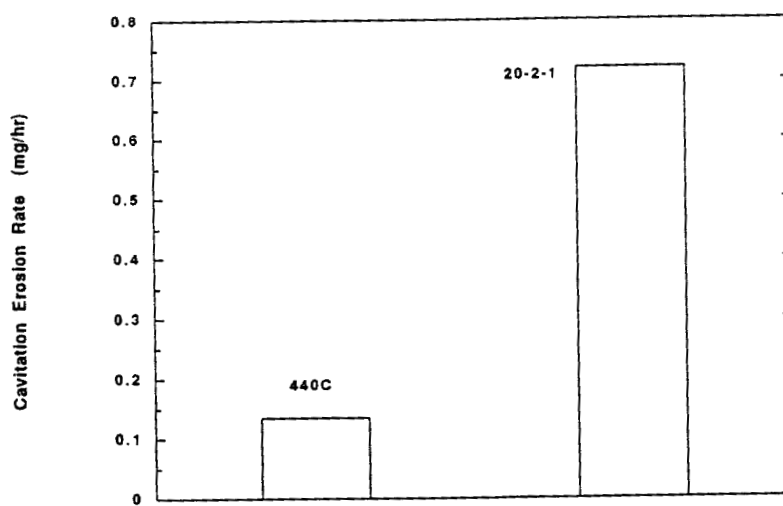


Figure 5.6. Local pressure pulse near a bar leading edge.



(a)



(b)

Figure 5.7. Performance ranking in pitting damage rate (a) and cavitation erosion rate (b) for 440C and 20-2-1 alloys.

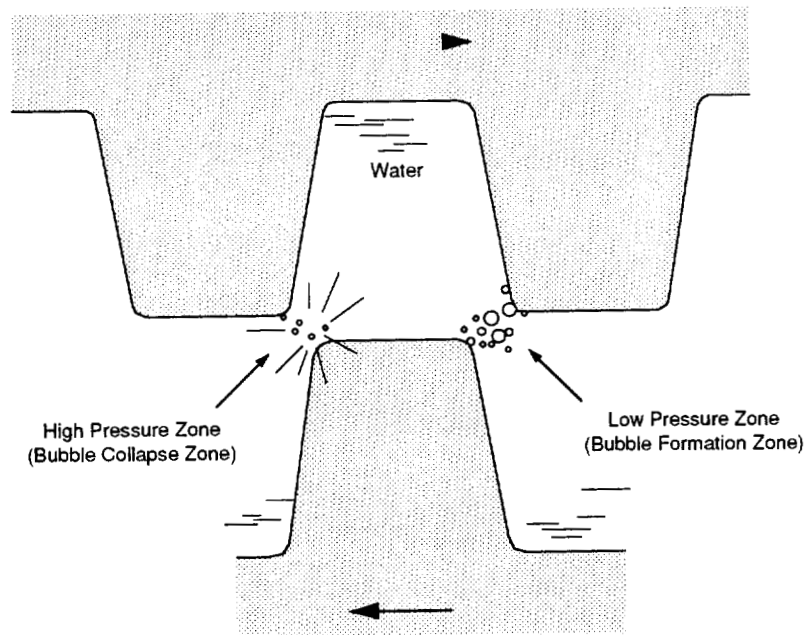


Figure 5.8. Cavitation erosion in the breaker bar zone.

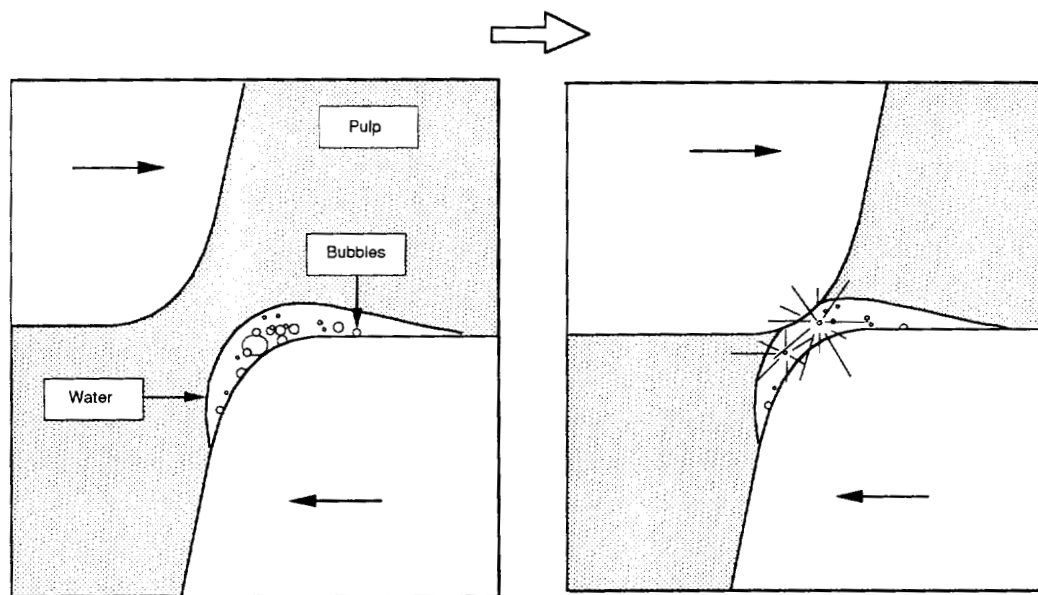


Figure 5.9. Cavitation erosion in the refining zone.

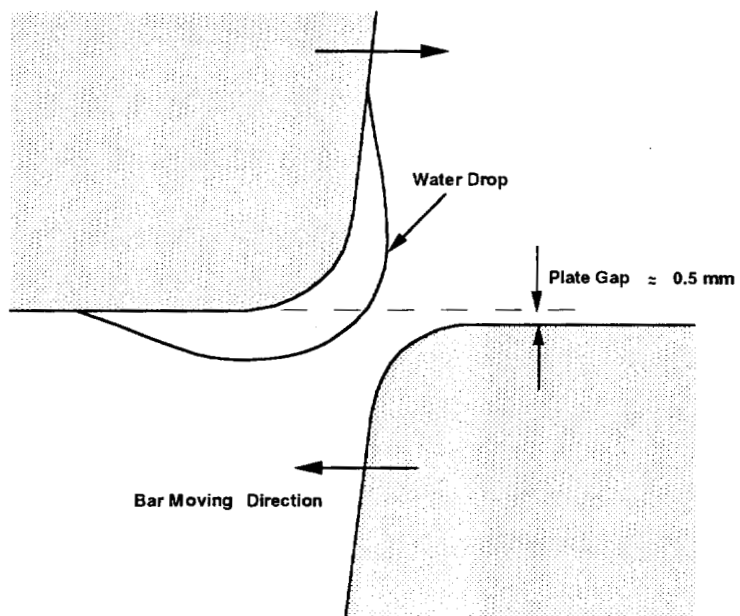


Figure 5.10. Liquid impingement erosion in the refining zone.

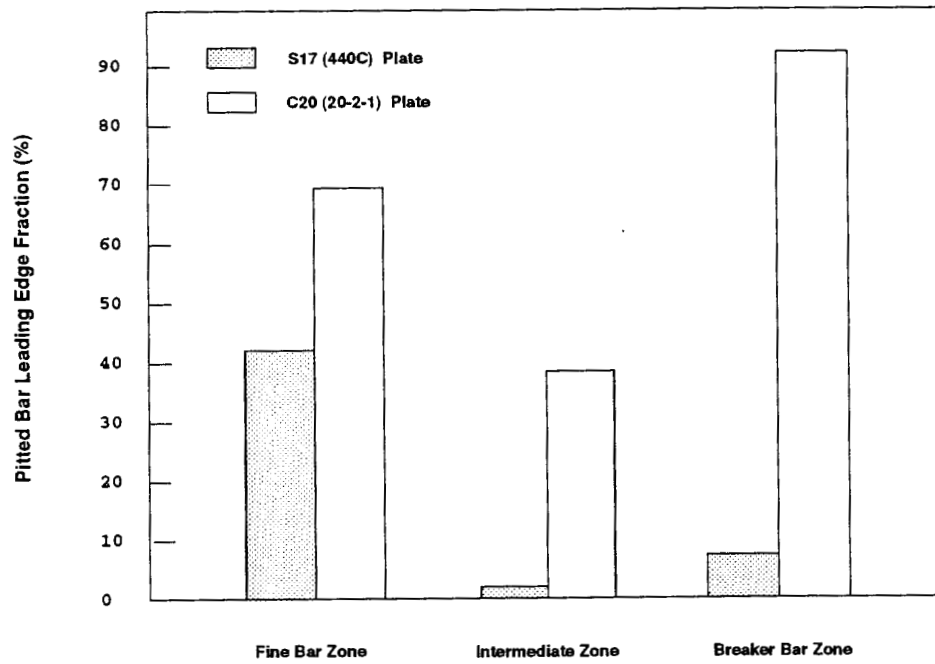
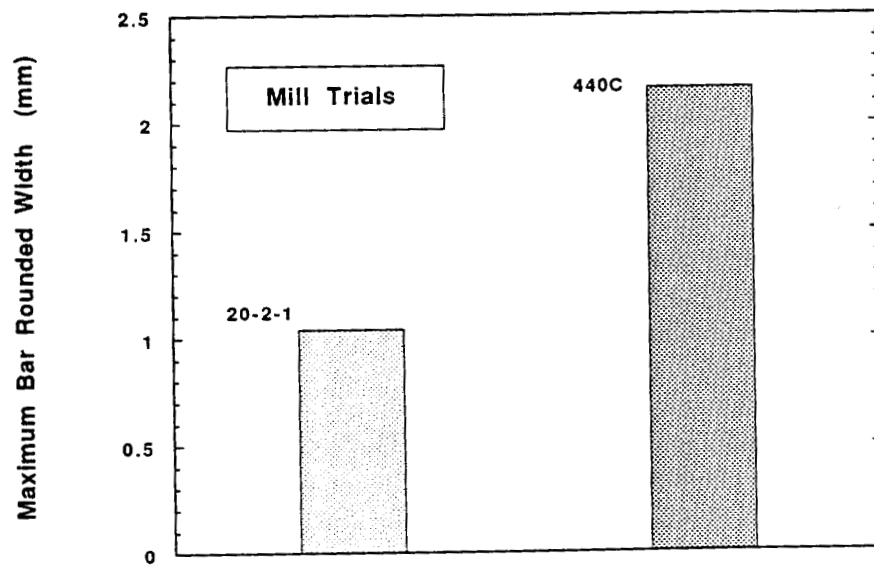
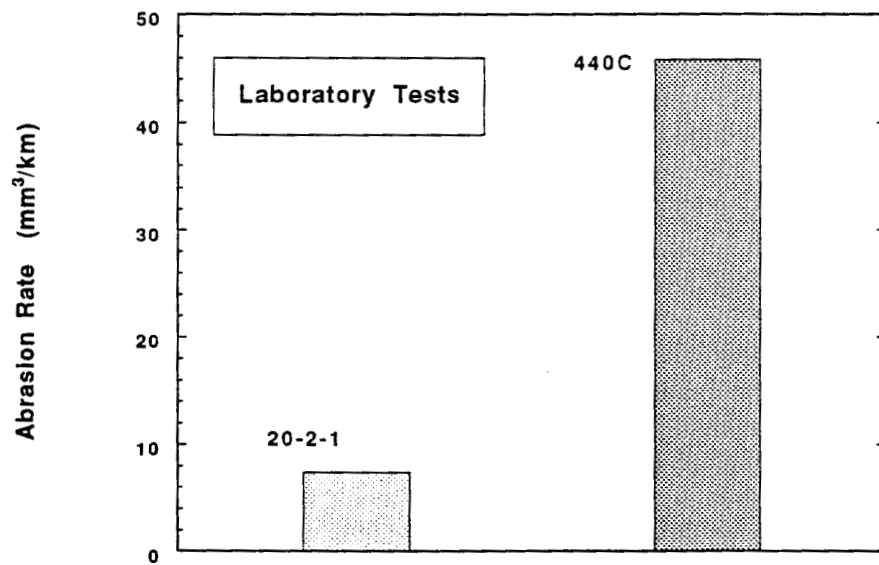


Figure 5.11. Pitting performance ranking for 440C and 20-2-1 plates worked with whitewood.



(a)



(b)

Figure 5.12. Comparison of bar rounding damage resistance (a) and abrasion resistance (b).

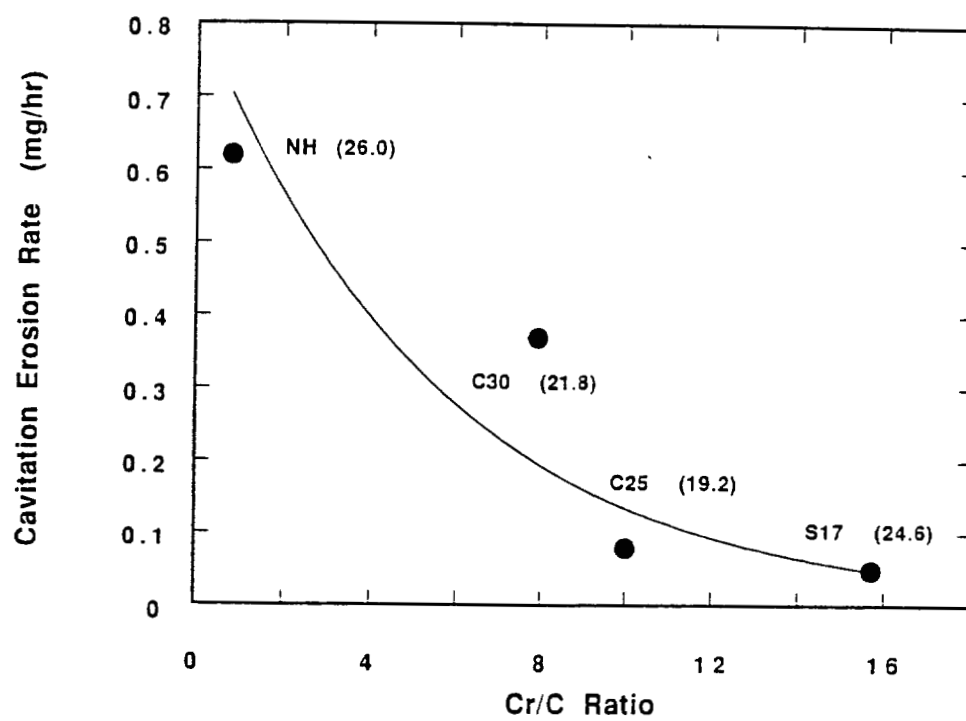
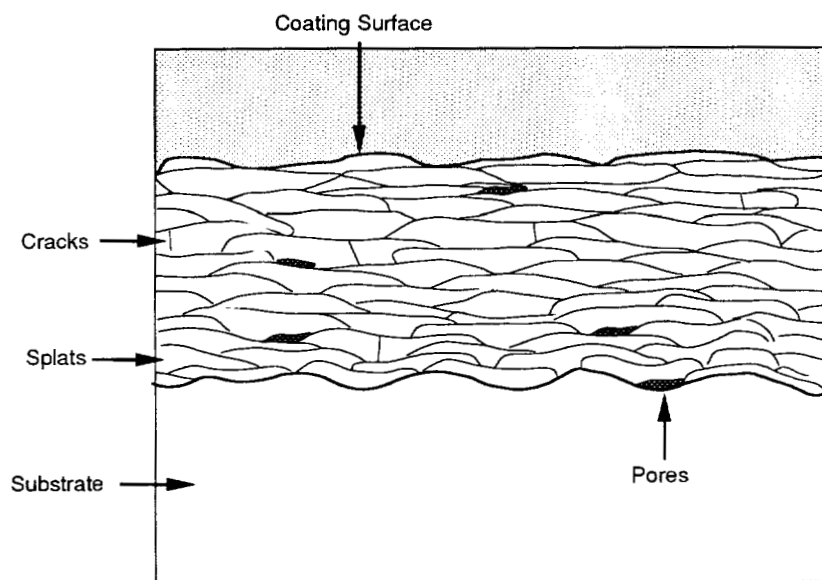
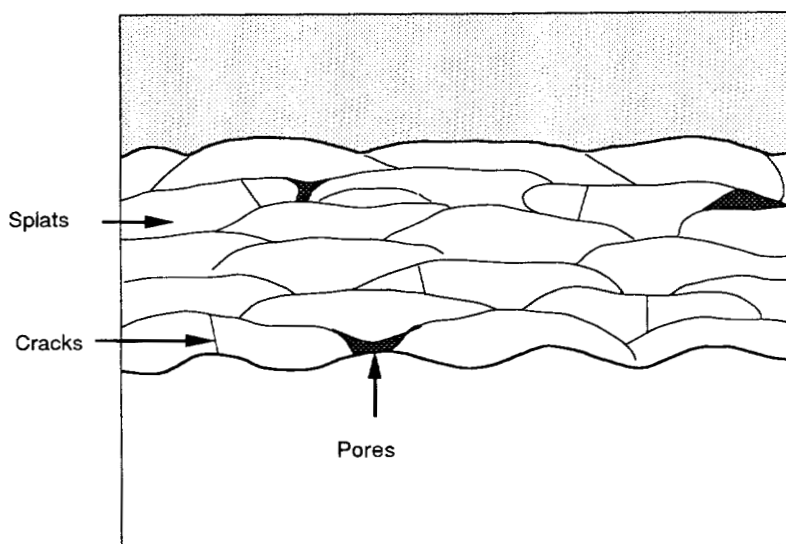


Figure 5.14. Cavitation damage versus Cr/C ratio for some carbide-containing alloys.

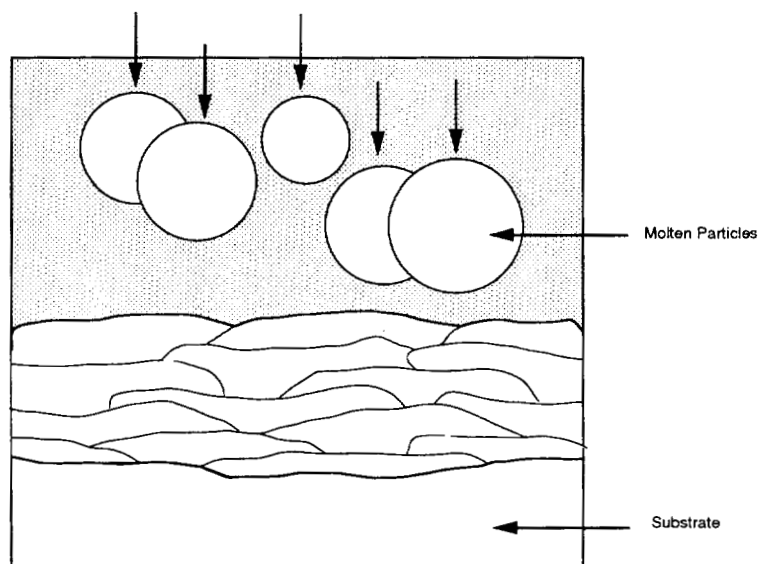


a. More interfaces.

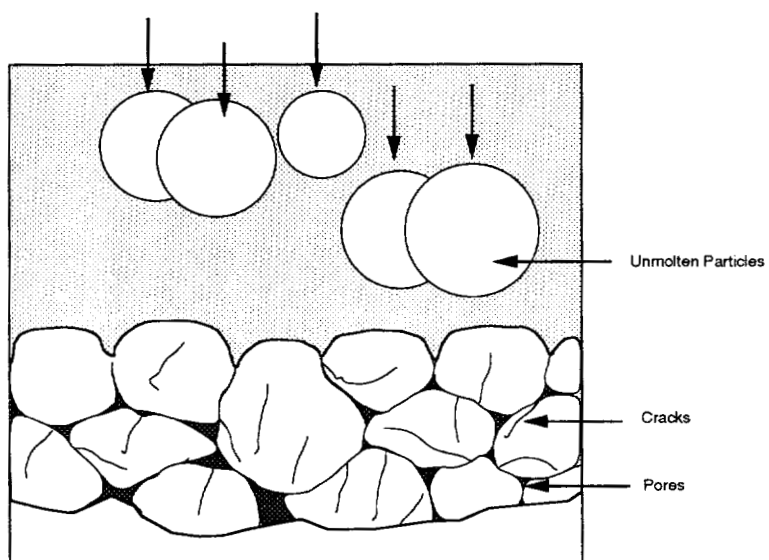


b. Less interfaces.

Figure 5.15. Total interfaces and splat size, porosity, and crack density.



(a). Higher powder melting point.



(b). Lower powder melting point.

Figure 5.16. Coating structure versus powder melting point.

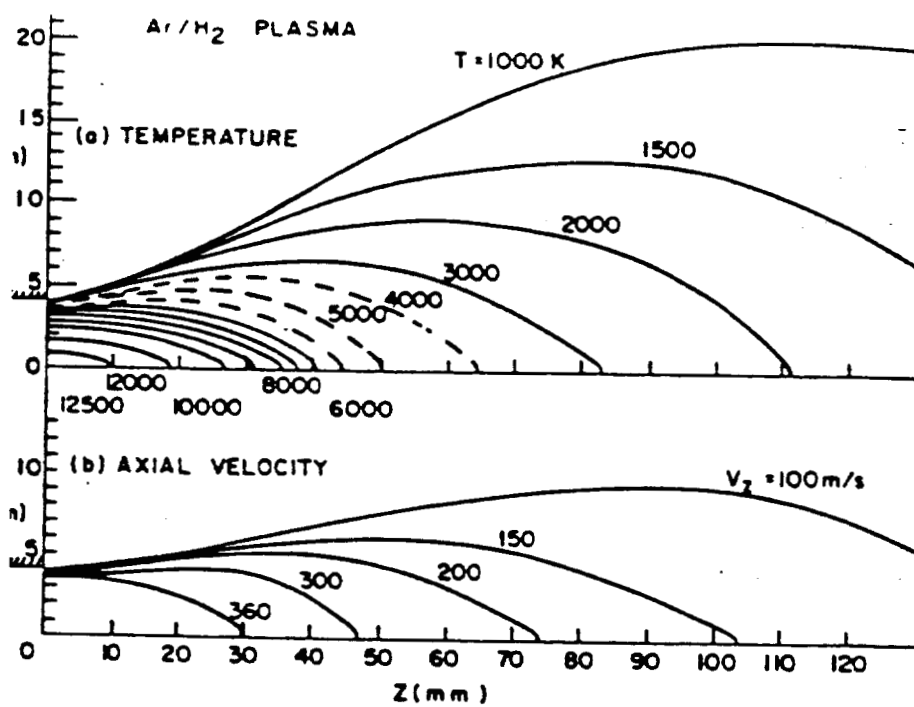
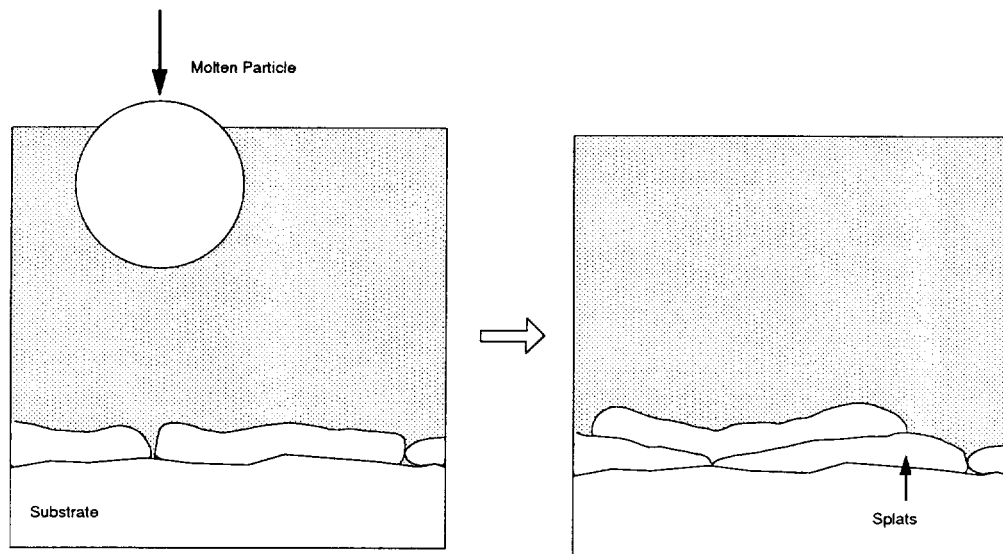
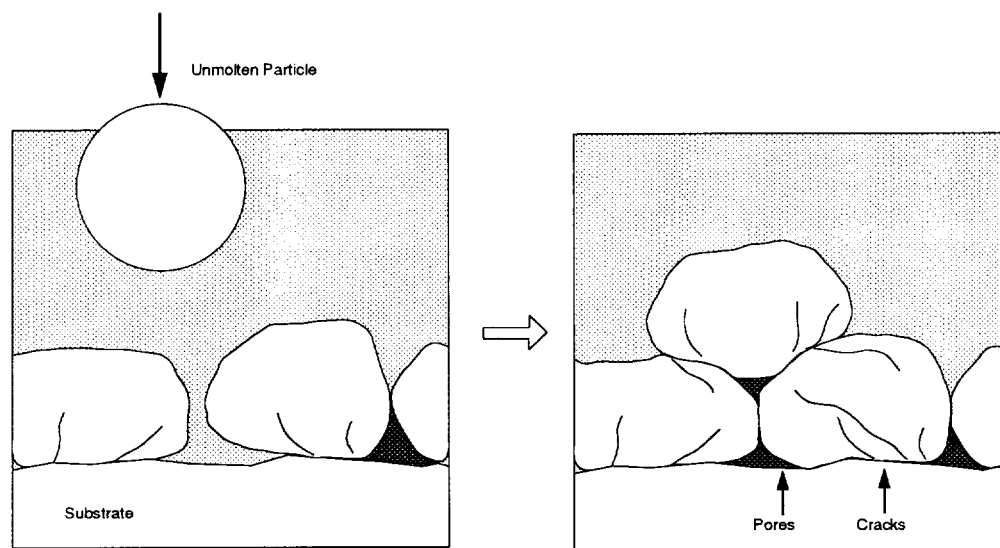


Figure 5.17. Temperature and axial velocity isocontours for an Ar/H₂ plasma.



(a) Higher spray energy.



(b) Lower spray energy.

Figure 5.18. Spray energy and coating microstructure.

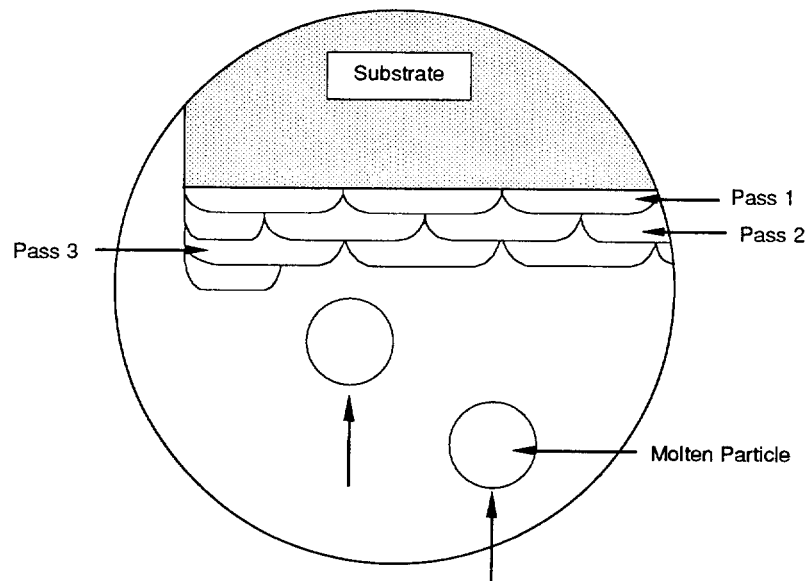
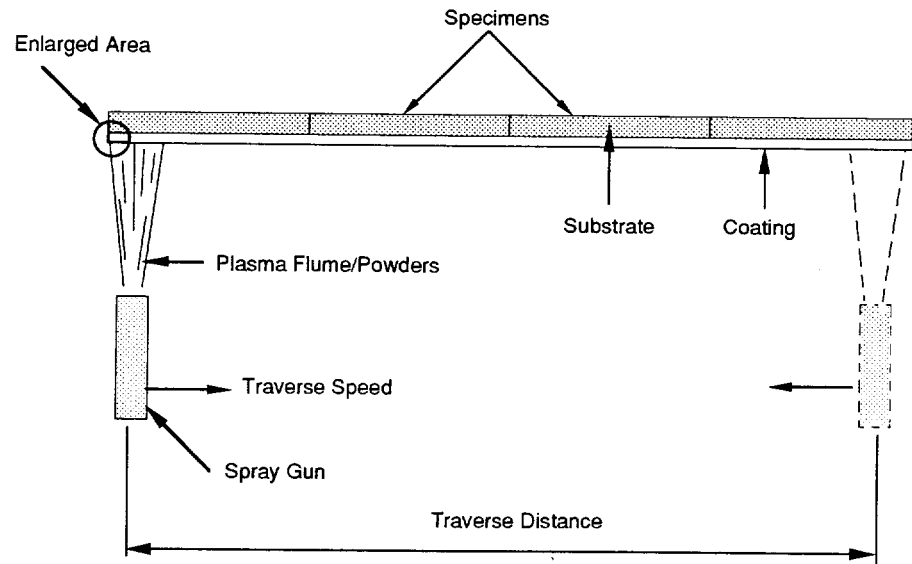


Figure 5.19. Traverse speed and Traverse distance.

CHAPTER 6 CONCLUSIONS

- There are three major plate surface damage modes: serration, bar rounding, and pitting.
- Although serration, bar rounding, and pitting all increased with service time, they generally occurred early, middle, and late in the plate life, respectively.
- Serration damage resulted mainly from sliding wear during plate-to-plate contact.
- Bar rounding damage was attributable primarily to abrasion and/or erosion.
- Breaker bar zone pitting was caused mainly by cavitation erosion, while refining zone pitting was caused by very similar mechanism(s).
- Compared to 20-2-1 plates, the 440C steel plates suffered more bar rounding damage but less serration and pitting damage.
- The laboratory abrasion and cavitation erosion tests are relevant to plate damage environment and can be used together to predict the durability of plate materials in TMP refining.
- Compared to the plate alloys, the plasma coatings were much less erosion and cavitation erosion resistant, but could be much more abrasion resistant.

- For both alloys and coatings tested, sufficient amount of hard phases can reduce abrasion damage, and smaller interface area can reduce cavitation damage.
- For a better trade-off wear resistance, the plate alloy should contain a certain amount of eutectic carbides of high hardness and medium size in a fully austenitic matrix, with the Cr/C ratio being sufficiently high.
- To reduce the cavitation damage rate, the coatings should be deposited using powders of lower melting point and larger size at shorter spray distance with higher spray energy.
- Plasma spraying is promising in some TMP refiner applications as it can effectively increase the plate surface roughness and abrasion behavior.

REFERENCES

1. Smook, G.A., *Handbook for Pulp & Paper Technologists*, M.J. Kocurek, ed., the Joint Textbook Committee of the Paper Industry, Montreal, Canada, 1982.
2. Clayton, P., M. Scholl, and D. Christensen, *Improving TMP Refiner Plate Performance by Surface Engineering (Forest Products Laboratory Preliminary Report)*, April 1989.
3. Browning, B.L., *The Chemistry of Wood*, Robert E. Krieger Publishing Company, Huntington, New York, 1975.
4. Akerlund, G., O. Danielsson, B. Falk, and G. Ryrberg, "Defibrator Bleaching - A New Concept in TMP", *Proc. of the 1979 Int. Mech. Pulping Conf.*, Toronto, Ontario, Canada, June 1979, pp.237-243.
5. Browning, B.L., *Methods of Wood Chemistry (Vol. I)*, John Wiley & Sons, Inc., New York, 1967.
6. Cote, W.A., "Wood Ultrastructure in Relation to Chemical Composition", in *Recent Advances in Phytochemistry*, Vol.11, The Structure, Biosynthesis, and Degradation of Wood, F.A. Loewus and V.C. Runeckles, ed., by Plenum Press, New York, 1976.
7. Parham, R.A., "Ultra-Structure and Chemistry", in *Pulp and Paper Manufacture: Vol.1 Properties of Fibrous Raw Materials and their Preparation for Pulping*, Kocurek, M.J., and C.F.B. Stevens, ed., the Joint Textbook Committee of the Paper Industry, Montreal, Canada, 1982, pp.35-45.
8. Leask, R.A., and M.J. Kocurek, in *Pulp and Paper Manufacture: Volume 2 Mechanical Pulping*, the Joint Textbook Committee of the Paper Industry, Montreal, Canada, 1987.
9. Frazier, W.C., "Cavitation In Large Wood Chip Refiner", *Cavitation and Polyphase Flow Forum - 1979 (Proc. of the Joint ASME-CSME Applied Mechanics, Fluids Engineering and Bioengineering Conf.)*, Niagara Falls, New York, June 1979, pp.13-15.
10. Kurdin, J.A., "Refiner Plates in Mechanical Pulping", *TAPPI Proceedings*, Pulping Conference, 1986, pp.689-693.
11. Pearson, A.J., "Towards a Unified Theory of Mechanical Pulping and Refining", *Proc. of the 1983 Int. Mech. Pulping Conf.*, Washington, DC, June 1983, pp.131-138.

12. Pearson, A.J., G.J. Trout, P.R. Sibly, and A.G. Tyler, "Refiner Pulp from *Pinus Radiata*", *Paperi ja Puu (Paper and Timber)*, Vol.60, No.4a, 1978, pp.247-254.
13. Miles, K.B., and W.D. May, "The Flow of Pulp in Chip Refiners", *Journal of Pulp and Paper Science*, Vol.16, No.2, March 1990, pp.63-72.
14. Wasikowski, P.L., "Diagnosing Refiner Plate Failure Modes in Thermomechanical Pulping". *Pulp & Paper Canada*, Vol.91, No.1, 1990, pp.121-126.
15. Skinner, R., "Optimization Strategies of the TMP-System at the Kotka Mills", *Proc. of the 1983 Int. Mech. Pulping Conf.*, Washington, DC, June 1983, pp.155-160.
16. Frazier, W.C., W.H. Arnold, T.C. Williams, and R.S. Charlton, "Performance, Design and Metallurgy of Refiner Plates for TMP", *Pulp & Paper Canada*, Vol.82, No.3, 1981, pp.45-55.
17. Clayton, P., and D. Christensen, "Metallurgical Aspects of Refiner Plates", *Proc. of the 5th Int. Symp. on Corrosion in the Pulp and Paper Industry*, Vancouver, BC, Canada, June 1986, pp.175-179.
18. Wasikowski, P.L., "Failure Modes and Requirements for Refiner Plate Alloys Used for Thermo-Mechanical Pulping", *Canadian Pulp and Paper Association 1987 Annual Meeting*, pp.189-196.
19. Thompson, C.B., and A. Garner, "The Resistance of Refiner Plate Alloys to Bar Rounding", *Tappi Journal*, Vol.71, No.6, June 1988, pp.95-100.
20. Thompson, C.B., and A. Garner, "The Metallurgy and Wear of Refiner Plate Alloys", *Tappi Proceedings*, 1985 Engineering Conference, pp.223-231.
21. Thompson, C.B., "The Cavitation Erosion Resistance of Refiner Plate Alloys", *Canadian Pulp and Paper Association 1989 Annual Meeting*, pp.125-135.
22. Clayton, P., and D. Christensen, *J & L (J & L Plate & Machine Works, Inc.) Metallurgical Program Phase II Report*, May 1986.
23. ASTM, "Standard Terminology Relating to Wear and Erosion", in *Annual Book of ASTM Standards*, Vol. 3.02. Wear and Erosion, Metal Corrosion, 1995, pp.145-151.
24. Thompson, C.B., and A. Garner, "Wear Characteristics of Refiner Plates", *Pulp & Paper Canada*, Vol.88, No.8, 1987, pp.80-83.

25. Leider, P.J., and A.H. Nissan, "Understanding the Disk Refiner: The Mechanical Treatment of the Fibers", *Tappi*, Vol.60, No.10, Oct. 1977, pp.85-89.
26. Hartler, N., "Aspects of Energy Reduction in Refiner Mechanical Pulping", *Proc. of the 1979 Int. Mech. Pulping Conf.*, Toronto, Ontario, Canada, June 1979, pp.383-390.
27. Kerekes, R.J., "Characterization of Pulp Refiners by a C-factor", *Nordic Pulp and Paper Research Journal*, No.1, 1990, pp.3-8.
28. Fahey, M.D., "Mechanical Treatment of Chemical Pulps", *Tappi*, Vol.53, No.11, Nov. 1970, pp.2050-2064.
29. Sundholm, J., A. Heikkurinen, and B. Mannstrom, "The Role of Rate of Rotation and Frequency in Refiner Mechanical Pulping", *Proc. of the 1987 Int. Mech. Pulping Conf.*, Vancouver, BC, June 1987, pp.45-51.
30. Arnevik, T.A., "Medium Consistency Post Refining of High Yield Pulps - Compared to Refining in a Double Disk Refiner and a Frotapulper", *Proc. of the 1987 Int. Mech. Pulping Conf.*, Vancouver, BC, June 1987, pp.129-135.
31. Stationwala, M.I., D. Atack, and A. Karnis, "Effect of Refiner Plate Design on the Development of Pulp Properties", *Proc. of the 1987 Int. Mech. Pulping Conf.*, Vancouver, BC, June 1987, pp.1-10.
32. Bergstrom, J., G. Dahlquist, B. Fredriksson, and V. Peterson, "The Design of Refiner Plates", *Pulp and Paper Magazine of Canada*, Vol.73, No.6, January 1972, pp.54-56.
33. Giffin, F.S., "Effect of TMP Primary Refiner Plate Rounding on Pulp Quality and Paper Machine Operation", *Proc. of the 68th Canadian Pulp and Paper Association Technical Section Annual Meeting*, Montreal, Jan. 1982, pp.B157-162.
34. Danforth, D.W., "Effect of Refining Parameters on Paper Properties", *TAPPI/PIMA Northeast Seminar*, Session IV, Paper 11, 1986.
35. Franzen, R.G., "Predicting a Simpler, More Energy Efficient, Less Polluting Process", *Tappi Journal*, Vol.68, No.4, April 1985, pp.69.
36. Clayton, P., and D. Christensen, *J & L (J & L Plate & Machine Works, Inc.) Metallurgical Program Phase III Report*, Nov. 25, 1987.
37. Kettunen, P.O., "Wear and Corrosion Resistant Materials for Refiner Blades", *Proc. of the 4th Int. Symp. on Corrosion in the Pulp and Paper Industry*, Stockholm, Sweden, 1983,

pp.98-102.

38. Mihelich, W.G., D.J. Wild, S.B. Beaulieu, and L.R. Beath, "Single-Stage Chip Refining - Some Major Operating Parameters and Their Effects on Pulp Quality", *Pulp and Paper Magazine of Canada*, Vol.73, No.5, 1972, pp.78-82.
39. Nystrom, E.W., and R.H. Okell, "Sawdust Refining at Crofton", *Pulp and Paper Magazine of Canada*, Vol.70, No.4, 1969, pp.83-87.
40. Beath, L.R., W.G. Mihelich, and D.J. Wild, "Refiner Groundwood - Costs Associated with Plate Life", *Pulp and Paper Magazine of Canada*, Vol.71, No.8, April 1970, pp.73-78.
41. Hill, J., H. Westin, and R. Bergstrom, "Monitoring Pulp Quality for Process Control Purposes", *Proc. of the 1979 Int. Mech. Pulping Conf.*, Toronto, Ontario, Canada, June 1979, pp.111-123.
42. Strand, B.C., and A. Mokvist, "On-line Modelling of Refiner Performance", *Pulp & Paper Canada*, Vol.90, No.12, 1989, pp.216-221.
43. Stationwala, M.I., D. Atack, J.R. Wood, D.J. Wild, and A. Karnis, "The Effect of Control Variables on Refining Zone Conditions and Pulp Properties", *Proc. of the 1979 Int. Mech. Pulping Conf.*, Toronto, Ontario, Canada, June 1979, pp.93-106.
44. Strand, B.C., and A. Mokvist, "Control and Optimization of Conical Disk Refiners", *Proc. of the 1987 Int. Mech. Pulping Conf.*, Vancouver, BC, Canada, June 1987, pp.11-18.
45. Hietanen, S., and K. Ebeling, "A New Hypothesis for the Mechanics of Refining", *Paperi ja Puu (Paper and Timber)*, Vol.72, No.2, 1990, pp.172-176.
46. Eyre, T.S., "Wear Characteristics of Metals", in *Source Book on Wear Control Technology*, American Society for Metals, 1978, pp.1-17.
47. Zum Gahr, K.H., *Microstructure and Wear of Materials (Tribology Series, Vol. 10)*, Elsevier Science Publishers B.V., New York, 1987.
48. Sedriks, A.J., and T.O. Mulhearn, "Mechanics of Cutting and Rubbing in Simulated, Abrasive Processes", *Wear*, Vol.6, 1963, pp.457-466.
49. Mulhearn, T.O., and L.E. Samuels, "The Abrasion of Metals: A Model of the Process", *Wear*, Vol.5, 1962, pp.478-498.
50. Sedriks, A.J., and T.O. Mulhearn, "The Effect of Work-Hardening on the Mechanics

of Cutting in Simulated Abrasive Processes", *Wear*, Vol.7, 1964, pp.451-459.

51. Ludema, K.C., "Selecting Material for Wear Resistance", in *Wear of Materials (Proc. of the Int. Conf. on Wear of Materials)*, S.K. Rhee et al., eds., ASME, New York, 1981, pp.1-6.

52. The ASM Committee on Analysis of Wear Failures, "Wear Failures", in *Metals Handbook, Vol.10, Failure Analysis and Prevention*, 8th Edition, American Society For Metals, Metals Park, Ohio, 1975, pp.134-153.

53. Khruschov, M.M., "Principles of Abrasive Wear", *Wear*, Vol.28, No.1, 1974, pp.69-88.

54. Richardson, R.C.D., "Abrasive Wear by Paper", *Wear*, Vol.14, 1968, pp.423-430.

55. Cole, G.F., "The Prediction of Wear by Paper", *Wear*, Vol.21, No.1, 1972, pp.141-153.

56. Larsen-Basse, J., "On Abrasive Wear by Paper", *Wear*, Vol.14, 1969, pp.133-136.

57. Bayer, R.G., "Aspects of Paper Abrasivity", *Wear*, Vol.100, No.1-3, 1984, pp.517-532.

58. Bayer, R.G., and T.C. Ku, "Abrasive Wear by Paper", *Wear*, Vol.12, 1968, pp.277-288.

59. Bayer, R.G., "Wear of 52100 Steel by Ribbon and Paper", in *Wear of Materials (Proc. of the Int. Conf. on Wear of Materials)*, St. Louis, Missouri, April, 1977, pp.204-210.

60. Richardson, R.C.D., "The Wear of Metals by Relatively Soft Abrasives", *Wear*, Vol.11, 1968, pp.245-275.

61. Budinski, K.G., *Surface Engineering for Wear Resistance*, Prentice Hall, Inc., Englewood Cliffs, New Jersey, 1988.

62. Blau, P.J., *Friction and Wear Transitions of Materials (Materials Science and Process Technology Series)*, by Noyes Publications, 1989.

63. Eyre, T.S., and A. Baxter, "The Formation of White Layers at Rubbing Surfaces", *Tribology*, Vol.5, Dec. 1972, pp.256-261.

64. Hogmark, S., and O. Vingsbo, "Adhesive Mechanisms in the Wear of Some Tool Steels", *Wear*, Vol.38, 1976, pp.341-359.

65. Farrell, R.M., and T.S. Eyre, "The Relationship between Load and Sliding Distance in the Initiation of Mild Wear in Steels", *Wear*, 1970, Vol.15, No.5, pp.359-372.

66. Rogers, M.D., "The Mechanism of Scuffing in Diesel Engines", *Wear*, Vol.15, No.2, 1970, pp.105-116.
67. Welsh, N.C., "Frictional Heating and Its Influence on the Wear of Steel", *J. Appl. Phys.*, Vol.28, No.9, 1957, pp.960-968.
68. Eyre, T.S., and A. Baxter, "The Formation of White Layers at Rubbing Surfaces", in *Source Book on Wear Control Technology*, by American Society for Metals, 1978, pp.142-146.
69. Blau, P.J., Glossary of Terms, *ASM Handbook*, Vol. 18, Friction, Lubrication, and Wear Technology, 1992, pp.1-21.
70. Jahanmir, S., and N.P. Suh, "Mechanics of Subsurface Void Nucleation in Delamination Wear", *Wear*, Vol.44, No.1, 1977, pp.17-38.
71. Suh, N.P., "The Delamination Theory of Wear", *Wear*, Vol.25, No.1, 1973, pp.111-124.
72. Suh, N.P., "An Overview of the Delamination Theory of Wear", *Wear*, Vol.44, No.1, 1977, pp.1-16.
73. Tucker, Jr., R.C., "Wear Failures", in *Metals Handbook*, 9th Edition, Vol.11, American Society for Metals, 1986, pp.145-162.
74. Kosel, T.H., "Solid Particle Erosion", in *ASM Handbook*, Vol. 18, 1992, pp.199-213.
75. Levy, A.V., "The Solid Particle Erosion Behavior of Steel as a Function of Microstructure", *Wear*, Vol.68, No.3, 1981, pp.269-288.
76. Aptekar, S.S., and T.H. Kosel, "Erosion of White Cast Irons and Stellite", in *Wear of Materials (Proc. of the Int. Conf. on Wear of Materials)*, K.C. Ludema, ed., ASME, New York, 1985, pp.677-686.
77. McCabe, L.P., G.A. Sargent, and H. Conrad, "Effect of Microstructure on the Erosion of Steel by Solid Particles", *Wear*, Vol.105, No.3, 1985, pp.257-277.
78. Hammitt, F.G., and F.J. Heymann, "Liquid-Erosion Failures", in *Metals Handbook, Vol.10, Failure Analysis and Prevention*, 8th Edition, American Society For Metals, Metals Park, Ohio, 1975, pp.160-167.
79. Hammit, F.G., "Cavitation and Liquid Impact Erosion", in *Wear Control Handbook*, M.B. Peterson and W.D. Winer, editors, The American Society of Mechanical Engineers, New

York, 1980, pp.161-230.

80. Zhou, Y., and F.G. Hammit, "Vibratory Cavitation Erosion in Aqueous Solutions", *Wear*, Vol.87, No.2, 1983, pp.163-171.

81. Zhou, K.S., and H. Hermann, "Cavitation Erosion of Titanium and Ti-6Al-4V: Effects of Nitriding", *Wear*, Vol.80, 1982, pp.101-113.

82. Essenmacher, D., M.F. Prezkop, D.E. Mikkola, and D.A. Koss, "Cavitation-Induced Erosion of Ti-6Al-4V", *Metall. Trans.*, Vol.9A, No.8, 1978, pp.1069-1074.

83. Vaidya, S., and C.M. Preece, "Cavitation Erosion of Age-Hardened Aluminum Alloys", *Metall. Trans.*, Vol.9A, No.3, 1978, pp.299-307.

84. Riddel, V., P. Pactor, and J.K. Appeldoorn, "Cavitation Erosion and Rolling Contact Fatigue", *Wear*, Vol.27, No.1, 1974, pp.99-108.

85. Tichler, J.W., and D. Scott, "A Note on the Correlation between Cavitation Erosion and Rolling Contact Fatigue Resistance of Ball Bearing Steels", *Wear*, Vol.16, No.3, 1970, pp.229-233.

86. Richman, R.H., A.S. Rao, and D.E. Hodgson, "Cavitation Erosion of two NiTi Alloys", *Wear*, Vol.157, No.2, 1992, pp.401-407.

87. Okada, T., Y. Iwai, and A. Yamamoto, "Cavitation Erosion of Cast Iron in 3% Salt Water", *Wear*, Vol.88, No.2, 1983, pp.167-179.

88. Tomlinson, W.J., J.H.P.C. Megaw, A.S. Bransden, and M. Girardi, "The Effect of Laser Surface Melting on the Cavitation Wear of Gray Cast Iron in Distilled and 3% Salt Waters", *Wear*, Vol.116, No.2, 1987, pp.249-260.

89. Li, Z., and J. Zou, "Effect of Laser Processing on the Cavitation Erosion of Cr-Mo-Cu Alloy Cast Iron", *Wear*, Vol.119, No.1, 1987, pp.13-27.

90. Wade, E.H.R., and C.M. Preece, "Cavitation Erosion of Iron and Steel", *Metall. Trans.*, Vol.9A, No.9, 1978, pp.1299-1310.

91. Preece, C.M., S. Dakshinamoorthy, S. Prasad and B. Vyas, "The Influence of Microstructure on the Cavitation Erosion Resistance of F.C.C. Metals and Alloys", *Proc. of the 4th Int. Conf. on the Strength of Metals and Alloys*, Nancy, France, 1976, pp.1397-1403.

92. Karimi, K., and F. Avellan, "Comparison of Erosion Mechanisms in Different Types of

Cavitation", *Wear*, Vol.113, 1986, pp.305-322.

93. Feller, H.G., and Y. Kharrazi, "Cavitation Erosion of Metals and Alloys", *Wear*, Vol.93, No.3, 1984, pp.249-260.

94. Preece, C.M., S. Vaidya, and S. Dakshinamoorthy, "Influence of Crystal Structure on the Failure Model of Metals by Cavitation Erosion", *ASTM Spec. Tech. Publ. 664*, 1979, pp.409-433.

95. Tomlinson, W.J., and M.G. Talks, "Laser Surface Processing and the Cavitation Erosion of a 16 wt% Cr White Cast Iron", *Wear*, Vol.139, No.2, 1990, pp.269-284.

96. Tomlinson, W.J., and M.G. Talks, "Cavitation Erosion of Laser Surface Melted Phosphoric Gray Irons", *Wear*, Vol.129, No.2, 1989, pp.215-222.

97. Heathcock, C.J., A. Ball, and B.E. Protheroe, "Cavitation Erosion of Cobalt-Based Stellite Alloys, Cemented Carbides and Surface-Treated Alloy Steels", *Wear*, Vol.74, No.1, 1981, pp.11-26.

98. Iwai, Y., T. Okada, T. Fujieda, and K. Awazu, "Effects of Hard Chromium Plating on Cavitation Erosion", *Wear*, Vol.128, No.2, 1988, pp.189-200.

99. Tomlinson, W.J., R.T. Moule, and G.N. Blount, "The Effect of Shot Peening on the Cavitation Erosion of Pure Iron and Austenitic Stainless Steel in Distilled and 1% Salt Water", *Wear*, Vol.118, No.2, 1987, pp.233-242.

100. Lichtman, J.Z., D.H. Kallas, C.K. Chatten, and Cdr. E.P. Cochran, Jr., "Cavitation Erosion of Structural Materials and Coatings", *Corrosion*, Vol.17, No.10, 1961, pp.119-127.

101. Mann, B.S., P.R. Krishnamoorthy, and P. Vivekananda, "Cavitation Erosion Characteristics of Nickel-Based Alloy - Composite Coatings Obtained by Plasma Spraying", *Wear*, Vol.103, No.1, 1985, pp.43-55.

102. Preece, C. M., "Cavitation Erosion", in *Treatise on Materials Science and Technology, Vol.16, Erosion*, C. M. Preece, ed., by Academic Press, New York, 1979, pp.249-308.

103. Heymann, F.J., "A Survey of Clues to the Relationship between Erosion Rate and Impact Parameters", *Proc. of the 3rd Int. Conf. on Rain Erosion and Associated Phenomena*, 1970, pp.683-741.

104. Hancox, N.L., and J.H. Brunton, "The Physics of Impact and Deformation: Multiple Impact", *Phil. Trans. R. Sco.*, Vol. 260. A., 1966, pp.121-139.

105. Hoff, G., G. Langbein, and H. Rieger, "Material Destruction due to Liquid Impact", *ASTM STP 408*, American Society for Testing and Materials, Philadelphia, Pennsylvania, 1967, pp.42-69.
106. Brunton, J.H., and M.C. Rochester, "Erosion of Solid Surfaces by the Impact of Liquid Drops", in *Treatise on Materials Science and Technology, Vol. 16*, C.M. Preece, ed., Academic Press, New York, 1979, pp.185-248.
107. Field, J.E., D.A. Gorham, and D.G. Rickerby, "High-Speed Liquid Jet and Drop Impact on Brittle Targets", in *Erosion: Prevention and Useful Applications*, W.F. Adler, ed., ASTM (American Society for Testing and Standards), 1979, pp.298-319.
108. Heymann, F.J., "Toward Quantitative Prediction of Liquid Impact Erosion", *ASTM STP 474*, American Society for Testing and Materials, 1970, pp. 212-248.
109. Jones, D.A., "Pitting and Crevice Corrosion", in *Principles and Prevention of Corrosion*, MacMillan Publishing Company, a Division of MacMillan, Inc., New York, 1992.
110. Rideout, D.J., R.M. Hopkins, and J. Molgaard, "Corrosion and Wear of Plates in the Production of Refiner Mechanical Pulp", *Pulp & Paper Canada*, Vol.83, No.5, 1982, pp.T134-138.
111. Beaudry, R.N., "Refiner Plate Wear Causes and Corrections", *Appita*, Vol.34, No.2, Sept. 1983.
112. Watson, J.D., P.J. Mutton, and I.R. Sare, "Abrasive Wear of White Cast Irons", *Metals Forum*, Vol.3, No.1, 1980, pp.74-88.
113. Laliberte, L.H., "Corrosion Problems in the Pulp and Paper Industry", in *Proc. of the 1977 Int. Symp. on Pulp and Paper Industry Corrosion Problems*, Denver, Colorado, May 1977, pp.1-11.
114. Scholl, M., and P. Clayton, "Abrasive and Erosive Wear of Some Hypervelocity Air Plasma Sprayed Coatings", *Proc. of the 4th National Thermal Spray Conf.*, Pittsburgh, Pennsylvania, May 1991, pp.39-52.
115. Christensen, D.E., P. Clayton, Y. Jia, D. McMurchie, and M. Scholl, *Improving the Performance of TMP Refiner Plates through Surface Engineering (Forest Products Laboratory Report, Part I)*, Mar. 1992.
116. Evans, J.C.W., "Exclusive Worldwide TMP Survey", *Pulp and Paper*, Vol.52, July 1978, pp.99-108.

117. Dahlqvist, G., "Optimization of TMP Systems", *Proc. of the 1983 Int. Mech. Pulping Conf.*, Washington, DC, 1983, pp.161-175.
118. Clayton, P., M. Scholl, and D.McMurchie, "Potential Use of Plasma Spray Coatings for Wheel/Rail Friction Modification", *AAR (Association of American Railroads) Report*, Oregon Graduate Institute of Science & Technology, June 1995, pp.5.
119. Anderson, C.W., and K.H. Heffner, "Precision Gas Bearing Plasma Sprayed Aluminum Oxide Coating Characterization", *Proc. of the Int. Thermal Spray Conf.*, Orlando, Florida, May 28 - June 6 1992, pp.695-704.
120. Bhushan, B., and B.K. Gupta, *Handbook of Tribology, Materials, Coatings, and Surface Treatments*, McGraw-Hill, Inc., 1991.
121. Kingswell, R., D.S. Rickerby, K.T. Scott, and S.J. Bull, "Comparison of the Erosive Wear Behavior of Vacuum Plasma Sprayed and Bulk Alumina", *Proc. of the 3rd National Thermal Spray Conf.*, Long Beach, California, May 1990, pp.179-191.
122. Steeper, T.J., A.J. Rotolico, J.E. Nerz, W.L. Riggs II, D.J. Varacalle Jr., and G.C. Wilson, "A Taguchi Experimental Design Study of Plasma Sprayed Alumina-Titania Coatings", *Proc. of the 4th National Thermal Spray Conf.*, Pittsburgh, Pennsylvania, May 1991, pp.13-20.
123. Chou, T., J.E. Nerz, B.A. Kushner, Jr., A.J. Rotolico, and W.L. Riggs II, "Design of Experiment Study of Plasma Sprayed Chromium Carbide/Nickel Chromium and Aluminum Oxide Coatings", *Proc. of the 4th National Thermal Spray Conf.*, Pittsburgh, May 1991, pp.3-11.
124. Varacalle, Jr., D.J., "An Analytical Methodology to Predict the Coating Characteristics of Plasma-Sprayed Ceramic Powders", *Proc. of the 3rd National Thermal Spray Conf.*, Long Beach, California, May 1990, pp. 271-283.
125. Steffens, H.D., Z. Babiak, and W. Brandl, "Thermal Barrier Coatings: Some Aspects of Properties Design", *Proc. of the 4th National Thermal Spray Conf.*, Pittsburgh, Pennsylvania, May 1991, pp.289-294.
126. Murakami, K., S. Nakazono, H. Asako, T. Okamoto, and H. Matsumoto, "Thermal Spraying as a Method of Producing Rapidly Solidified Materials", *Proc. of the 3rd National Thermal Spray Conf.*, Long Beach, California, May 1990, pp.351-355.
127. Ito, H., R. Nakamura, M. Shiroyama, and T. Sasaki, "Post-Treatment of Plasma Sprayed WC-Co Coatings by Hot Isostatic Pressing", *Proc. of the 3rd National Thermal Spray Conf.*, Long Beach, California, May 1990, pp.233-238.

128. Willen, W.S., "Parametric Sensitivities of Copper-Nickel-Indium and Inconel 718 Plasma Sprayed Coatings", *Proc. of the 4th National Thermal Spray Conf.*, Pittsburgh, Pennsylvania, May 1991, pp.21-28.
129. Bartnik, Z., P. Bialucki, S. Kozerski, G. Clinton, K. Davies, P. Bork, B. Schrader, F. Guglielmi, and L. Pawlowski, "Improvements in Manufacturing Technology of Wear Resistant Plasma Sprayed Cr₂O₃ Coatings", *Proc. of the Int. Thermal Spray Conf.*, Orlando, Florida, May 28 - June 6 1992, pp.983-993.
130. Smith, R. W., and Z. Z. Mutasim, "Plasma Sprayed Refractory Metal Structures and Properties", *Proc. of the 3rd National Thermal Spray Conf.*, Long Beach, California, May 1990, pp.369-374.
131. Angers, L.M., J.R. Auhl, and T.N. Meyer, "Characterization of Dispersion Strengthened Aluminum Alloys Produced by Plasma Deposition", *Proc. of the 4th National Thermal Spray Conf.*, Pittsburgh, Pennsylvania, May 1991, pp.337-351.
132. Dallaire, S., B. Arsenault, and A. DeSantis, "Investigation of Selected Plasma-Sprayed Coatings for Bonding Glass to Metal in Hermetic Seal Applications", *Proc. of the 4th National Thermal Spray Conf.*, Pittsburgh, Pennsylvania, May 1991, pp.417-423.
133. Karthikeyan, J., R. Ratnaraj, A.J. Hill, Y.C. Fayman, and C.C. Berndt, "A Parametric Study in the Plasma Spraying of YBCO Powder", *Proc. of the 4th National Thermal Spray Conf.*, Pittsburgh, Pennsylvania, May 1991, pp.497-501.
134. Kawase, R., K. Tanaka, T. Hamamoto, and H. Haraguchi, "Study on Elastic Constant and Residual Stress Measurements during Ceramic Coatings", *Proc. of the 3rd National Thermal Spray Conf.*, Long Beach, California, May 1990, pp.339-342.
135. Smith, R.W., Z. Mutasim, E. Lugscheider, R. Limbach, H. Jungklaus, J. Roos, J.P. Celis, M. DeBonte, and S. Economou, "Wear Test Characterization of TiC Reinforced Thermal Sprayed Coatings", *Proc. of the 4th National Thermal Spray Conf.*, Pittsburgh, Pennsylvania, May 1991, pp. 59-66.
136. Y. Wang, and P. Kettunen, "The Optimization of Spraying Parameters for WC-Co Coatings by Plasma and Detonation-Gun Spraying", *Proc. of the Int. Thermal Spray Conf.*, Orlando, Florida, May 28 - June 5 1992, pp.575-580.
137. Nerz, J.E., B.A. Kushner, and A.J. Rotolico, "Taguchi Analysis of Thick Thermal Barrier Coatings", *Proc. of the 3rd National Thermal Spray Conf.*, Long Beach, California, May 1990, pp. 669-673.

138. Mutasim, Z.Z., R.W. Smith, and L. Sokol, "Vacuum Plasma Spray Deposition of WC-Co", *Proc. of the 3rd National Thermal Spray Conf.*, Long Beach, California, May 1990, pp.165-169.
139. Kobayashi, A., "Property of an Alumina coating Sprayed with a Gas Tunnel Plasma Spraying", *Proc. of the Int. Thermal Spray Conf.*, Orlando, Florida, May 28 - June 5 1992, pp.57-62.
140. Nerz, T.C., J.E. Nerz, B.A. Kushner, A.J. Rotolico, and W.L. Riggs, "Evaluation of HEP Sprayed Tungsten Carbide/Cobalt Coating Using Design of Experiment Method", *Proc. of the Int. Thermal Spray Conf.*, Orlando, Florida, May 28 - June 5 1992, pp.405-414.
141. Hermanek, F., and W.L. Riggs, "Iterative Design of Experiments to Optimize Plasma Sprayed Chrome Carbide/Nickel Chromium", *Proc. of the 3rd National Thermal Spray Conf.*, Long Beach, California, May 1990, pp.695-710.
142. Lenling, W.L., M.F. Smith, and J.A. Henfling, "Beneficial Effects of Austempering Post-Treatment on Tungsten Carbide Based Wear Coatings", *Proc. of the 3rd National Thermal Spray Conf.*, Long Beach, California, May 1990, pp.227-232.
143. Ishida, M., M. Sasaki, and H. Seto, "Characteristics of Low Pressure Plasma Sprayed High C-High Cr-Steel", *Proc. of the 4th National Thermal Spray Conf.*, Pittsburgh, PA, May 1991, pp.75-79.
144. Jones, S.A., J.R. Auhl, and T.N. Meyer, "Particulate-Reinforced Aluminum-Based Composites Produced by Low Pressure RF Plasma Spraying", *Proc. of the 4th National Thermal Spray Conf.*, Pittsburgh, PA, May 1991, pp.329-335.
145. Mann, B.S., P.R. Krishnamoorthy, and P. Vivekananda, "Cavitation Erosion Characteristics of Nickel-Based Alloy-Composite Coatings Obtained by Plasma Spraying", *Wear*, Vol.103, No.1, 1985, pp.43-55.
146. Sampath, S., B. Gudmundsson, R. Tiwari, and H. Herman, "Plasma Spray Consolidation of Ni-Al Intermetallics", *Proc. of the 3rd National Thermal Spray Conf.*, Long Beach, California, May 1990, pp.357-361.
147. Kuroda, S., T. Fukushima, and S. Kitahara, "Significance of the Quenching Stress in the Cohesion and Adhesion of Thermally Sprayed Coatings", *Proc. of the Int. Thermal Spray Conf.*, Orlando, Florida, May 28 - June 5 1992, pp.903-909.
148. Mulheran, P.A., J.H. Harding, R. Kingswell, and K.T. Scott, "Modeling the Structure Development in a Plasma Sprayed Coating", *Proc. of the Int. Thermal Spray Conf.*, Orlando,

Florida, May 28 - June 5 1992, pp.749-753.

149. Lugscheider, E., and M. Kuelkens, "Air Plasma Sprayed Coatings of a New Type of H-Phase Containing Hardalloys", *Proc. of the 11th Int. Thermal Spraying Conf.*, Montreal, Canada, Sept. 1986, pp.137-146.

150. Nicoll, A.R., "The Effect of Varying Plasma Gun Nozzle Diameter on the Surface Roughness; Hardness and Bond Strength of Al_2O_3 and Cr_2O_3 Coatings", *Proc. of the National Thermal Spray Conf.*, Cincinnati, OH, Oct. 1988, pp.19-25.

151. Heimann, R.B., D. Lamy, and T.N. Sopkow, "Parameter Optimization of Alumina-Titania Coatings by a Statistical Experimental Design", *Proc. of the 3rd National Thermal Spray Conf.*, Long Beach, California, May 1990, pp.491-501.

152. Slavin, T. P., and J. Nerz, "Material Characteristics and Performance of WC-Co Wear-Resistant Coatings", *Proc. of the 3rd National Thermal Spray Conf.*, Long Beach, California, May 1990, pp.159-164.

153. Taylor, T.A., D.L. Appleby, A.E. Weatherill, and J. Griffiths, "Plasma-Sprayed Yttria-Stabilized Zirconia Coatings: Structure-Property Relationships", *Surface and Coatings Technology*, 43/44, 1990, pp.470-480.

154. Rangaswamy, S., and H. Herman, "Metallurgical Characterization of Plasma Sprayed WC-Co Coatings", *Proc. of the 11th Int. Thermal Spraying Conf.*, Montreal, Canada, Sept. 1986, pp.101-110.

155. Nerz, J.E., R. Kaufold, B.A. Kushner, Jr., and A. Rotolico, "Reduction of Solid Particle Erosion by Using HVOF and HEP Coating Deposition Methods", *Proc. of the 4th National Thermal Spray Conf.*, Pittsburgh, PA, May 1991, pp.67-74.

156. Bhat, H., H. Herman, and M.F. Smith, "Cavitation-Erosion of Plasma-Sprayed Alloys", *Proc. of the Second National Conf. on Thermal Spray*, Long Beach, California, Oct.-Nov. 1984, pp.101-104.

157. Asahi, N., T. Tamamura, T. Iizuka, and T. Nemoto, "Cavitation-Erosion of Plasma-Sprayed Alloys", *Proc. of the 8th Int. Therm. Spraying Conf.*, 1976, Vol.1, pp.259-263.

158. Guo, X., H. Herman, and S. Rangaswamy, "Cavitation-Erosion of Plasma-Sprayed WC/Co", *Proc. of the Eleventh Int. Thermal Spraying Conf.*, Montreal, Canada, Sept. 1986, pp.37-46.

159. Guo, X., and H. Herman, "Cavitation-Erosion Testing of Thermal Sprayed Tribaloy (T-

400) Coatings", *Proc. of the National Thermal Spray Conf.*, Cincinnati, OH, 1988, pp.159-165.

160. *The CRC Materials Science and Engineering Handbook*, J.F. Shackelford and W. Alexander, et., CRC Press, Inc., 1992.

161. Wang, X., "Edge Wear Mechanisms of Woodcutting Tools", *Ph.D. Thesis*, Oregon Graduate Institute of Science and Technology, 1994, pp.171.

162. Dyson, A., "Scuffing", in *Treatise of Materials Science and Technology*, Vol.13, Wear, D. Scott, ed., Academic Press, New York, 1979, pp.175-216.

163. Bird, C.R., "Stainless Steel Casting Alloys", in *Metals Handbook*, Vol.9, Metallography and Microstructures, 9th Edition, American Society For Metals, Metals Park, Ohio, 1985, pp.297-304.